An *Ab-Initio* Approach to
Pairing Phenomena Using
Modern Effective Interactions

Vom Fachbereich Physik
der Technischen Universität Darmstadt

zur Erlangung des Grades
eines Doktors der Naturwissenschaften
(Dr. rer. nat.)

genehmigte Dissertation von
Dipl.-Phys. Heiko Hergert
aus Büdingen

Darmstadt 2008
D17

Abstract

The Unitary Correlation Operator Method (UCOM) and the Similarity Renormalization Group (SRG) allow the derivation of 'tamed' phase-shift equivalent nucleon-nucleon interactions which are a suitable starting point for a wide array of many-body methods, from simple mean-field approaches like Hartree-Fock to the exact No-Core Shell Model. While the UCOM and the SRG are conceptually very different, we explicitly show that the generators of both types of unitary transformations have the same structure, and therefore treat the same kind of physics, i.e., the short-range central and tensor correlations induced by realistic nucleon-nucleon interactions.

Mean-field calculations with the correlated interaction V_{UCOM} yield bound nuclei over the whole mass chart, and by including long-range correlations which are not explicitly described by the UCOM transformation in many-body perturbation theory, very good agreement with experimental binding energies is achieved. In conventional approaches, this is only possible by using phenomenological interactions which are explicitly tailored to mean-field calculations and therefore unable to describe nucleon scattering phase shifts.

To extend our calculations to open-shell nuclei and allow for the treatment of pairing phenomena, we develop a fully consistent Hartree-Fock-Bogoliubov (HFB) approach in this work. Exact and approximate projection techniques are generalized to a simultaneous restoration of the neutron and proton number symmetries, which are broken by the introduction of quasiparticles in the HFB method. The use of V_{UCOM} in this framework enables us to study the pairing properties of nuclei from first principles, and provides insight into the effect of short-range correlations on the pair formation. We present results from the application of the HFB method with and without projection to the study of the tin isotopic chain.

While the effect of three-nucleon forces on the binding energies can be minimized by an appropriately chosen UCOM transformation, the HF and HFB ground states calculated with such a two-body interaction exhibit too-small radii and a low level density, which are caused by the strong non-locality of the corresponding V_{UCOM}. Naturally, the low level density is found to be a strong impediment to pairing. In exploratory HF calculations, a three-nucleon contact force was able to improve the radii and level densities. Since the use of such a force in HFB calculations is more demanding, we approximate it by a zero-range density-dependent two-body interaction in order to assess the impact of three-nucleon effects in our HFB framework.

The ground states obtained from the HFB method serve as the basis for a fully self-consistent Quasiparticle Random Phase Approximations (QRPA), which can be used to study pairing effects on collective excitations. We present selected results on electromagnetic resonances in the tin isotopes, in particular the pygmy dipole resonance in the neutron-rich isotopes ^{130}Sn and ^{132}Sn. In addition, we apply the charge-exchange version of our QRPA to the isobaric analog and Gamow-Teller resonances in ^{90}Zr.

Zusammenfassung

Die Methode der unitären Korrelatoren (UCOM) und die Ähnlichkeits-Renormierungs-gruppe (SRG) stellen mächtige Werkzeuge zur Herleitung von effektiven streuphasenäquivalenten Nukleon-Nukleon-Wechselwirkungen dar. Obwohl sich UCOM und SRG konzeptionell unterscheiden, demonstrieren wir in dieser Arbeit, daß die Generatoren der jeweils eingesetzten unitären Transformationen dieselbe Struktur besitzen und daher dieselbe Physik beschreiben, nämlich kurzreichweitige Zentral- und Tensorkorrelationen, welche von allen realistischen NN-Wechselwirkungen induziert werden.

Mean-Field-Rechnungen mit einer korrelierten Wechselwirkung V_{UCOM} resultieren in gebundenen Kernen in allen Massenbereichen. Werden zusätzlich langreichweitige Korrelationen, die per Konstruktion nicht durch die UCOM-Transformation beschrieben werden, in Vielteilchen-Störungstheorie behandelt, erzielen wir eine gute Übereinstimmung mit experimentellen Bindungsenergien. In konventionellen Zugängen ist dies nur möglich, wenn phänomenologische Wechselwirkungen eingesetzt werden, die mittels eines Fits explizit auf Mean-Field-Rechnungen zugeschnitten sind, daher jedoch zur Beschreibung der NN-Streuphasen völlig ungeeignet sind.

Um unsere Behandlung auf Kerne mit offenen Schalen ausdehnen zu können und die Behandlung von Paarphänomenen zu ermöglichen, entwickeln wir eine völlig konsistente Version der Hartree-Fock-Bogoliubov-Methode. Die durch die Einführung des Quasiteilchen-Bildes explizit gebrochene Teilchenzahl-Symmetrien für Neutronen und Protonen werden durch die Anwendung exakter und näherungsweiser Projektionsmethoden simultan wiederhergestellt. Die Verwendung von V_{UCOM} in diesem Rahmen erlaubt es uns, die Paar-Eigenschaften von Kernen in einem echten Ab-Initio-Kontext zu untersuchen, und dabei den Effekt kurzreichweitiger Korrelationen auf die Bildung von nukleonischen Cooper-Paaren studieren. Wir stellen Resultate aus der Anwendung der HFB-Methode mit und ohne Teilchenzahlprojektion auf die Zinn-Isotopenkette vor.

Während der Einfluss von Dreiteilchenkräften auf die Bindungsenergien durch eine geeignete UCOM-Transformation minimiert werden kann, sind die Radien und Niveaudichten der HF- und HFB-Grundzustände für solch eine reine Zweiteilchen-Wechselwirkung deutlich zu klein, was durch die starke Nicht-Lokalität des entsprechenden V_{UCOM} verursacht wird. Die reduzierte Niveaudichte erweist sich naturgemäß als Hindernis für die Entwicklung einer gepaarten Phase im Grundzustand. Im Rahmen von HF-Rechnungen wurde gezeigt, daß eine abstoßende Dreiteilchen-Kontaktwechselwirkung zur Verbesserung von Radien und Niveaudichten beiträgt. Da die Implementation einer echten Dreiteilchenkraft im Rahmen der HFB-Methode aufwendiger ist als im HF-Fall, verwenden wir eine dichteabhängige Zweiteilchen-Wechselwirkung als Näherung, um den Einfluß von Dreiteilchen-Effekten zu untersuchen.

Die mit der HFB-Methode ermittelten Grundzustände stellen die Grundlage für eine vollständig selbstkonsistente Quasiteilchen-Random-Phase-Approximation (QRPA) dar, mit deren Hilfe der Einfluss von Paar-Korrelationen auf kollektive Anregungen studiert werden kann. Wir zeigen ausgewählte Resultate für elektromagnetische Resonanzen in den Zinn-Isotopen, insbesondere für die Pygmy-Dipolresonanzen in ^{130}Sn und ^{132}Sn. Weiterhin wenden wir die Ladungsaustausch-Variante der QRPA zur Untersuchung der isobarischen Analog- und Gamow-Teller-Resonanzen in ^{90}Zr an.

Meinen Eltern

Adelheid Hergert
(1935 — 1998)

und

Heinrich Hergert

Albert! Stop telling God what to do!

— Attributed to Enrico Fermi

Whatever nature has in store for mankind, unpleasant as it may be, men must accept, for ignorance is never better than knowledge.

— Enrico Fermi

Contents

Introduction

In the Standard Model of Particle Physics, Quantum Chromodynamics (QCD) is the fundamental theory of the strong interaction, describing the interaction of quarks and gluons. While QCD can be handled perturbatively at high energies due to the so-called asymptotic freedom, the perturbative treatment breaks down in the low-energy regime relevant for nuclear structure. Moreover, it is an empirically established fact that QCD is confining: while quarks and gluons carry individual color charges, only color-neutral bound states of quarks, the baryons and mesons, appear in the physical spectrum in this energy regime. Hence, nucleons and π-mesons, being the lightest particles of the respective classes, constitute the appropriate degrees of freedom for an *effective* theory of the strong interaction in the domain of nuclear structure.

The most consistent approach to such an effective theory is given by chiral effective field theory (EFT), which has been developed systematically over the past two decades. Prior to this, the key ingredient in *ab initio* studies of nuclear structure are realistic nucleon-nucleon interactions, which reproduce the experimental two-nucleon observables such as scattering phase-shifts with high precision. There has been a variety of approaches to the construction of such interactions, ranging from the combination of the well-established one-pion exchange with phenomenological short-range terms in the case of Argonne V18 [1], to the refined meson-exchange picture underlying CD-Bonn [2] (reviews can be found in [3, 4]).

Generally, when used, e.g., in a No-Core Shell Model (NCSM) framework [5], these interactions exhibit very slow convergence with increasing model-space size due to the strong central and tensor correlations induced by the realistic NN interactions [6]. These correlations give rise to large off-diagonal matrix elements which connect the low-energy and low-momentum states of the model space with very high-lying states which are typically not included in the model space. While one can still obtain well-converged results for light nuclei, the situation becomes worse as the model space size grows for larger nuclei. Eventually, we have to rely on mean-field approaches like Hartree-Fock, which describes the nucleus as a single Slater determinant of independent particles. In the shell-model language, the Hartree-Fock approximation corresponds to the use of a one-dimensional many-body Hilbert space, which is unable to describe correlations at all. Consequently, Hartree-Fock calculations with realistic interactions do not yield bound nuclei.

In order to address this issue, different schemes have been proposed to derive soft effective interactions that preserve the physically constrained properties of the original potential, i.e., the phase-shifts and deuteron properties. The Unitary Correlation Operator Method (UCOM) [7, 8], was devised as a means to describe the dominant

correlations induced by the short-range repulsion and the tensor interaction by an explicit unitary transformation. The unitary transformation of the Hamiltonian leads to a phase-shift equivalent correlated interaction V_{UCOM} which is suitable for simple model spaces. It has been successfully employed in a wide range of many-body calculations, from the No-Core Shell Model to Hartree-Fock and its extensions [6, 9, 10, 11, 12]. In these calculations, one benefits from the dramatically improved convergence behavior of the correlated interaction, which results from a pre-diagonalization of the interaction in momentum space. The observed band-diagonal structure indicates that low and high momenta have been decoupled.

Recently, Bogner *et al.* [13, 14] have proposed the application of the Similarity Renormalization Group (SRG) to the NN interaction, and demonstrated the derivation of an effective interaction in this framework. The SRG employs a continuous unitary transformation whose generator is dynamically determined by solving an RG flow equation to band-diagonalize a given parent interaction in momentum space. The resulting effective interaction is qualitatively similar to V_{UCOM}, which prompted an investigation of the underlying connection between both methods [15].

The ability to use an interaction which explicitly preserves the NN phase shifts in Hartree-Fock and methods like many-body perturbation theory (MBPT) or the Random Phase Approximation (RPA) opens up new perspectives for a truly unified description of nuclear structure. While computationally effective and often successful in describing nuclear bulk properties, the phenomenological interactions of the Gogny and Skyrme type (see [16]) are fit to experimental binding energies and nuclear matter properties, and therefore obscure the connection to the more fundamental NN interaction. A prominent example is the tensor interaction, which has long been neglected in fits of phenomenological density-dependent forces. While the effect of short-range tensor correlations on nuclear binding energies can be simulated by an adjustment of the fit parameters of the phenomenological interaction [17, 18], such a procedure will not properly account for the implications of these correlations for other observables.

The experimental observation of the odd-even mass staggering is one of many fingerprints for superfluidity in the nucleus. Other indications can be found in the systematics of rotational spectra, where superfluidity affects the nuclear moment of inertia, the formation of $2n$ or $4n$ halos as the neutron dripline is approached in light nuclei, etc. (see the recent review [19], for instance). In solid state physics, BCS theory [20] provides a useful theoretical tool for the description of superconductivity and other phenomena related to the formation of phases of paired fermions, and it was realized early on that it could be adapted to the setting of the nuclear many-body problem. There is, however, a notable difference between the both cases: while the electrons in a solid repel each other and the formation of Cooper pairs is only possible due to the attractive interaction induced by their interaction with the ionic lattice, the interaction between nucleons is attractive by itself. Moreover, the NN interaction has a rich structure, which leads to more diverse pairing phenomena like the competition of like-nucleon and proton-neutron pairing.

The proper generalization of the HF method to allow the description of pairing in nuclei is given by the Hartree-Fock-Bogoliubov approach, which treats particle-hole and particle-particle type interactions on the same footing in a quasiparticle mean-field picture [21]. As in the Hartree-Fock case, such a mean-field theory is only the initial step
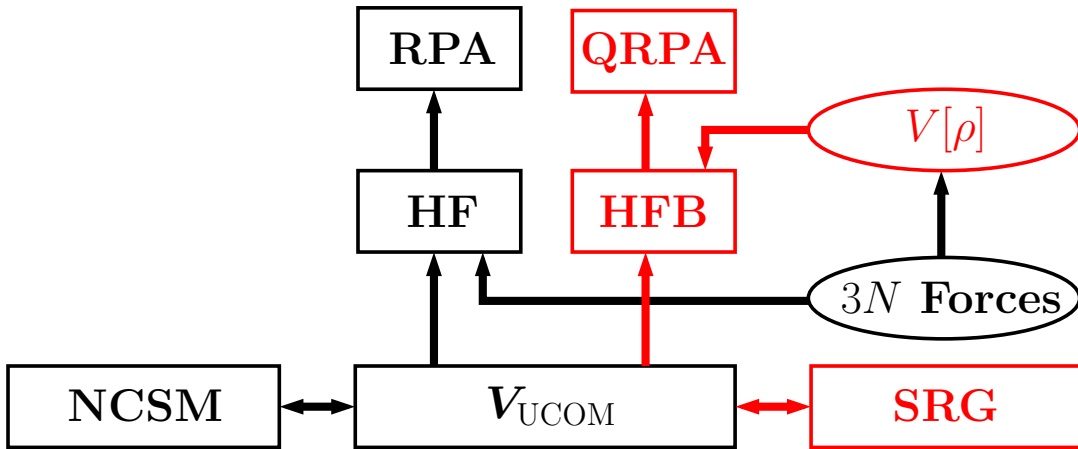
Figure 1: Simplified schematic of the UCOM framework.

towards a description of nuclear structure. A first refinement is suggested by considering the breaking of the particle-number symmetry in the HFB ground state, which is clearly inappropriate for a finite system like the nucleus. Since the intrinsic ground state is a superposition of states with different particle numbers, one can carry out a particle-number projection (PNP) on the component corresponding to the nucleus of interest [21]. The resulting projected HFB ground state is a superposition of quasiparticle Slater determinants, and therefore able to describe pairing correlations beyond the simple mean-field approach.

Another natural extension is the construction of the Quasiparticle Random Phase Approximation (QRPA) based on the HFB ground state, which provides a unified treatment of particle-hole as well as particle-particle and hole-hole excitations. This framework allows the study of the impact of pairing correlations on collective excitations.

The developments presented in this work are shown in the context of the UCOM framework in Fig. 1. As described above, HFB with and without particle-number projection and QRPA allow the extension of nuclear structure studies away from closed-shell nuclei. The numerical development proceeded roughly in parallel to the standard HF and RPA cases. The inclusion of a $3N$ contact force in HF calculations is a more recent development [22], which motivated the inclusion of a density-dependent two-body interaction in the HFB and PNP approaches to account for $3N$ effects in an approximate manner. Similarly, the exploration of the connection between the SRG and UCOM approaches has begun only recently. Early results from using the SRG to optimize the UCOM correlators show great promise [23].

This work is organized as follows. Chapter 1 introduces the UCOM and SRG approaches to the derivation of 'tamed' effective interactions V_{UCOM} and V_α, respectively. The relation between both methods is explored, and the momentum space matrix elements of the effective interactions are compared in some detail. The optimization of the main parameters of these interactions — the tensor correlator ranges of V_{UCOM}, and the SRG flow parameter α — is discussed in the framework of No-Core Shell Model calculations for few-body systems. The chapter ends with some remarks on the role and nature of many-body forces in the nuclear many-body problem.

In Chapter 2, the UCOM and SRG interactions are applied in Hartree-Fock calculations. Improved descriptions of ground-state correlations by means of many-body perturbation theory (MBPT) and the Random Phase Approximation (RPA) are reviewed briefly, as is the inclusion of $3N$ forces for the simple case of a contact force.

Chapter 3 introduces Hartree-Fock-Bogoliubov theory. Exact and approximate particle-number projection (PNP) methods are derived for simultaneous projection on sharp proton and neutron numbers. Since the use of $3N$ forces in our HFB implementation is presently not feasible numerically, a density-dependent two-body interaction is introduced to account for $3N$ effects. Technical aspects as well as problems of the particle-number projection with density-dependent interactions are discused.

Results from HFB calculations with and without (PNP) are presented in Chapter 4. First, we perform calculations with the established Gogny interactions in order to test our implementation and disentangle the effects of the many-body methods from the particular properties of V_{UCOM}. Subsequently, we discuss results from HFB and HFB+PNP calculations with V_{UCOM} as well as V_{UCOM} with an additional density-dependent interaction.

Chapter 5 outlines the derivation of the Quasiparticle Random Phase Approximation (QRPA) for like-particle and charge-exchange excitations, and gives some details on our implementation. First results from QRPA calculations of various electromagnetic as well as charge-exchange resonances are presented.

The results of this work are summarized in Chapter 6, and an outlook on future developments is given.

Various appendices collect material which supplements the theoretical presentation in the main body of this work. Appendix A collects UCOM formulae, including commutators required for the derivation of the operator representation of V_{UCOM} and reduced matrix elements for its non-typical operators. Appendix B deals with the derivation of HFB theory for explicit spherical symmetry, including phase factors, and gives expressions for reduced densities, fields, and matrix elements. The derivation of various expressions appearing in exact PNP as well as the approximate Lipkin-Nogami method is carried out in detail in Appendix C. Appendix D list formulae used in the QRPA for reference, in particular the reduced matrix elements of the transition operators. In Appendix E, we give some details on the calculation of interaction matrix elements, including the Talmi transformation, and the two-body matrix elements of the density-dependent interaction. The parameters of AV18 and the used Gogny interactions are provided for reference, and the two-body matrix element of the Gogny- and Skyrme-type zero-range spin-orbit force is derived in the relative HO basis for use with our matrix element codes. Conventions, Acronyms, etc. are summarized in Appendix F.

Chapter 1

Modern Effective Interactions

1.1   The Unitary Correlation Operator Method

Modern realistic nucleon-nucleon interactions induce strong correlations in the two-nucleon system, which are manifest in the deuteron solution. The deuteron two-body density shown in Fig. 1.1 exhibits two distinct features: a strong suppression at small inter-particle distances, caused by the repulsive core of the interaction, as well as a strong dependence on the relative distance and the spin alignments of the nucleon pair, which leads to the characteristic doughnut and dumbbell shapes for anti-parallel and parallel spins, respectively. The latter are due to the mixing of different orbital angular momenta caused by the action of the tensor force in the spin triplet channels.

In order to describe these properties, one could either use a very large Hilbert space, implying a prohibitive computational effort, or a space of tractable size and treat these types of correlations explicitly. In the Unitary Correlation Operator Method (UCOM) we choose the latter approach and imprint correlations onto the many-body states by means of a suitable unitary transformation. While the general idea of treating correlations in this manner is not new, the UCOM differs from older approaches by using an explicit ansatz for the generators of the transformation, which is motivated by the physics of the problem and designed to conserve the symmetries of the NN interaction. In the following sections, we will outline the construction of the generators and the corresponding correlation operators in the two-nucleon system, and then discuss the implications for the many-body system.

1.1.1   The Correlation Operators

In order to generate a short-range correlation hole in a simple model state, one needs to construct an operator which shifts the nucleons out of the range of the repulsive core. Since this shift has to occur in the radial direction, along the relative distance vector $\boldsymbol{r}$ of the two nucleons, the obvious choice is to use the radial momentum operator

$$q_r = \frac{1}{2} \left(\mathbf{q} \cdot \hat{\mathbf{r}} + \hat{\mathbf{r}} \cdot \mathbf{q} \right) , \quad \hat{\mathbf{r}} = \frac{\mathbf{r}}{r} , \tag{1.1}$$
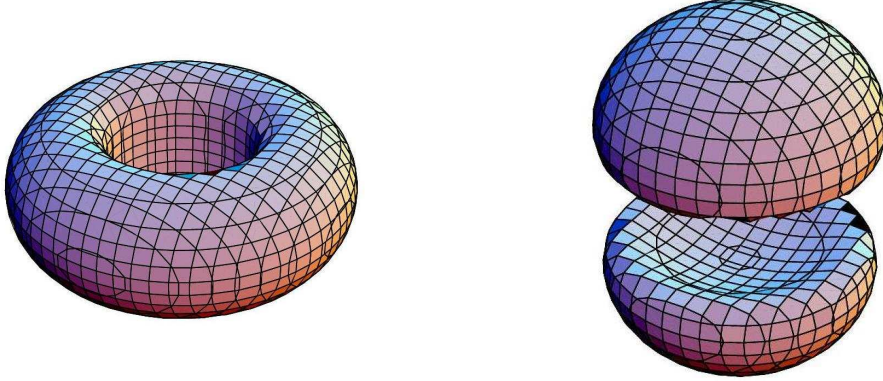
$$S = 1, M_S = 0, \ |\chi\rangle = \tfrac{1}{\sqrt{2}}\left(|\uparrow\downarrow\rangle + |\downarrow\uparrow\rangle\right) \qquad S = 1, M_S = \pm 1, \ |\chi\rangle = |\uparrow\uparrow\rangle, |\downarrow\downarrow\rangle$$

Figure 1.1: Spin-projected two-body density of the AV18 deuteron solution. Shown are the isodensity surfaces at $\rho^{(2)}_{1M_S} = 0.005$ fm^{-3}.

(see Appendix A.1) to construct the generator g_r[1]. The strength of the shift is modeled by an r-dependent function $s(r)$, because it needs to be large for relative distances smaller than the core radius, and small at large distances. A suitable Hermitian generator reflecting the spin and isospin symmetries of the NN interaction is then given by [7, 24]

$$g_r \equiv \sum_{ST} \frac{1}{2}\left(q_r s_{ST}(r) + s_{ST}(r) q_r\right) \Pi_{ST} = \sum_{ST} \left(s_{ST}(r) q_r - \frac{i}{2} s'_{ST}(r)\right) \Pi_{ST}\,, \qquad (1.2)$$

where Π_{ST} projects on the spin S and isospin T of the nucleon pair. The corresponding central correlation operator in two-body space reads

$$c_r \equiv e^{-ig_r}\,. \qquad (1.3)$$

The tensor correlations in the NN system are a result of the strong interdependence between the spin of the neutron pair and its relative distance vector which is caused by the tensor operator

$$s_{12}(\hat{\mathbf{r}}, \hat{\mathbf{r}}) = 3(\boldsymbol{\sigma}_1 \cdot \hat{\mathbf{r}})(\boldsymbol{\sigma}_2 \cdot \hat{\mathbf{r}}) - \boldsymbol{\sigma}_1 \cdot \boldsymbol{\sigma}_2\,. \qquad (1.4)$$

The spin and coordinate space parts of $s_{12}(\hat{\mathbf{r}}, \hat{\mathbf{r}})$ are rank 2 tensor operators, coupled to a rotationally invariant operator. The generator of tensor correlations g_Ω needs to have a similar structure in order to reproduce the particular correlations caused by $s_{12}(\hat{\mathbf{r}}, \hat{\mathbf{r}})$. Since g_Ω evidently has to generate angular shifts of the probability density, as seen in Fig. 1.1, the $\hat{\mathbf{r}}$ operators need to be replaced by the so-called *orbital momentum operator*

$$q_\Omega \equiv \frac{1}{2r}(\mathbf{l} \times \hat{\mathbf{r}} - \hat{\mathbf{r}} \times \mathbf{l})\,, \qquad (1.5)$$

---

[1]Small letters will be used to indicate n-body operators acting in n-body space, while operators in Fock space will be denoted by large letters, see Appendix F.

which is the remainder of the relative momentum after subtraction of the radial component. Although $\mathbf{q}_\Omega$ and $\mathbf{q}_r$ are perpendicular, the two operators *do not commute* (see Appendix A.1) because of the explicit r-dependence of (1.5). Constructing an appropriate rank 2 tensor operator with $\mathbf{q}_\Omega$ and combining it with the spin-space tensor operator, one obtains

$$s_{12}(\mathbf{r}, \mathbf{q}_\Omega) = \frac{3}{2} \left((\boldsymbol{\sigma}_1 \cdot \mathbf{r})(\boldsymbol{\sigma}_2 \cdot \mathbf{q}_\Omega) + (\boldsymbol{\sigma}_1 \cdot \mathbf{q}_\Omega)(\boldsymbol{\sigma}_2 \cdot \mathbf{r}) \right) , \tag{1.6}$$

and from this the generator [8]

$$g_\Omega \equiv \sum_T \vartheta_T(\mathrm{r}) s_{12}(\mathbf{r}, \mathbf{q}_\Omega) \Pi_{1T} , \tag{1.7}$$

where the tensor correlation function $\vartheta_T(r)$ regulates the strength and range of the unitary transformation, similar to the radial shift function $s_{ST}(r)$.

1.1.2 Correlated Wavefunctions

To demonstrate the effect of the correlation operators, we consider a state describing a nucleon pair with coupled angular momenta $\left| \phi(LS)JM \right\rangle$. The isospin quantum numbers T and M_T are omitted for brevity, as are the center-of-mass coordinates, which are not affected by the correlation operators. In coordinate representation, the application of c_r resembles a norm-conserving coordinate transformation of the radial wavefunction [6, 24, 7],

$$\left\langle r \middle| c_r \middle| \phi \right\rangle = \frac{R_-(r)}{r} \sqrt{R'_-(r)} \left\langle R_-(r) \middle| \phi \right\rangle \tag{1.8}$$

and

$$\left\langle r \middle| c_r^\dagger \middle| \phi \right\rangle = \frac{R_+(r)}{r} \sqrt{R'_+(r)} \left\langle R_+(r) \middle| \phi \right\rangle , \tag{1.9}$$

where the so-called *correlation functions* $R_\pm(r)$ are mutually inverse:

$$R_\pm[R_\mp(r)] = r ; \tag{1.10}$$

the (S, T)-dependence of the correlation functions has been suppressed for brevity again. Eqs. (1.8) and (1.9), together with this inversion property, reflect the unitarity of the transformation generated by g_r.

The correlation functions are connected to the shift function $s(r)$ by the integral equation

$$\int_r^{R_\pm(r)} \frac{d\xi}{s(\xi)} = \pm 1 , \tag{1.11}$$

which implies

$$R_\pm(r) \approx r \pm s(r) \tag{1.12}$$

for a weakly r-dependent $s(r)$. Hence, $s(r)$ can be interpreted as the distance of the radial shift of two nucleons at a relative distance r in this approximation. Although
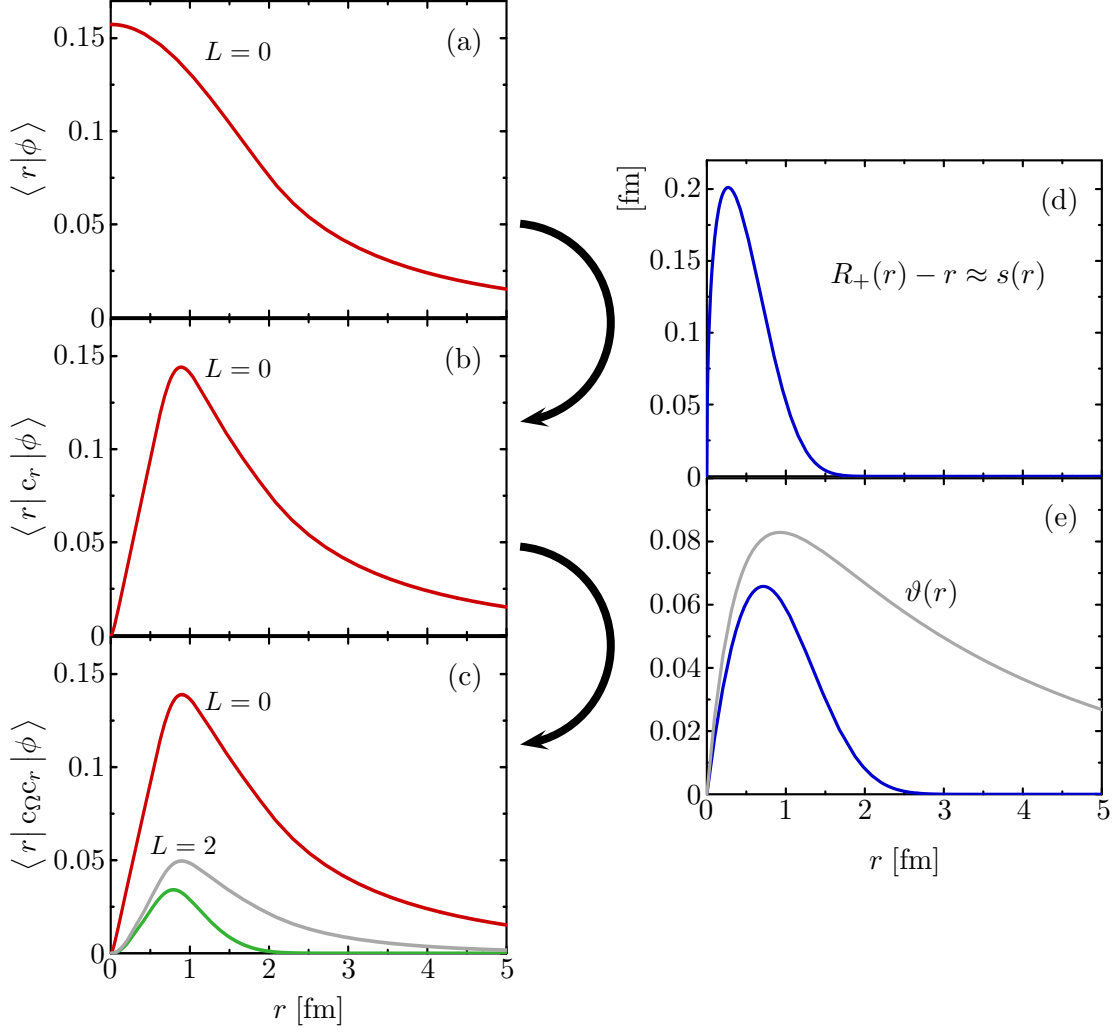
Figure 1.2: Action of the correlation operators. (a) Uncorrelated, (b) central correlated, and (c) fully correlated radial wavefunctions, as well as the corresponding (d) central and (e) tensor correlation functions (see text). The grey lines are the AV18 deuteron wavefunction $L = 2$ component and corresponding $\vartheta(r)$, respectively.

$s(r)$ appears in the generators, all transformed quantities depend only on $R_\pm(r)$ or their derivatives, hence it is simpler to actually specify a correlator by $R_+(r)$ ($R_-(r)$ is then fixed by the condition (1.10)). In fact, the notion 'central correlator' will be used synonymously for both the correlation function and the operator in the remainder of this work.

The tensor correlator, does not affect the radial part of the wavefunction at all, but leads to a mixing of orbital angular momenta in the angular part. Since the matrix elements of $s_{12}(\mathbf{r}, \mathbf{q}_\Omega)$ are given by (cf. Appendix A.3.4)

$$\left\langle \phi(J \pm 1, 1)J \middle| s_{12}(\mathbf{r}, \mathbf{q}_\Omega) \middle| \phi(J \mp 1, 1)J \right\rangle = \pm 3i\sqrt{J(J+1)}, \qquad (1.13)$$

total angular momentum is conserved, and the matrix exponential can be carried out in a given finite-dimensional J-subspace. Thus, for angular-momentum eigenstates with

$L = J \pm 1$, the tensor-correlated state is given by [8]

$$c_\Omega \left| \phi(J \pm 1, 1)J \right\rangle = \cos\theta_J(r) \left| \phi(J \pm 1, 1)J \right\rangle \mp \sin\theta_J(r) \left| \phi(J \mp 1, 1)J \right\rangle, \qquad (1.14)$$

with

$$\theta_J(r) = 3\sqrt{J(J+1)}\vartheta(r), \qquad (1.15)$$

and states with $L = J$ remain unaffected because the generator g_Ω has no diagonal matrix elements. It is important to notice that the L-dependence of the radial wavefunction is *not* affected by this transformation, since the shift occurs *in the angular variables only*.

Figure 1.2 illustrates how the effect of the central and tensor correlators changes a simple two-nucleon trial wavefunction into an almost realistic deuteron solution. Starting from a simple s-wave trial state $\left| \phi(LS)JT \right\rangle = \left| \phi(01)10 \right\rangle$ in the $(S,T) = (1,0)$ channel whose radial wavefunction is shown in Fig. 1.2(a), we apply the central correlator with the correlation function $R_+(r)$ depicted in Fig. 1.2(d), and obtain the central correlated radial wavefunction $\left\langle r \right| c_r \left| \phi \right\rangle$ (Fig. 1.2(b)). The radial wavefunction is now suppressed at short distances, which is due to the short range correlations induced by the repulsive core of the interaction. The subsequent application of the tensor correlator creates a d-wave admixture to the trial state, i.e., a radial wavefunction with $L = 2$, and the structure of the resulting wavefunction matches that of the deuteron. Compared to the d-wave component of the AV18 deuteron solution, which is also shown in the figure, the correlated d-wave wavefunction is of significantly shorter range. Recall that the aim of the UCOM is to describe only *short-range correlations* by means of the correlation operators, although one could obtain the full long-range deuteron solution by using the corresponding correlation function shown in Fig. 1.2(e). We will discuss this subject more extensively in Sect. 1.1.5.

1.1.3 Correlations in the Many-Body System — Cluster Expansion

The discussion of the previous sections was focusing on the two-nucleon system to introduce the correlation operators. The generalization of c_r and c_Ω to the many-nucleon system is straightforward: one simply has to take the correlations in all possible nucleon pairs into account, i.e.,

$$C_r \equiv \exp\left(-i\sum_{i<j} g_{r,ij}\right), \qquad (1.16)$$

$$C_\Omega \equiv \exp\left(-i\sum_{i<j} g_{\Omega,ij}\right), \qquad (1.17)$$

where $i, j = 1, \dots, A$. From the definitions (1.16) and (1.17), it is clear that a correlated wavefunction will not only contain two-body, but up to A-body correlations. Since such wavefunctions become increasingly complicated with the number of particles involved, it is technically more advantageous to make use of the unitarity of the correlation operators, and switch to correlated operators, i.e.,

$$\left\langle \widetilde{\Psi} \right| O \left| \widetilde{\Psi}' \right\rangle = \left\langle \Psi \right| C_r^\dagger C_\Omega^\dagger O C_\Omega C_r \left| \Psi' \right\rangle = \left\langle \Psi \right| \widetilde{O} \left| \Psi' \right\rangle. \qquad (1.18)$$

In the remainder of this chapter, the tilde will be used to indicate the application of the correlation operators to either a many-body state or operator.

As in other effective-interaction methods like the Lee-Suzuki approach, the correlated operator now contains contributions from up to A-body clusters. Starting from an i-body operator O and denoting *irreducible* contributions with particle number k by $\widetilde{O}^{[k]}$, one can define a *cluster expansion* of the correlated operator,

$$\widetilde{O} = C^{\dagger}OC = \sum_{k=i}^{A} \widetilde{O}^{[k]} \,, \tag{1.19}$$

where the $\widetilde{O}^{[k]}$ are defined recursively by

$$\widetilde{O}^{[n]} = \widetilde{O} - \sum_{k=2}^{n-1} \widetilde{O}^{[k]} \,, \quad \widetilde{O}^{[i]} = O \,, \tag{1.20}$$

and it is clear that irreducible contributions with $k < i$ vanish.

For practical applications, one would like to truncate the cluster expansion as early as the two-body level, since already the three-body cluster contributions are very involved. This *two-body approximation* will be justified if the density of the system and the range of the correlators are sufficiently small, so that the mean particle distance is larger than the correlator range. This constraint needs to be considered when the correlation functions are constructed, and will be addressed in Sect. 1.1.5.

1.1.4   The Correlated Interaction V_{UCOM}

Let us now apply the correlation operators to the nuclear many-body Hamiltonian, considering only a NN interaction for the time being — the generalization for 'genuine' $3N$ or higher many-nucleon forces is obvious. The correlated Hamiltonian then defines the correlated NN interaction (and the corresponding $3N, 4N, \dots$ interactions) by collecting all terms of a given cluster order:

$$\widetilde{H} = \widetilde{T}^{[1]} + \widetilde{T}^{[2]} + \widetilde{V}^{[2]} + \widetilde{T}^{[3]} + \widetilde{V}^{[3]} + \dots \equiv T + V_{\text{UCOM}} + V_{\text{UCOM}}^{[3]} + \dots \,. \tag{1.21}$$

Note that the kinetic energy generates contributions to all cluster orders because its relative part is affected by the correlators; these terms are absorbed in the definition of V_{UCOM}.

In the two-body approximation introduced in the previous section, it is sufficient to consider the correlated interaction in the two-nucleon system. For the bare NN interaction, we assume the following form:

$$v = \sum_{p} \frac{1}{2} \left(v_p(r) o_p + o_p v_p(r) \right) \,, \tag{1.22}$$

where the set of operators

$$o_p \in \big\{ \mathbb{1}, \; \boldsymbol{\sigma}_1 \cdot \boldsymbol{\sigma}_2, \; q_r^2, \; q_r^2 \boldsymbol{\sigma}_1 \cdot \boldsymbol{\sigma}_2, \; l^2, \; l^2 \boldsymbol{\sigma}_1 \cdot \boldsymbol{\sigma}_2, $$
$$l \cdot s, \; s_{12}(\hat{\mathbf{r}}, \hat{\mathbf{r}}), \; s_{12}(l, l) \big\} \otimes \{1, \; \boldsymbol{\tau}_1 \cdot \boldsymbol{\tau}_2\} \tag{1.23}$$

is sufficient to express most of the current realistic potentials like AV18 [1], Bonn-A/B [25], or Nijmegen I/II [26] in operator form, but charge-dependence is omitted for the sake of simplicity at this point. Thus, we have the Hamiltonian

$$\mathrm{h} = \mathrm{t_{cm}} + \mathrm{t_{rel}} + \mathrm{v} \,, \tag{1.24}$$

where we have split the kinetic energy operator into a relative and a center-of-mass contribution, which is not affected by the correlation operators. For the evaluation of the correlated Hamiltonian, we use the unitarity of the correlators and rewrite it as

$$\mathrm{c}_r^\dagger \mathrm{c}_\Omega^\dagger \mathrm{h c}_\Omega \mathrm{c}_r = \left(\mathrm{c}_r^\dagger \mathrm{c}_\Omega^\dagger \mathrm{c}_r \right) \left(\mathrm{c}_r^\dagger \mathrm{h c}_r \right) \left(\mathrm{c}_r^\dagger \mathrm{c}_\Omega \mathrm{c}_r \right) = \left(\mathrm{c}_r^\dagger \mathrm{c}_\Omega \mathrm{c}_r \right)^\dagger \left(\mathrm{c}_r^\dagger \mathrm{h c}_r \right) \left(\mathrm{c}_r^\dagger \mathrm{c}_\Omega \mathrm{c}_r \right)$$

$$= \widetilde{\mathrm{c}}_\Omega^\dagger \left(\mathrm{c}_r^\dagger \mathrm{h c}_r \right) \widetilde{\mathrm{c}}_\Omega = e^{i\widetilde{\mathrm{g}}_\Omega} \left(\mathrm{c}_r^\dagger \mathrm{h c}_r \right) e^{-i\widetilde{\mathrm{g}}_\Omega} \,, \tag{1.25}$$

where

$$\widetilde{\mathrm{c}}_\Omega = \mathrm{c}_r^\dagger \mathrm{c}_\Omega \mathrm{c}_r = \vartheta(R_+(\mathrm{r})) \mathrm{s}_{12}(\mathbf{r}, \mathbf{q}_\Omega) \,. \tag{1.26}$$

When we are working in an angular momentum eigenbasis, it is most convenient to apply $\widetilde{\mathrm{c}}_\Omega$ to the state (cf. Eq. (1.14)) in order to obtain correlated matrix elements (see Appendix A.2 and Ref. [6]). Otherwise, the fully correlated Hamiltonian (1.25) can be calculated by using the Baker-Campbell-Hausdorff formula,

$$e^{i\widetilde{\mathrm{g}}_\Omega} \left(\mathrm{c}_r^\dagger \mathrm{h c}_r \right) e^{-i\widetilde{\mathrm{g}}_\Omega} = \left(\mathrm{c}_r^\dagger \mathrm{h c}_r \right) + i \left[\widetilde{\mathrm{g}}_\Omega, \left(\mathrm{c}_r^\dagger \mathrm{h c}_r \right) \right] + \frac{i^2}{2} \left[\widetilde{\mathrm{g}}_\Omega, \left[\widetilde{\mathrm{g}}_\Omega, \left(\mathrm{c}_r^\dagger \mathrm{h c}_r \right) \right] \right] + \dots \,. \tag{1.27}$$

Unfortunately, the series (1.27) only terminates for the operators r, q_r, and q_r^2, while the commutators of operators like $\mathbf{l}^2$ or $\mathbf{l} \cdot \mathbf{s}$ with $\mathrm{s}_{12}(\mathbf{r}, \mathbf{q}_\Omega)$ generate increasing powers of orbital angular momentum and non-local tensor operators (see Appendix A.3). The explicit operator representation of the correlated interaction is given by

$$\mathrm{v_{UCOM}} \equiv \mathrm{c}_r^\dagger \mathrm{c}_\Omega^\dagger \mathrm{h c}_\Omega \mathrm{c}_r - (\mathrm{t_{cm}} + \mathrm{t_{rel}}) = \sum_p \frac{1}{2} \left(\widetilde{v}_p(\mathrm{r}) \widetilde{\mathrm{o}}_p + \widetilde{\mathrm{o}}_p \widetilde{v}_p(\mathrm{r}) \right) \,, \tag{1.28}$$

with an expanded set of operators

$$\widetilde{\mathrm{o}}_p \in \big\{ \mathbb{1}, \; \boldsymbol{\sigma}_1 \cdot \boldsymbol{\sigma}_2, \; \mathrm{q}_r^2, \; \mathrm{q}_r^2 \boldsymbol{\sigma}_1 \cdot \boldsymbol{\sigma}_2, \; \mathbf{l}^2, \; \mathbf{l}^2 \boldsymbol{\sigma}_1 \cdot \boldsymbol{\sigma}_2, \mathbf{l} \cdot \mathbf{s}, \; \mathrm{s}_{12}(\hat{\mathbf{r}}, \hat{\mathbf{r}}), \; \mathrm{s}_{12}(\mathbf{l}, \mathbf{l}),$$

$$\bar{\mathrm{s}}_{12}(\mathbf{q}_\Omega, \mathbf{q}_\Omega), \; \mathbf{l}^2 \mathbf{l} \cdot \mathbf{s}, \; \mathrm{q}_r \mathrm{s}_{12}(\mathbf{r}, \mathbf{q}_\Omega), \; \mathbf{l}^2 \bar{\mathrm{s}}_{12}(\mathbf{q}_\Omega, \mathbf{q}_\Omega), \dots \big\} \otimes \{ 1, \; \boldsymbol{\tau}_1 \cdot \boldsymbol{\tau}_2 \} \,. \tag{1.29}$$

Operators which appear in the BCH series up to third order are listed explicitly in (1.29), while dots indicate higher order contributions. Usually, the BCH series is truncated at third order [8, 18], which is sufficient to provide very good agreement with the exact matrix elements obtained by applying the tensor correlator to the states. While the higher-order terms grow rapidly in higher partial waves due to their strong angular momentum-dependence, their radial dependencies are very short-ranged because they are generated by the correlation operators, and the suppression due to the strong centrifugal barrier prevents the two-nucleon wavefunctions from probing these interactions.

1.1.5 Optimal Correlation Functions and Range Constraints

With the formalism for the treatment of central and tensor correlations set up, the task of actually determining the UCOM correlation functions for a given interaction — in our case, the AV18 potential — remains. The current approach to their construction is based on an energy minimization in the lowest partial wave of each (S,T)-channel of the two-nucleon system [8, 6] using simple trial states like the free zero-energy scattering solutions $\phi_L(r) \sim r^L$, which do not contain any short-range correlations. The variational degrees of freedom are the correlation functions, which are typically parameterized in terms of three parameters:

$$R_+^{\mathrm{I}}(r) = r + \alpha \, (r/\beta)^{\eta} \exp[-\exp(r/\beta)] \,, \tag{1.30}$$

$$R_+^{\mathrm{II}}(r) = r + \alpha \, [1 - \exp(-r/\gamma)] \exp[-\exp(r/\beta)] \,, \tag{1.31}$$

and

$$\vartheta(r) = \alpha \, [1 - \exp(-r/\gamma)] \exp[-\exp(r/\beta)] \,. \tag{1.32}$$

The $S = 0$ channels are only affected by the central correlators. While the minimization is easily carried out in the $(S,T) = (0,1)$ channel, the AV18 interaction is purely repulsive in the $(S,T) = (0,0)$, and the resulting correlation functions would be of very long range. Since the aim of the UCOM is to describe only *short-range* correlations explicitly, the variation is carried out under the constraint

$$I_{R_+} = \int dr \, r^2 \left[R_+(r) - r \right] \,, \tag{1.33}$$

which is fixed to the value $I_{R_+} = 0.1$ fm^4 to give a range similar to the central correlators for the other (S,T)-channels [6].

In the $S = 1$ channel, the energy minimization has to be carried out with respect to the central and tensor correlators. The tensor interaction, as already discussed in Sect. 1.1.2 causes long-range correlations, whose full description by means of a tensor correlation operator runs contrary to the repeatedly stated UCOM strategy of describing only short-range correlations by means of the correlator, and leaving long-range correlations to be described by the many-body Hilbert space. This approach is motivated both technically and physically:

(i) the two-body approximation to the cluster expansion (cf. Sect. 1.1.3) is only justified if the correlator ranges are small compared to the mean particle distance, and

(ii) the long-ranged deuteron-like $L = 2$ wavefunction admixture does not reflect the situation in heavier nuclei, where the presence of other nucleons within the correlator range will cause a screening of the tensor correlations.

For these reasons, we introduce explicit range constraints by means of the integrals

$$I_{\vartheta}^{(1,T)} = \int dr \, r^2 \vartheta_T(r) \,. \tag{1.34}$$
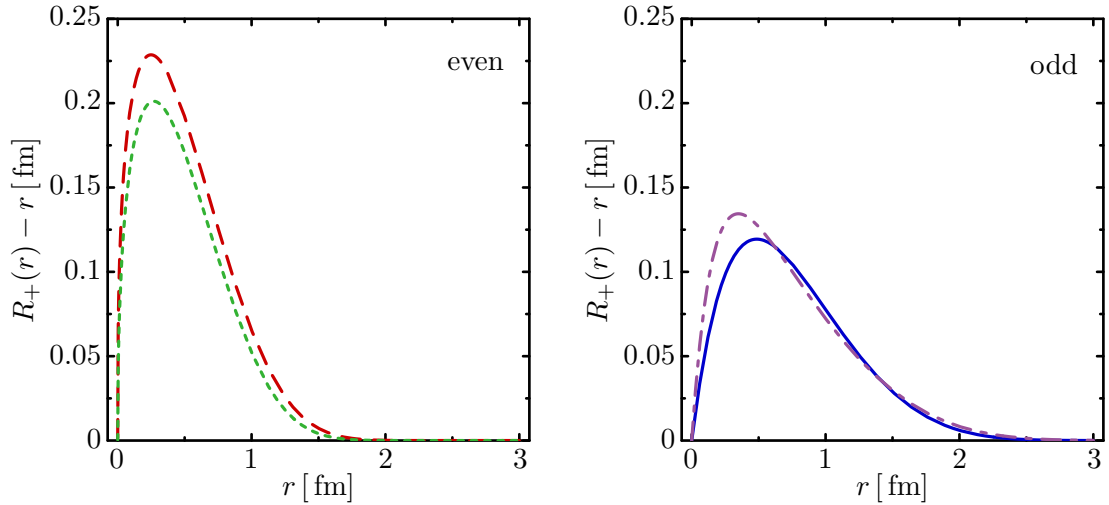
Figure 1.3: Optimal central correlation functions for AV18 in the $(S, T) = (0, 0)$ (———), $(0, 1)$ (— — —), $(1, 0)$ (-------), and $(1, 1)$ (-----) channels. Taken from [6].

The parameters of the central and tensor correlators for various constraints are listed in Tables A.3 and A.4. Since the optimal parameters for the central correlators are rather insensitive to variations in the $I_\vartheta^{(1,T)}$, we adopt the fixed set of central correlators listed in Tab. A.3 for all further applications [6].

The optimal AV18 central correlation functions, as well as the triplet-even tensor correlation function for various range constraints are shown in Figs. 1.3 and 1.4. The central correlation functions are rather similar, with those in the odd channels being somewhat weaker but slightly longer-ranged. In Fig. 1.4, we also show the $L = 2$ radial wavefunction generated by the application of the tensor correlator (cf. Sect. 1.1.2), and we see that the range restriction on $\vartheta_{T=0}(r)$ directly affects the range of the d-wave admixture, just as expected; with the exact deuteron tensor correlation function, the exact AV18 deuteron solution can be recovered [8]. The situation is similar for the triplet-odd tensor correlation function (not shown), but its amplitude is roughly an order of magnitude smaller than the amplitude of $\vartheta_{T=0}(r)$, since the tensor force is significantly weaker in the $T = 1$ than in the $T = 0$ channel

Let us conclude this section by considering the construction of the correlation functions, and in particular the introduction of the range constraints I_{R_+}, $I_\vartheta^{(1,0)}$, and $I_\vartheta^{(1,1)}$ from a slightly different point of view. The repulsive core of the central interaction has a very steep slope at $r_0 \sim 0.5 - 0.6$ fm, which represents a very distinct scale separation point between repulsive and attractive regions of the interaction. A proper treatment of the repulsion requires a transformation which affects the interaction or states primarily at ranges $r \leq r_0$, or corresponding high relative momenta. The energy minimization in the $(S, T) = (1, 0)$ yields a correlation function which automatically reflects this particular behavior.

The $(S, T) = (1, 0)$ tensor interaction, however, is always attractive, and extends smoothly over a wide range up to $r \sim 2 - 3$ fm, hence it *lacks* a physically motivated scale separation. By introducing $I_\vartheta^{(1,0)}$, we make an *artificial* separation of what we consider short-range correlations, treated explicitly by the correlation operators, and long-range correlations. Therefore, we have to expect a significant $I_\vartheta^{(1,0)}$-dependence of
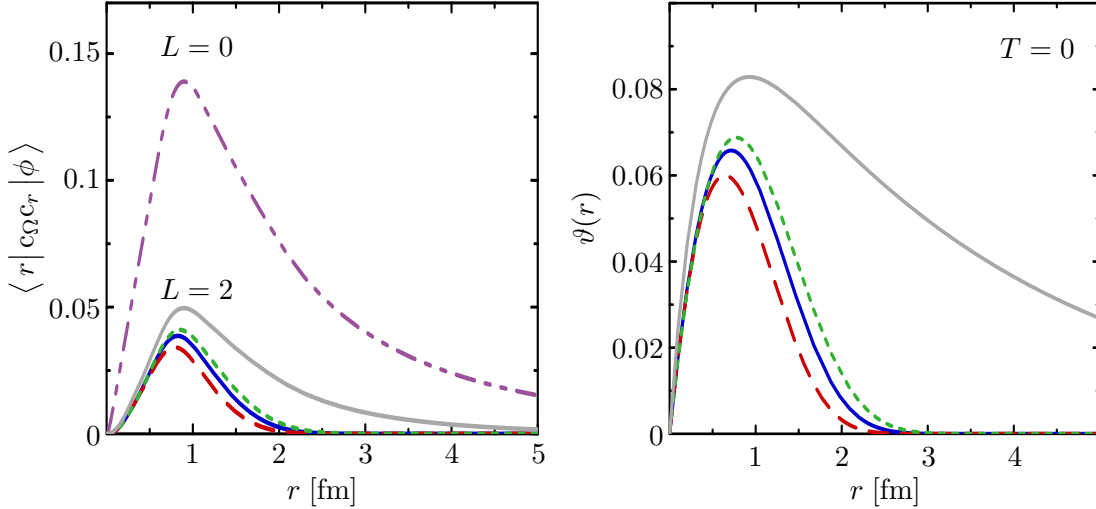
Figure 1.4: $\langle r | c_\Omega c_r | \phi \rangle$ and $\vartheta(r)$ for $I_\vartheta^{(1,0)} = 0.06\,\text{fm}^3$ (------), $0.09\,\text{fm}^3$(———), and $0.12\,\text{fm}^3$(———). The grey lines are the AV18 deuteron wavefunction $L = 2$ component and corresponding $\vartheta(r)$, respectively (cf. [6]).

nuclear binding energies at the level of the two-body approximation, which is indeed the case. The situation is similar for $I_\vartheta^{(1,1)}$, but the impact of this parameter is less dramatic because of the weaker odd-channel tensor force. In addition, this part of the interaction only comes into play for orbital momenta $L \geq 1$, where the centrifugal barrier starts to suppress the wavefunctions at short distances.

Varying $I_\vartheta^{(1,0)}$ and $I_\vartheta^{(1,1)}$ (as mentioned, I_{R_+} is kept fixed for applications of V_{UCOM}) is not unlike varying the cutoff Λ of a renormalization-group interaction $V_{\text{low-k}}$ [27], or the band cutoff scale/momentum of the Similarity Renormalization Group (cf. Sect. 1.2). In these approaches, however, one does not discern between the different physical origin of the short-range effects — in the UCOM language, this would roughly correspond to using range constraints with the *same value* for *each* correlation function. One has to realize, though, that the $V_{\text{low-k}}$ and SRG methods are conceptually rather different from the UCOM.

1.2 Similarity Renormalization Group

The Similarity Renormalization Group (SRG) was independently developed by Glazek and Wilson [28, 29], and Wegner [30]. The former were studying renormalization in a Hamiltonian framework, particularly for Light-Front Quantum Field Theory, while the latter was researching flow equations to pre-diagonalize Hamiltonians encountered in solid-state physics. Only after some time it was realized that Wegner's flow equation is equivalent to Glazek and Wilson's approach for a specific choice of the similarity transformation (see, e.g. [31]).

Contrary to other established renormalization group approaches, the SRG does not introduce a hard cutoff in momentum space, but rather aims to *decouple* momentum scales by means of a dynamically generated unitary transformation [13, 15]. When applied to the nuclear many-body problem, this unitarity ensures the reproduction of

the NN scattering phase shifts, and avoids possible pathologies resulting from the use of a hard cutoff in the $V_{\text{low-k}}$ approach [27]. Moreover, the inclusion of $3N$ forces in the $V_{\text{low-k}}$ flow equation is not obvious, whereas the extension of the SRG to higher many-nucleon forces is straightforward.

1.2.1 The SRG Flow Equation

Following Wegner's formulation of the SRG [30], one can write down a flow equation for the many-body Hamiltonian H (or any other observable of interest). Denoting the flow parameter α, the operator evolves via

$$\frac{d\mathrm{H}_\alpha}{d\alpha} = \big[\eta(\alpha), \mathrm{H}_\alpha\big], \quad \mathrm{H}_0 = \mathrm{H}, \tag{1.35}$$

where the effective Hamiltonian at a scale α is defined by

$$\mathrm{H}_\alpha \equiv \mathrm{U}(\alpha)\mathrm{H}\mathrm{U}^\dagger(\alpha) \equiv \mathrm{T}_{\text{int}} + \mathrm{V}_\alpha. \tag{1.36}$$

All α-dependent contributions have been absorbed in the many-body interaction $\mathrm{V}_\alpha = \mathrm{H}_\alpha - \mathrm{T}_{\text{int}}$ and the α-independent intrinsic kinetic energy $\mathrm{T}_{\text{int}} = \mathrm{T} - \mathrm{T}_{\text{cm}}$ has been separated. The anti-hermitian generator $\eta(\alpha)$ formally satisfies the relation

$$\eta(\alpha) = \frac{d\mathrm{U}(\alpha)}{d\alpha}\mathrm{U}^\dagger(\alpha) = -\eta^\dagger(\alpha), \tag{1.37}$$

and has to be chosen appropriately for practical applications. Wegner's original choice was

$$\eta(\alpha) = \big[\text{diag}(\mathrm{H}_\alpha), \mathrm{H}_\alpha\big], \tag{1.38}$$

which one can understand intuitively: if H_α commutes with its diagonal part with respect to a certain basis, then the generator vanishes and one has reached a fixed point of the flow. Trivial cases aside, this can only happen if H_α is, in fact, diagonal in that basis. Thus, the generator *dynamically* drives H_α towards a diagonal structure with increasing α. The price one has to pay for this simplification is that one has to deal with complicated many-body interactions in V_α even if one starts with a two-body potential [32].

A simpler choice for the generator was suggested by Szpigel and Perry [31] and employed successfully by Bogner et al. [13]. First of all, one confines the evolution to a two-body space, discarding induced multi-nucleon interactions from the outset — this assumption corresponds to the two-body approximation used in the UCOM framework (cf. Sect. 1.1.3). The two-body generator is defined as

$$\eta(\alpha) \equiv \big[\mathrm{t}_{\text{rel}}, \mathrm{h}_\alpha\big] = \big[\frac{\mathbf{q}^2}{2\mu}, \mathrm{h}_\alpha\big], \tag{1.39}$$

where

$$\mathrm{h}_\alpha = \mathrm{t}_{\text{rel}} + \mathrm{v}_\alpha, \tag{1.40}$$

and the flow equation now reads

$$\frac{d\mathrm{h}_\alpha}{d\alpha} = \big[\big[\frac{\mathbf{q}^2}{2\mu}, \mathrm{h}_\alpha\big], \mathrm{h}_\alpha\big], \quad \mathrm{h}_0 = \mathrm{h}. \tag{1.41}$$

With the choice (1.39), the generator aims to diagonalize the two-body Hamiltonian h_α in a basis of eigenstates of both q_r^2 and $\mathbf{l}^2$. In a partial-wave momentum-space basis $\left| q\,(LS)J\,T \right\rangle$, the generator drives the matrix elements towards a band-diagonal structure with respect to (q, q') and (L, L').

Evaluating Eq. (1.41) for the spin-singlet partial waves in this basis, one has

$$\frac{dv_\alpha(q, q')}{d\alpha} = - \frac{1}{(2\mu)^2} \left(q^2 - q'^2\right)^2 v_\alpha(q, q')$$
$$+ \frac{1}{2\mu} \int dQ\, Q^2 \left(q^2 + q'^2 - 2Q^2\right) v_\alpha(q, Q) v_\alpha(Q, q'), \qquad (1.42)$$

with

$$v_\alpha(q, q') = \left\langle q(LS)JT \right| \mathrm{v}_\alpha \left| q'(LS)JT \right\rangle, \qquad (1.43)$$

where we have assumed rotational symmetry as well as charge-independence (i.e., no M- or M_T-dependence in the matrix elements). For convenience, the mass factors can be absorbed into the scale parameter α and the matrix elements by defining[2]

$$\bar{\alpha} \equiv \frac{1}{(2\mu)^2}\alpha, \quad [\bar{\alpha}] = \mathrm{fm}^4, \qquad (1.44)$$

$$\bar{v}_\alpha(q, q') \equiv 2\mu v_\alpha(q, q'), \quad [\bar{v}_\alpha] = \mathrm{fm}. \qquad (1.45)$$

In these quantities, the $S = 0$ flow equation now reads

$$\frac{d\bar{v}_\alpha(q, q')}{d\bar{\alpha}} = - \left(q^2 - q'^2\right)^2 \bar{v}_\alpha(q, q')$$
$$+ 2\mu \int dQ\, Q^2 \left(q^2 + q'^2 - 2Q^2\right) \bar{v}_\alpha(q, Q) \bar{v}_\alpha(Q, q'). \qquad (1.46)$$

For $S = 1$, the SRG evolution is a coupled-channel problem due to the mixing of orbital angular momenta L caused by the tensor interaction. The coupled-channel flow equation can be obtained from Eq. (1.46) by replacing $\bar{v}_\alpha(q, q')$ with a matrix in (L, L'), i.e.,

$$\frac{d\,\bar{\mathrm{v}}_\alpha(q, q')}{d\bar{\alpha}} = - \left(q^2 - q'^2\right)^2 \bar{\mathrm{v}}_\alpha(q, q')$$
$$+ 2\mu \int dQ\, Q^2 \left(q^2 + q'^2 - 2Q^2\right) \bar{\mathrm{v}}_\alpha(q, Q) \bar{\mathrm{v}}_\alpha(Q, q'). \qquad (1.47)$$

with

$$\bar{\mathrm{v}}_\alpha(q, q') = \begin{pmatrix} \bar{v}_\alpha^{LL}(q, q') & \bar{v}_\alpha^{LL'}(q, q') \\ \bar{v}_\alpha^{L'L}(q, q') & \bar{v}_\alpha^{L'L'}(q, q') \end{pmatrix} \qquad (1.48)$$

and $L' = L \pm 2$.

---

[2]In scattering units $\hbar/(m_N) = \hbar/(2\mu) = 1$, the flow equation agrees with Ref. [13] up to a different choice of normalization for the momentum states, which leads to an explicit additional factor $2/\pi$ in front of the integral.

1.2.2 SRG Evolution and the Deuteron

To illustrate the SRG evolution, we show the momentum space matrix elements in the deuteron partial waves and the deuteron solutions for the bare AV18 interaction and the SRG-evolved effective interaction for $\bar{\alpha} = 0.1000\,\mathrm{fm}^4$ in Fig. 1.5.

The effect of the evolution on the AV18 potential is striking: the strong off-diagonal matrix elements in the $^3S_1$ and $^3S_1 - {}^3D_1$ partial waves which are caused by the hard core and the tensor interaction are strongly suppressed. The repulsion in the $^3S_1$ wave has been accumulated on the diagonal in the high-momentum region, and the attraction at low-momenta has been enhanced significantly. One has to keep in mind, however, that part of the interaction strength from these partial waves has been shifted to higher many-nucleon forces, which have not been explicitly considered because the evolution was carried out in two-body space.

The suppression of the off-diagonal matrix elements for large $|q - q'|$ which are inducing the short range correlations has a dramatic effect on the interaction's deuteron solution. The short-range correlation hole in the $L = 0$ radial wavefunction of AV18 is removed by the SRG evolution, and the $L = 2$ admixture has been all but eliminated, i.e., the short-range correlations have been "integrated out". In this respect, the effect of the SRG evolution is found to be very similar to the situation for the UCOM, discussed in Sect. 1.1.2, where the unitary transformation via the correlation operators turns a simple, uncorrelated trial state into a strongly correlated, realistic NN state, or vice versa.

1.2.3 The SRG Generator and Its Relation to the UCOM

Since the SRG evolution of the deuteron wavefunctions has indicated that the SRG and the UCOM seem to share more than just the concept of obtaining an effective interaction by means of a unitary transformation, it is worthwile to take a closer look at the SRG generator itself.

Using the operator form (1.23) of the AV18 interaction (without charge dependence), and splitting the relative kinetic energy into a radial and an angular part, we evaluate the generator (1.39) at $\alpha = 0$, which determines the initial flow in Eq. (1.35):

$$\eta(0) = \frac{1}{2\mu}\left[\mathrm{q}_r^2 + \frac{\mathbf{l}^2}{\mathrm{r}^2}, \mathrm{v}\right]. \tag{1.49}$$

Using the elementary commutators

$$\left[\mathrm{a}, \mathrm{l}_k\right] = 0\,, \tag{1.50}$$

$$\left[\mathrm{b}_i, \mathrm{l}_j\right] = i\varepsilon_{ijk}\mathrm{b}_k\,, \tag{1.51}$$

where a and **b** are arbitrary scalar and vector operators in coordinate space, respectively, as well as the commutators from Appendix A.1, we find that the commutator of the interaction with q_r^2 in each (S, T)-channel (omitting the ST-index for brevity) is given by

$$\left[\mathrm{q}_r^2, \mathrm{v}\right] = \sum_p \left[\mathrm{q}_r^2, v_p(\mathrm{r})\mathrm{o}_p\right] = -i\sum_p \left(\mathrm{q}_r v_p'(\mathrm{r}) + v_p'(\mathrm{r})\mathrm{q}_r\right)\mathrm{o}_p\,, \tag{1.52}$$
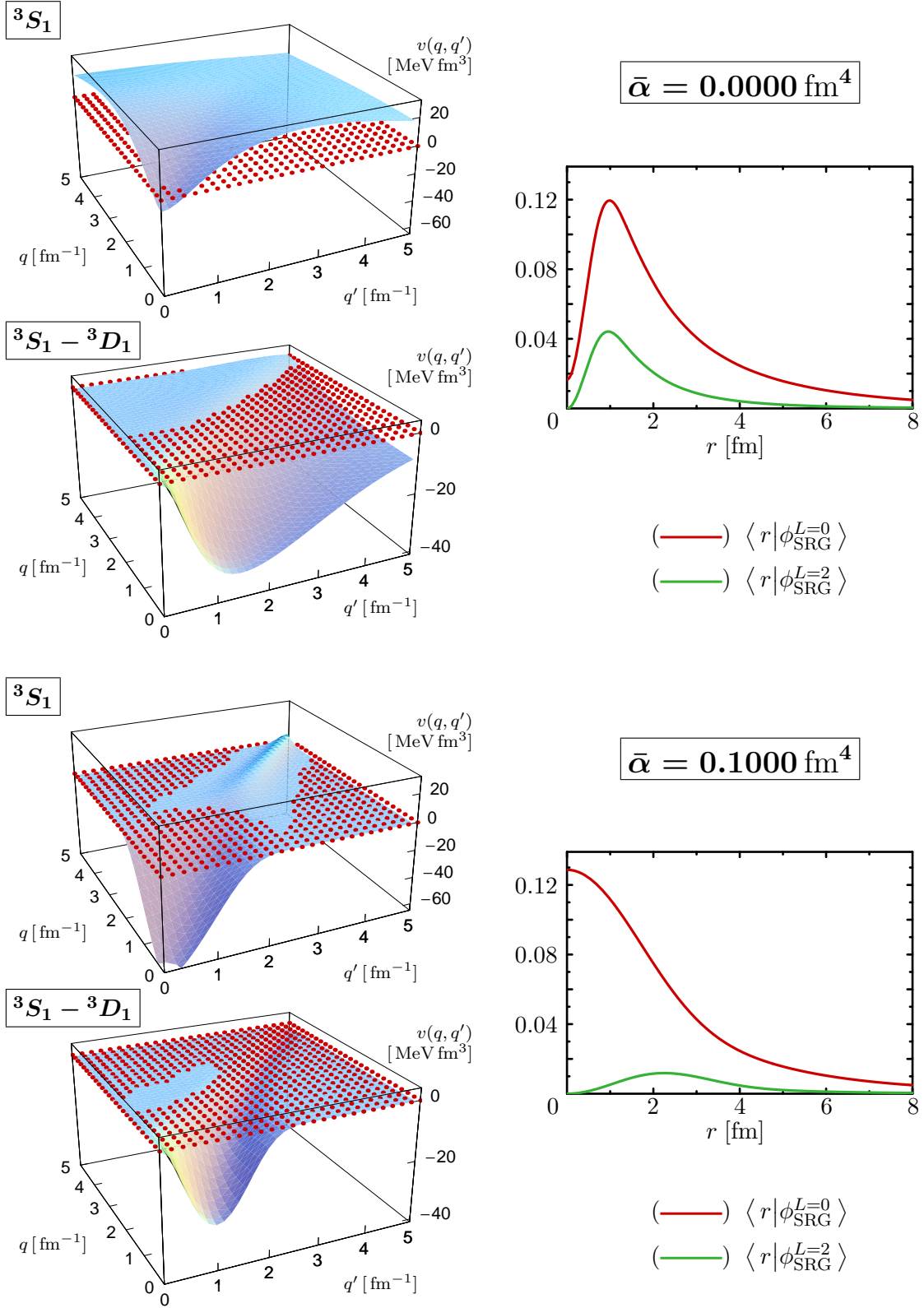
Figure 1.5: Momentum-space matrix elements and deuteron wavefunctions of the SRG-evolved AV18 interaction for $\bar{\alpha} = 0$ fm^4 (usual AV18, top), and 0.1000 fm^4 (bottom).

since q_r commutes with all of the operators o_p. For the angular component we get

$$\left[\frac{\mathbf{l}^2}{r^2}, v\right] = \left[\frac{\mathbf{l}^2}{r^2}, v_t(r)s_{12}(\hat{\mathbf{r}}, \hat{\mathbf{r}})\right] = -4i\frac{v_t(r)}{r^2}s_{12}(\mathbf{r}, \mathbf{q}_\Omega), \tag{1.53}$$

because all but the tensor component of the interaction commute with $\mathbf{l}^2$. Thus, we obtain the following form for the initial generator :

$$\eta(0) = \frac{i}{2}(q_r S(r) + S(r)q_r) + i\Theta(r)s_{12}(\mathbf{r}, \mathbf{q}_\Omega), \tag{1.54}$$

with

$$S(r) \equiv -\frac{1}{\mu}\left(\sum_p v'_p(r)o_p\right) \tag{1.55}$$

and

$$\Theta(r) \equiv -\frac{2}{\mu}\frac{v_t(r)}{r^2}. \tag{1.56}$$

This is a remarkable result: the structure of $\eta(0)$ resembles the sum of the UCOM generators g_r and g_Ω defined in Eqs. (1.2) and (1.7). The symmetrized radial momentum operator and the non-trivial momentum-dependent tensor operator $s_{12}(\mathbf{r}, \mathbf{q}_\Omega)$, which have been constructed based on the structure of the short-range correlations in the UCOM framework, result directly from the commutation relation defining the generator of the renormalization group flow. This result connects the SRG flow picture with a physically intuitive picture of central and tensor correlations in a many-body state.

Conversely, the flow equation provides guidance for generalizing the UCOM scheme. The definition of the central correlators (1.2) and (1.7) only allows an (S, T)-dependence for the corresponding shift or correlation functions. However, in the SRG framework the shift function $S(r)$ in (1.55) is operator-valued and therefore sensitive to orbital and total angular momentum as well. Furthermore, the operator-valued tensor correlation function $\Theta(r)$ will acquire operators like the non-linear tensors (1.29) encountered in the operator expansion of V_{UCOM} (see Sect. 1.1.4) during the flow. In principle, we should be able to recover the net effect of the additional operator terms by using different correlation functions in each partial wave.

Let us return to the flow equation to discuss one inherent difference between the SRG and UCOM schemes. By solving Eq. (1.41), we evolve h_α along a non-linear trajectory in the manifold of unitarily equivalent operators towards the fixed point, i.e. diagonality. The structure of the generator $\eta(\alpha)$ will adapt *dynamically* at each step of the flow, starting from $\eta(0)$. The UCOM scheme, in contrast, uses a static generator to evolve the Hamiltonian in a single step from the initial point to the final point of the flow trajectory. If one would assume an SRG generator independent of α, the flow equation could be integrated,

$$h_\alpha = e^{-\alpha\eta(0)}h_0 e^{\alpha\eta(0)}, \tag{1.57}$$

and one would recover an explicit unitary transformation as in the UCOM case, corresponding to a linear flow trajectory along the direction specified by $\eta(0)$. A further
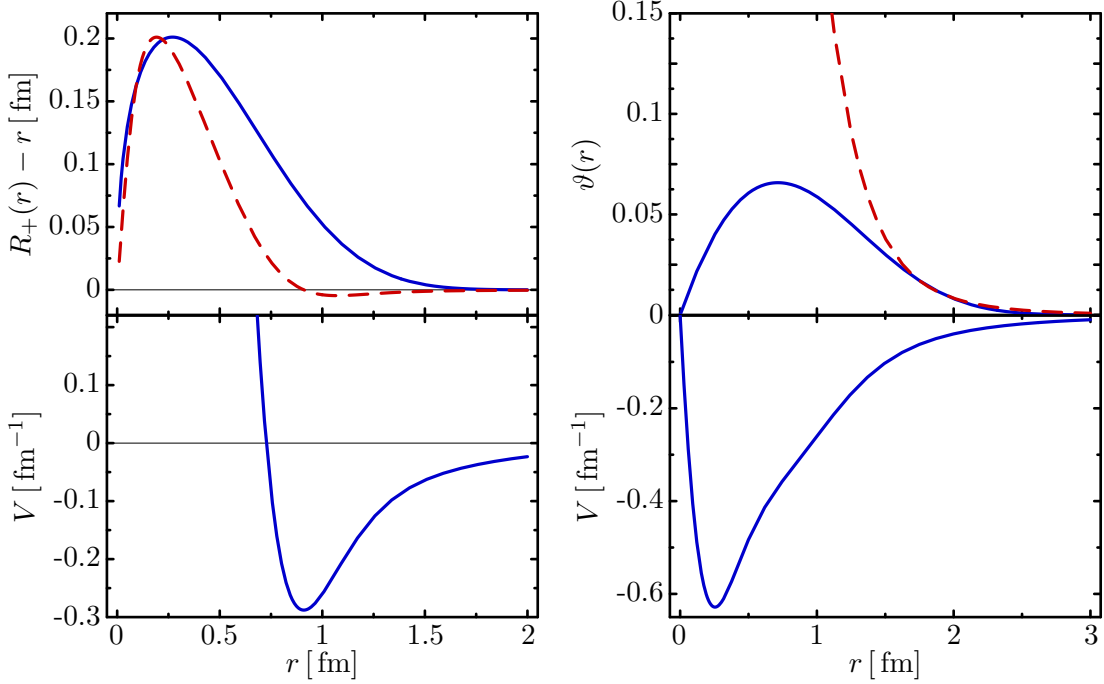
Figure 1.6: Initial SRG "correlation functions" for AV18 in the $(S,T) = (1,0)$ channel. *Left:* optimal UCOM $R_+(r)$ (———), SRG $R_+(r)$ at $\alpha = 0$ ($-\ -\ -$) (top), and radial dependency of the bare central interaction (bottom). *Right:* UCOM tensor correlator for $I_\vartheta^{(1,0)} = 0.09\,\mathrm{fm}^3$, $\Theta(r)$ ($-\ -\ -$) (top), and radial dependency of the bare tensor interaction (bottom).

difference is that the UCOM formulation assumes *separate* unitary transformations with g_r and g_Ω. In the SRG picture this amounts to separate evolutions with two flow parameters α_r and α_Ω, using the generators

$$\eta_r(\alpha_r) = \frac{1}{2\mu}\big[\mathrm{q}_r^2, \mathrm{h}_{\alpha_r}\big] \quad \text{and} \quad \eta_\Omega(\alpha_\Omega) = \frac{1}{2\mu}\Big[\frac{\mathbf{l}^2}{\mathrm{r}^2}, \mathrm{h}_{\alpha_\Omega}\Big], \qquad (1.58)$$

respectively.

The difference between the static generators of the UCOM and the dynamic generators of the SRG affect the choice of the correlation functions. One could be tempted to use the radial dependencies (1.55) and (1.56) of the initial SRG generator in the UCOM, since they are directly given by the original potential. In Fig. 1.6, we compare the SRG correlation function obtained by solving (cf. Eq. (1.11))

$$1 = \int_r^{R_+(r)} d\xi \frac{1}{S(\xi)} \qquad (1.59)$$

and $\Theta(r)$ for the $(S,T) = (1,0)$ channel with the optimal UCOM central correlator and the tensor correlator for $I_\vartheta^{(1,0)} = 0.09\,\mathrm{fm}^3$ (see Sect. 1.1.5). The central and tensor radial dependencies of AV18 are shown for orientation.

The initial SRG central correlation function is very similar to its UCOM counterpart at very short distances, but at the surface of the core region, it drops off more rapidly, and changes sign roughly at the minimum of the central interaction, which is of course

due to the explicit dependence of Eq. (1.55) on $v'_c(r)$. The UCOM correlation function, on the other hand, is strictly positive. This implies that the $R^{\text{UCOM}}_+(r)$ will actually push nucleons *out of the region of the minimum*, while $R^{\text{SRG}}_+(r)$ will also draw nucleons from larger ranges back towards the minimum, where they can experience a larger attraction. While $R^{\text{SRG}}_+(r)$ seems to have reasonable properties, the same cannot be said for $\Theta(r)$. Due to its explicit $1/r^2$-dependence, it strongly diverges at short distances. This shows that using the initial SRG "correlation functions" for the UCOM is not appropriate, because the UCOM correlation functions effectively integrate over the complete flow trajectory. Instead, one would have to use the dynamic flow picture to determine the UCOM correlation functions that *directly connect* the initial and the final point of the flow trajectory by means of mapping a trial state onto the SRG deuteron solution. Such mappings of trial states onto exact deuteron or scattering solutions have been studied extensively in the UCOM framework [7, 24, 8]. Interestingly, research along these lines confirms that the central correlation functions extracted from the SRG flow indeed undergo a sign change in the region of the minimum, as discussed for the initial "correlation function" [23].

1.3 Effective Interactions in Momentum Space

When we compare the matrix elements of the effective interactions obtained by either the UCOM or the SRG evolution in momentum space, we notice immediately that both transformations pre-diagonalize the Hamiltonian in momentum space. This is hardly surprising for the SRG, which was constructed precisely with this goal in mind (cf. Sect. 1.2). For the UCOM, on the other hand, the pre-diagonalization in momentum space was at first only an empirical result [8], which could be understood from general considerations regarding the explicit treatment of short-range correlations, until the connection of both methods was established more firmly in [15] (see Sect. 1.2.3).

1.3.1 Even Channels — $(S, T) = (0, 1)$ and $(1, 0)$

In Figs. 1.7 and 1.8, we compare the matrix elements in the lowest even partial waves of two UCOM and SRG interactions to the AV18 interaction from which they were derived. Specifically, V_{UCOM} has been optimized for calculations without $3N$ interactions (see Sect. 1.4.2) by using the tensor-correlator range constraints $I^{(1,0)}_\vartheta = 0.9\,\text{fm}^3$, and $I^{(1,1)}_\vartheta = 0\,\text{fm}^3$. The flow parameter

$$\bar{\alpha} \equiv \frac{\alpha}{(2\mu)^2} \tag{1.60}$$

of the corresponding SRG interactions was determined by matching the $v(0,0)$ matrix elements of V_α to the particular V_{UCOM}, resulting in $\bar{\alpha} = 0.0215\,\text{fm}^4$. Unless variations of the tensor-correlator constraints or the flow parameter are studied, we will only refer to these particular interactions in the following.

While AV18 has strong diagonal and off-diagonal matrix elements, particularly in the $^1S_0$ and $^3S_1$ partial waves, the off-diagonal matrix elements of the effective interactions are suppressed significantly, and the attraction at low momenta has been enhanced considerably. In the first mixed partial wave $^3S_1 - {}^3D_1$, the off-diagonal contributions which are solely caused by the tensor force have been reduced notably as well, which is
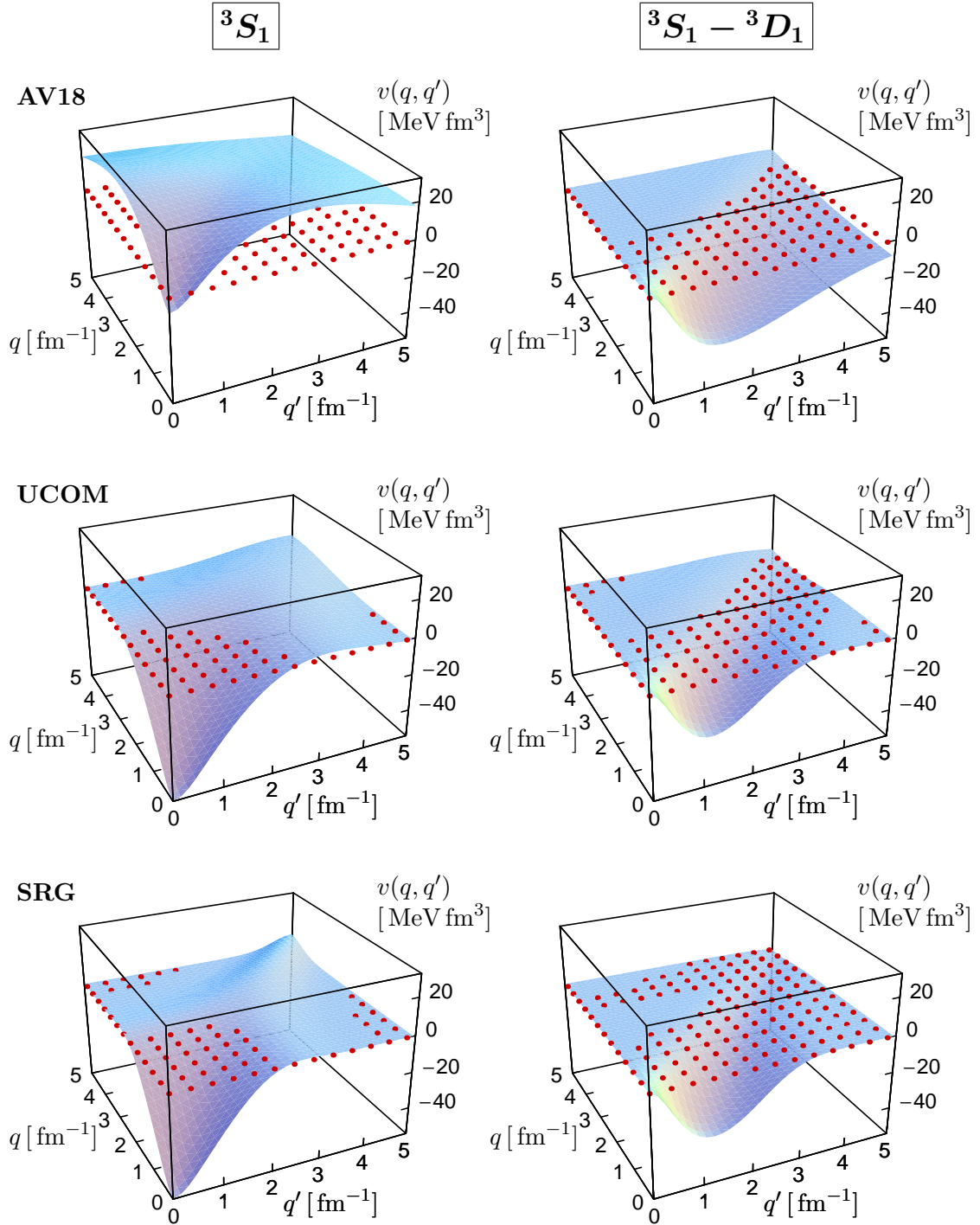
Figure 1.7: Momentum space-matrix elements in the deuteron partial waves of AV18 (top), V_{UCOM} for $I_{\vartheta}^{(1,0)} = 0.09\,\text{fm}^3$ (center), and V_{α} for $\bar{\alpha} = 0.0215\,\text{fm}^4$ (bottom).
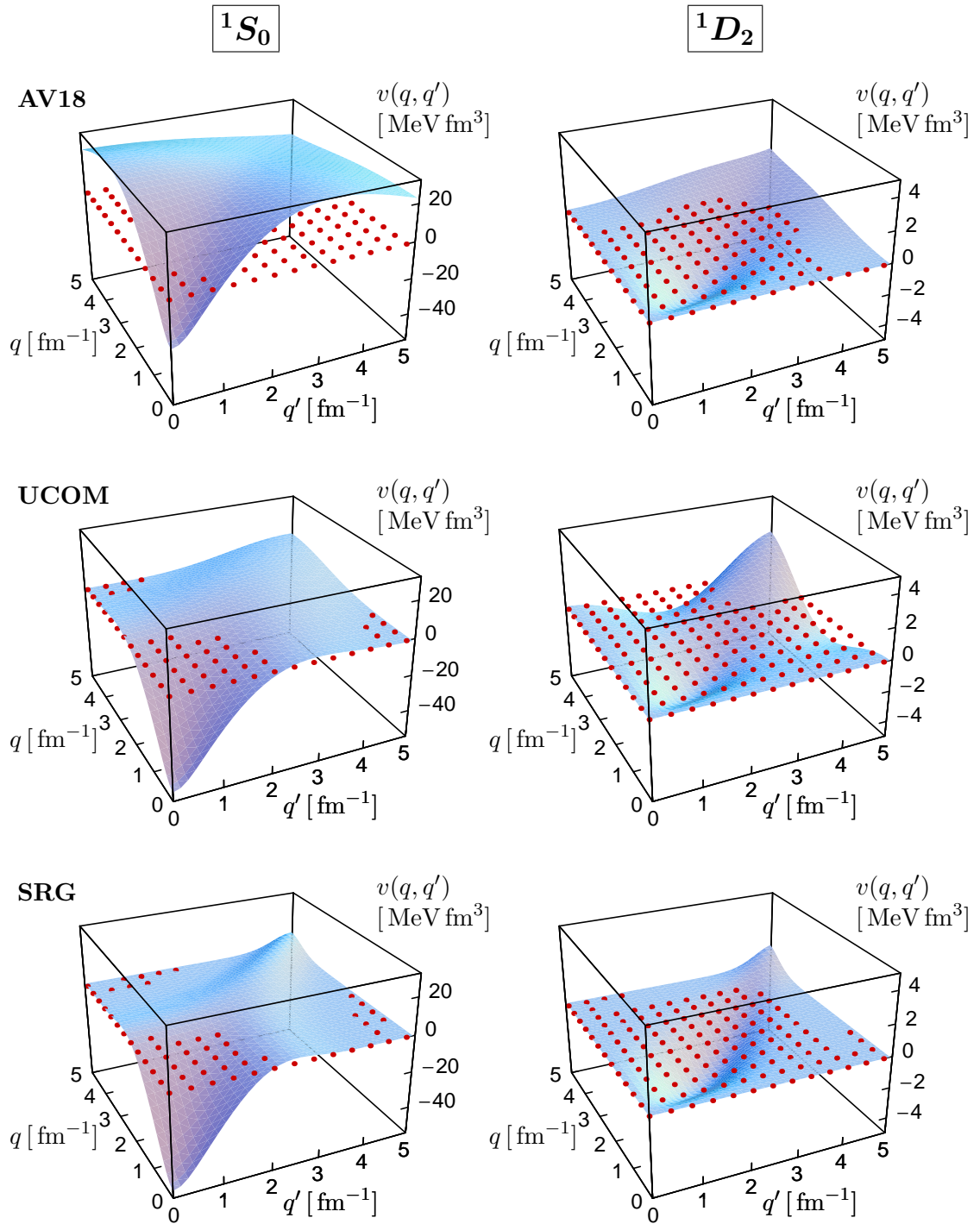
Figure 1.8: Momentum-space matrix elements in the $^1S_0$ and $^1D_2$ partial waves of AV18 (top), V_{UCOM} for $I_\vartheta^{(1,0)} = 0.09\,\text{fm}^3$ (center), and V_α for $\bar{\alpha} = 0.0215\,\text{fm}^4$ (bottom).
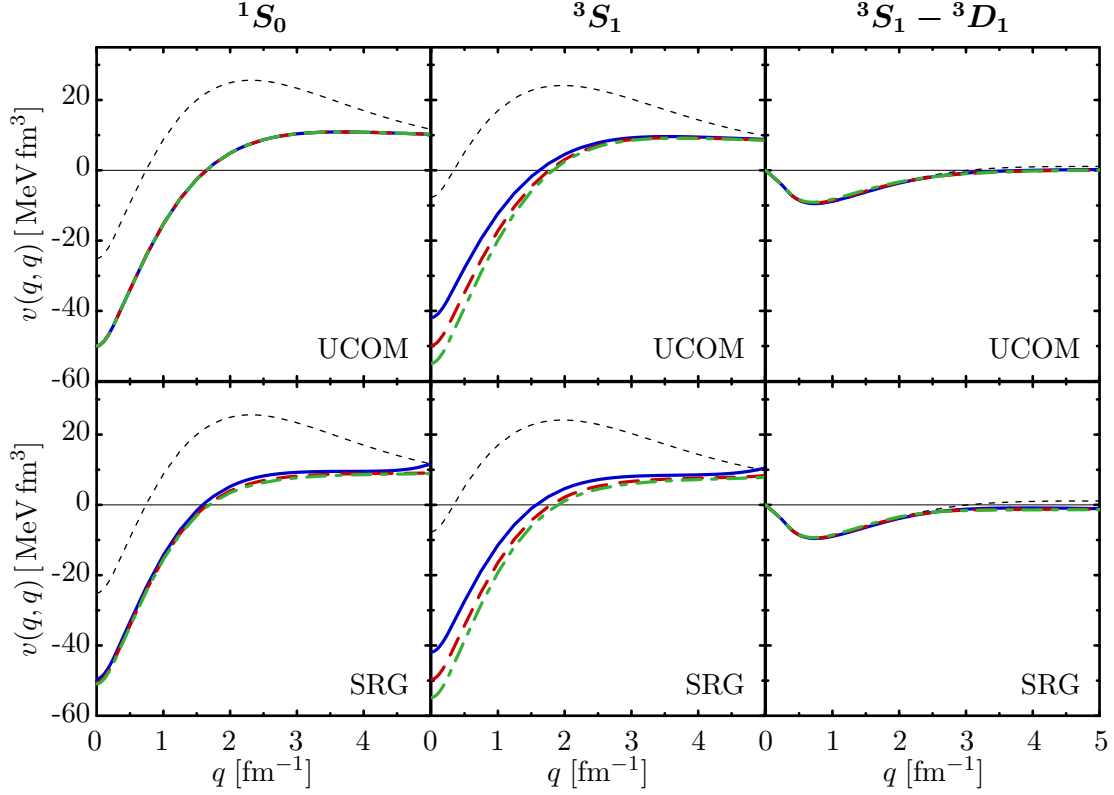
Figure 1.9: Pre-diagonalization in momentum space. Diagonal matrix elements of V_{UCOM} for $I_{\vartheta}^{(1,0)} = 0.03\,\text{fm}^3$ (——), $0.06\,\text{fm}^3$ (– – –), $0.09\,\text{fm}^3$ (–·–·–), and V_{α} for flow parameter values $\bar{\alpha} = 0.0055\,\text{fm}^4$ (——), $0.0125\,\text{fm}^4$ (– – –), and $0.0215\,\text{fm}^4$ (–·–·–)(see text). AV18 matrix elements are indicated by (·······).

due to the redistribution of the attractive strength of the tensor interaction to channels which are diagonal in L (cf. 1.1.4).

As discussed in Sect. 1.1.5, the range constraints $I_{\vartheta}^{(1,T)}$ are the main free parameters of V_{UCOM} — of the two, $I_{\vartheta}^{(1,0)}$ produces larger effects because the tensor force is significantly stronger in the $(S,T) = (1,0)$ channel. In Figs. 1.9 and 1.10, we therefore compare the off-diagonal and diagonal matrix elements for various values of $I_{\vartheta}^{(1,0)}$ and $\bar{\alpha}$, respectively. Obviously, variations of the tensor-correlator range do not affect V_{UCOM} in the $^1S_0$ channel.

For the diagonal matrix elements, the effect of the parameter variation is most noticeable in the low-momentum region of the $^3S_1$ partial wave — in particular, the depth of the attractive region increases with $I_{\vartheta}^{(1,0)}$ and $\bar{\alpha}$. The accumulation of attractive strength along the diagonal makes additional binding energy accessible for simple mean-field states which can only probe the diagonal matrix elements of the NN interaction by construction (in other words, we successively integrate out correlations, see Sect. 1.2.2).

In the off-diagonal matrix elements, we observe that an increase of $I_{\vartheta}^{(1,0)}$ improves the decoupling of different momenta, just as the increase of $\bar{\alpha}$ renders V_{α} more diagonal.
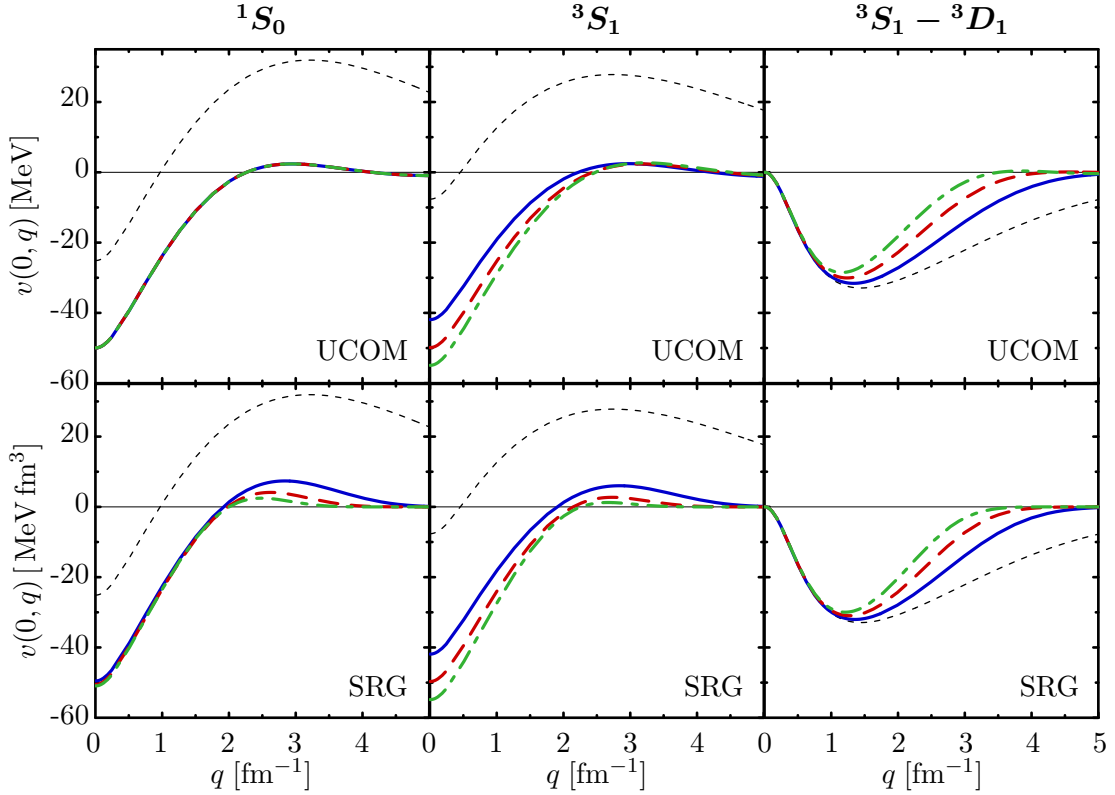
Figure 1.10: Pre-diagonalization in momentum space. Off-diagonal matrix elements $v(0, q)$ of V_{UCOM} for $I_{\vartheta}^{(1,0)} = 0.03 \, \text{fm}^3$ (———), $0.06 \, \text{fm}^3$ (— — —), $0.09 \, \text{fm}^3$ (— · — ·), and V_{α} for flow parameter values $\bar{\alpha} = 0.0055 \, \text{fm}^4$ (———), $0.0125 \, \text{fm}^4$ (— — —), and $0.0215 \, \text{fm}^4$ (— · — ·)(see text), in comparison to AV18 (- - - - - - -).

We note that the SRG evolution smoothly suppresses the off-diagonal matrix elements for large $|q - q'|$, whereas tiny residual contributions remain at large momenta in V_{UCOM}. This is most likely related to the particular parameterization of the UCOM correlation functions (cf. Sect. 1.1.5), and can likely be remedied by extracting them directly from solutions of the SRG flow equation in the future. Given that only the $q = q' = 0$ matrix elements in the $^1S_0$ and $^3S_1$ channels were used to optimize UCOM correlation functions, the overall agreement of both interactions in these partial waves is impressive. The same observation holds for the $^3S_1 - ^3D_1$ channel, which was not considered in the optimization of the UCOM correlators at all: the matrix elements obtained by the UCOM and the SRG evolution are almost indistinguishable.

The next even partial waves are $^1D_2$ (see Fig. 1.8) in the $(0, 1)$- and the ^3D waves in the $(1, 0)$-channel. For $^1D_2$, we notice that off-diagonal matrix elements of the SRG interaction are suppressed much stronger than those of V_{UCOM}. While the size of the matrix elements is about an order of magnitude smaller than in the lowest partial waves, V_{UCOM} has attractive strength in off-diagonal matrix elements with quite large $|q - q'| \approx 4 \, \text{fm}^{-1}$. For V_{α}, these contributions are accumulated in the more pronounced attractive region near the diagonal, and a reduced repulsion at large q. The observed difference between both interactions is a consequence of optimizing the UCOM correla-
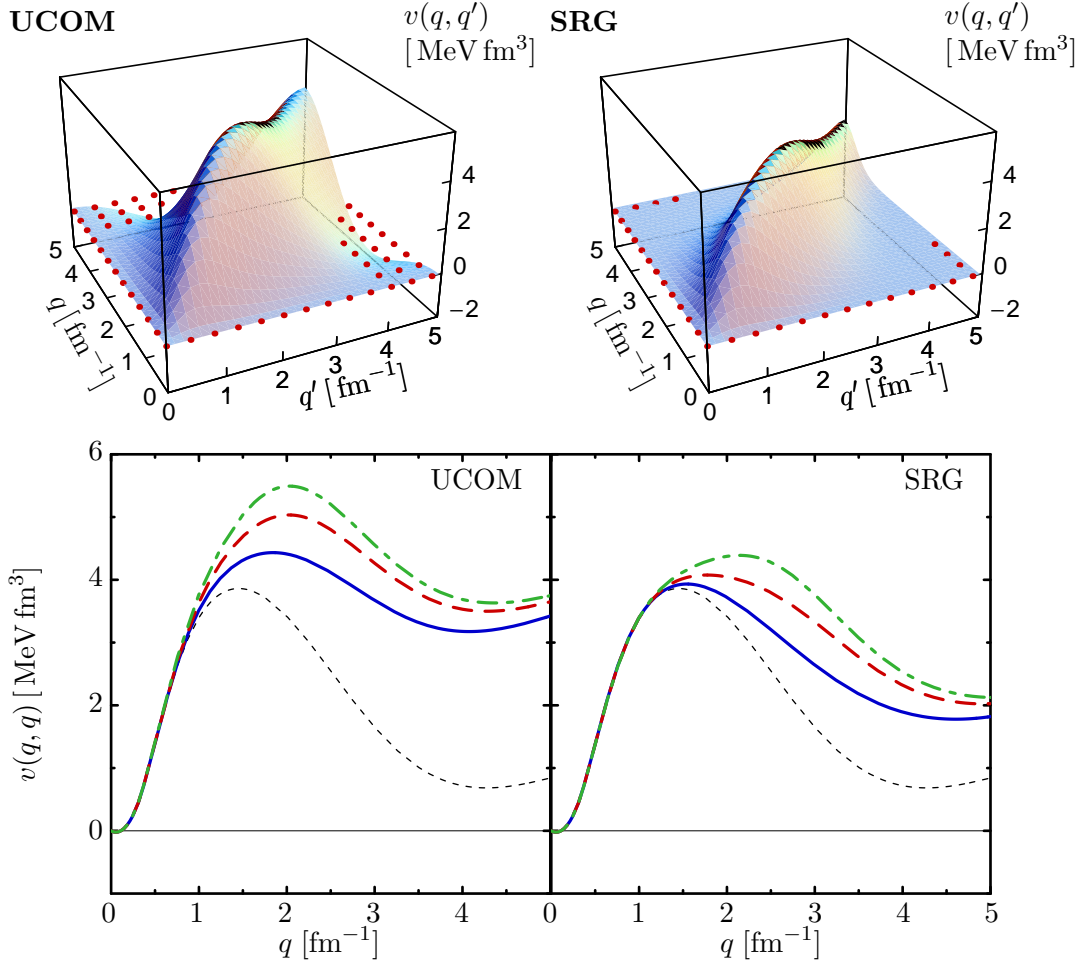
Figure 1.11: Low-momentum enhancement of $^3D_1$. *Upper panel:* Momentum space matrix elements of V_{UCOM} for $I_\vartheta^{(1,0)} = 0.09\,\text{fm}^3$ (left), and V_α for $\bar{\alpha} = 0.0215\,\text{fm}^4$ (right). *Lower panel:* Diagonal matrix elements of V_{UCOM} for $I_\vartheta^{(1,0)} = 0.03\,\text{fm}^3$ (———), $0.06\,\text{fm}^3$ (———), $0.09\,\text{fm}^3$ (—·—·—), and V_α for flow parameter values $\bar{\alpha} = 0.0055\,\text{fm}^4$ (———), $0.0125\,\text{fm}^4$ (———), and $0.0215\,\text{fm}^4$ (—·—·—), in comparison to AV18 (·······).

tion functions in the lowest partial waves of a given (S,T)-channel only, while the SRG evolves independently in each partial wave. Also, recall from the discussion of the SRG generator in Sect. 1.2.3 that the commutator with the radial kinetic energy contains derivatives of all interaction terms along with operators like $\mathbf{l}^2$ or $\mathbf{l}\cdot\mathbf{s}$ — in the UCOM, this could be mimicked by optimizing the correlation functions in *each partial wave separately*. As for the off-diagonal residual contributions discussed for the S-waves, the stiffness of the parameterization of the UCOM correlation functions might be relevant here, since the parent AV18 interaction was purely repulsive in these regions and the UCOM and especially the SRG transformations tend to suppress off-diagonal matrix elements in a monotonous fashion in other partial waves.

While we omit the $^3D_2$ and $^3D_3$ partial waves since they are rather similar for both interactions, $^3D_1$ is worth a closer look because it is the only partial wave up to $L = 3$ which exhibits a small but notable enhancement of the *repulsion* at low momenta for both interactions (see Fig. 1.11). The maximum, lying on the diagonal at
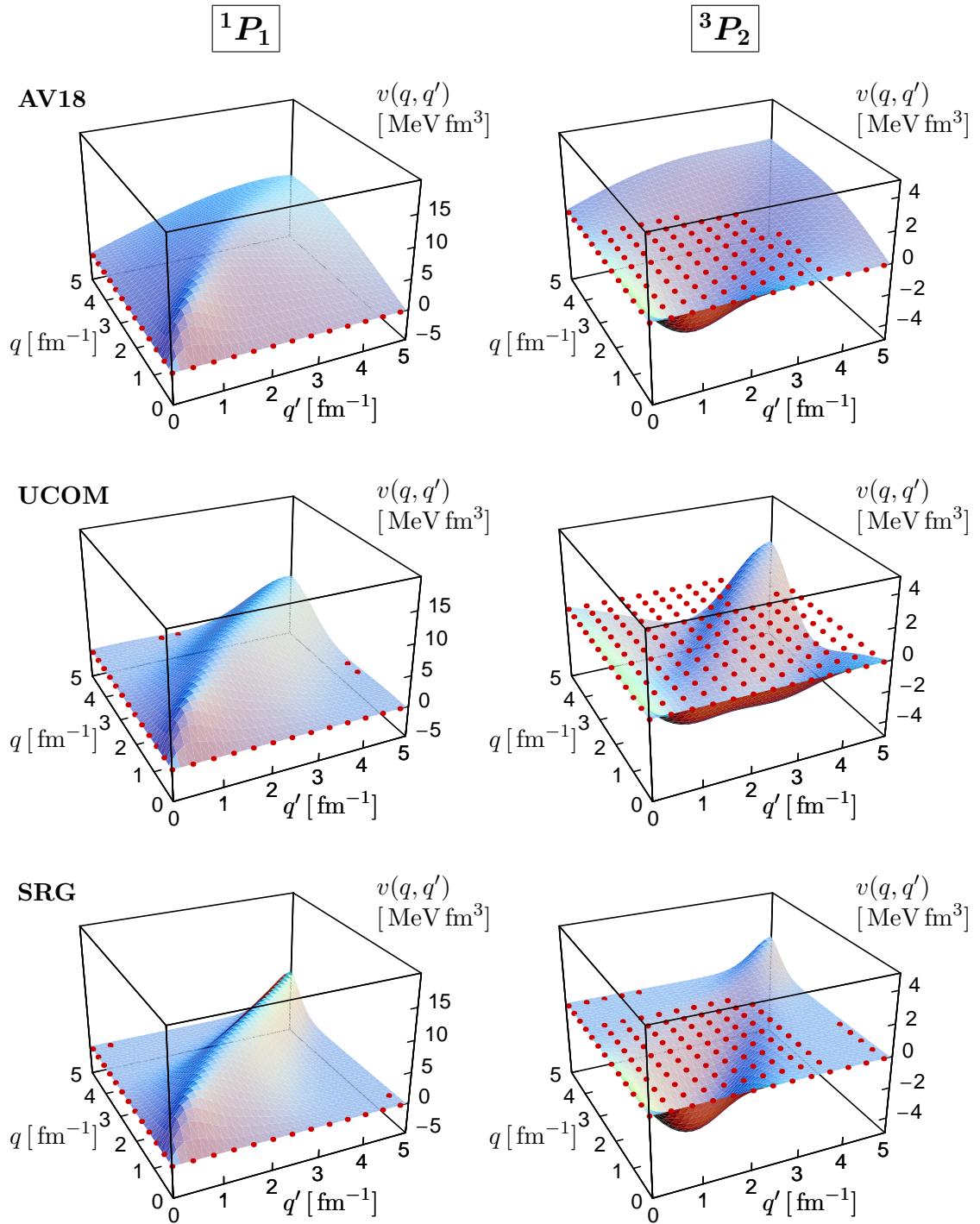
Figure 1.12: Momentum-space matrix elements in the $^1P_1$ and $^3P_2$ partial waves of AV18 (top), V_{UCOM} for $I_\vartheta^{(1,0)} = 0.09\,\text{fm}^3$ (center), and V_α for $\bar{\alpha} = 0.0215\,\text{fm}^4$ (bottom).
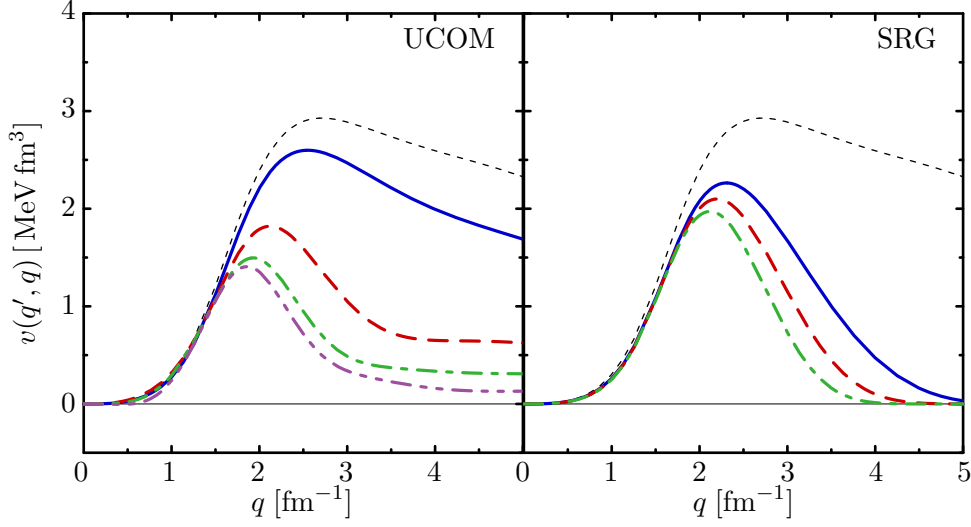
Figure 1.13: Evolution of off-diagonal matrix elements in the $^3P_2 - {}^3F_2$ partial wave at $q' = 1.5\,\mathrm{fm}^{-1}$. Shown are V_{UCOM} with $I_\vartheta^{(1,0)} = 0.09\,\mathrm{fm}^3$ and $I_\vartheta^{(1,1)} = 0.0\,\mathrm{fm}^3$ (———), $0.02\,\mathrm{fm}^3$ (— — —), $0.05\,\mathrm{fm}^3$ (— · — ·), $0.07\,\mathrm{fm}^3$ (— · · —), and V_α for $\bar\alpha = 0.0055\,\mathrm{fm}^4$ (———), $0.0125\,\mathrm{fm}^4$ (— — —), and $0.0215\,\mathrm{fm}^4$ (— · — ·), as well as AV18 (·······).

about $q = 2\,\mathrm{fm}^{-1}$, is more pronounced in V_{UCOM}; note, however, that V_{UCOM} again has slightly attractive off-diagonal 'wings', while the corresponding matrix elements are very close to zero in V_α, implying that the shift of these contributions towards the diagonal is responsible for the smaller increase in the repulsion. The size of the enhancement with $I_\vartheta^{(1,0)}$ and α is somewhat similar in the low-momentum range, suggesting that it primarily results from the redistribution of the short-range tensor interaction strength in the coupled $^3S1$, $^3D1$, and $^3S_1 - {}^3D_1$ partial waves.

1.3.2 Odd Channels — $(S,T) = (0,0)$ and $(1,1)$

Most of the general features discussed in the previous subsection are also observed in the matrix elements of the odd channels. The $^1P_1$ partial wave shown in Fig. 1.12, for instance, is the lowest partial wave for $(S,T) = (0,0)$. Since this is a non-coupled channel, there is only a redistribution of repulsion within the partial wave, resulting in the familiar decoupling which is more pronounced in the SRG case.

For the first partial waves affected by the odd-channel tensor force are $^3P_2$, $^3F_2$, and $^3P_2 - {}^3F_2$. The matrix elements of $^3P_2$ are shown in Fig. 1.12 — their overall structure resembles the $^1D_2$ wave discussed before. The appearance of the off-diagonal attractive 'wings' in $^3P_2$ clearly implies that this particular behavior is not tied to the tensor correlations.

For V_{UCOM}, the matrix elements of the $^3F_2$ partial wave (not shown) hardly vary with $I_\vartheta^{(1,1)}$ — variations by $\Delta I_\vartheta^{(1,1)} \approx 0.7\,\mathrm{fm}^3$ change the matrix elements by less than $10\,\mathrm{keV\,fm}^3$. The reduction of the repulsion is caused by the central correlator alone; for the SRG-evolved interaction, the effect is similar, but the suppression of off-diagonal matrix elements is more pronounced. The $^3P_2$ and $^3P_2 - {}^3F_2$ waves, on the other hand show a notable sensitivity to the values of $I_\vartheta^{(1,1)}$, which is illustrated in Fig. 1.13.

Looking at the off-diagonal matrix element, we see that the central correlator alone causes a suppression of about $0.5 \, \mathrm{MeV \, fm^3}$, and leaves a quite extended tail for large $|q - q'|$. A tensor correlator with $I_\vartheta^{(1,1)} = 0.02 \, \mathrm{fm^3}$ leads to a significant reduction of the off-diagonal matrix elements, which increases with $I_\vartheta^{(1,1)}$. For $I_\vartheta^{(1,1)} = 0.05 \, \mathrm{fm^3}$, the width of the peak in the diagonal region is comparable to that of the SRG interaction with $\bar\alpha = 0.0215 \, \mathrm{fm^4}$; the V_{UCOM} matrix elements, however, still exhibit a flat extended off-diagonal tail, while the repulsive strength contained in these matrix elements has been shifted to the diagonal more efficiently in the SRG evolution, causing off-diagonal matrix elements with $|q - q'| \approx 2 - 3 \, \mathrm{fm^{-1}}$ to vanish. The structure and evolution of the off-diagonal tail are most likely another indication for a too-rigid parameterization of the UCOM correlation functions, and warrant further studies beyond this work.

Summarizing, we note that the effect of the $(S, T) = (1, 1)$ correlator is significantly smaller than the effect of the $(S, T) = (1, 0)$ correlator, which is of crucial importance to obtain bound nuclei at the mean-field level. Nevertheless, a triplet-odd correlator of non-vanishing range can provide additional binding energies of $1 - 2 \, \mathrm{MeV}$ per nucleon in heavier nuclei, as we will see in Chapter 2.

1.4   Few-Body Systems

In the discussion of Sect. 1.3, we have repeatedly noted that the pre-diagonalization of the Hamiltonian in momentum space results in the suppression of off-diagonal matrix elements. In the shell-model language, strong off-diagonal matrix elements couple states with low- and high-energy particle-hole configurations. Counting the energy of single-particle excitations in units of $\hbar\Omega$, it takes a large $\mathcal{N}_{\mathrm{max}}\hbar\Omega$ model space to fully converge the eigenstates of the nuclear Hamiltonian in such a calculation. In this context, V_{UCOM} and V_α are expected to exhibit an improved convergence behavior, because low- and high-energy configurations are decoupled. Consequently, simple many-body states like the mean-field Slater determinants, corresponding to a $0\hbar\Omega$ space, can access the attractive interaction strength which is otherwise contained in off-diagonal matrix elements.

The ideal tool to study these properties is the quasi-exact, translationally invariant No-Core Shell Model (NCSM) developed by Navrátil et al. [33]. We use the relative matrix elements of V_{UCOM}, derived from the AV18 interaction, including charge-dependent and electromagnetic parts as described in [1] (see also Appendices E.1 and E.3). A NCSM study using SRG-evolved interactions which leads to similar results has recently been published in [34].

1.4.1   Convergence in the No-Core Shell Model

By studying $^3\mathrm{H}$ and $^4\mathrm{He}$, the simplest bound few-body systems beyond the deuteron, one can gain insight into correlations beyond the two-body level. Figure 1.14 shows the ground-state energy of $^4\mathrm{He}$, calculated in the NCSM using AV18 and V_{UCOM} with $I_\vartheta^{(1,0)} = 0.09 \, \mathrm{fm^3}$, $I_\vartheta^{(1,1)} = 0 \, \mathrm{fm^3}$, as a function of the oscillator parameter $\hbar\Omega$ and the model space size indicated by the largest included relative oscillator quantum number $\mathcal{N}_{\mathrm{max}} = 2N_{\mathrm{max}} + L_{\mathrm{max}}$. We stress that no additional Lee-Suzuki transformation has
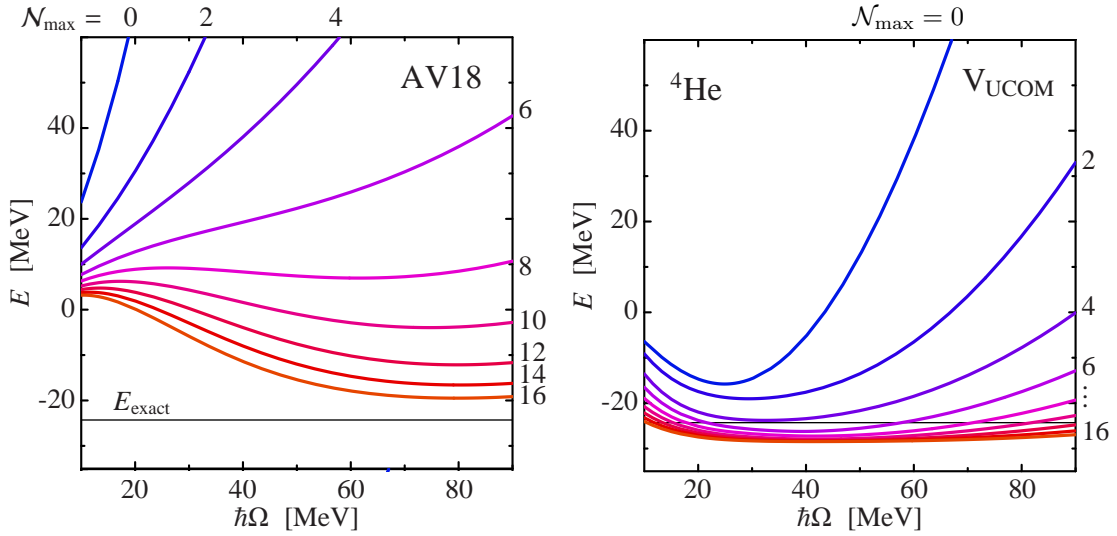
Figure 1.14: Ground-state energy of ^{4}He as a function of $\hbar\Omega$ for AV18 (top) and V_{UCOM} with $I_\vartheta^{(1,0)} = 0.09\,\mathrm{fm}^3$. $\mathcal{N}_{\max}$ denotes the model space size, the solid horizontal lines indicate results from exact Faddeev-Yakubovsky calculations [35]. Figures taken from [6].

been carried out in these calculations, i.e., the effective interaction is generated by the UCOM alone.

For the uncorrelated AV18, results barely start to converge for model-space sizes of $\mathcal{N}_{\max} \approx 14 - 16$, which are already at the limit of what is computationally feasible, and there is still some binding energy missing compared to the result of an exact Faddeev-Yakubovsky calculation [35]. The situation improves dramatically if we use V_{UCOM}. First of all, we notice that a bound nucleus is already obtained with a $0\hbar\Omega$ model space consisting of a single Slater determinant, i.e., at the mean-field level. This is the result of the pre-diagonalization of the Hamiltonian in momentum space discussed in Sect. 1.3: the explicit treatment of short-range correlations (i.e., correlations between states with a large difference in the relative momenta) recovers the bulk of the binding energy. As the model-space size increases, the excited states start to probe the off-diagonal matrix elements, and since these are also suppressed at large momentum differences, the energy gain is more moderate, and convergence is obtained already at $6 - 8\hbar\Omega$ for a wide range of oscillator parameters, in contrast to the uncorrelated AV18.

In the discussion of the correlation operators in Sect. 1.1, we argued that only short-range correlations are to be treated by the unitary transformation, while residual long-range correlations (corresponding to small changes in the relative momenta) should be described by the model space. This is exactly what is observed here: as the description of the long range-correlations improves with increasing model-space size, about $10\,\mathrm{MeV}$ additional binding energy are obtained.

Another important observation is the larger binding energy obtained with V_{UCOM}, visible in greater detail for the ground-state energies of ^{3}H and ^{4}He in Fig. 1.15. V_{UCOM} differs from its parent interaction due to the truncation of the cluster expansion at the two-body level (cf. Sect. 1.1.3). If all terms of the cluster expansion were kept, one would obviously not change the energy eigenvalues of the Hamiltonian at all because of
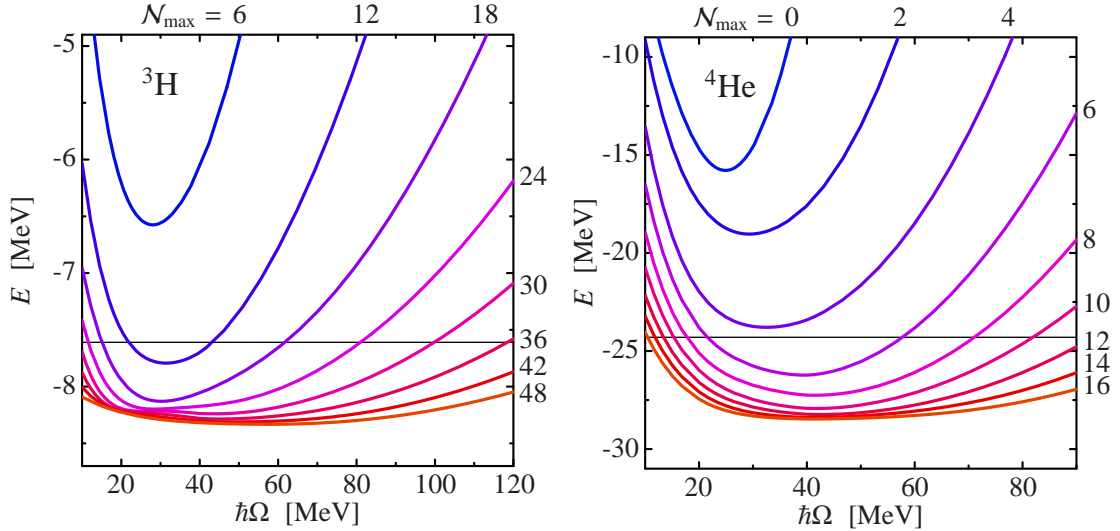
Figure 1.15: Ground-state energies of ^{3}H and ^{4}He for V_{UCOM} with $I_\vartheta^{(1,0)} = 0.09\,\mathrm{fm}^3$. $\mathcal{N}_{\mathrm{max}}$ denotes the model space size, the solid horizontal lines indicate results from exact Faddeev-Yakubovsky calculations [35]. Figures taken from [6].

the unitarity of the transformation, and we would end up in agreement with the exact Faddeev-Yakubovsky results for AV18. Therefore, the surplus binding energy provides a direct estimate for the energy contributions from the omitted higher cluster order terms.

1.4.2 The Tjon Line

By repeating the NCSM study of ^{3}H and ^{4}He for various values of $I_\vartheta^{(1,0)}$ (the triplet-odd correlator range $I_\vartheta^{(1,1)}$ is irrelevant for these nuclei because the nucleons occupy even states) or $\bar\alpha$, we can assess the range-dependence of the omitted higher-order many-body terms which are induced by the UCOM and SRG transformations, respectively. In Fig. 1.16 we show the result of this investigation as a correlation plot of the ^{3}H and ^{4}He ground-state energies. The plot reveals a striking feature — by varying the respective parameters, we map out the so-called Tjon line, which results from a correlation between the two binding energies for phase-shift equivalent NN interactions [35, 36]. Since V_{UCOM} and V_α are phase-shift equivalent to their parent interaction by construction, it is not surprising that the Tjon line emerges in both approaches. There is, however, a subtle difference: in the UCOM, movement along the Tjon line is solely related to the treatment of the tensor correlations, while the SRG flow affects central and tensor parts of the interaction at the same time. As a result, the SRG curve was found to inflect and reverse direction once the flow parameter assumes a critical value [34].

As discussed in Sect. 1.1.4, the application of the correlation operators shifts strength from the repulsive local core of the interaction to non-local momentum-dependent terms. In the case of the tensor correlator, in particular, non-local tensors are generated which encode partial-wave-dependent redistributions between local and non-local terms. From the connection between the UCOM and SRG generators, we can conclude that the SRG acts similarly, although the mechanism is hidden in the
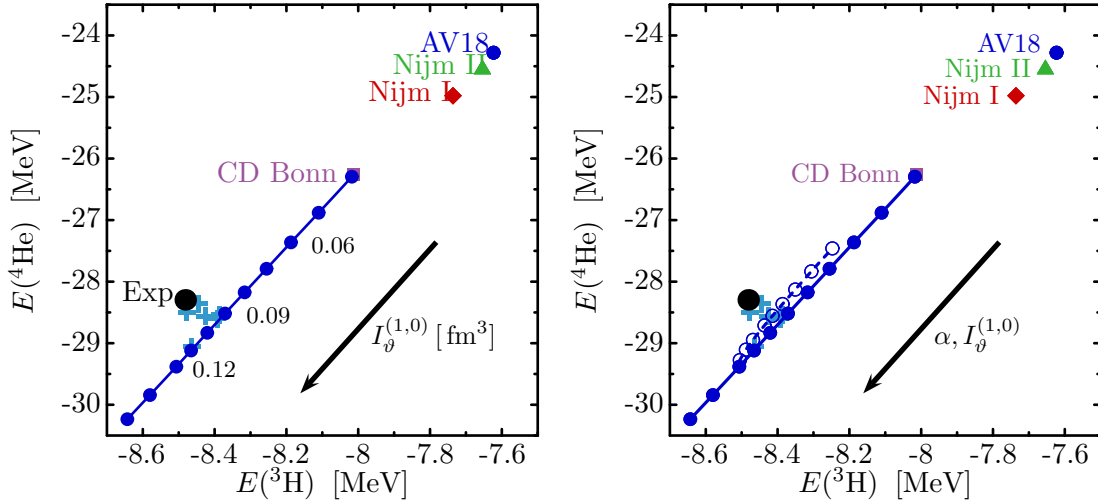
Figure 1.16: Tjon line for ^{3}H and ^{4}He binding energies. Shown are results for V_{UCOM} with different $I_\vartheta^{(1,0)}$ (●) and V_α for various $\bar\alpha$ (○), both derived from AV18, as well as results for AV18 (●) and the Nijmegen I (◆) and II (◆), as well as CD-Bonn (■) (upper right corners); (✚) include $3N$ interactions [35]. The experimental point is indicated by (●).

momentum-space matrix elements. Thus, the binding energies of ^{3}H and ^{4}He are systematically improved with respect to the experimental value by introducing additional non-locality. Indeed, among the realistic two-body interactions included in Fig. 1.16, the CD-Bonn retains more non-local structures than the other interactions, and consequently lies closest to the experimental point, while the purely local AV18 is farthest away. This observation has been made by several authors in the past [37, 38, 39]. In Ref. [38], in particular, Doleschall et al. have constructed a potential with short-range non-locality which describes the ^{3}H and ^{3}He binding energy at the cost of sacrificing some accuracy in the reproduction of phase shifts. The UCOM and SRG transformations, however, allow for a study of the impact of non-local potential terms in a more systematic fashion.

The ability to tune the tensor correlator range or the flow parameter opens an interesting prospect for many-body calculations with V_{UCOM} and V_α. Realistic interactions like AV18, CD-Bonn or the Nijmegen potentials need to be supplemented with different phenomenological $3N$ interactions like the Urbana [40] or Tucson-Melbourne [41] models in order to provide additional attraction and achieve agreement with experiment[3] [35, 43]. Since neither *genuine* nor *induced* $3N$ forces were included in the calculations with V_{UCOM} and V_α which are shown in Fig. 1.16, the net contribution of these terms has to be small for those interactions which yield results in the proximity of the experimental point. Thus, by selecting $I_\vartheta^{(1,0)} = 0.09$ fm^3 or $\bar\alpha = 0.03$ fm^4, respectively, we have chosen those phase-shift equivalent two-body forces which require the *weakest* additional $3N$ forces. It is important to realize that this does *not* mean that a $3N$ force is unnecessary altogether: the binding energy is an observable which is somewhat insensi-

---

[3]From the theoretical point of view, these calculations are somewhat unsatisfactory, because the NN and $3N$ interactions are inconsistent in the sense that they are not derived from the same underlying theory. For these reasons, there is presently considerable theoretical effort to construct these interactions from chiral EFT [4, 42].
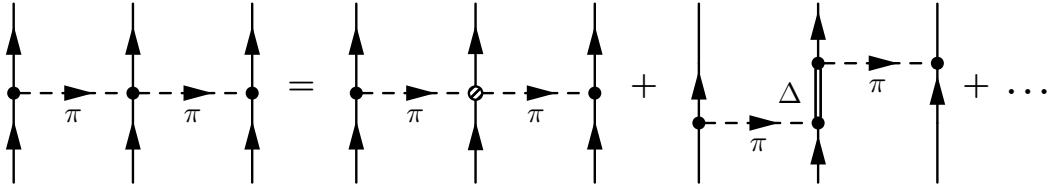
Figure 1.17: 2π-exchange diagrams in chiral EFT. The corresponding matrix elements depend on the degrees of freedom of the EFT, e.g., an explicit Δ (see text).
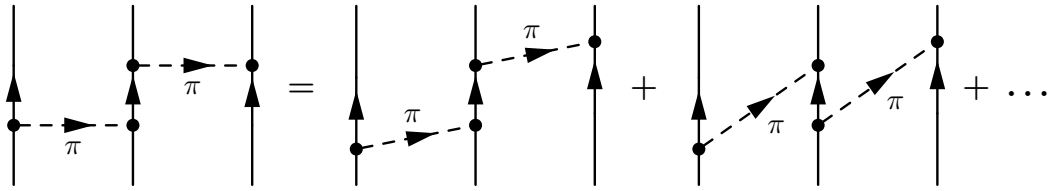
Figure 1.18: Reduction of iterated π-exchange in a non-relativistic theory: covariant (left-hand side) and time-ordered diagrams (right-hand side).

tive to the details of the many-body wavefunction. Indeed, while published theoretical results are sparse, it is nevertheless a very distinctive trend that the more non-local the NN interaction is, the more it underpredicts nuclear radii, even in the quasi-exact NCSM (see e.g. [44]). This problem will turn up in our HF and HFB calculations in Chapters 2 and 4. Furthermore, one cannot assume automatically that the same cancellation will work out in larger systems, or in nuclear matter (cf. Sect. 2.1.4).

1.4.3 Many-Nucleon Forces

We conclude the discussion of this chapter with some remarks on many-nucleon forces. The fundamental theories of the Standard Model do not contain interactions of more than two fermions due to renormalizability arguments [45, 46]. Effective field theories (EFTs), on the other hand, do not use the degrees of freedom which are considered fundamental. As a result, there are infinitely many interaction terms, including effective many-body interactions. The only constraints on the EFT are imposed by the symmetries of the underlying theory. Since one obviously cannot deal with infinitely many interaction terms in practical applications, one has to introduce a power-counting scheme to decide which terms are relevant.

Chiral EFT (see e.g. [4] and references therein) has been established as an appropriate description of the strong interaction at low energies and momenta. While quarks and gluons are the degrees of freedom of Quantum Chromodynamics, the fundamental theory of the strong interaction, the description of processes in chiral EFT is based on nucleons and pions; the inclusion of heavier particles like the Δ-resonance is also a widely discussed subject.

The effective chiral Lagrangian for interactions between nucleons gives rise to $3N$ interactions starting at next-to-next-to-leading order (N2LO) of the power-counting scheme. An example is the 2π-exchange diagram shown in Fig. 1.17. The contribution of this diagram is contingent on the actual degrees of freedom in the theory. In the Δ-less

theory, the intermediate Δ-propagator is shrunk to a point, and implicitly accounted for by the fit of the theory's low-energy constants appearing in the vertex. Note that this also implies that this particular diagram is promoted to NLO for a theory with an explicit Δ degree of freedom.

A further source of many-nucleon forces is the reduction of the relativistic effective field theory to the non-relativistic limit. For chiral EFT, this is a necessity, because the nucleon mass provides a further characteristic scale which causes divergences in loop diagrams unless a so-called heavy-baryon expansion in the inverse nucleon mass $\frac{1}{m_N}$ is carried out [47]. This has consequences for processes like the iterated pion exchange shown in Fig. 1.18. Whereas the Feynman diagrams of the relativistic theory contain all time-orderings in a manifestly covariant manner, the time-ordering becomes relevant in the non-relativistic limit. While the first time-ordered diagram in Fig. 1.18 contributes to the two-nucleon interaction, the second time-ordered diagram gives rise to a non-relativistic $3N$ force because the pion exchange overlaps temporally.

These considerations show that the notion of a single *definite NN*, $3N$ or higher many-nucleon force is ill-defined in the low-energy setting relevant for nuclear structure. Indeed, as the UCOM or the SRG show, there are infinitely many unitarily equivalent nuclear Hamiltonians which describe the same low-energy observables, i.e., scattering phase shifts and deuteron binding energy. Since these only constrain the matrix elements of the interaction on the energy shell, it is not surprising that these interactions can differ considerably off-shell. The off-shell parts of the interaction are probed in many-nucleon calculations of binding energies, for example, and calculations with different forces will therefore yield different results. Consequently, one needs at least a $3N$ force to obtain proper binding energies, as the Green's Function Monte Carlo (GFMC) calculations with the AV18 NN and Illinois $3N$ interactions, for example [40, 48, 49, 50]. If the NN and $3N$ forces are not derived consistently, however, one cannot discern whether the chosen interaction terms and/or parameters are not merely required to cancel unwanted contributions from the off-shell NN interaction. The best approach in this respect is the derivation of potentials from chiral EFT, which gives *consistent NN* and many-nucleon forces.

The discussion of the Tjon line has shown that the net $3N$ force, i.e., the sum of genuine and induced $3N$ terms (cf. Sects. 1.1.3 and 1.2), can be minimized. This is demonstrated quite impressively in a NCSM calculation of ^{10}B by P. Navratil: it was long believed that the proper 3^+ ground state can only be obtained if a $3N$ interaction is included. While this is true for CD-Bonn and even the chiral N3LO interaction, Fig. 1.19 shows the result of a NCSM calculation using our standard V_{UCOM} ($I_{\vartheta}^{(1,0)} = 0.09\,\text{fm}^3, I_{\vartheta}^{(1,1)} = 0\,\text{fm}^3$). We see that a two-nucleon interaction can produce the proper ground state as well.

One needs to be aware, however, that the UCOM and the SRG evolution redistribute interaction strength between the various NN and many-nucleon terms. While NN and $3N$ forces may be sufficient to reproduce experimental data for parent interactions like AV18, the effective interactions might need accompanying many-nucleon forces with $A > 3$. For the chiral interactions, for example, the $4N$ force at N3LO has recently been worked out [51], and is expected to contribute on the order of $1\,\text{MeV}$ to the binding in nuclear matter. Moreover, the consistent evolution of the chiral $NN + 3N(+4N)$
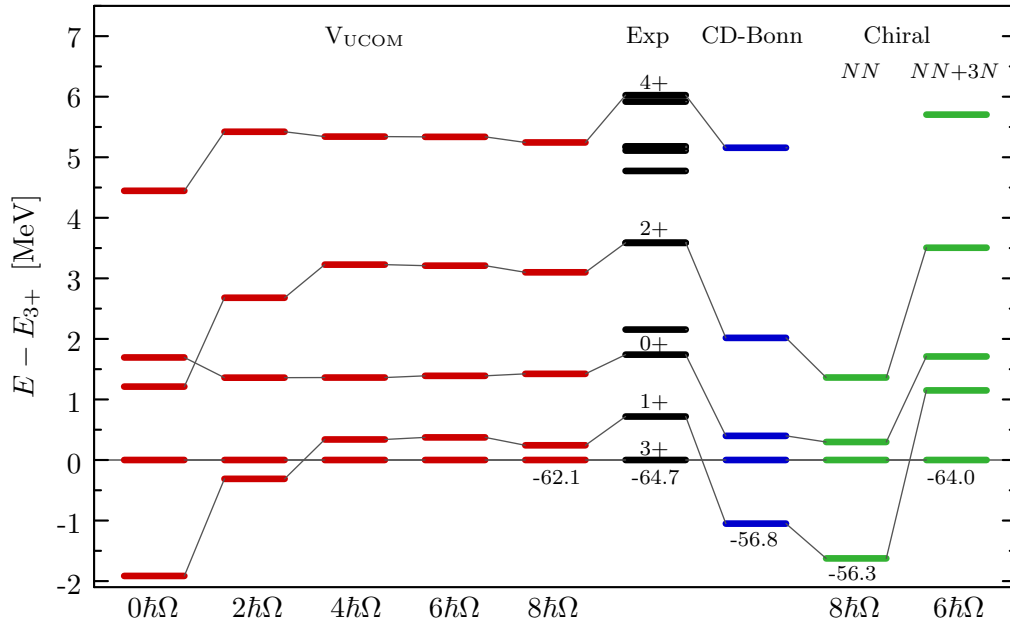
Figure 1.19: Spectrum of ^{10}B in the NCSM for V_{UCOM}, compared to experiment and calculations with CD-Bonn and the chiral N3LO NN-interaction with or without N2LO $3N$ interaction. All calculations were done by P. Navratil.

interaction at N3LO in either the UCOM or SRG schemes should ultimately remove the dependence of the observables on the transformation parameters. While there are indications, like the absorption of the dependence of the ^{3}H and ^{4}He binding energies on the flow parameter in the low-energy constants of the N2LO chiral $3N$ force in the SRG approach [52], there is no conclusive evidence yet due to the technically involved transformation of the many-nucleon forces.

Chapter 2

Hartree-Fock with Modern Effective Interactions

2.1 Hartree-Fock

Before we present and discuss results from Hartree-Fock calculations and their extensions, we give a short overview of the implementation. The basic tenets of HF theory are not discussed here, because HF is simply obtained by taking the limit of vanishing pairing correlations in the Hartree-Fock-Bogoliubov theory discussed extensively in the next chapter.

2.1.1 Configuration Space and Convergence

The single-particle states used to construct the Slater determinants are expanded in a spherical harmonic oscillator (SHO) basis,

$$\left| \nu l j m m_t \right\rangle = \sum_{n'l'j'm'} C^{m_t}_{\nu l j m, n'l'j'm'} \left| n'l'j'm'm_t \right\rangle, \tag{2.1}$$

where we have suppressed the spin and isospin quantum numbers $s = t = \frac{1}{2}$. Since we will be dealing with closed-shell nuclei in this chapter, we restrict ourselves to the spherically symmetric case

$$\left| \nu l j m m_t \right\rangle = \sum_{n} C^{(lj)m_t}_{\nu n} \left| n l j m m_t \right\rangle. \tag{2.2}$$

The configuration space basis is truncated either in the main oscillator quantum number

$$e = 2n + l \leq e_{\max} \tag{2.3}$$

or simultaneously in e and the orbital angular momentum l. Results are typically well-converged with respect to the basis size at $e_{\max} = 12$, even for nuclei as heavy as ^{208}Pb, due to the improved convergence behavior of the UCOM and SRG interactions [10]. Since the SHO single-particle states depend on the oscillator length a_{HO}, we carry out the calculations for a given set of these parameters and take the minimal energy. In most cases, the a_{HO}-dependence is already very flat for $e_{\max} \approx 8 - 10$ [10].

2.1.2 Intrinsic Kinetic Energy

Since the SHO basis of our configuration space is localized, it is bound to break the translational invariance of the nuclear Hamiltonian while solving the HF equations. As a result, states and expectation values will contain spurious contaminations from the center-of-mass motion of the nucleus. In practical calculations, several schemes are used to correct for this effect, the simplest consisting of an essentially perturbative subtraction of $\langle \, T_{cm} \, \rangle$ after the variation is performed.

In our approach, we employ a somewhat more sophisticated approach by minimizing the energy of the *intrinsic Hamiltonian*

$$H_{int} = T_{int} + V \equiv T - T_{cm} + V \,, \tag{2.4}$$

where the *intrinsic kinetic energy* is given by the operator

$$T_{int} \equiv \frac{1}{A} \sum_{i,j=1}^{A} \frac{(\mathbf{p}_i - \mathbf{p}_j)^2}{2\mu} \,, \quad \mu = \frac{m_N}{2} \,, \tag{2.5}$$

with i and j running over all A nucleons. Technically, the intrinsic Hamiltonian is a two-body operator and can be correlated as described in Sect. 1.1.4.

2.1.3 Radii

In the many-nucleon system, the intrinsic mean-square radius is defined by

$$R_{ms} = \frac{1}{A} \sum_{i}^{A} (\mathbf{x}_i - \mathbf{X})^2 \,, \tag{2.6}$$

where $\mathbf{X}$ is the center of mass. After some algebra, the mean-square radii for nucleons, protons, and neutrons can be expressed as sums of translationally invariant two-body operators [53],

$$R_{ms} = \frac{1}{2A^2} \sum_{ij} \mathbf{r}_{ij}^2 \,, \tag{2.7}$$

$$R_{ms}^{p} = \frac{1}{AZ} \sum_{ij} \mathbf{r}_{ij}^2 \Pi_p - \frac{1}{2A^2} \sum_{ij} \mathbf{r}_{ij}^2 \,, \tag{2.8}$$

$$R_{ms}^{n} = \frac{1}{AN} \sum_{ij} \mathbf{r}_{ij}^2 \Pi_n - \frac{1}{2A^2} \sum_{ij} \mathbf{r}_{ij}^2 \,, \tag{2.9}$$

where i, j run over all nucleons, and Π_p and Π_n project on protons and neutrons, respectively. Using these forms, one can easily apply the UCOM central correlation operator or perform an SRG evolution to determine the effective radius operator. In numerical studies in the UCOM framework, however, we have found that the corresponding change in the expectation values is small [10]. The same holds for the transition operators in the Random Phase Approximation (RPA), and is a result of the dominant long-range character of these operators, which renders them insensitive to the short-range correlations [11]. These findings are corroborated by similar observations in the framework of the No-Core Shell Model [54, 55].

The charge radius is defined as

$$R_{\text{ch}} = \sqrt{R_{p,\text{ms}} + r_{p,\text{ch}}^2 + \frac{N}{Z} r_{n,\text{ch}}^2}, \quad\quad (2.10)$$

where we use

$$r_{p,\text{ch}}^2 = (0.875 \text{ fm})^2 \quad\quad \text{and} \quad\quad r_{n,\text{ch}}^2 = -0.116 \text{ fm}^2 \quad\quad (2.11)$$

for the squared proton and neutron charge radii, respectively [56].

2.1.4 Ground State Energies and Radii

Since Hartree-Fock is best suited for the description of nuclear bulk properties, we first consider ground-state energies and charge radii along the nuclear chart. In Chapter 1, we have discussed the origin of the dependence of the UCOM and SRG interactions on the tensor-correlator range constraints I_ϑ, and the flow parameter $\bar{\alpha}$, respectively, and the effects these parameters have in the two- or few-body system. In the course of this chapter, we will extend this study to medium and heavy mass nuclei [10].

Closed-Shell Nuclei

In Figs. 2.1, we show ground-state energies per nucleon as well as the charge radii of several closed shell-nuclei for V_{UCOM}. The first, obvious observation is that we are able to obtain bound nuclei at all from a realistic NN interaction. This is in agreement with the NCSM calculations of Sect. 1.4.1, where bound states for ^{3}H and ^{4}He could be obtained already in a $0\hbar\Omega$ model space consisting of a single Slater determinant. Although the nuclei are underbound by about 4 MeV per nucleon, it is remarkable that the systematics of the ground state energies is reproduced very well, from the p-shell nucleus ^{16}O up to ^{208}Pb. The charge radii, on the other hand, are systematically underestimated.

This apparent discrepancy is resolved by recalling that the correlation operators only describe *short-range* correlations explicitly, and that the definition of what is to be considered a short range is somewhat arbitrary in the case of the tensor correlator. As is evident from Fig. 2.1, we can increase the binding energy and reduce the charge radii further by increasing $I_\vartheta^{(1,0)}$, thereby describing more and more tensor correlations by the correlation operator alone [8]. In the NCSM calculations for few-body systems, we have seen that a proper treatment of long-range correlations, as by increasing the model-space size, provides a considerable amount of additional binding energy for the tensor correlator $I_\vartheta^{(1,0)} = 0.09 \text{ fm}^3$, which was optimized with the help of the Tjon line (cf. Sect. 1.4.2). If the tensor correlator range is increased, the additional energy gain from long-range correlations will *decrease* (cf. Sect. 2.2), and the *total* contribution from both kinds of correlations to the relevant quantities should ultimately reproduce experimental data. In other words, this means that one has to check 'convergence' of the results with respect to the employed many-body methods as well, and HF is clearly only the first step in this regard.

Another important point to consider are the omitted higher-order cluster contributions in the correlated interaction, as well as the omission of genuine many-nucleon forces. Although the net effect of genuine and induced $3N$ forces in ^{3}H and ^{4}He could be
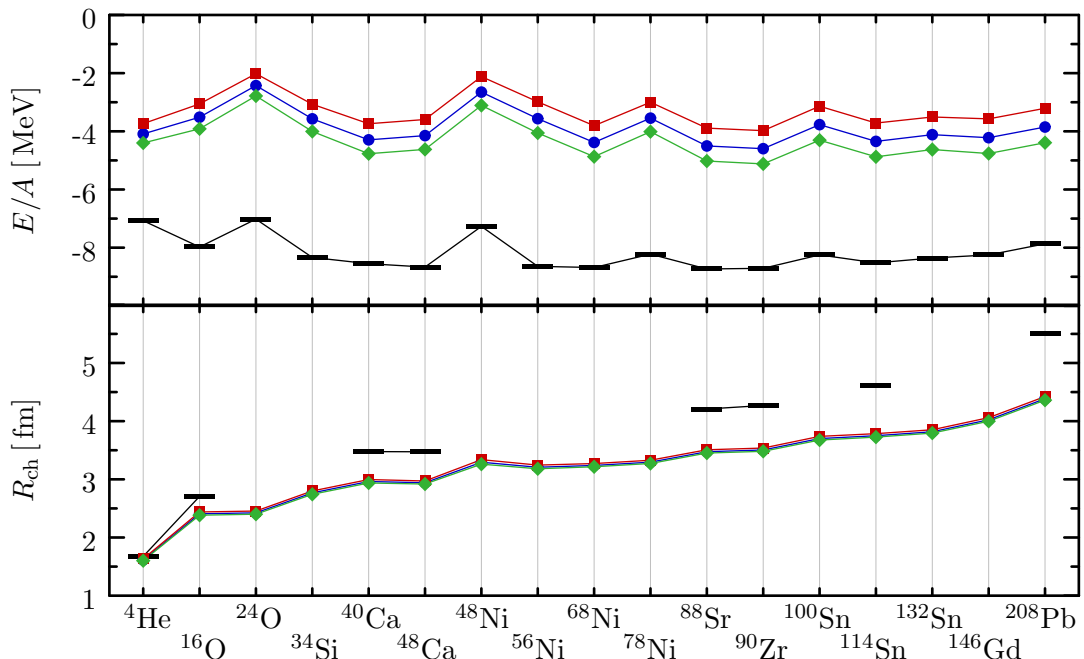
Figure 2.1: Ground-state energies and charge radii of closed-shell nuclei for $e_{max} = 12$. Shown are V_{UCOM} with $I_\vartheta^{(1,0)} = 0.08 \, \text{fm}^3$ (—■—), $0.09 \, \text{fm}^3$ (—●—), and $0.10 \, \text{fm}^3$ (—◆—), compared to experimental data (———). Figure taken from [10].

minimized by choosing the optimal tensor-correlator range constraint $I_\vartheta^{(1,0)} = 0.09 \, \text{fm}^3$, the cancellation between these particular contributions need not hold in larger systems. Furthermore, from nuclei with $A \leq 4$ we do not gain significant insight into the importance of genuine or induced four- or higher many-body forces, which may be necessary to obtain proper binding in heavy nuclei or saturation in nuclear matter (cf. Sects. 1.4.2, 1.4.3 and Ref. [34]).

In light of these considerations, the almost constant offset between the energy per nucleon obtained for the optimized V_{UCOM} and experiment for all A is all the more remarkable. Since the energy contribution of a $3N$ force naively scales by an additional power of A compared to the NN interaction, this implies that the net $3N$ force indeed stays small over the whole mass range, and the required energy shift is due to the missing long-range correlations. Consequently, we observe that the variation of $I_\vartheta^{(1,0)}$ — the control parameter for the separation between short- and long-range tensor correlations — around the optimal value only changes the size of the energy offset, but not the ground-state energy systematics.

The ground-state energy is less sensitive to the structural details of the many-body wavefunction than observables like the radii or transition operators. For these operators, counting arguments do not apply, because a few particles can significantly affect the expectation values — think of the radii in halo nuclei, for example. In that case, it is hard to disentangle which features of the many-body wavefunction are due to the NN, $3N$ or higher terms in the Hamiltonian. While the underestimation of the charge radii shown in Fig. 2.1 gets worse with increasing A, the overall experimental trends are reproduced quite well — the theoretical curves just seem to be tilted around ^{4}He from the experimental to smaller radii. As demonstrated in [22] (cf. Sect. 2.3), this
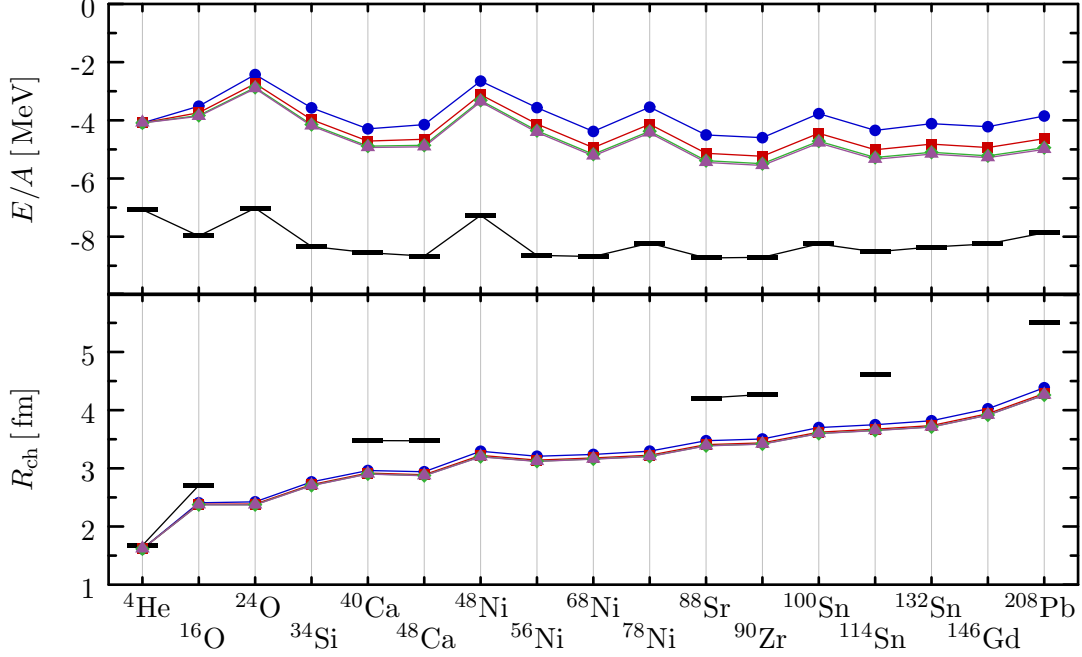
Figure 2.2: Ground-state energies and charge radii of closed-shell nuclei for $e_{\max} = 12$. Shown V_{UCOM} with $I_\vartheta^{(1,0)} = 0.09\,\text{fm}^3$ and $I_\vartheta^{(1,1)} = 0\,\text{fm}^3$ (——●——), $0.02\,\text{fm}^3$ (——■——), $0.05\,\text{fm}^3$ (——◆——), and $0.07\,\text{fm}^3$ (——▲——), compared to experimental data (———).

discrepancy *can* be removed by including a repulsive $3N$ force, but it should be stressed that this is not necessarily the only possible approach.

In Fig. 2.2, we illustrate how ground-state energies and charge radii change with $I_\vartheta^{(1,1)}$. Due to the weaker $(S,T) = (1,1)$ tensor force, the effect of the variation is much smaller than for the $(1,0)$ tensor correlator. We also note that the results for $I_\vartheta^{(1,1)} = 0.05\,\text{fm}^3$ and $0.07\,\text{fm}^3$ are almost identical, which suggests that essentially all of the odd-channel tensor correlations are described by the tensor correlator. That this happens already at smaller values of $I_\vartheta^{(1,1)}$ than for the $I_\vartheta^{(1,0)}$ can be explained by the longer range of the triplet-odd tensor correlator (see Sect. 1.1.5). The additional energy gain and simultaneous reduction of the charge radii becomes slightly stronger as the mass increases. For the energy, this can be understood by counting the number of possible two-nucleon states in each (S,T) channel [18], which is largest for the $(1,1)$-channel because it has the most degrees of freedom in spin and isospin. The decrease of the charge radii is then caused by the tighter binding.

As in the UCOM case, the ground-state energies and charge radii calculated with the SRG interaction V_α vary strongly with the flow parameter. In Fig. 2.3, we show the ground state energies for flow parameters around $\bar{\alpha} = 0.03\,\text{fm}^4$, which was fixed by using the Tjon line (cf. Sect. 1.4.2). Contrary to V_{UCOM}, V_α produces strong overbinding, starting already in the medium-mass range. In fact, for a pure two-body V_α, the optimization of $\bar{\alpha}$ in light nuclei to minimize the net $3N$ force will in general not prevent overbinding in large nuclei or guarantee nuclear matter saturation at sensible densities [34]. Thus, when considering SRG interactions, $3N$ (and perhaps $4N$ or higher order) forces need to be included consistently in the calculations. In principle, these
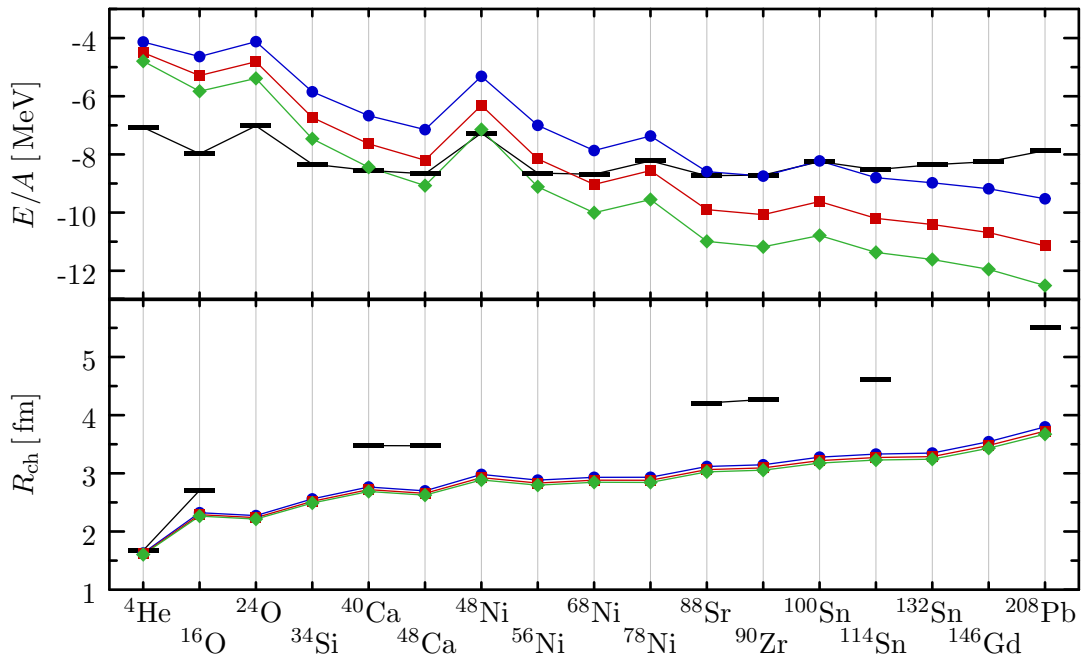
Figure 2.3: Ground-state energies and charge radii of closed-shell nuclei ($e_{max} = 12$) for V_α with $\bar\alpha = 0.025\,\text{fm}^4$ (——●——), $0.030\,\text{fm}^4$ (——■——), and $0.035\,\text{fm}^4$ (——◆——), compared to experimental data (——).

forces must also be included in the flow equation (cf. Sect. 1.2), which complicates its solution quite a bit — so far, an SRG evolution in three-body space has only been carried out in a simple toy model[1] [58].

That the minimization of the net $3N$ force in heavier nuclei works in the case of V_{UCOM} but not for the V_α is related to the particular redistribution of the interaction strength. As we have seen in Sect. 1.3, the SRG is more efficient in pre-diagonalizing the two-body part of the interaction, i.e., it shifts more of the repulsive contributions to high momenta or higher many-nucleon terms. Part of this is due to the independent running of the flow in each partial wave, whereas the UCOM considers only the four different (S,T)-channels. Whether a partial-wave dependent determination of the UCOM correlation functions will improve the pre-diagonalization — and perhaps cause the same overbinding by doing so — remains a subject for further study. If this is not the case, this would imply that an additional non-central and non-tensorial type of short-range correlations has not been taken into account in the UCOM approach. However, the task of identifying a particular *physical* mechanism — i.e., a *state-independent* effect — is severely complicated by the existence of infinitely many possible representations of the two-nucleon interaction, and the infinitely many proper many-body forces accompanying each of these representations (cf. Sect. 1.4.3).

---

[1]Proof-of-principle calculations in a simplified approach, using a chiral N2LO three-nucleon force whose flow with α (or rather the cutoff $\lambda \sim \alpha^{-4}$ in appropriate units) is contained in the low-energy constants alone, and used to absorb the α-dependence of the results, produce satisfactory binding energies and density distributions [57].
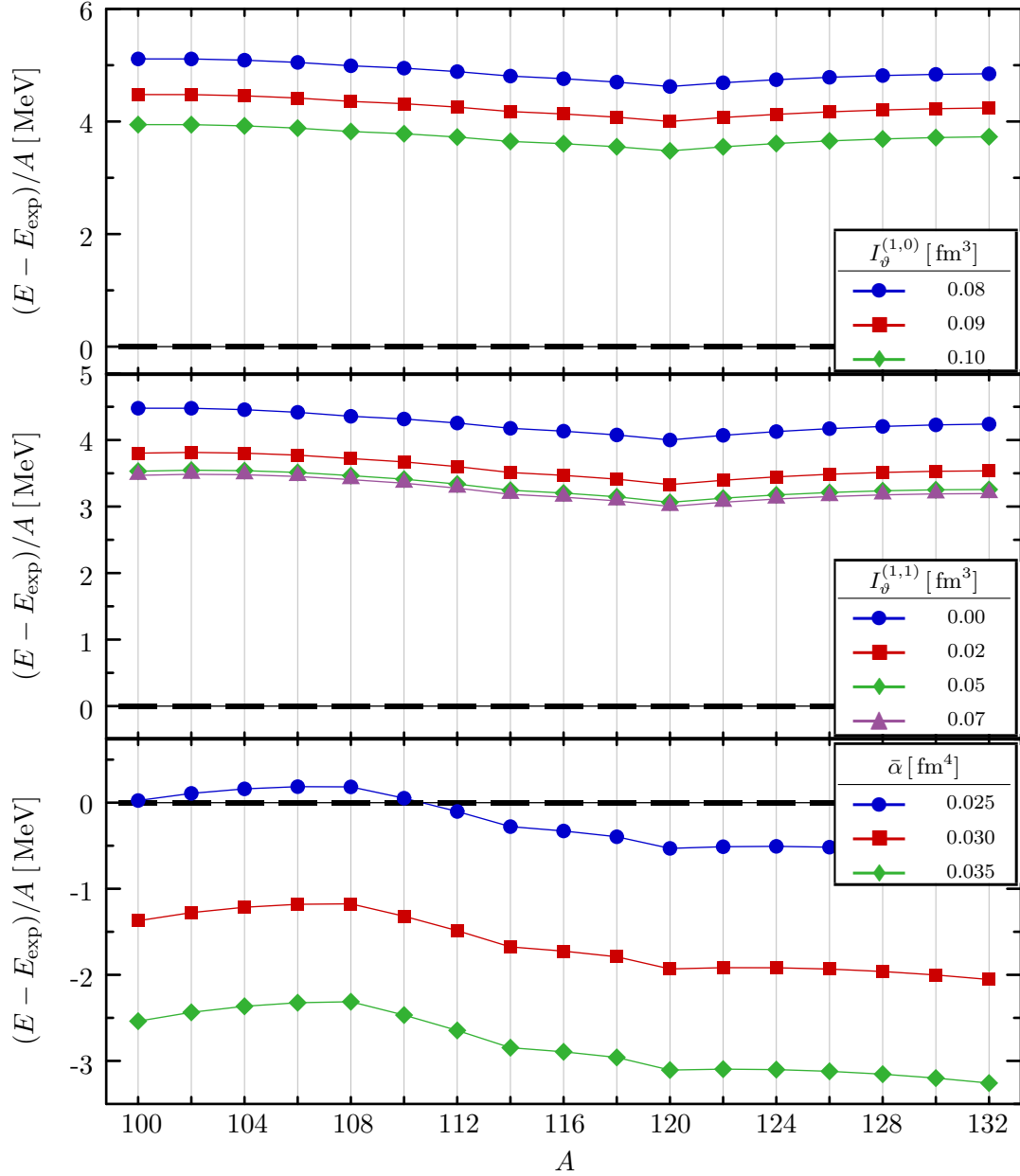
Figure 2.4: Deviation of ground-state energies from experiment (———) for the Sn isotopic chain. *Top:* V_{UCOM} with $I_{\vartheta}^{(1,1)} = 0$ fm^3 and various $I_{\vartheta}^{(1,0)}$. *Center:* V_{UCOM} with $I_{\vartheta}^{(1,0)} = 0.09$ fm^3 and varying $I_{\vartheta}^{(1,1)}$. *Bottom:* SRG interaction V_{α} for different flow parameters $\bar{\alpha}$. All calculations were performed in a basis with $e_{\max} = 12$.

Tin Isotopes

In Fig. 2.4, we compare the ground-state energies of the tin isotopic chain for the same V_{UCOM} and V_α interactions as for the closed-shell nuclei. The charge radii are not shown since they change only weakly over the isotopic chain, and ^{100}Sn, ^{114}Sn, and ^{132}Sn can be found in the figures of the previous subsection.

For V_{UCOM}, the deviation $\Delta E/A = (E - E_{\text{exp}})/A$ of the ground-state energy from experimental data varies by 0.25 to 0.5 MeV per nucleon with increasing neutron number N. Varying the tensor correlator range yields mostly the same results as for the closed-shell nuclei. Increasing $I_\vartheta^{(1,0)}$ or $I_\vartheta^{(1,1)}$ produces almost N-independent shifts of $\Delta E/A$ to smaller values. For the triplet-odd tensor correlator range, we observe the same 'saturation' as for closed-shell nuclei once we pass $I_\vartheta^{(1,1)} = 0.05$ fm^3. The V_{UCOM} curves exhibit a kink at ^{120}Sn, which is due to the closure of a HF major shell by filling the single-particle level $2s_{1/2}$ (cf. the ^{132}Sn spectrum in Fig. 2.5). This major-shell closure at $N = 70$ is a first evidence that the structure of the single-particle spectrum has been distorted by applying the correlation operators, and we will come back to this issue in the next section.

For the SRG interactions, the change in the flow parameter also causes an almost N-independent shift. Combined with the results for closed shell nuclei, this implies that the effect which leads to the overbinding in medium-mass to heavy nuclei can only be weakly isospin-dependent. It is also noteworthy that the addition of further neutrons keeps on reducing the ground state energy even further, as opposed to the increase observed beyond $N = 70$ in the case of V_{UCOM}, which implies that V_α cannot yield a sensible neutron dripline without including (at least) a $3N$ force to improve nuclear saturation.

2.1.5 Single-Particle Spectra

The appearance of the unrealistic $N = 70$ major-shell closure in the HF calculation with V_{UCOM} hints at possible problems with the single-particle spectra of the HF solutions. The single-particle energies themselves are no well-defined observables — experimentally, the closest analogue are energy differences between neighboring nuclei. Naturally, one would expect a truly quantitative description of data only for many-body methods which incorporate the long-range correlations not included in the simple HF Slater determinants, but then the notion of a single-particle energy may be even less well-defined (in the NCSM, e.g., one would ultimately have to resort to comparing the many-body binding energy differences, just as in experiment).

The use of the intrinsic Hamiltonian in our HF formulation requires a modification of the usual single-particle energies: the eigenvalues ϵ_β of the HF Hamiltonian, which are otherwise directly connected to the single-particle removal energy by Koopmans' theorem, are corrected by a shift depending on the intrinsic kinetic energy as well as a state-dependent correction [60, 61]. Thus, for energies below the Fermi energy ϵ_F, one
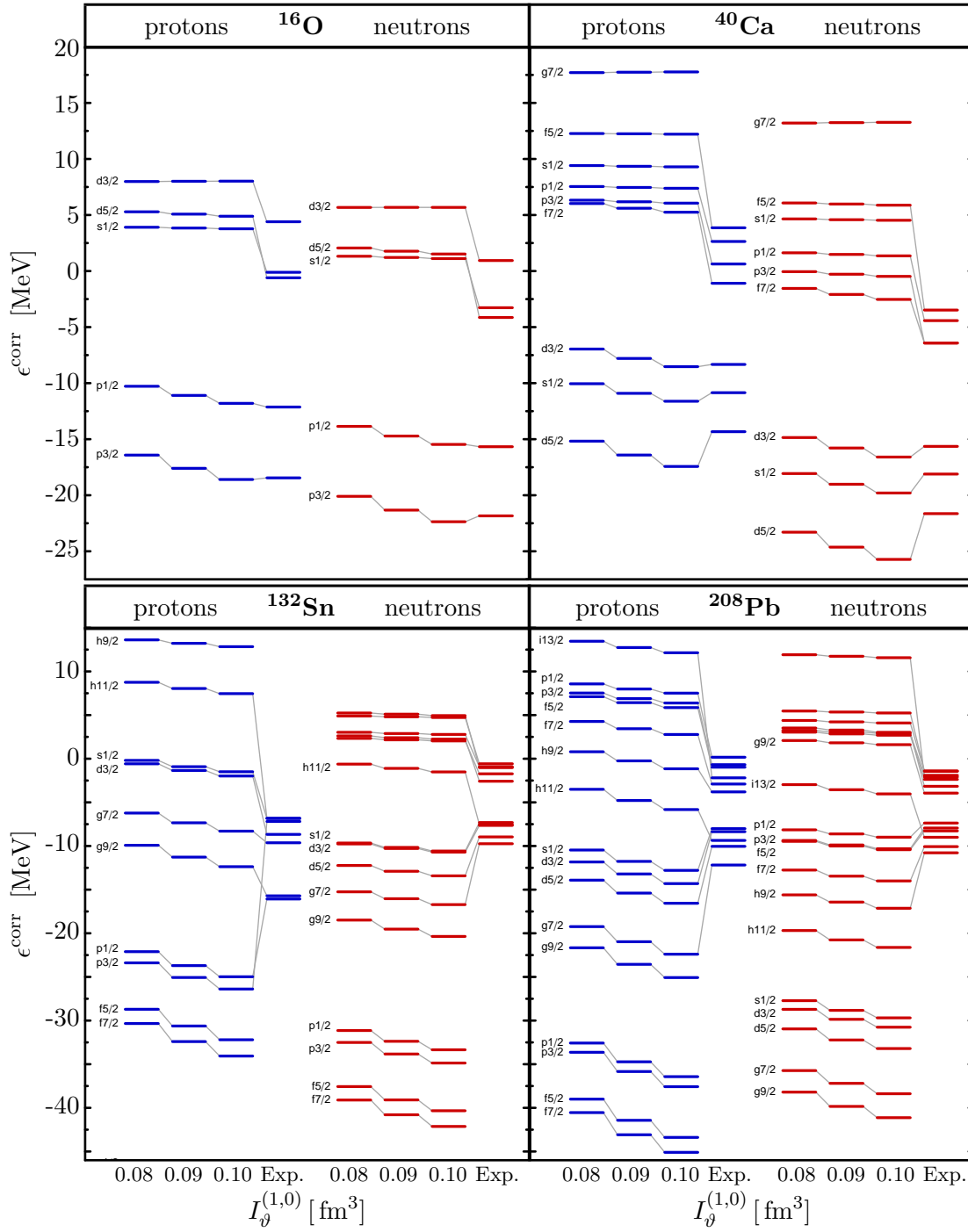
Figure 2.5:   Single-particle energies for V_{UCOM} with various $I_{\vartheta}^{(1,0)}$, compared to experimental values [59] ($e_{\max} = 12$). ^{40}Ca spectra as in Ref. [10].
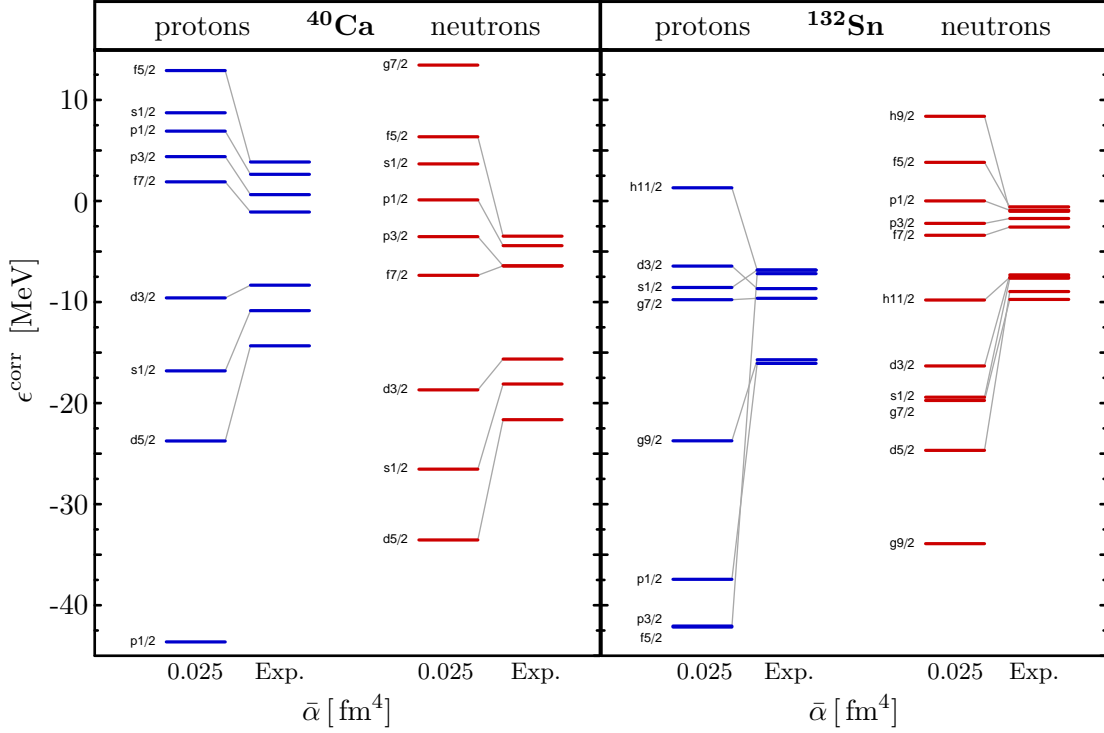
Figure 2.6:   Single-particle energies for the SRG interaction V_α with $\bar{\alpha} = 0.025$ fm^4, compared to experimental values [59] ($e_{\max} = 12$).

has

$$\epsilon_\beta^{\mathrm{corr}} = E_A - E_{A-1}(\beta \text{ removed}) =$$

$$= \epsilon_\beta - \frac{\langle \mathrm{T}_{\mathrm{int}} \rangle}{A - 1} + \frac{2}{mA(A-1)} \sum_\alpha^{<\epsilon_F} \langle \alpha\beta | \mathbf{q}^2 | \alpha\beta \rangle , \qquad (2.12)$$

and for $\epsilon_\beta > \epsilon_F$,

$$\epsilon_\beta^{\mathrm{corr}} = E_{A+1}(\beta \text{ added}) - E_A =$$

$$= \epsilon_\beta - \frac{\langle \mathrm{T}_{\mathrm{int}} \rangle}{A + 1} - \frac{2}{mA(A+1)} \sum_\alpha^{<\epsilon_F} \langle \alpha\beta | \mathbf{q}^2 | \alpha\beta \rangle . \qquad (2.13)$$

Figure 2.5 shows the single-particle spectra for closed shell-nuclei over the whole mass range, obtained for V_{UCOM} with different constraints on the triplet-even tensor correlator around the optimal $I_\vartheta^{(1,0)} = 0.09$ fm^3. For ^{16}O and ^{40}Ca, the highest occupied states — $0p_{1/2}$ and $1d_{3/2}$, respectively — are reproduced reasonably well, but overall, the spectrum is spread wide compared to experimental values. In ^{132}Sn and ^{208}Pb, the levels of the highest occupied major shell, which lie between -10 and -5 MeV experimentally, are spread out over an energy interval of more than twice this size. The lowest single-particle states, in particular, are very deeply bound, and consequently, the shell closures in medium-mass and heavy nuclei — $\pi 0g_{9/2}$, $\nu 0h_{11/2}$ for ^{132}Sn and $\pi 0h_{11/2}$, $\nu 0i_{13/2}$ for ^{208}Pb — occur several MeV above the experimental values in order to compensate.
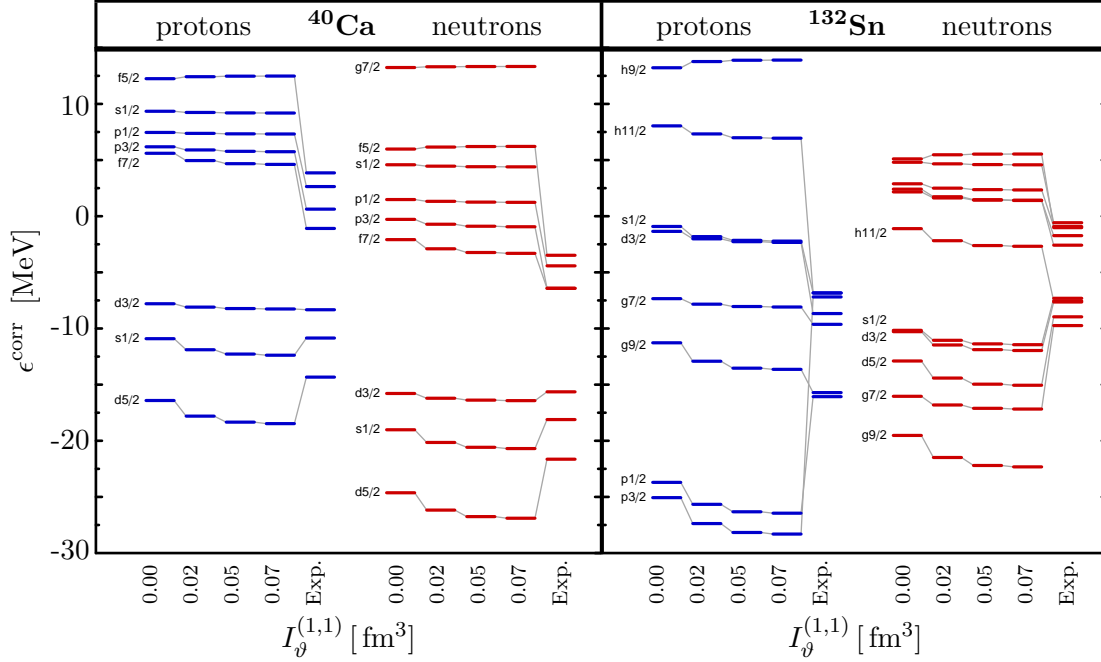
Figure 2.7: Single-particle energies for V_{UCOM} with various $I_\vartheta^{(1,1)}$, compared to experimental values [59] ($e_{\max} = 12$).

At a first glance, the single-particle spectra for the SRG interactions exhibit an even lower level density than the V_{UCOM} interactions. As an example, we show the spectra of ^{40}Ca and ^{132}Sn for V_α with $\bar{\alpha} = 0.025$ fm^4 in Fig. 2.6. It is important to keep in mind, however, that the corresponding SRG interaction yields a much higher binding energy in these nuclei than the V_{UCOM} interactions discussed above. To obtain similar binding energies with a V_{UCOM}, we have use longer-ranged tensor correlators. The observed systematics imply that increasing tensor correlator ranges lead to a decrease of the level densities, hence we expect that the level densities will be reduced to equally low values as for the SRG interactions.

The spreading of the spectra seems to be connected to the degree of pre-diagonalization (i.e. decoupling) in momentum space. Low level densities imply low effective masses, which is consistent with V_{UCOM} saturating above the empirical density in a Hartree-Fock calculation of nuclear matter ($k_F \approx 1.8$ fm^{-1}) [62], and V_α not saturating at all in the regions studied so far [34]. Since the effective mass serves as an empirical measure for the non-locality of the underlying microscopic interaction in nuclear matter calculations, we can conclude that V_α for $\bar{\alpha} = 0.025$ fm^4 is more non-local than V_{UCOM}. This argument resonates with the discussion in Sect. 1.4.2, where we pointed out that the UCOM and SRG transformations systematically introduce non-locality in the interaction, and it reveals that the underestimation of the radii (see e.g. [44]) and the low level density have the same origin.

While the neutron and proton shell structures seem mostly intact in the case of the stable nucleus ^{208}Pb, ^{132}Sn exhibits level rearrangements, most notably for $\pi 0_{11/2}$ and $\pi 1 p_{3/2}$ for V_{UCOM} as well as V_α. In addition, V_{UCOM} exhibits a major-shell closure for $N = 70$ due to the shift of the $\nu 0 h_{11/2}$ state. For V_α, the wider spread of the spectrum

Nucleus	Orbital	$I_\vartheta^{(1,0)}$ [fm^3]			Exp.
		0.08	0.09	0.10	
^{16}O	$\pi\,0p$	6.14	6.50	6.79	6.32
	$\pi\,0d$	2.70	2.93	3.12	5.00
	$\nu\,0p$	6.24	6.61	6.90	6.18
	$\nu\,0d$	3.62	3.91	4.16	5.08
^{40}Ca	$\pi\,0d$	8.22	8.62	8.90	6.00
	$\pi\,0f$	6.24	6.64	6.96	4.95
	$\pi\,1p$	1.22	1.28	1.33	2.01
	$\nu\,0d$	8.44	8.84	9.13	6.00
	$\nu\,0f$	7.62	8.07	8.41	4.88
	$\nu\,1p$	1.68	1.77	1.83	2.00
^{48}Ca	$\nu\,1d$	0.52	0.52	0.52	2.02
	$\nu\,0f$	6.56	6.93	7.20	8.38
^{100}Sn	$\pi\,0g$	4.40	4.71	4.91	6.82
	$\pi\,1p$	1.61	1.72	1.79	2.85
	$\nu\,0g$	4.41	4.71	4.91	7.00
	$\nu\,1d$	2.29	2.45	2.56	1.93
^{132}Sn	$\pi\,0g$	3.69	3.93	4.07	6.08
	$\pi\,1d$	2.08	2.21	2.29	1.48
	$\nu\,0h$	5.85	6.21	6.45	6.53
	$\nu\,1d$	2.57	2.73	2.84	1.65
	$\nu\,2p$	0.69	0.72	0.74	0.81
^{208}Pb	$\pi\,1d$	2.08	2.19	2.26	1.33
	$\pi\,0h$	4.30	4.54	4.67	5.56
	$\nu\,1f$	3.39	3.57	3.69	1.77
	$\nu\,0i$	6.49	6.83	7.05	5.84
	$\nu\,2p$	1.32	1.39	1.43	0.90

Table 2.1:   Proton (π) and neutron (ν) spin-orbit splittings in MeV for V_{UCOM} with different constraints $I_\vartheta^{(1,0)}$ (cf. [10]), compared to experimental values [59] ($e_{\mathrm{max}} = 12$).

causes the appearance of equally wide gaps above and below $\nu 0h_{11/2}$, which are of the order of the experimentally extracted ≈ 5 MeV major shell gap, so the $\nu 0h_{11/2}$ would constitute a major shell in its own right. Looking at the whole spectrum, the overall shell structure seems to be rather dissolved. One has to keep in mind that ^{132}Sn is already quite removed from the valley of stability, and therefore expected to be more susceptible to the influence of the missing long-range correlations.

The spin-orbit splittings obtained from our HF calculations provide valuable information on the spin-orbit structure of the effective interactions, while being less sensitive to the absolute shifts of the spectra due to the UCOM and SRG transformations. The calculated spin-orbit splittings for a series of parameters $I_\vartheta^{(1,0)}, I_\vartheta^{(1,1)}$, and $\bar{\alpha}$, respectively, are summarized in Tabs. 2.1 to 2.3. When comparing to experimental splittings, it is important to keep in mind that these can only be accessed indirectly, leading to significant differences of up to a few MeV, depending on the data and method used for

Nucleus	Orbital	$I_\vartheta^{(1,1)}$ [fm³]				Exp.
		0.0	0.02	0.05	0.07	
^{16}O	$\pi\,0p$	6.50	7.18	7.44	7.51	6.32
	$\pi\,0d$	2.93	3.29	3.45	3.50	5.00
	$\nu\,0p$	6.61	7.29	7.56	7.63	6.18
	$\nu\,0d$	3.91	4.37	4.56	4.61	5.08
^{40}Ca	$\pi\,0d$	8.62	9.71	10.12	10.21	6.00
	$\pi\,0f$	6.64	7.47	7.79	7.87	4.95
	$\pi\,1p$	1.28	1.48	1.56	1.58	2.01
	$\nu\,0d$	8.84	9.96	10.38	10.47	6.00
	$\nu\,0f$	8.07	9.06	9.44	9.52	4.88
	$\nu\,1p$	1.77	2.04	2.15	2.17	2.00
^{48}Ca	$\nu\,1d$	0.52	0.60	0.63	0.64	2.02
	$\nu\,0f$	6.93	8.10	8.52	8.61	8.38
^{100}Sn	$\pi\,0g$	4.71	5.98	6.43	6.49	6.82
	$\pi\,1p$	1.72	2.13	2.28	2.30	2.85
	$\nu\,0g$	4.71	6.04	6.51	6.57	7.00
	$\nu\,1d$	2.45	3.01	3.23	3.25	1.93
^{132}Sn	$\pi\,0g$	3.93	5.08	5.49	5.55	6.08
	$\pi\,1d$	2.21	2.75	2.94	2.96	1.48
	$\nu\,0h$	6.21	7.65	8.14	8.21	6.53
	$\nu\,1d$	2.73	3.36	3.59	3.61	1.65
	$\nu\,2p$	0.72	0.87	0.93	0.93	0.81
^{208}Pb	$\pi\,1d$	2.19	2.70	2.89	2.90	1.33
	$\pi\,0h$	4.54	5.77	6.21	6.25	5.56
	$\nu\,1f$	3.57	4.34	4.60	4.63	1.77
	$\nu\,0i$	6.83	8.40	8.93	8.98	5.84
	$\nu\,2p$	1.39	1.67	1.78	1.78	0.90

Table 2.2:   Proton (π) and neutron (ν) spin-orbit splittings in MeV for V_{UCOM} with $I_\vartheta^{(1,0)} = 0.09\,\mathrm{fm}^3$ and different $I_\vartheta^{(1,1)}$, compared to experimental values [59] ($e_{\max} = 12$).

their extraction. In the tables, we are using the values reported in Ref. [59].

For V_{UCOM}, the splittings turn out to be reasonable for the closed-shell nuclei studied, hence there seem to be no major problems with the spin-orbit structure. Therefore, the shift of the $\nu 0h_{11/2}$ level in ^{132}Sn between major shells appears to be a bulk effect related to the overall spreading of the spectrum. The variation of the $I_\vartheta^{(1,T)}$ reveal the close connection between spin-orbit and tensor interactions. In fact, the tensor correlator shifts interaction strength from the tensor interaction to the central and spin-orbit terms, as can be seen from the structure of the correlated tensor interaction [17]:

$$c_\Omega^\dagger s_{12}(\hat{\mathbf{r}}, \hat{\mathbf{r}}) c_\Omega = e^{-3\vartheta(\mathrm{r})} s_{12}(\hat{\mathbf{r}}, \hat{\mathbf{r}}) + 8(1 - e^{-3\vartheta(\mathrm{r})}) \Pi_{S=1} + 6(1 - e^{-3\vartheta(\mathrm{r})}) \mathbf{l} \cdot \mathbf{s} + \ldots, \quad (2.14)$$

where we have omitted small higher order interaction terms (see Sect. 1.1.4 and Refs. [18, 63]). The size of the spin-orbit splittings clearly increases with the tensor correlator ranges, i.e., the amount of the tensor interaction strength that is redistributed to the

Nucleus	Orbital	$\bar{\alpha}$ [fm^4]			Exp.
		0.025	0.030	0.035	
^{16}O	$\pi\,0p$	9.02	9.61	10.04	6.32
	$\pi\,0d$	4.62	5.15	5.60	5.00
	$\nu\,0p$	9.41	10.04	10.51	6.18
	$\nu\,0d$	6.25	6.89	7.43	5.08
^{40}Ca	$\pi\,0d$	14.16	15.19	15.98	6.00
	$\pi\,0f$	11.01	12.07	12.92	4.95
	$\pi\,1p$	2.52	2.83	3.10	2.01
	$\nu\,0d$	14.85	15.95	16.79	6.00
	$\nu\,0f$	13.71	14.90	15.85	4.88
	$\nu\,1p$	3.64	4.04	4.37	2.00
^{48}Ca	$\nu\,1d$	1.15	1.27	1.38	2.02
	$\nu\,0f$	14.66	15.96	16.98	8.38
^{100}Sn	$\pi\,0g$	14.79	16.46	17.80	6.82
	$\pi\,1p$	5.30	5.90	6.38	2.85
	$\nu\,0g$	15.81	17.63	19.08	7.00
	$\nu\,1d$	7.41	8.29	9.00	1.93
^{132}Sn	$\pi\,0g$	13.97	15.61	16.95	6.08
	$\pi\,1d$	7.10	7.95	8.64	1.48
	$\nu\,0h$	18.18	20.12	21.69	6.53
	$\nu\,1d$	8.35	9.30	10.07	1.65
	$\nu\,2p$	2.22	2.52	2.77	0.81
^{208}Pb	$\pi\,1d$	7.26	8.12	8.83	1.33
	$\pi\,0h$	15.98	17.85	19.38	5.56
	$\nu\,1f$	10.81	12.03	13.02	1.77
	$\nu\,0i$	20.70	22.92	24.72	5.84
	$\nu\,2p$	4.21	4.70	5.10	0.90

Table 2.3:   Proton (π) and neutron (ν) spin-orbit splittings in MeV for V_α with different parameters $\bar{\alpha}$, compared to experimental values [59] ($e_{\mathrm{max}} = 12$).

spin-orbit interaction (see also Figs. 2.5 and 2.7). In the case of the triplet-odd tensor correlator, we again confirm the saturation behavior starting at $I_\vartheta^{(1,1)} \approx 0.05$ fm^3. For the SRG interaction V_α, the splittings are overestimated by a factor of $3 - 4$, with a more pronounced overestimation occurring for the heavier nuclei. This indicates that the $3N$ (or higher) force needed to stabilize the SRG interactions for large A will need to have a spin-orbit component of its own. The evaluation of these involved additional forces is left open for future study, and we only continue the discussion for V_{UCOM} in the remainder of this work.

2.2   Many-Body Perturbation Theory

The discussion of the NCSM results in Sect. 1.4.1 demonstrated that long-range correlations which are not explicitly described by the UCOM correlators or the SRG evolution
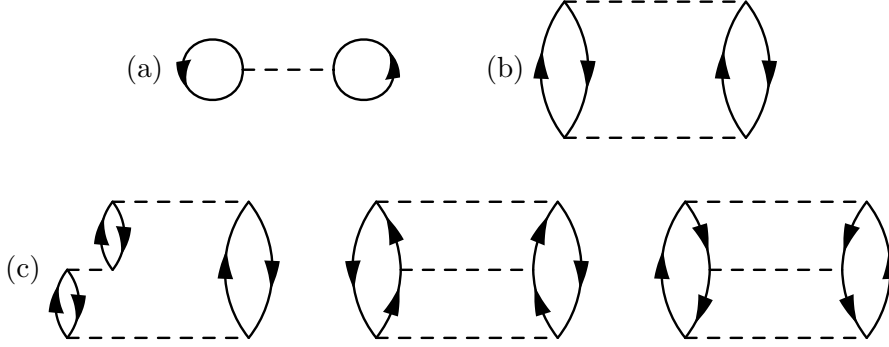
Figure 2.8: Goldstone diagrams of first (a), second (b), and third order (c).

yield significant contributions to the binding energy. While the HF approximation yields bound nuclei if V_{UCOM} or V_α are used as interactions, its simple Slater determinants correspond to an independent-particle picture, and are therefore incapable of describing long-range correlations. The easiest remedy for this shortcoming is the use of many-body perturbation theory (MBPT) starting from the HF solutions obtained for V_{UCOM} [10]. As noted in the previous section, $3N$ interactions of spin-orbit type are necessary to obtain sensible results with the SRG interactions, and the treatment of these forces is left as a subject for future work.

2.2.1   Formulation

In nuclear physics, many-body perturbation theory is usually formulated in terms of the Goldstone expansion [64, 65]. Fig. 2.8 shows the Goldstone diagrams contributing to the ground-state energy up to third order. Since the first-order diagram is implicitly contained in the HF single-particle energies, the leading correction to the ground-state energy is due to the second-order diagram Fig. 2.8(b). The corresponding analytic expression is

$$E^{(2)} = \frac{1}{4} \sum_{\alpha,\alpha'}^{<\epsilon_F} \sum_{\beta,\beta'}^{>\epsilon_F} \frac{|\langle \alpha\alpha'| \, \mathrm{H_{int}} \, |\beta\beta'\rangle|^2}{(\epsilon_\alpha + \epsilon_{\alpha'} - \epsilon_\beta - \epsilon_{\beta'})} \,, \tag{2.15}$$

where α, α' are *hole* (i.e., $\epsilon_\alpha, \epsilon_{\alpha'} \leq \epsilon_F$), and β, β' are *particle* states ($\epsilon_\beta, \epsilon_{\beta'} > \epsilon_F$). Note that *all two-body terms* in the Hamiltonian need to be considered consistently in the second-order correction, and therefore the full correlated intrinsic Hamiltonian consisting of the intrinsic kinetic energy and the two-body V_{UCOM} enters Eq. (2.15).

The third-order contributions are given by the diagrams in Fig. 2.8(c). In the order depicted, the third-order ring diagram has an additional intermediate particle-hole interaction, and gives the contribution

$$E^{(3)}_{ph} = \sum_{\alpha\alpha'\alpha''}^{<\epsilon_F} \sum_{\beta\beta'\beta''}^{>\epsilon_F} \frac{\langle \alpha\alpha'| \, \mathrm{H_{int}} \, |\beta\beta'\rangle \langle \alpha''\beta| \, \mathrm{H_{int}} \, |\alpha\beta''\rangle \langle \beta'\beta''| \, \mathrm{H_{int}} \, |\alpha''\alpha'\rangle}{(\epsilon_\alpha + \epsilon_{\alpha'} - \epsilon_\beta - \epsilon_{\beta'})(\epsilon_{\alpha'} + \epsilon_{\alpha''} - \epsilon_{\beta'} - \epsilon_{\beta''})} \,, \tag{2.16}$$

(a)   (b)   (c)   (d)

Figure 2.9:   Diagrammatic representation of the perturbative corrections to the density matrix. The labels correspond to the indices of the various contributions.

the particle-particle ladder diagram gives

$$E_{pp}^{(3)} = \frac{1}{8} \sum_{\alpha,\alpha'}^{<\epsilon_F} \sum_{\beta\beta'\beta''\beta'''}^{>\epsilon_F} \frac{\langle \alpha\alpha'| \, \mathrm{H_{int}} \, |\beta\beta'\rangle \langle \beta\beta'| \, \mathrm{H_{int}} \, |\beta''\beta'''\rangle \langle \beta''\beta'''| \, \mathrm{H_{int}} \, |\alpha\alpha'\rangle}{(\epsilon_\alpha + \epsilon_{\alpha'} - \epsilon_\beta - \epsilon_{\beta'})(\epsilon_\alpha + \epsilon_{\alpha'} - \epsilon_{\beta''} - \epsilon_{\beta'''})} \,, \quad (2.17)$$

and the hole-hole ladder diagram

$$E_{hh}^{(3)} = \frac{1}{8} \sum_{\alpha\alpha'\alpha''\alpha'''}^{<\epsilon_F} \sum_{\beta\beta'}^{>\epsilon_F} \frac{\langle \alpha\alpha'| \, \mathrm{H_{int}} \, |\beta\beta'\rangle \langle \beta\beta'| \, \mathrm{H_{int}} \, |\alpha''\alpha'''\rangle \langle \alpha''\alpha'''| \, \mathrm{H_{int}} \, |\alpha\alpha'\rangle}{(\epsilon_\alpha + \epsilon_{\alpha'} - \epsilon_\beta - \epsilon_{\beta'})(\epsilon_{\alpha''} + \epsilon_{\alpha'''} - \epsilon_\beta - \epsilon_{\beta'})} \,. \quad (2.18)$$

Analogous to the energy, one can construct perturbative corrections to the many-body states, which can be formulated conveniently in terms of the single-particle density matrix [66]. The corrected density matrix can be written as

$$\rho_{ij} = \underbrace{\rho_{ij}^{(0)}}_{0p-0h(\mathrm{HF})} + \underbrace{\rho_{ij}^{(a)} + \rho_{ij}^{(b)}}_{1p-1h} + \underbrace{\rho_{ij}^{(c)} + \rho_{ij}^{(d)}}_{2p-2h}, \quad (2.19)$$

where the contributions correspond to the diagrams in Fig. 2.9, and the character of the contributing particle-hole excitations has been indicated. The matrix elements of the corrections are given by

$$\rho_{\beta\alpha}^{(a)} = \sum_{\alpha'\alpha''}^{<\epsilon_F} \sum_{\beta'}^{>\epsilon_F} \frac{\langle \beta\beta'| \, \mathrm{H_{int}} \, |\alpha'\alpha''\rangle \langle \alpha'\alpha''| \, \mathrm{H_{int}} \, |\alpha\beta'\rangle}{(\epsilon_\beta - \epsilon_\alpha)(\epsilon_{\alpha'} + \epsilon_{\alpha''} - \epsilon_\beta - \epsilon_{\beta'})} \,, \quad (2.20)$$

$$\rho_{\alpha\beta}^{(b)} = \sum_{\alpha'}^{<\epsilon_F} \sum_{\beta'\beta''}^{>\epsilon_F} \frac{\langle \alpha\alpha'| \, \mathrm{H_{int}} \, |\beta'\beta''\rangle \langle \beta'\beta''| \, \mathrm{H_{int}} \, |\beta\alpha'\rangle}{(\epsilon_\alpha - \epsilon_\beta)(\epsilon_\alpha + \epsilon_{\alpha'} - \epsilon_{\beta'} - \epsilon_{\beta''})} \,, \quad (2.21)$$

$$\rho_{\alpha\alpha'}^{(c)} = -\frac{1}{2} \sum_{\alpha''}^{<\epsilon_F} \sum_{\beta\beta'}^{>\epsilon_F} \frac{\langle \alpha\alpha''| \, \mathrm{H_{int}} \, |\beta\beta'\rangle \langle \beta\beta'| \, \mathrm{H_{int}} \, |\alpha'\alpha''\rangle}{(\epsilon_\alpha + \epsilon_{\alpha''} - \epsilon_\beta - \epsilon_{\beta'})(\epsilon_{\alpha'} + \epsilon_{\alpha''} - \epsilon_\beta - \epsilon_{\beta'})} \,, \quad (2.22)$$

and

$$\rho_{\beta\beta'}^{(d)} = \frac{1}{2} \sum_{\alpha\alpha'}^{<\epsilon_F} \sum_{\beta''}^{>\epsilon_F} \frac{\langle \beta\beta''| \, \mathrm{H_{int}} \, |\alpha\alpha'\rangle \langle \alpha\alpha'| \, \mathrm{H_{int}} \, |\beta'\beta''\rangle}{(\epsilon_\alpha + \epsilon_{\alpha'} - \epsilon_\beta - \epsilon_{\beta''})(\epsilon_\alpha + \epsilon_{\alpha'} - \epsilon_{\beta'} - \epsilon_{\beta''})} \,. \quad (2.23)$$
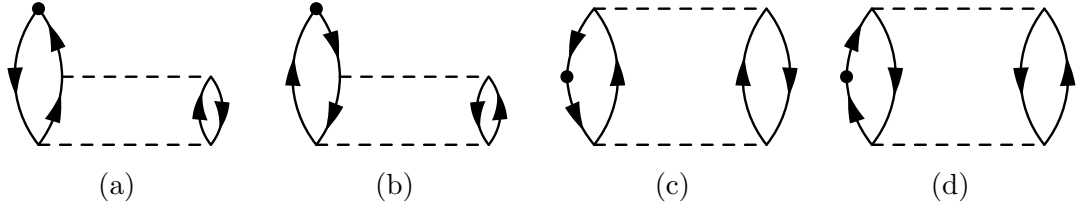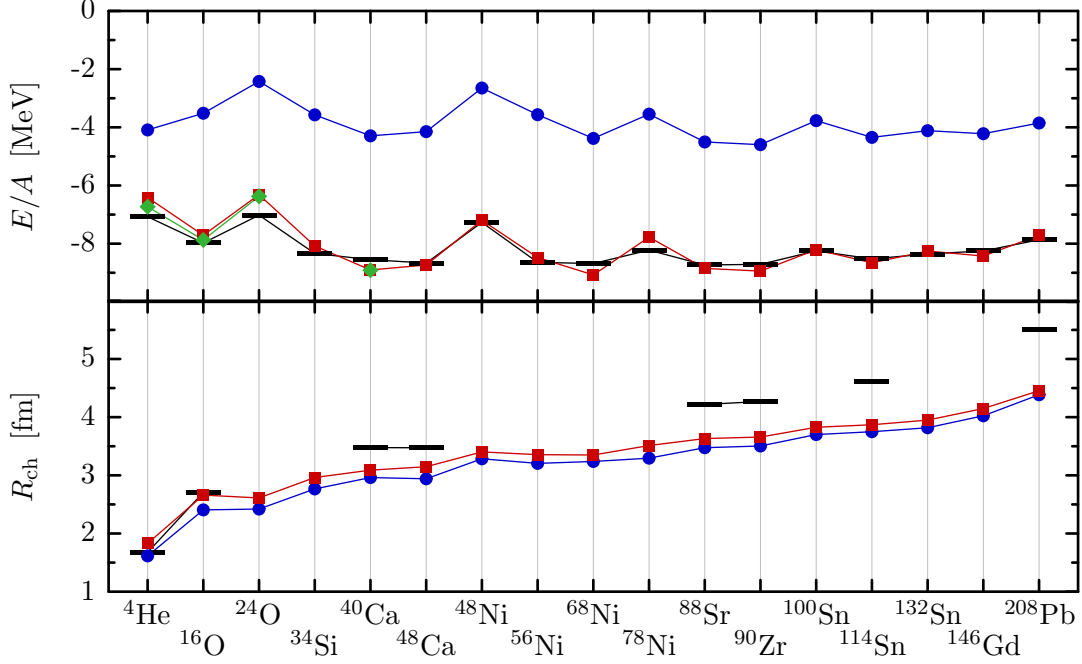
Figure 2.10: Ground-state energies and charge radii for V_{UCOM} ($I_\vartheta^{(1,0)} = 0.09\,\mathrm{fm}^3$) including 2nd (—■—) and 3rd order (—◆—) perturbative corrections, compared to HF (—●—) and experimental data (——). The 3rd order MBPT calculations were done for $e_{\max} = 8$, for HF and 2nd order MBPT $e_{\max} = 12, l_{\max} = 10$ was used. Figures from [10].

2.2.2 Results

Figure 2.10 shows the ground-state energies and charge radii of selected closed-shell nuclei for the optimized two-body V_{UCOM} ($I_\vartheta^{(1,0)} = 0.09\,\mathrm{fm}^3, I_\vartheta^{(1,1)} = 0\,\mathrm{fm}^3$). The improvement of the ground-state energies due to the perturbative corrections is impressive, yielding very good agreement with experimental data. Moreover, it confirms that short-range correlations which cannot be treated in perturbation theory are successfully described by the correlation operators, while the long-range correlations are perturbative. The latter claim is substantiated by noting that for light nuclei, the energy contributions from third order in Fig. 2.10 are small [10]. There are some limitations, however: due to the numerical effort required to evaluate the terms (2.16) to (2.18), the basis size was restricted to $e_{\max} = 8$. Furthermore, it is well-known that the Goldstone expansion cannot be guaranteed to converge. For this reason, we can pursue an alternative approach to testing the convergence by calculating the energy corrections due to RPA correlations [67],

$$E_{\mathrm{RPA}} = -\sum_{\omega_\mu > 0} \hbar\omega_\mu \sum_{ph} |Y_{ph}^\mu|^2 , \qquad (2.24)$$

where Y^μ is the backward-going RPA amplitude with energy $\hbar\omega_\mu > 0$ (i.e., excluding zero modes), and p, h label particle and hole states, respectively. Evaluating E_{RPA} from Eq. (2.24) is equivalent to carrying out a partial summation of ring diagrams to all orders, as indicated in Fig. 2.11), and taking into account the double-counting of the second-order contribution (see [68] and references therein). The resulting corrected ground-state energies are compared to the second-order MBPT results in Fig. 2.11. The
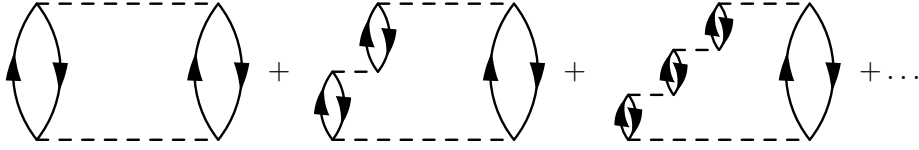
Figure 2.11: RPA ring summation.
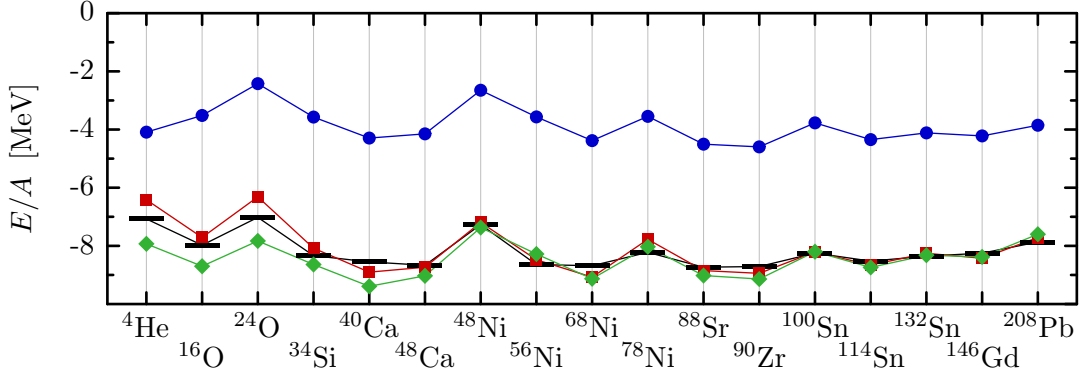
Figure 2.12: Ground state energies with RPA ring summation for V_{UCOM} with $I_{\vartheta}^{(1,0)} = 0.09\,\text{fm}^3$. Shown are HF (——●——), second-order MBPT (——■——), and RPA ring summation (——◆——), in comparison to experimental data (———)($e_{\max} = 12$, $l_{\max} = 10$). Figure adapted from Ref. [68].

ring summation produces some overbinding in the lighter nuclei, but agrees well with the MBPT result overall, which indicates that higher-order ring diagrams indeed give only small contributions, or at least small *net* contributions in the case of cancellations.

Having established that perturbation theory is well-suited to describe missing correlations, we compare the HF and second-order MBPT results for various $I_{\vartheta}^{(1,0)}$ around the optimal value 0.09 fm^3 in Fig. 2.13. As expected from our discussion of the UCOM, we observe that the energy gain from long-range correlations depends on the range of the tensor correlator. While the increase of $I_{\vartheta}^{(1,0)}$ by 0.01 fm^3 produces rather similar shifts in the HF results, the perturbative corrections are slightly larger for the *shorter-ranged* tensor correlators, leading to rather similar ground-state energies for $I_{\vartheta}^{(1,0)} = 0.09$ fm^3 and 0.10 fm^3. Since perturbation theory also probes the off-diagonal matrix elements of the interaction, switching to basis sizes beyond $e_{\max} = 12$, $l_{\max} = 8$ will likely reduce the remaining energy differences for larger nuclei whereas the HF results are well-converged. To conclude, we find that we obtain more binding energy from the tensor correlator alone if we separate short- and long-range tensor correlations at increasing distances, and consequently a smaller energy gain from the residual long-range correlations.

In Fig. 2.14 we show the ground-state energies of the O, Ca, Ni and Sn chains in second-order MBPT, confirming that the perturbative treatment of long-range correlations works in open-shell nuclei as well, independent of mass and isospin. The so-called *filling approximation* was employed in these calculations, i.e., it is assumed that the nucleons in the open shell are distributed equally over all possible magnetic quantum numbers, thereby enforcing spherical symmetry[2].

---

[2]A different prescription was used in Ref. [10], where the spherical-symmetry constraint was re-
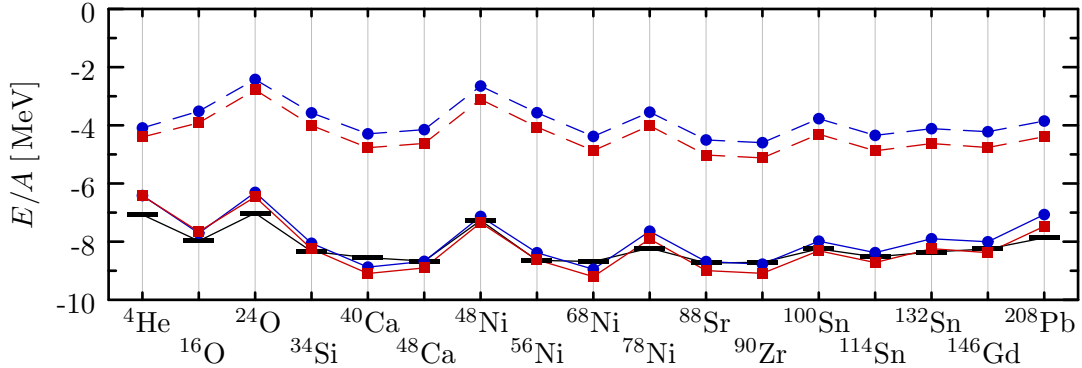
Figure 2.13: Ground-state energies of closed-shell nuclei in 2nd order MBPT for V_{UCOM} with $I_\vartheta^{(1,0)} = 0.09\,\mathrm{fm}^3$ (———●———)and $0.10\,\mathrm{fm}^3$ (———■———), compared to the HF results (dashed lines) and experimental data (————)($e_{\max} = 12$, $l_{\max} = 8$).

We conclude the discussion of this section by pointing out that MBPT is not sufficient to produce agreement of the charge radii with experimental data, as is evident in Fig. 2.10. The perturbative corrections obtained by calculating the expectation value of the radius with the corrected density matrix (2.19) increase the radii by about 0.1 to 0.2 fm. While our choice of a rather limited many-body Hilbert space built from a spherical single-particle basis precludes the treatment of effects which can lead to increased radii, like static deformations, skins and halos, collective vibrations, etc. unless the symmetry restrictions are relaxed or more advanced many-body techniques like RPA or configuration mixing in the generator coordinate method are employed, the underestimation of the radii is still consistent with the quasi-exact methods like the NCSM [69] or coupled cluster (CC). In the UCOM language, this means that the issue of the charge radii likely cannot be resolved by a better treatment of long-range correlations, and is therefore considered a clear indication for the lack of a net $3N$ (or higher) force.

2.3   Inclusion of $3N$ Forces

Motivated by the results discussed in the previous section, a $3N$ contact force

$$\mathrm{w} = t_3 \delta^{(3)}(\mathbf{r}_1 - \mathbf{r}_2)\delta^{(3)}(\mathbf{r}_2 - \mathbf{r}_3) \tag{2.25}$$

was constructed by A. Zapp [22] to try and model the net contribution from genuine and induced $3N$ interactions. The main focus of this study was the improvement of the charge radii, which requires that w is repulsive. In order to compensate for the additional repulsion, a longer-ranged tensor correlator is employed in the triplet-even channel by using the constraint $I_\vartheta^{(1,0)} = 0.20\,\mathrm{fm}^3$. In addition, a non-vanishing triplet-odd tensor correlator with $I_\vartheta^{(1,1)} = 0.1\,\mathrm{fm}^3$ provides additional attraction to counteract the (naive) A^3-scaling of the $3N$ interaction, because the binding energies of heavier nuclei are more sensitive to the odd-channel tensor force due to the larger number of spin- and isospin degrees of freedom (cf. Sect. 2.1.4).

laxed by allowing explicit m-dependence, but enforcing diagonality in l and j. Results in the filling approximation are quite similar, and require significantly less computing time.
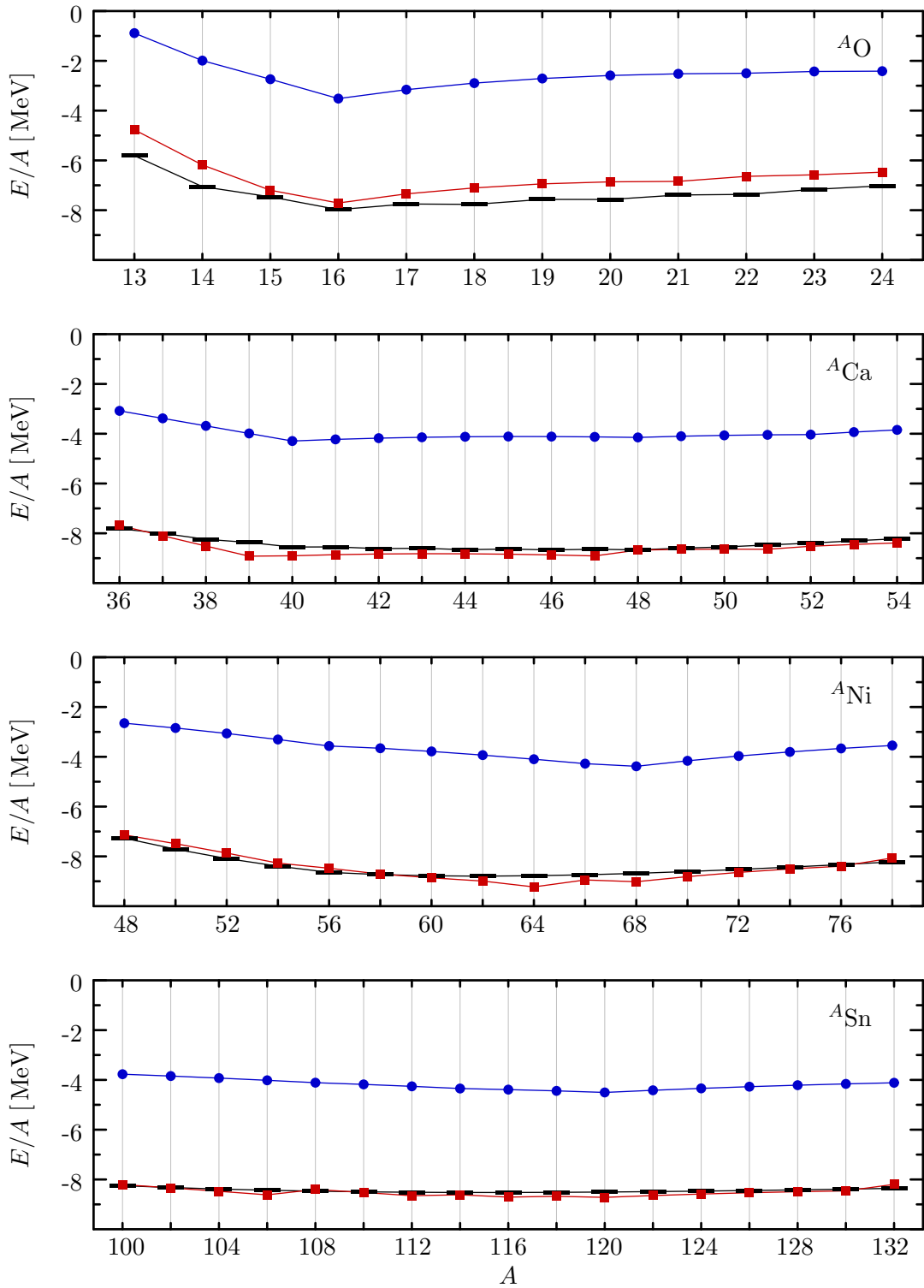
Figure 2.14: Ground-state energies of isotopic chains for V_{UCOM} with $I_\vartheta^{(1,0)} = 0.09 \, \text{fm}^3$. Comparison of HF (—●—) and second-order MBPT (—■—) with experimental data (——)($e_{\max} = 12$, $l_{\max} = 10$). Figure taken from [10].
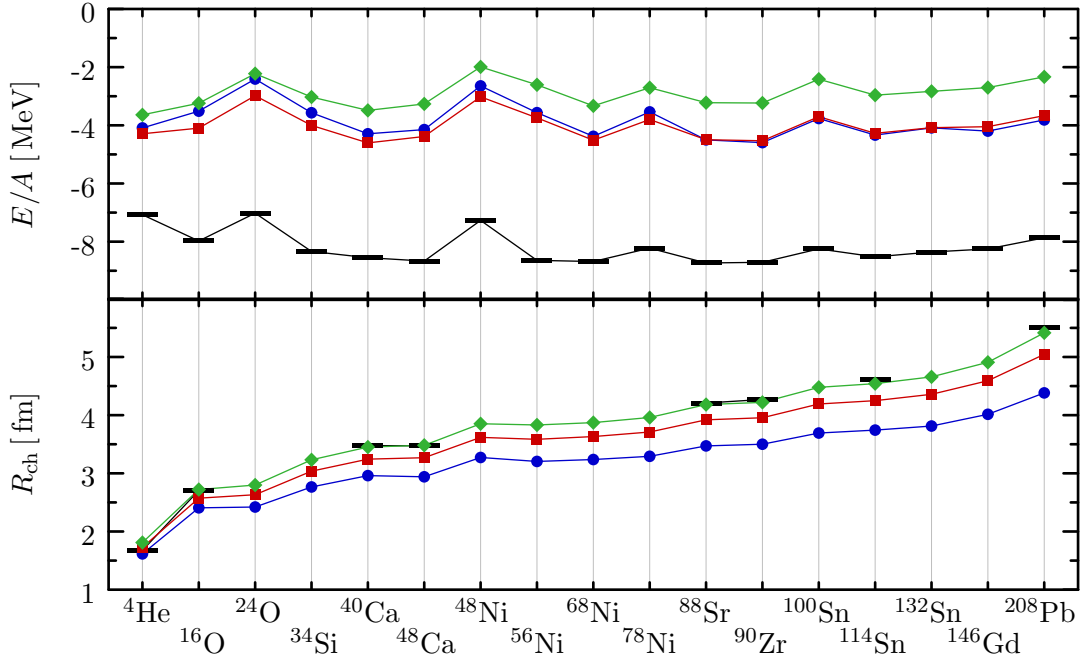
Figure 2.15: Ground-state energies and charge radii of closed-shell nuclei for V_{UCOM} with $I_{\vartheta}^{(1,0)} = 0.20\ \mathrm{fm}^3$, $I_{\vartheta}^{(1,1)} = 0.10\ \mathrm{fm}^3$ and $t_3 = 1.5\ \mathrm{GeV\,fm}^6$ (——■——), $2.5\ \mathrm{GeV\,fm}^6$ (——◆——) compared to the optimized two-body V_{UCOM} ($I_{\vartheta}^{(1,0)} = 0.09\ \mathrm{fm}^3$, $t_3 = 0$) (——●——) and experimental data (———)($e_{\max} = 10$).

In Fig. 2.15, we compare HF results for the retuned V_{UCOM} and two different contact strengths with the optimal two-body V_{UCOM} ($I_{\vartheta}^{(1,0)} = 0.09\ \mathrm{fm}^3, I_{\vartheta}^{(1,1)} = 0\ \mathrm{fm}^3$). The basis size was limited to $e_{\max} = 10$ due to the considerable computational effort caused by the $3N$ force. It turns out that the choice $t_3 = 2.5\ \mathrm{GeV\,fm}^6$ allows a near-perfect reproduction of the experimental charge radii without ruining the ground-state energies completely. Given that we can recover a significant portion of the experimental binding by means of perturbation theory, the overall reduction of the binding energy is not too problematic — note, however, that the $3N$ force would then need to be included consistently in MBPT, and lead to infinite results due to the singular behavior of the delta function. To avoid this, the use of a finite-range $3N$ force is presently under investigation; alternatively, it might be possible to construct an appropriate regularization scheme in order to deal with the divergence.

In light of the discussion of the previous section, the weaker contact strength $t_3 = 1.5\ \mathrm{GeV\,fm}^6$ may actually be the better choice, because it brings the radii much closer to experiment almost without changing the ground-state energies or their systematics. As we have seen in the previous section, the remaining difference in the charge radii of about 0.1–0.5 fm is at least comparable with what we can expect from perturbative corrections; especially once a suitable $3N$ interaction is included in the perturbation expansion as well.

The single-particle spectra of ^{40}Ca and ^{132}Sn which are shown in Fig. 2.3 also support the choice $t_3 = 1.5\ \mathrm{GeV\,fm}^6$. Generally, the added repulsion undoes some of the extensive spreading we observed for the pure two-body V_{UCOM} (and, in a more
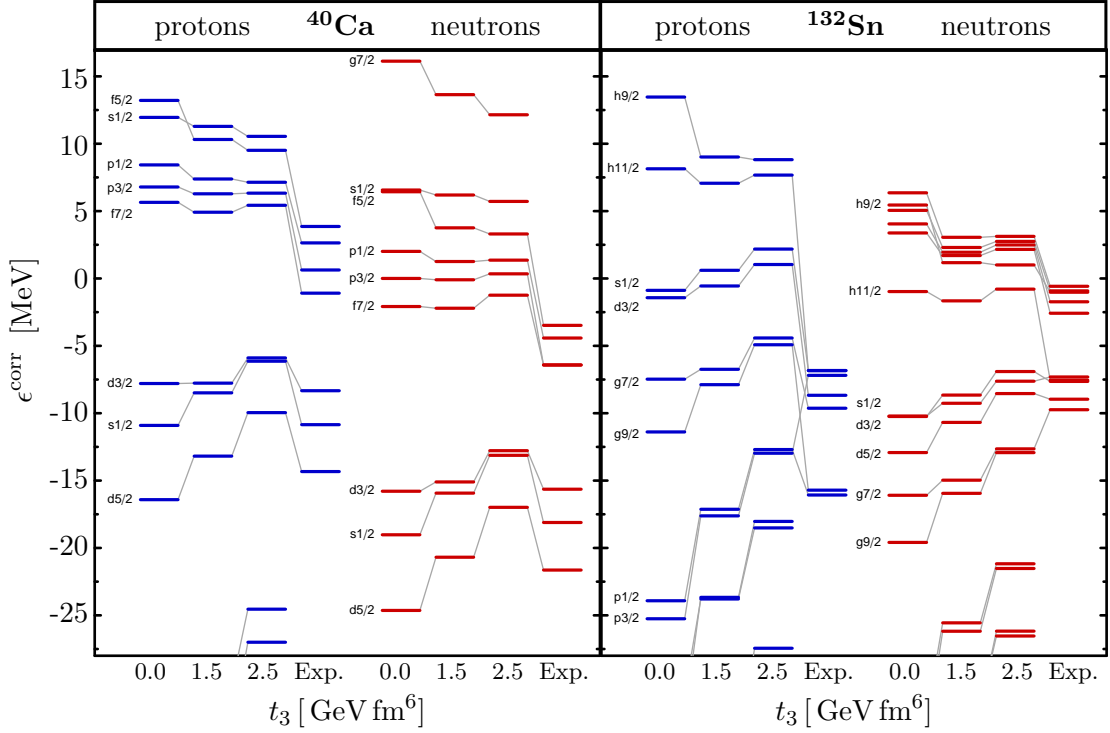
Figure 2.16: Single-particle energies for V_{UCOM} with $I_\vartheta^{(1,0)} = 0.2$ fm^3, $I_\vartheta^{(1,1)} = 0$ fm^3, and V_{UCOM} ($I_\vartheta^{(1,0)} = 0.2$ fm^3, $I_\vartheta^{(1,1)} = 0.1$ fm^3) plus $3N$ contact interaction for various t_3, compared to experimental values [59]. Figure taken from [22].

pronounced fashion, for the SRG interaction V_α), and leads to a more realistic level density. While the reproduction of the levels extracted from experiment is far from perfect, some of the theoretical levels like the $0d$ doublet for protons and neutrons in ^{40}Ca or the $\pi 0g9/2$ state in ^{132}Sn are much better reproduced for $t_3 = 1.5$ GeV fm^6 than for 2.5 GeV fm^6, and some of the level splittings look more reasonable, particularly those of spin-orbit partners.

Evidently, the changes in the level splittings occur even if only t_3 is varied, and can therefore not be explained by the increased tensor correlator ranges alone. For the spin-orbit splittings, we observe a distinct reduction for all doublets as t_3 increases. In the case of the $\nu 0h$ doublet in ^{132}Sn, this shifts the $\nu 0h_{11/2}$ level responsible for the new $N = 70$ magic shell closure to lower energies, but not sufficiently to restore the experimentally observed magic number $N = 82$. Some degree of spin-orbit dependence will likely be needed in the $3N$ force as well to correct this particular shortcoming.

Chapter 3

Theoretical Description of Pairing Phenomena

In the discussion of the previous chapter, we have pointed out that the Hartree-Fock approximation is only the starting point for the description of nuclear structure based on effective interactions. To properly describe long-range correlations which are not treated by the UCOM or SRG approaches, we have to systematically improve our many-body methods. Many-Body Perturbation Theory and RPA are useful extensions of the HF approach, but these methods are unable to describe pairing correlations, which are an important feature of open-shell systems.

Hartree-Fock-Bogoliubov (HFB) theory is the simplest approach to the consistent inclusion of pairing effects on the mean-field basis. It generalizes the frequently used combination of HF and BCS theory by treating the particle-hole (described by HF) and the particle-particle channel (described by BCS) on the same footing, thereby rendering the method fully variational [21]. This is achieved by describing the nucleus in terms of independent *quasiparticles*, which are constructed as superpositions of particle and hole states, i.e., states above and below the nucleus' Fermi energy, respectively.

In the course of this chapter, we will first summarize the HFB method, and introduce the so-called *canonical basis* which emphasizes the character of HFB as a generalization of BCS theory. The transition from the particle to the quasiparticle description implies the breaking of the gauge symmetries associated with proton and neutron number conservation, i.e., the HFB ground state is a superposition of states with different particle numbers. While this feature of the theory is inconsequential in nuclear matter, the situation is not satisfactory in finite systems like nuclei. Thus, the bulk of this chapter is dedicated to particle-number projection (PNP) methods, which restore the number symmetries. PNP provides an additional benefit: while HFB is only able to describe *static pairing correlations*, i.e, states with a well-pronounced pairing content, it fails in the description of pairing fluctuations. These *dynamical pairing correlations* become particularly important in weak-pairing regimes, e.g., in nuclei with major shell closures. While the HFB solution collapses onto the unpaired HF ground state in these cases, the PNP approach recovers at least part of these correlations and is therefore better suited to the description of the superfluid properties of the corresponding nuclei.

The derivation of the HFB+PNP method generalizes the publications of Sheikh et

al. [70, 71] to the simultaneous restoration of proton and neutron numbers. Since the method can become numerically demanding, we derive the Lipkin-Nogami equations from the PNP expressions, which serve as a well-tested (albeit not always well-understood) fallback method (see [72, 73] and references therein).

Section 3.3 deals with the use of a zero-range density-dependent interaction in the HFB+PNP framework, which is known to present a useful if somewhat peculiar approximation to the $3N$ contact force briefly discussed at the end of Sect. 2.3 (see Refs. [74, 75, 76]). We argue for the use of the so-called mixed-density prescription rather than the projected-density description as a theoretically more sound approach to PNP calculations with the density-dependent interaction, in contrast to [77, 78].

While the density-dependent force is presently the only feasible way to numerically account for $3N$ forces in the HFB framework, it causes significant problems as soon as PNP is considered, which is related to the use of the complex-valued transition densities in the density-dependent interaction. This can prevent the cancellation of singularities, or introduce branch cuts in gauge space in the case of a non-linear density-dependence. We briefly summarize the recent discussions of this subject by Anguiano et al. [78] and Dobaczewski et al. [79] at the end of this chapter.

3.1   Hartree-Fock-Bogoliubov Theory

3.1.1   The Bogoliubov Transformation

We make the transition from the independent-particle picture to an independent-quasi-particle picture by performing a canonical transformation, generally referred to as the Bogoliubov transformation [21]:

$$\beta_k^\dagger = \sum_l U_{lk} c_l^\dagger + V_{lk} c_l \,, \tag{3.1}$$

$$\beta_k = \sum_l U_{lk}^* c_l + V_{lk}^* c_l^\dagger \,, \tag{3.2}$$

where $c^\dagger$ and c are the creation and annihilation operators in the particle basis, respectively. The canonicity of the transformation, i.e., the preservation of the canonical anticommutation relations

$$\{\beta_k, \beta_l^\dagger\} = \delta_{kl} \,, \tag{3.3}$$

$$\{\beta_k, \beta_l\} = \{\beta_k^\dagger, \beta_l^\dagger\} = 0 \,, \tag{3.4}$$

implies the following conditions for the matrices U and V:

$$U^\dagger U + V^\dagger V = 1 \,, \qquad\qquad UU^\dagger + V^* V^T = 1 \,, \tag{3.5a}$$

$$U^T V + V^T U = 0 \,, \qquad\qquad UV^\dagger + V^* U^T = 0 \,. \tag{3.5b}$$

In matrix form, the Bogoliubov transformation can be written as

$$\begin{pmatrix} \beta \\ \beta^\dagger \end{pmatrix} = \begin{pmatrix} U^\dagger & V^\dagger \\ V^T & U^T \end{pmatrix} \begin{pmatrix} c \\ c^\dagger \end{pmatrix} = \mathcal{W}^\dagger \begin{pmatrix} c \\ c^\dagger \end{pmatrix} \,, \tag{3.6}$$

where the matrix $\mathcal{W}$ is defined as

$$\mathcal{W} \equiv \begin{pmatrix} U & V^* \\ V & U^* \end{pmatrix} . \tag{3.7}$$

The conditions (3.5) are then equivalent to the unitarity of $\mathcal{W}$, i.e.

$$\mathcal{W}\mathcal{W}^\dagger = \mathcal{W}^\dagger\mathcal{W} = 1 \, .$$

The nuclear groundstate $\big| \Psi \big\rangle$ is now given by the *quasiparticle vacuum*,

$$\beta_k \big| \Psi \big\rangle = 0 \, , \tag{3.8}$$

and associated with the so-called *generalized density matrix*

$$\mathcal{R} = \begin{pmatrix} \rho & \kappa \\ -\kappa^* & 1 - \rho^* \end{pmatrix} , \tag{3.9}$$

where

$$\rho_{kk'} = \big\langle \Psi \big| a_{k'}^\dagger a_k \big| \Psi \big\rangle = \left(V^* V^T \right)_{kk'} \tag{3.10}$$

is the 'normal' density matrix, and

$$\kappa_{kk'} = \big\langle \Psi \big| a_{k'} a_k \big| \Psi \big\rangle = \left(U^* V^T \right)_{kk'} , \tag{3.11}$$

defines the *pairing tensor* (also referred to as 'anomalous' density). From the definitions (3.10) and (3.11), one can easily deduce that ρ is hermitian while κ is antisymmetric. The latter symmetry property is due to κ being related to the nucleon-pair wavefunction. As a direct consequence of the conditions (3.5), ρ and κ satisfy the following relations:

$$\rho(1 - \rho) = \kappa\kappa^\dagger \, , \tag{3.12}$$

$$\rho\kappa = \kappa\rho^* \, . \tag{3.13}$$

3.1.2   The HFB Equations

Using Wick's theorem, the HFB approximation to the energy expectation value of the many-nucleon Hamiltonian

$$\mathrm{H} = \mathrm{T} + \mathrm{V_{NN}} \tag{3.14}$$

can be expressed in terms of the densities (3.10) and (3.11) as

$$
\begin{aligned}
E[\rho, \kappa, \kappa^*] &= \frac{\big\langle \Psi \big| \mathrm{H} \big| \Psi \big\rangle}{\big\langle \Psi \big| \Psi \big\rangle} \\
&= \sum_{kk'} t_{kk'} \rho_{k'k} + \frac{1}{2} \sum_{kk'qq'} \bar{v}_{kq'k'q} \rho_{k'k} \rho_{qq'} - \frac{1}{4} \sum_{kk'qq'} \bar{v}_{kk'qq'} \kappa_{k'k}^* \kappa_{qq'} \, ,
\end{aligned} \tag{3.15}
$$

where t denotes the matrix element of the kinetic energy and $\bar{v}$ is the antisymmetrized matrix element of the NN interaction or, more generally, the matrix elements of the one- and two-body parts of the Hamiltonian, which will be relevant when we consider the intrinsic kinetic energy.

The HFB groundstate can now be obtained by performing a variation of the energy with respect to the densities, in accordance with Ritz' variational principle. Since the quasiparticle vacuum used as a trial state is generally not an eigenstate of the particle-number operator, the variation is performed under the constraint

$$\operatorname{tr}\rho = N\,, \tag{3.16}$$

i. e., the *mean* particle number should equal the number of particles in the system:

$$\delta(E - \lambda\operatorname{tr}\rho) = \sum_{kk'}\left[\frac{\partial E}{\partial\rho_{kk'}} - \lambda\delta_{kk'}\right]\delta\rho_{kk'} + \frac{1}{2}\sum_{kk'}\left[\frac{\partial E}{\partial\kappa_{kk'}^*}\delta\kappa_{kk'}^* + \frac{\partial E}{\partial\kappa_{kk'}}\delta\kappa_{kk'}\right]\,, \tag{3.17}$$

where the factor $\frac{1}{2}$ results from the antisymmetry of κ (and κ^*). Introducing the *Hartree-Fock* and *pairing fields* h and Δ,

$$h_{kk'} \equiv \frac{\partial E}{\partial\rho_{k'k}} = t_{kk'} + \Gamma_{kk'} \equiv t_{kk'} + \sum_{qq'}\bar{v}_{kq'k'q}\rho_{qq'} = h_{k'k}^*\,, \tag{3.18}$$

$$\Delta_{kk'} \equiv \frac{\partial E}{\partial\kappa_{kk'}^*} = \frac{1}{2}\sum_{qq'}\bar{v}_{kk'qq'}\kappa_{qq'} = -\Delta_{k'k}\,, \tag{3.19}$$

and defining the *HFB Hamiltonian* $\mathcal{H}$, we obtain the Hartree-Fock-Bogoliubov equations

$$\mathcal{H}\begin{pmatrix}U\\V\end{pmatrix} \equiv \begin{pmatrix}h-\lambda & \Delta\\-\Delta^* & -h^*+\lambda\end{pmatrix}\begin{pmatrix}U\\V\end{pmatrix} = E\begin{pmatrix}U\\V\end{pmatrix}\,. \tag{3.20}$$

The Lagrange multiplier λ in Eq. (3.20) is readily identified with the Fermi energy of the system. Equation (3.20) constitutes an eigenvalue problem, which has to be solved self-consistently due to the dependence of $\mathcal{H}$ on ρ and κ.

If we multiply the HFB equations (3.20) by (-1) and take the complex conjugate, we obtain

$$\begin{pmatrix}h-\lambda & \Delta\\-\Delta^* & -h^*+\lambda\end{pmatrix}\begin{pmatrix}V^*\\U^*\end{pmatrix} = -E\begin{pmatrix}V*\\U^*\end{pmatrix}\,. \tag{3.21}$$

Thus, to each eigenvector $(U, V)^T$ of H with eigenvalue E, there is an *adjoint* eigenvector $(V^*, U^*)^T$ with eigenvalue $-E$. This is a consequence of the twofold increased dimension of the quasiparticle space, where creation and annihilation operators are considered 'independently' at first. Physical solutions are obtained by choosing N out of the $2N$ eigenstates, corresponding to either the positive or the negative energy of each mutually adjoint pair — otherwise, the anticommutation relations would be violated. As pointed out in [21], this freedom of choice corresponds to keeping levels occupied or empty in the HF case.

It is common in the literature to choose the N positive energy states $(U, V)^T$ for the construction of densities and fields. In the corresponding quasiparticle basis, the two-body Hamiltonian can be written as (see Appendix D.1)

$$\mathrm{H} = E_{\mathrm{HFB}} + \sum_k E_k\beta_k^\dagger\beta_k + \mathrm{H}_{\mathrm{res}}\,, \tag{3.22}$$

where E_{HFB} is the energy of the quasiparticle vacuum, E_k are the quasiparticle energies, and H_{res} contains higher many-quasiparticle interactions. If indeed $E_k > 0$, Eq. (3.22) implies that excited states built on top of the HFB vacuum will have positive energies, as one would expected from physical intuition.

In the light of the HF limit of HFB theory, the notion that the density matrix is constructed from eigenstates with positive quasiparticle energy — which would eventually reduce to $\varepsilon - \lambda > 0$, i.e., states above the Fermi level — may appear confusing at first. By looking at the generalized density matrix (3.9), however, we find that (cf. [80])

$$\mathcal{R} = \sum_{k=1}^{N} \begin{pmatrix} V_k^* \\ U_k^* \end{pmatrix} \begin{pmatrix} V_k^T & U_k^T \end{pmatrix} , \qquad (3.23)$$

where we have used the conditions (3.5). Thus, rather than selecting the positive energy solutions $(U, V)^T$ and plugging the matrices U and V in the generalized density matrix, we may just as well write $\mathcal{R}$ as the matrix product of the *negative energy states* — we "choose the positive energy solutions" to construct the quasiparticle many-body state in a manner of speaking only.

Similar to the HF case, the HFB equations (3.20) are equivalent to the condition [21]

$$\left[\mathcal{H}, \mathcal{R}\right] = 0 . \qquad (3.24)$$

This equation simply expresses the fact that $\mathcal{H}$ and $\mathcal{R}$ are both diagonal in the quasiparticle basis. The quasiparticle states $(U, V)^T$ are eigenvectors of $\mathcal{R}$ to the eigenvalue 0, as can be shown easily using the conditions (3.5):

$$\mathcal{R} \begin{pmatrix} U \\ V \end{pmatrix} = 0 \begin{pmatrix} U \\ V \end{pmatrix} . \qquad (3.25)$$

The negative energy states $(V^*, U^*)^T$, on the other hand, are eigenstates to the eigenvalue 1:

$$\mathcal{R} \begin{pmatrix} V^* \\ U^* \end{pmatrix} = \begin{pmatrix} V^* \\ U^* \end{pmatrix} . \qquad (3.26)$$

We can therefore interpret the negative energy states $(V^*, U^*)^T$ as a generalization of the occupied levels in HF, and the positive energy solutions $(U, V)^T$ as a generalization of empty levels.

3.1.3   The Canonical Basis

As can easily be seen from Eq. (3.8), a quasiparticle vacuum $\left| \Psi \right\rangle$ defines quasiparticle annihilation operators only up to a unitary transformation among themselves. Aside from the quasiparticle basis given by the $\beta_k^\dagger$, there is another basis set which turns out to be very useful for the evaluation and discussion of the HFB wavefunctions — the so-called *canonical basis*, associated with the quasiparticle operators $\alpha_k^\dagger$. Their connection to the operators $\beta_k^\dagger$ defined by the Bogoliubov transformation is due to the Bloch-Messiah theorem (see [21] and references therein), which states that the unitary matrix $\mathcal{W}$ can be decomposed in the following way:

$$\mathcal{W} = \begin{pmatrix} D & 0 \\ 0 & D^* \end{pmatrix} \begin{pmatrix} \bar{U} & \bar{V} \\ \bar{V} & \bar{U} \end{pmatrix} \begin{pmatrix} C & 0 \\ 0 & C^* \end{pmatrix} , \qquad (3.27)$$

or

$$U = D\bar{U}C\,, \quad V = D^*\bar{V}C\,. \tag{3.28}$$

D and C are unitary transformations among the particle and quasiparticle operators, respectively,

$$a_\mu^\dagger = \sum_{k'} D_{k'\mu} c_{k'}^\dagger\,, \tag{3.29}$$

$$\beta_k^\dagger = \sum_\mu C_{\mu k} \alpha_\mu^\dagger\,, \tag{3.30}$$

and the real matrices $\bar{U}$ and $\bar{V}$ define the *special Bogoliubov transformation* (also referred to as Bogoliubov-Valatin transformation)[1]

$$\alpha_\mu^\dagger = u_\mu a_\mu^\dagger - v_\mu \alpha_{\bar{\mu}}\,, \tag{3.31}$$

$$\alpha_{\bar{\mu}}^\dagger = u_\mu a_{\bar{\mu}}^\dagger + v_\mu \alpha_\mu\,, \tag{3.32}$$

analogous to standard BCS theory. The canonical conjugate states $(\mu, \bar{\mu})$ are interpreted as generalizations of the usual particle and hole states with respect to some reference state — one has to keep in mind, however, that there is no well-defined *level* associated with the Fermi energy in a quasiparticle picture.

Considering the operator space spanned by $\{a_{\bar{\mu}}^\dagger,\ a_\mu^\dagger,\ a_{\bar{\mu}},\ a_\mu\}$, the transformation (3.31) can be written as

$$\begin{pmatrix} \alpha_{\bar{\mu}}^\dagger \\ \alpha_\mu^\dagger \\ \alpha_{\bar{\mu}} \\ \alpha_\mu \end{pmatrix} = \begin{pmatrix} u_\mu & & & v_\mu \\ & u_\mu & -v_\mu & \\ & v_\mu & u_\mu & \\ -v_\mu & & & u_\mu \end{pmatrix} \begin{pmatrix} a_{\bar{\mu}}^\dagger \\ a_\mu^\dagger \\ a_{\bar{\mu}} \\ a_\mu \end{pmatrix}, \tag{3.33}$$

where the occupation probabilities satisfy

$$u_\mu^2 + v_\mu^2 = 1 \tag{3.34}$$

as a consequence of the conditions (3.5). Comparing with Eqs. (3.1) and (3.27), one finds that $\bar{U}$ and $\bar{V}$ have the following block structure for paired levels with $(u_\mu > 0, v_\mu > 0)$:

$$\bar{U}: \quad \begin{pmatrix} u_\mu & \\ & u_\mu \end{pmatrix} \qquad \Rightarrow \quad \bar{U}_{\mu\nu} = u_{\bar{\mu}}\delta_{\nu\mu}\,, \quad u_{\bar{\mu}} = u_\mu\,, \tag{3.35}$$

$$\bar{V}: \quad \begin{pmatrix} & v_\mu \\ -v_\mu & \end{pmatrix} \qquad \Rightarrow \quad \bar{V}_{\mu\nu} = -v_\mu\delta_{\bar{\mu}\nu}\,, \quad v_{\bar{\mu}} = -v_\mu\,. \tag{3.36}$$

For unpaired, so-called *blocked levels*, one has either $(u_\mu = 1, v_\mu = 0)$ or $(u_\mu = 0, v_\mu = 1)$, corresponding to

$$\alpha_\mu^\dagger = a_\mu^\dagger\,, \quad \alpha_\mu = a_\mu\,, \tag{3.37}$$

---

[1] As a convention, we will use Greek indices to label states in the canonical basis.

and

$$\alpha_\mu^\dagger = \mathrm{a}_\mu , \quad \alpha_\mu = \mathrm{a}_\mu^\dagger , \tag{3.38}$$

i. e., empty or occupied single-particle levels, respectively, as in standard HF theory.

In terms of the canonical basis creation and annihilation operators, the quasiparticle vacuum can be expressed as

$$| \Psi \rangle = \prod_\nu \alpha_\nu^\dagger | 0 \rangle = \prod_i \mathrm{a}_i^\dagger \prod_{\mu>0} \left(u_\mu + v_\mu \mathrm{a}_\mu^\dagger \mathrm{a}_{\bar\mu}^\dagger \right) | 0 \rangle , \tag{3.39}$$

where ν runs over the whole canonical basis, i over the blocked occupied levels, and μ over the paired levels (hence the restriction $\mu > 0$ to count pairs only once). From the structure of $| \Psi \rangle$, one can immediately see that the quasiparticle vacuum can only be a superposition of states with either odd or even particle number, depending on the number of blocked states. This symmetry of the HFB wavefunctions is referred to as *signature symmetry* or conservation of *number parity* in the literature [21, 81].

Plugging (3.28) into Eqs. (3.10) and (3.11) for the densities, one obtains

$$\rho = D \bar{V}^2 D^\dagger , \quad \kappa = D \bar{V} \bar{U} D^T . \tag{3.40}$$

Thus, ρ is diagonal in the canonical basis, and the occupation probabilities v_μ^2 are its eigenvalues, while κ consists of canonical blocks

$$\begin{pmatrix} & u_\mu v_\mu \\ -u_\mu v_\mu & \end{pmatrix} \tag{3.41}$$

for paired levels and vanishes otherwise. It is noteworthy that the expressions (3.40) are, as stated above, indeed independent of the unitary transformation C of the quasiparticle basis — the physical content of the quasiparticle vacuum is completely contained in the canonical basis (given via the transformation D) and the occupation probabilities v_μ.

3.1.4   The Intrinsic Kinetic Energy in HFB

As outlined in Sect. 2.1.2, the intrinsic kinetic energy is given as a sum of two-body operators, and as a result, the kinetic-energy contribution to the Hartree-Fock field (cf. (3.18)) is shifted into the contraction term Γ,

$$h_{kk'} = \Gamma_{kk'} = \sum_{qq'} \left(\frac{2}{A} \bar{t}_{\mathrm{int},kq'k'q} + \bar{v}_{kq'k'q} \right) \rho_{qq'} , \tag{3.42}$$

where $\bar{t}_{\mathrm{int}}$ is the antisymmetrized two-body matrix element of $\mathrm{t}_{\mathrm{int}}$. More significant, though, is the addition of a *repulsive* kinetic energy contribution to the pairing field as well:

$$\Delta_{kk'} = \frac{1}{2} \sum_{qq'} \left(\frac{2}{A} \bar{t}_{\mathrm{int},kk'qq'} + \bar{v}_{kk'qq'} \right) \kappa_{qq'} , \tag{3.43}$$

This contribution to the pairing field and the pairing energy, which has an *anti-pairing effect*, is often omitted in the literature (see, however, Refs. [82], [83], and Chapter 4).

3.1.5 Spherically Symmetric HFB

In this section, we will derive the HFB equations for nucleons in a spherical harmonic oscillator (HO) configuration space, and assume explicit rotational and reflection symmetry as well as like-nucleon pairing only. The corresponding Bogoliubov transformation is given by

$$\beta^\dagger_{nljm} = \sum_{n'} U^{(lj)}_{n'n} c^\dagger_{n'ljm} + (-1)^{j+m} V^{(lj)}_{n'n} c_{n'lj-m} \tag{3.44}$$

$$\beta_{nljm} = \sum_{n'} U^{(lj)}_{n'n} c_{n'ljm} + (-1)^{j+m} V^{(lj)}_{n'n} c^\dagger_{n'lj-m}, \tag{3.45}$$

where we have suppressed the single-particle spin $s = \frac{1}{2}$. The Bogoliubov transformation for spherically symmetric systems is derived in detail in Appendix B. Spherical symmetry renders the matrices U and V diagonal in j, and independent of m aside from the explicit phase factor in Eq. (3.44). Reflection symmetry prevents a mixing of states with different parity, i.e. different l, hence the transformation is diagonal in l, and for like-particle pairing, the transformation is diagonal in the isospin quantum numbers as well, so we can consider neutrons and protons separately and suppress the isospin indices, too. Furthermore, under the imposed restrictions, U and V are *real* matrices.

Using the matrices U and V from Eq. (3.44), one can define the reduced matrices $\rho^{(lj)}_{nn'}$ and $\kappa^{(lj)}_{nn'}$ (cf. Sect. B.3.2) via

$$\rho_{nljm,n'l'j'm'} = \left[VV^T\right]^{(lj)}_{nn'} \delta_{jj'}\delta_{ll'}\delta_{mm'} \equiv \rho^{(lj)}_{nn'}\delta_{jj'}\delta_{ll'}\delta_{mm'}, \tag{3.46}$$

$$\kappa_{nljm,n'l'j'm'} = (-1)^{j-m}\left[VU^T\right]^{(lj)}_{nn'} \delta_{jj'}\delta_{ll'}\delta_{m-m'} \equiv (-1)^{j-m}\kappa^{(lj)}_{nn'}\delta_{jj'}\delta_{ll'}\delta_{m-m'}, \tag{3.47}$$

which are both symmetric and real — the antisymmetry of the pairing tensor is now contained entirely in the phase factor. Correspondingly, the reduced fields are defined by

$$\Gamma_{n_1 l_1 j_1 m_1, n_1' l_1' j_1' m_1'} = \delta_{j_1 j_1'}\delta_{m_1 m_1'} \sum_{\substack{l_2 j_2 J \\ n_2 n_2'}} \frac{2J+1}{2j_1+1} \frac{\langle n_1 l_1 j_1 n_2 l_2 j_2 J || \bar{v} || n_1' l_1 j_1 n_2' l_2 j_2 J \rangle}{\sqrt{2J+1}} \rho^{(l_2 j_2)}_{n_2' n_2}$$

$$\equiv \delta_{j_1 j_1'}\delta_{l_1 l_1'}\delta_{m_1 m_1'} \Gamma^{(l_1 j_1)}_{n_1 n_1'} \tag{3.48}$$

and

$$\Delta_{n_1 l_1 j_1 m_1, n_1' l_1' j_1' m_1'} = \delta_{j_1 j_1'}\delta_{l_1 l_1'}\delta_{m_1,-m_1'}(-1)^{j_1-m_1}$$

$$\times \frac{1}{2} \sum_{l_2 j_2 n_2 n_2'} \sqrt{\frac{2j_2+1}{2j_1+1}} \langle n_1 l_1 j_1 n_1' l_1 j_1 0 || \bar{v} || n_2 l_2 j_2 n_2' l_2 j_2 0 \rangle \kappa^{(l_2 j_2)}_{n_2 n_2'}$$

$$\equiv \delta_{j_1 j_1'}\delta_{l_1 l_1'}\delta_{m_1,-m_1'}(-1)^{j_1-m_1}\Delta^{(l_1 j_1)}_{n_1 n_1'}. \tag{3.49}$$

(see App. B.3.3 and B.3.4).

With these definitions, the reduced HFB equations read

$$\begin{pmatrix} h^{(lj)} - \lambda & -\Delta^{(lj)} \\ -\Delta^{(lj)} & -h^{(lj)} + \lambda \end{pmatrix} \begin{pmatrix} U^{(lj)} \\ V^{(lj)} \end{pmatrix} = E \begin{pmatrix} U^{(lj)} \\ V^{(lj)} \end{pmatrix}. \tag{3.50}$$

3.2 Particle-Number Projection

Nowadays, it is widely accepted that one has to go beyond the mean-field in order to obtain a proper description of nuclear ground states beyond simple bulk properties like the binding energy (see e.g. [16]). Observables like transition rates are sensitive to correlations between the nucleons, part of which can be recovered by restoring the broken symmetries. The method of choice are projection techniques based on the *generator coordinate method* (cf. [21]).

The transition to the quasiparticle picture in HFB inevitably implies that the resulting quasiparticle vacua no longer have a well-defined particle number, i.e., the mean-field solution breaks the particle-number symmetry of the many-nucleon Hamiltonian. While this feature of HFB (and BCS) theory is of little concern in nuclear matter calculations, the situation is unsatisfactory in finite nuclei: the symmetry-breaking intrinsic ground-state of a nucleus with mass number A_0, obtained by solving the HFB equations (3.20), is a superposition of states with $\Delta A = 2a, a \in \mathbb{N}$ (unless, of course, the pairing phase has broken down), and only the mean nucleon number is fixed by constraining the variation. Thus, many-body states with a fixed particle number need to be obtained via projection, either from an intrinsic state after variation (*projection after variation*, PAV), or by varying a symmetry-projected energy (*variation after projection*, VAP).

Solving Symmetry-projected HFB equations equations is equivalent to diagonalizing the nuclear many-body Hamiltonian in a subspace spanned by symmetry-transformed (e.g., rotated, translated, gauge-rotated) Slater determinants, including more correlations and providing a better approximation to an exact shell-model type diagonalization in the 'full' Hilbert space. Calculations of the latter type, e. g. in the No-Core Shell Model, serve as a crucial benchmark to which all approximate results need to be compared to, but they are only feasible for light-medium nuclei [33, 84, 85, 86].

3.2.1 Projection for Abelian Symmetry Groups

In Refs. [70, 87], Sheikh et al. derive general expressions for the evaluation of the symmetry-projected energy for Abelian symmetry groups, and the $U(1)$ gauge group for particle-number projection in particular. For a given Abelian symmetry group $\mathcal{G}$, a continuous normalized set of so-called *generating functions* is defined by applying the operators of the unitary representation of $\mathcal{G}$ on the many-body Hilbert space to the intrinsic state $\big| \Phi \big\rangle$:

$$\big| g \big\rangle = \frac{\mathrm{R}(g) \big| \Phi \big\rangle}{\big\langle \Phi \big| \mathrm{R}(g) \big| \Phi \big\rangle} \, , \tag{3.51}$$

where $g \in \mathcal{G}$, and $\big| 0 \big\rangle = \big| \Phi \big\rangle$. The usual conventions are used for labeling the elements of the Abelian group: the neutral element is denoted by 0 and $-g$ is the inverse of g.

The states $\big| g \big\rangle$ are used in an ansatz for the symmetry-conserving state,

$$\big| \Psi \big\rangle = \int dg \, f(g) \mathrm{R}(g) \big| \Phi \big\rangle \, , \tag{3.52}$$

where dg denotes the Haar measure of $\mathcal{G}$, and the weight function $f(g)$ becomes an additional degree of freedom in the minimization of the energy expectation value of

the trial state $\left| \Psi \right\rangle$. When applied to symmetry restoration, the weight function $f(g)$ is determined by the group structure of $\mathcal{G}$, and one can define (usually generalized) projection operators via

$$\mathrm{P}^I \equiv \int dg\, f^I(g) \mathrm{R}_\gamma(g)\,, \tag{3.53}$$

where I labels the representations of the symmetry group $\mathcal{G}$ on the Hilbert space — that is, P^I projects onto the subspace with good quantum number (or combination of quantum numbers) I. Examples would be (J, M) for the rotation group $SU(2)$, or a fixed particle number for the $U(1)$ gauge group associated with particle-number conservation.

Using (3.51) and (3.53), the projected energy reads

$$E^I = \frac{\left\langle \Phi \right| \mathrm{H} \mathrm{P}^I \left| \Phi \right\rangle}{\left\langle \Phi \right| \mathrm{P}^I \left| \Phi \right\rangle} = \frac{\int dg\, f^I(g) \left\langle \Phi \right| \mathrm{H} \mathrm{R}(g) \left| \Phi \right\rangle}{\int dg\, f^I(g) \left\langle \Phi \right| \mathrm{R}(g) \left| \Phi \right\rangle} = \frac{\int dg\, x(g) \left\langle 0 \right| \mathrm{H} \left| g \right\rangle}{\int dg\, x(g)}$$

$$= \int dg\, y(g) \left\langle 0 \right| \mathrm{H} \left| g \right\rangle\,, \tag{3.54}$$

where the norm overlap

$$x(g) = f^I(g) \left\langle \Phi \right| \mathrm{R}(g) \left| \Phi \right\rangle = f^I(g) \left\langle 0 \right| \mathrm{R}(g) \left| 0 \right\rangle \tag{3.55}$$

and the auxiliary

$$y(g) = \frac{x(g)}{\int dg\, x(g)}\,, \quad \int dg\, y(g) = 1\,, \tag{3.56}$$

have been introduced. For the inverse transformation $\mathrm{R}(-g) = \mathrm{R}^\dagger(g)$, these quantities are given by

$$x(-g) = x^*(g)\,, \quad y(-g) = y^*(g)\,. \tag{3.57}$$

The matrix elements $\left\langle \Phi \right| \mathrm{R}(g) \left| \Phi \right\rangle$ and $\left\langle 0 \right| \mathrm{H} \left| g \right\rangle$ can be evaluated using the generalized Wick theorem for non-orthogonal Slater determinants [21]. Denoting the representation of the symmetry operator $\mathrm{R}(g)$ in the single-particle basis defining $\left| \Phi \right\rangle$ by

$$(D_g)_{kk'} = \left\langle k \right| \mathrm{R}(g) \left| k' \right\rangle\,, \tag{3.58}$$

one obtains the symmetry-transformed densities

$$\rho_g = D_g \rho D_g^\dagger\,, \tag{3.59}$$

$$\kappa_g = D_g \kappa D_g^T\,, \tag{3.60}$$

where ρ and κ are the intrinsic density matrix and pairing tensor. Defining the auxiliary matrix

$$C_g^{-1} = \rho \rho_g - \kappa \kappa_g^*\,, \tag{3.61}$$

the overlap $\left\langle \Phi \right| \mathrm{R}(g) \left| \Phi \right\rangle$ can be written as

$$\left\langle \Phi \right| \mathrm{R}(g) \left| \Phi \right\rangle = \pm \frac{\det D_g}{\sqrt{\det \rho \det C_g}}\,, \tag{3.62}$$

where the phase remains open until the symmetry group is specified further (see [70] and references therein, and Sect. 3.2.2). Applying the generalized Wick theorem, the Hamiltonian matrix element is given by

$$
\langle 0| \, \mathrm{H} \, |g\rangle = \sum_{kk'} t_{kk'} \langle 0| \, \mathrm{a}_k^\dagger \mathrm{a}_{k'} \, |g\rangle + \frac{1}{2} \sum_{kk'qq'} \bar{v}_{kk'qq'} \langle 0| \, \mathrm{a}_k^\dagger \mathrm{a}_q \, |g\rangle \langle 0| \, \mathrm{a}_{k'}^\dagger \mathrm{a}_{q'} \, |g\rangle
$$

$$
+ \frac{1}{4} \sum_{kk'qq'} \bar{v}_{kk'qq'} \langle 0| \, \mathrm{a}_k^\dagger \mathrm{a}_{k'}^\dagger \, |g\rangle \langle 0| \, \mathrm{a}_{q'} \mathrm{a}_q \, |g\rangle \,, \tag{3.63}
$$

which can be written more compactly by introducing the *transition densities*

$$
\rho_{kk'}(g) = \langle 0| \, \mathrm{a}_{k'}^\dagger \mathrm{a}_k \, |g\rangle = (\rho_g C_g \rho)_{kk'} \,, \tag{3.64}
$$

$$
\kappa_{kk'}(g) = \langle 0| \, \mathrm{a}_{k'} \mathrm{a}_k \, |g\rangle = (\rho_g C_g \kappa)_{kk'} \,, \tag{3.65}
$$

$$
\bar{\kappa}_{kk'}^*(g) = \langle 0| \, \mathrm{a}_k^\dagger \mathrm{a}_{k'}^\dagger \, |g\rangle = (\kappa_g^* C_g \rho)_{kk'} \,, \tag{3.66}
$$

and fields

$$
\Gamma_{kk'}(g) = \sum_{qq'} \bar{v}_{kq'k'q} \rho_{qq'}(g) \,, \tag{3.67}
$$

$$
\Delta_{kk'}(g) = \frac{1}{2} \sum_{qq'} \bar{v}_{kk'qq'} \kappa_{qq'}(g) \,, \tag{3.68}
$$

$$
\bar{\Delta}_{kk'}(g) = \frac{1}{2} \sum_{qq'} \bar{\kappa}_{qq'}^*(g) \bar{v}_{qq'kk'} \,, \tag{3.69}
$$

analogous to the unprojected case. One obtains

$$
H(g) = H_{\mathrm{sp}}(g) + H_{\mathrm{ph}}(g) + H_{\mathrm{pp}}(g) \,, \tag{3.70}
$$

where

$$
H_{\mathrm{sp}}(g) = \sum_{kk'} t_{kk'} \rho_{k'k}(g) = \mathrm{tr} \, (t\rho(g)) \,, \tag{3.71}
$$

$$
H_{\mathrm{ph}}(g) = \frac{1}{2} \sum_{kk'qq'} \bar{v}_{kq'k'q} \rho_{k'k}(g) \rho_{qq'}(g) = \frac{1}{2}\mathrm{tr} \, (\Gamma(g)\rho(g)) \,, \tag{3.72}
$$

$$
H_{\mathrm{pp}}(g) = \frac{1}{4} \sum_{kk'qq'} \bar{v}_{kk'qq'} \bar{\kappa}_{kk'}^*(g) \kappa_{qq'}(g)
$$

$$
= -\frac{1}{2}\mathrm{tr} \, (\Delta(g)\bar{\kappa}^*(g)) = -\frac{1}{2}\mathrm{tr} \, (\bar{\Delta}^*(g)\kappa(g)) \,, \tag{3.73}
$$

are the single-particle, particle-hole, and particle-particle Hamiltonian overlaps, respectively.

3.2.2   Exact Proton- and Neutron-Number Projection

The Projected Energy

Starting from the general expressions presented in the previous section, we will now derive the required transitional densities and fields for a simultaneous restoration of

proton and neutron number, i.e. a $U(1) \otimes U(1)$ symmetry group. We limit ourselves to the case of like-particle pairing in the present discussion[2].

For given N_0 and Z_0, a projection operator is defined by

$$\mathrm{P}^{N_0 Z_0} = \mathrm{P}^{N_0} \mathrm{P}^{Z_0} = \frac{1}{(2\pi)^2} \int_0^{2\pi} d\phi_n \int_0^{2\pi} d\phi_p \, e^{i\phi_n (\mathrm{N} - N_0)} e^{i\phi_p (\mathrm{Z} - Z_0)} \,, \tag{3.74}$$

and correspondingly, the number-projected energy is given by

$$E^{N_0 Z_0} = \frac{\langle \Phi | \, \mathrm{H} \mathrm{P}^{N_0 Z_0} \, | \Phi \rangle}{\langle \Phi | \, \mathrm{P}^{N_0 Z_0} \, | \Phi \rangle} = \int_0^{2\pi} d\phi_n \int_0^{2\pi} d\phi_p \, y(\phi_n, \phi_p) H(\phi_n, \phi_p) \,. \tag{3.75}$$

The matrix representation of $\mathrm{R}(\phi_n, \phi_p)$ in the single-particle basis is given by

$$D_{\phi_n \phi_p} = \begin{pmatrix} e^{i\phi_n} & \\ & e^{i\phi_p} \end{pmatrix} \,, \tag{3.76}$$

where we have suppressed the unit matrices in the neutron and proton sectors of the single-particle space for brevity. The transformed densities and pairing tensors of Sect. 3.2.1 as well as the auxiliary matrix $C_{\phi_n \phi_p}$ (3.61) have analogous block structures:

$$\rho_{\tau; \phi_\tau} = \rho_\tau \,, \tag{3.77}$$

$$\kappa_{\tau; \phi_\tau} = e^{2i\phi_\tau} \kappa_\tau \,, \tag{3.78}$$

$$C_{\tau; \phi_\tau}^{-1} = \rho_\tau \rho_{\tau; \phi_\tau} - \kappa_\tau \kappa_{\tau; \phi_\tau}^* \,, \tag{3.79}$$

where $\tau = n, p$ labels neutron and proton blocks, respectively. Rather than using $C_{\tau; \phi_\tau}$, we evaluate the last equation further using the relation (3.12) and define the auxiliary matrix

$$C_\tau(\phi_\tau) = C_{\tau; \phi_\tau} \rho_\tau = e^{2i\phi_\tau} (1 + \rho_\tau \cdot (e^{2i\phi_\tau} - 1))^{-1} \,, \tag{3.80}$$

with

$$C_\tau^\dagger(\phi_\tau) = C_\tau(-\phi_\tau) \,. \tag{3.81}$$

The definition of $C_\tau(\phi_\tau)$ in terms of an inverse matrix deserves further discussion, which we are going to postpone until the end of the chapter (see Sect. 3.4).

Using Eq. (3.62), the norm overlap x is given by (cf. Eqs. (3.55), (3.62))

$$x(\phi_n, \phi_p) = \frac{1}{(2\pi)^2} e^{-i(\phi_n N_0 + \phi_p Z_0)} \frac{\det D_{\phi_n \phi_p}}{\sqrt{\det \left(\rho C_{\phi_n \phi_p} \right)}} \,. \tag{3.82}$$

The sign ambiguity is removed because $| \Psi \rangle$ and $e^{i(\phi_n \mathrm{N} + \phi_p \mathrm{Z})} | \Psi \rangle$ have the same number parity, which, in conjunction with Thouless' theorem, implies that the matrix $\rho C_{\phi_n \phi_p}$ can be decomposed into two matrices with identical determinant [21, 70] — this will become evident when we consider PNP in the canonical basis representation. To further evaluate the overlap, we note that

$$\det D_{\phi_n \phi_p} = \left(e^{i\phi_n} \right)^{M_n} \left(e^{i\phi_p} \right)^{M_p} \,, \tag{3.83}$$

---

where M_n and M_p are the numbers of the proton and neutron states of the single-particle space, respectively[3]. Likewise,

$$\det\left(\rho C_{\phi_n\phi_p}\right) = \det\rho \det C_{\phi_n\phi_p} = \prod_\tau \det\rho_\tau \det C_{\tau;\phi_\tau}$$
$$= \prod_\tau \det C_{\tau;\phi_\tau} \det\rho_\tau = \prod_\tau \det C_\tau(\phi_\tau) \,, \qquad (3.84)$$

so the overlap factorizes into proton and neutron overlaps,

$$x(\phi_n,\phi_p) = x_n(\phi_n)x_p(\phi_p) \equiv \left(\frac{1}{2\pi}\frac{e^{i\phi_n(M-N_0)}}{\sqrt{\det C_n(\phi_n)}}\right)\cdot\left(\frac{1}{2\pi}\frac{e^{i\phi_p(M-Z_0)}}{\sqrt{\det C_p(\phi_p)}}\right) \,, \qquad (3.85)$$

and it is clear that $y(\phi_n,\phi_p)$ factorizes as well:

$$y(\phi_n,\phi_p) = y_n(\phi_n)y_p(\phi_p) \,. \qquad (3.86)$$

With the matrices $C_\tau(\phi_\tau)$, the transition densities and pairing tensors can be expressed as

$$\rho_\tau(\phi_\tau) = C_\tau(\phi_\tau)\rho_\tau \,, \qquad (3.87)$$
$$\kappa_\tau(\phi_\tau) = C_\tau(\phi_\tau)\kappa_\tau \,, \qquad (3.88)$$
$$\bar\kappa_\tau(\phi_\tau) = e^{2i\phi_\tau}\kappa_\tau C_\tau^*(\phi_\tau) = e^{2i\phi_\tau}C_\tau^\dagger(\phi_\tau)\kappa_\tau \,, \qquad (3.89)$$

and for the inverse rotation in gauge space, we have

$$\rho_\tau(-\phi_\tau) = C_\tau^\dagger(\phi_\tau)\rho_\tau = \rho_\tau^\dagger(\phi_\tau) \,, \qquad (3.90)$$
$$\kappa_\tau(-\phi_\tau) = C_\tau^\dagger(\phi_\tau)\kappa_\tau = e^{-2i\phi_\tau}\bar\kappa_\tau(\phi_\tau) \,, \qquad (3.91)$$
$$\bar\kappa_\tau(-\phi_\tau) = e^{-2i\phi_\tau}\kappa_\tau C_\tau^T(\phi_\tau) = e^{-2i\phi_\tau}\kappa_\tau(\phi_\tau) \,. \qquad (3.92)$$

The Hamiltonian overlaps (3.71)–(3.73) become somewhat involved due to the simultaneous projection. The single-particle part is simply given by the sum of proton and neutron terms,

$$H_{\rm sp}(\phi_n,\phi_p) = \sum_{kk'}\left(t_{kk'}^n\rho_{k'k}^n(\phi_n) + t_{kk'}^p\rho_{k'k}^p(\phi_p)\right) \qquad (3.93)$$

because one-body operators are diagonal in (or independent of) the particle's isospin. For the particle-hole part, we have

$$H_{\rm ph}(\phi_n,\phi_p)$$
$$= \frac{1}{2}\sum_{kk'll'}\left(\bar v_{kl'k'l}^{pp}\rho_{k'k}^p(\phi_p)\rho_{ll'}^p(\phi_p) + \bar v_{kl'k'l}^{pn}\rho_{k'k}^p(\phi_p)\rho_{ll'}^n(\phi_n) + (p\leftrightarrow n)\right)$$
$$\equiv \frac{1}{2}{\rm tr}\left(\Gamma_p(\phi_n,\phi_p)\rho_p(\phi_p) + \Gamma_n(\phi_n,\phi_p)\rho_n(\phi_n)\right) \,, \qquad (3.94)$$

---

[3]A caveat is in order here — when symmetry considerations are used to reduce the involved matrices, it is crucial to keep eventually occurring multiplicities (e.g., $(2j+1)$ for m-independent blocks in the case of spherical symmetry) in mind when calculating the determinants.

where the upper labels $pp, pn, \dots$ indicate the (ordered) isospin of the particles in the two-particle state. Since we are only considering like-particle pairing, the particle-particle Hamiltonian overlap reads

$$
\begin{aligned}
H_{\mathrm{pp}}(\phi_n, \phi_p) &= \frac{1}{4} \sum_{kk'll'} \left(\bar{v}^{pp}_{kk'll'} \bar{\kappa}^{p*}_{kk'}(\phi_p) \kappa^p_{ll'}(\phi_p) + (p \leftrightarrow n) \right) \\
&\equiv -\frac{1}{2} \mathrm{tr} \left(\bar{\Delta}^*_p(\phi_p) \kappa_p(\phi_p) + \bar{\Delta}^*_n(\phi_n) \kappa_n(\phi_n) \right) \\
&\equiv -\frac{1}{2} \mathrm{tr} \left(\Delta_p(\phi_p) \bar{\kappa}^*_p(\phi_p) + \Delta_n(\phi_n) \bar{\kappa}^*_n(\phi_n) \right) .
\end{aligned}
\tag{3.95}
$$

In the formulae above, we have used the transition fields defined by ($\tau, \tau' \in \{p, n\}$)

$$
\Gamma^\tau_{kk'}(\phi_n, \phi_p) = \sum_{\tau'} \sum_{ll'} \bar{v}^{\tau\tau'}_{kl'k'l} \rho^{\tau'}_{ll'}(\phi_{\tau'}) ,
\tag{3.96}
$$

$$
\Delta^\tau_{kk'}(\phi_\tau) = \frac{1}{2} \sum_{ll'} \bar{v}^{\tau\tau}_{kk'll'} \kappa^\tau_{ll'}(\phi_\tau) ,
\tag{3.97}
$$

$$
\bar{\Delta}^{\tau*}_{ll'}(\phi_\tau) = \frac{1}{2} \sum_{ll'} \bar{v}^{\tau\tau}_{kk'll'} \bar{\kappa}^\tau_{kk'}(\phi_\tau) ,
\tag{3.98}
$$

which have the properties

$$
\Gamma_\tau(-\phi_n, -\phi_p) = \Gamma^\dagger_\tau(\phi_n, \phi_p) ,
\tag{3.99}
$$

$$
\Delta_\tau(-\phi_\tau) = e^{-2i\phi_\tau} \bar{\Delta}_\tau(\phi_\tau) ,
\tag{3.100}
$$

$$
\bar{\Delta}_\tau(-\phi_\tau) = e^{-2i\phi_\tau} \Delta_\tau(\phi_\tau) .
\tag{3.101}
$$

Expressed in terms of the transition fields and densities, the projected energy reads

$$
\begin{aligned}
E^{N_0 Z_0} &= \int_0^{2\pi} d\phi_n \int_0^{2\pi} d\phi_p \, y(\phi_n, \phi_p) (H_{\mathrm{sp}}(\phi_n, \phi_p) + H_{\mathrm{ph}}(\phi_n, \phi_p) + H_{\mathrm{pp}}(\phi_n, \phi_p)) \\
&= \int_0^{2\pi} d\phi_n \int_0^{2\pi} d\phi_p \, y_n(\phi_n) y_p(\phi_p) \Bigg\{ \mathrm{tr} \left[t_n \rho_n(\phi_n) + t_p \rho_p(\phi_p) \right] \\
&\quad + \frac{1}{2} \mathrm{tr} \Bigg[\Gamma_p(\phi_n, \phi_p) \rho_p(\phi_p) + \Gamma_n(\phi_n, \phi_p) \rho_n(\phi_n) \\
&\quad - \bar{\Delta}^*_p(\phi_p) \kappa_p(\phi_p) - \bar{\Delta}^*_n(\phi_n) \kappa_n(\phi_n) \Bigg] \Bigg\}
\end{aligned}
\tag{3.102}
$$

Since the dependence of $\Gamma_\tau(\phi_n, \phi_p)$ on both gauge angles is somewhat inconvenient[4], we define a modified HF field where one of the gauge angles has been explicitly integrated out:

$$
\tilde{\Gamma}_p(\phi_p) = \int_0^{2\pi} d\phi_n \, y_n(\phi_n) \Gamma_p(\phi_n, \phi_p) ,
\tag{3.103}
$$

---

[4]In a numerical implementation, one would need to store n^2 transition fields, where n is the number of angles used to discretize the integral.

and analogously for the neutrons. In terms of these new fields, the energy is given by

$$
E^{N_0 Z_0} = \int_0^{2\pi} d\phi_n y_n(\phi_n) \left\{ \text{tr}\, [t_n \rho_n(\phi_n)] + \frac{1}{2} \text{tr}\, \left[\tilde{\Gamma}_n(\phi_n)\rho_n(\phi_n) - \bar{\Delta}_n^*(\phi_n)\kappa_n(\phi_n) \right] \right\}
$$
$$
+ \int_0^{2\pi} d\phi_p y_p(\phi_p) \left\{ \text{tr}\, [t_p \rho_p(\phi_p)] + \frac{1}{2} \text{tr}\, \left[\tilde{\Gamma}_p(\phi_p)\rho_p(\phi_p) - \bar{\Delta}_p^*(\phi_p)\kappa_p(\phi_p) \right] \right\},
$$
$$
\tag{3.104}
$$

where we have used

$$
\int_0^{2\pi} d\phi_\tau \, y_\tau(\phi_\tau) = 1 \,. \tag{3.105}
$$

The Projected HF Field

With the definitions of the previous subsection, we are now ready to calculate the projected fields by variation of the energy (3.104), proceeding as in Ref. [70]. From the definition of the projected energy, it is clear that the matrices ρ_τ and κ_τ are still the only variational degrees of freedom — the gauge rotation matrices are completely determined by ρ_τ, and in the projected energy (and other expectation values), the gauge angles are integrated out. Considering the variation with respect to ρ_τ first, we obtain the following result for the norm overlap:

$$
\frac{\partial x_\tau(\phi_\tau)}{\partial \rho_{k'k}^{\tau'}} = \frac{1}{2} x_\tau(\phi_\tau)(1 - e^{-2i\phi_\tau})C_{kk'}^\tau(\phi_\tau)\delta_{\tau\tau'}
$$
$$
\equiv x_\tau(\phi_\tau)X_{kk'}^\tau(\phi_\tau)\delta_{\tau\tau'} \,. \tag{3.106}
$$

Using this, one easily obtains

$$
\frac{\partial y_\tau(\phi_\tau)}{\partial \rho_{k'k}^{\tau'}} = y_\tau(\phi_\tau) \left(X_{kk'}^\tau(\phi_\tau) - \int_0^{2\pi} d\phi'_\tau \, y_\tau(\phi'_\tau)X_{kk'}^\tau(\phi'_\tau) \right) \delta_{\tau\tau'}
$$
$$
\equiv y_\tau(\phi_\tau)Y_{kk'}^\tau(\phi_\tau)\delta_{\tau\tau'} \,. \tag{3.107}
$$

Varying $E^{N_0 Z_0}$ with respect to ρ_τ, we obtain the HF field

$$
h_{kk'}^{P\tau} = \frac{\partial E^{N_0 Z_0}}{\partial \rho_{k'k}^\tau}
$$
$$
= \int d\phi_n \int d\phi_p \, y_n(\phi_n)y_p(\phi_p) \left(Y_{kk'}^\tau(\phi_\tau)H(\phi_n,\phi_p) + \frac{\partial H(\phi_n,\phi_p)}{\partial \rho_{k'k}^\tau} \right) \,. \tag{3.108}
$$

In the following, we will omit the single-particle basis indices k, k' unless they are absolutely necessary, and only keep the isospin index τ. We split the projected field into contributions from the single-particle, particle-hole, and particle-particle overlaps [70],

$$
h_\tau^P = t_\tau^P + \Gamma_\tau^P + \Lambda_\tau^P \,, \tag{3.109}
$$

with

$$t_\tau^P = \int d\phi_n \int d\phi_p \, y_n(\phi_n) y_p(\phi_p) \left(Y_\tau(\phi_\tau) H_{\mathrm{sp}}(\phi_n, \phi_p) + \frac{\partial H_{\mathrm{sp}}(\phi_n, \phi_p)}{\partial \rho_\tau} \right) , \qquad (3.110)$$

$$\Gamma_\tau^P = \int d\phi_n \int d\phi_p \, y_n(\phi_n) y_p(\phi_p) \left(Y_\tau(\phi_\tau) H_{\mathrm{ph}}(\phi_n, \phi_p) + \frac{\partial H_{\mathrm{ph}}(\phi_n, \phi_p)}{\partial \rho_\tau} \right) , \qquad (3.111)$$

$$\Lambda_\tau^P = \int d\phi_n \int d\phi_p \, y_n(\phi_n) y_p(\phi_p) \left(Y_\tau(\phi_\tau) H_{\mathrm{pp}}(\phi_n, \phi_p) + \frac{\partial H_{\mathrm{pp}}(\phi_n, \phi_p)}{\partial \rho_\tau} \right) . \qquad (3.112)$$

The derivatives can be evaluated using (cf. Appendix C)

$$\frac{\partial C_{jj'}^\tau(\phi_\tau)}{\partial \rho_{k'k}^{\tau'}} = \left(e^{-2i\phi_\tau} - 1 \right) C_{jk'}^\tau(\phi_\tau) C_{kj'}^\tau(\phi_\tau) \delta_{\tau\tau'} , \qquad (3.113)$$

$$\frac{\partial \rho_{jj'}^\tau(\phi_\tau)}{\partial \rho_{k'k}^{\tau'}} = e^{-2i\phi_\tau} C_{jk'}^\tau(\phi_\tau) C_{kj'}^\tau(\phi_\tau) \delta_{\tau\tau'} , \qquad (3.114)$$

$$\frac{\partial \kappa_{jj'}^\tau(\phi_\tau)}{\partial \rho_{k'k}^{\tau'}} = \left(e^{-2i\phi_\tau} - 1 \right) C_{jk'}^\tau(\phi_\tau) \kappa_{kj'}^\tau(\phi_\tau) \delta_{\tau\tau'} \qquad (3.115)$$

$$\frac{\partial \bar\kappa_{jj'}^{\tau*}(\phi_\tau)}{\partial \rho_{k'k}^{\tau'}} = \left(e^{-2i\phi_\tau} - 1 \right) \bar\kappa_{jk'}^{\tau*}(\phi_\tau) C_{kj'}^\tau(\phi_\tau) \delta_{\tau\tau'} , \qquad (3.116)$$

and we obtain

$$\frac{\partial H_{\mathrm{sp}}(\phi_n, \phi_p)}{\partial \rho_{k'k}^\tau} = e^{-2i\phi_\tau} \left(C_\tau(\phi_\tau) t_\tau C_\tau(\phi_\tau) \right)_{kk'} , \qquad (3.117)$$

$$\frac{\partial H_{\mathrm{ph}}(\phi_n, \phi_p)}{\partial \rho_{k'k}^\tau} = e^{-2i\phi_\tau} \left(C_\tau(\phi_\tau) \Gamma_\tau(\phi_n, \phi_p) C_\tau(\phi_\tau) \right)_{kk'} , \qquad (3.118)$$

and

$$\frac{\partial H_{\mathrm{pp}}(\phi_n, \phi_p)}{\partial \rho_{k'k}^\tau} = ie^{-i\phi_\tau} \sin\phi_\tau$$
$$\times \left(C_\tau(\phi_\tau) \Delta_\tau(\phi_\tau) \bar\kappa_\tau^*(\phi_\tau) + \kappa_\tau(\phi_\tau) \bar\Delta_\tau^*(\phi_\tau) C_\tau(\phi_\tau) \right)_{kk'} . \qquad (3.119)$$

The various contributions now become

$$t_\tau^P = \frac{1}{2} \int d\phi_n \int d\phi_p \, y_n(\phi_n) y_p(\phi_p) \left(Y_\tau(\phi_\tau) \sum_{\tau'} \mathrm{tr} \left[t_{\tau'} \rho_{\tau'}(\phi_{\tau'}) \right] \right.$$
$$\left. + e^{-2i\phi_\tau} C_\tau(\phi_\tau) t_\tau C_\tau(\phi_\tau) \right) + h.c. , \qquad (3.120)$$

$$\Gamma_\tau^P = \frac{1}{2} \int d\phi_n \int d\phi_p \, y_n(\phi_n) y_p(\phi_p) \left(Y_\tau(\phi_\tau) \sum_{\tau'} \frac{1}{2} \mathrm{tr} \left[\Gamma_{\tau'}(\phi_n, \phi_p) \rho_{\tau'}(\phi_{\tau'}) \right] \right.$$
$$\left. + e^{-2i\phi_\tau} C_\tau(\phi_\tau) \Gamma_\tau(\phi_n, \phi_p) C_\tau(\phi_\tau) \right) + h.c. , \qquad (3.121)$$

$$\Lambda_\tau^P = \frac{1}{2} \int d\phi_n \int d\phi_p \, y_n(\phi_n) y_p(\phi_p) \left(Y_\tau(\phi_\tau) \sum_{\tau'} \left(-\frac{1}{2} \right) \text{tr} \left[\Delta_{\tau'}(\phi_{\tau'}) \bar{\kappa}_{\tau'}^*(\phi_{\tau'}) \right] \right.$$

$$\left. + i e^{-i\phi_\tau} \sin \phi_\tau \left(C_\tau(\phi_\tau) \Delta_\tau(\phi_\tau) \bar{\kappa}_\tau^*(\phi_\tau) + \kappa_\tau(\phi_\tau) \bar{\Delta}_\tau^*(\phi_\tau) C_\tau(\phi_\tau) \right) \right) + h.c. .$$

$$(3.122)$$

Noting that Eq. (3.107) implies

$$\int d\phi_\tau \, y_\tau(\phi_\tau) Y_\tau(\phi_\tau) = 0 \tag{3.123}$$

and using the modified fields $\tilde{\Gamma}_\tau(\phi_\tau)$ introduced in (3.103), we can further simplify the above expressions:

$$t_\tau^P = \frac{1}{2} \int d\phi_\tau y_\tau(\phi_\tau) \left(Y_\tau(\phi_\tau) \text{tr} \left[t_\tau \rho_\tau(\phi_\tau) \right] + e^{-2i\phi_\tau} C_\tau(\phi_\tau) t_\tau C_\tau(\phi_\tau) \right) + h.c. , \quad (3.124)$$

$$\Gamma_\tau^P = \frac{1}{2} \int d\phi_n \int d\phi_p \, y_n(\phi_n) y_p(\phi_p) Y_\tau(\phi_\tau) \sum_{\tau'} \frac{1}{2} \text{tr} \left[\Gamma_{\tau'}(\phi_n, \phi_p) \rho_{\tau'}(\phi_{\tau'}) \right]$$

$$+ \frac{1}{2} \int d\phi_\tau y_\tau(\phi_\tau) e^{-2i\phi_\tau} C_\tau(\phi_\tau) \tilde{\Gamma}_\tau(\phi_\tau) C_\tau(\phi_\tau) + h.c. , \tag{3.125}$$

$$\Lambda_\tau^P = \frac{1}{2} \int d\phi_\tau y_\tau(\phi_\tau) \left(Y_\tau(\phi_\tau) \left(-\frac{1}{2} \right) \text{tr} \left[\Delta_\tau(\phi_\tau) \bar{\kappa}_\tau^*(\phi_\tau) \right] \right.$$

$$\left. + i \, e^{-i\phi_\tau} \sin \phi_\tau \left(C_\tau(\phi_\tau) \Delta_\tau(\phi_\tau) \bar{\kappa}_\tau^*(\phi_\tau) + \kappa_\tau(\phi_\tau) \bar{\Delta}_\tau^*(\phi_\tau) C_\tau(\phi_\tau) \right) \right) + h.c. .$$

$$(3.126)$$

The Projected Pairing Field

The projected pairing field is obtained by varying the energy with respect to κ_τ^*, keeping in mind that the pairing tensor is antisymmetric and therefore only matrix elements with $k < k'$ are actual degrees of freedom for the variation (cf. Eq. (3.17) and Appendix C). Thus,

$$\Delta_{kk'}^{P\tau} = \frac{\partial E^{N_0 Z_0}}{\partial \kappa_{kk'}^{\tau*}} = \int d\phi_n \int d\phi_p y_n(\phi_n) y_p(\phi_p) \frac{\partial H_{\text{pp}}(\phi_n, \phi_p)}{\partial \kappa_{kk'}^{\tau*}} , \qquad \text{for } (k < k'), \quad (3.127)$$

and using

$$\frac{\partial}{\partial \kappa_{kk'}^{\tau*}} H_{\text{pp}}(\phi_n, \phi_p) = \frac{1}{2} \sum_{j'} e^{-2i\phi_\tau} \left(C_{kj'}^\tau(\phi_\tau) \Delta_{j'k'}^\tau(\phi_\tau) - C_{k'j'}^\tau(\phi_\tau) \Delta_{j'k}^\tau(\phi_\tau) \right) , \tag{3.128}$$

we obtain

$$\Delta_\tau^P = \frac{1}{2} \int d\phi_\tau \, y_\tau(\phi_\tau) \left(C_\tau(\phi_\tau) \Delta_\tau(\phi_\tau) - \Delta_\tau^T(\phi_\tau) C_\tau^T(\phi_\tau) \right) . \tag{3.129}$$

The HFB Equations for Variation after PNP

Having determined the projected fields, we can now write down the projected HFB equations. Since the variational degrees of freedom are the same as in the standard HFB case, the structure of the HFB equations is not altered at all by the projection:

$$
\begin{pmatrix} h_\tau^P & \Delta_\tau^P \\ -\Delta_\tau^{P*} & -h_\tau^{P*} \end{pmatrix}
\begin{pmatrix} U_\tau^P \\ V_\tau^P \end{pmatrix}
= E_\tau^P \begin{pmatrix} U_\tau^P \\ V_\tau^P \end{pmatrix} .
\tag{3.130}
$$

Note that there is no longer a constraint on the particle number — indeed, since

$$
\left\langle \Psi_{N_0 Z_0} \middle| \mathrm{N} \middle| \Psi_{N_0 Z_0} \right\rangle = N_0 \,,
\tag{3.131}
$$

adding the constraint $\lambda_n \mathrm{N}$ changes the energy by a constant and makes no difference when $E^{N_0 Z_0}$ is varied. The nonlinear eigenvalue problem (3.130) is solved iteratively, with the new intrinsic densities given by

$$
\rho_\tau = \left[V^{P*} V^{PT} \right]_\tau \,, \quad \kappa_\tau = \left[V^{P*} U^{PT} \right]_\tau \,,
\tag{3.132}
$$

in every iteration.

Canonical Basis Representation

Since the matrices $C_\tau(\phi_\tau)$ are defined as functions of the density matrix (cf. Eq. (3.80)), it is immediately clear that they are diagonal in the canonical basis of ρ. This implies that all transition densities $\rho_\tau(\phi_\tau)$ and $\kappa_\tau(\phi_\tau)$ *share the same canonical basis*. Plugging in the expressions from Sect. 3.1.3, we find

$$
C_{\mu\nu}^\tau(\phi_\tau) = \frac{e^{2i\phi_\tau}}{u_{\tau\mu}^2 + v_{\tau\mu}^2 e^{2i\phi_\tau}} \delta_{\mu\nu} \equiv C_\mu^\tau(\phi_\tau)\delta_{\mu\nu} \,, \qquad C_{\bar\mu}^\tau(\phi_\tau) = C_\mu^\tau(\phi_\tau) \,,
\tag{3.133}
$$

$$
\rho_{\mu\nu}^\tau(\phi_\tau) = \frac{v_{\tau\mu}^2 e^{2i\phi_\tau}}{u_{\tau\mu}^2 + v_{\tau\mu}^2 e^{2i\phi_\tau}} \delta_{\mu\nu} \equiv \rho_\mu^\tau(\phi_\tau)\delta_{\mu\nu} \,, \qquad \rho_{\bar\mu}^\tau(\phi_\tau) = \rho_\mu^\tau(\phi_\tau) \,,
\tag{3.134}
$$

$$
\kappa_{\mu\nu}^\tau(\phi_\tau) = \frac{u_{\tau\mu} v_{\tau\mu} e^{2i\phi_\tau}}{u_{\tau\mu}^2 + v_{\tau\mu}^2 e^{2i\phi_\tau}} \delta_{\bar\mu\nu} \equiv \kappa_{\bar\mu}^\tau(\phi_\tau)\delta_{\bar\mu\nu} \,, \qquad \kappa_{\bar\mu}^\tau(\phi_\tau) = -\kappa_\mu^\tau(\phi_\tau) \,.
\tag{3.135}
$$

Noting that

$$
e^{i\phi_\tau \mathrm{A}_\tau} \mathrm{a}_{\tau\mu}^\dagger e^{-i\phi_\tau \mathrm{A}_\tau} = e^{i\phi_\tau} \mathrm{a}_{\tau\mu}^\dagger \,,
\tag{3.136}
$$

$$
e^{i\phi_\tau \mathrm{A}_\tau} \mathrm{a}_{\tau\mu} e^{-i\phi_\tau \mathrm{A}_\tau} = e^{-i\phi_\tau} \mathrm{a}_{\tau\mu} \,,
\tag{3.137}
$$

we see that we can write the rotated vacuum as

$$
\begin{aligned}
e^{i(\phi_n \mathrm{N} + \phi_p \mathrm{Z})} \left| \Psi \right\rangle &= \prod_\tau \prod_{\mu>0} \left(u_{\tau\mu} + v_{\tau\mu} e^{2i\phi_\tau} \mathrm{a}_{\tau\mu}^\dagger \mathrm{a}_{\tau\bar\mu}^\dagger \right) \left| 0 \right\rangle \\
&= \prod_\tau \Big(u_{\tau 1} \dots u_{\tau\mu} \dots \left| 0_{\tau\bar 1}, 0_{\tau 1}, \dots 0_{\tau\bar\mu}, 0_{\tau\mu}, \dots \right\rangle \\
&\quad + e^{2i\phi_\tau} u_{\tau 1} \dots v_{\tau\mu} u_{\tau\mu+1} \dots \left| 0_{\tau\bar 1}, 0_{\tau 1}, \dots 1_{\tau\bar\mu}, 1_{\tau\mu}, \dots \right\rangle + \dots \\
&\quad + e^{2i\phi_\tau} \dots e^{2i\phi_\tau} v_{\tau 1} \dots v_{\tau\mu} \dots \left| 1_{\tau\bar 1}, 1_{\tau 1}, \dots 1_{\tau\bar\mu}, 1_{\tau\mu}, \dots \right\rangle \Big) \,,
\end{aligned}
\tag{3.138}
$$

and using the orthogonality relations of the number states, we can easily see that the overlap becomes

$$x(\phi_n, \phi_p) = e^{-i(\phi_n N_0 + \phi_p Z_0)} \prod_\tau \prod_{\mu>0} \left(u_{\tau\mu}^2 + v_{\tau\mu}^2 e^{2i\phi_\tau} \right) . \tag{3.139}$$

If we plug the canonical form of $C_\tau(\phi_\tau)$ into Eq. (3.85), we obtain exactly the same result. Equation (3.139) has the additional benefit that it is not necessary to evaluate multivalued complex functions, which makes it more robust in the numerical implementation of PNP.

As mentioned in the brief discussion following Eq. (3.85), the sign ambiguity of the overlap is removed because the matrix $C_\tau(\phi_\tau)$ can be decomposed into two matrices with identical determinant. Looking at its canonical form, this is obvious: for occupied blocked levels, the eigenvalue is 1, hence the determinant is determined by the eigenvalues for the paired levels alone, and these are two-fold degenerate.

3.2.3 The Lipkin-Nogami Method

While the numerical effort for performing an exact variation after particle number projection (VAP) along the lines explained in the previous sections is not entirely prohibitive, it is nevertheless considerable. This is especially true once the single-particle basis size cannot be reduced by symmetry considerations. In these cases, the Lipkin-Nogami [89, 90, 77] method provides a well-tested fallback to allow at least for an approximate restoration of the particle number.

The Kamlah Expansion

The form of the particle-number projection operator $\mathrm{P}^{N_0 Z_0}$ (Eq. (3.74)) suggests a case where an approximate projection might be sufficient: the integration over the respective gauge angles for neutrons and protons selects only contributions with the desired particle number from the quasiparticle vacuum $\left| \Psi \right\rangle$. Thus, if the Hamiltonian and norm overlaps $\left\langle \mathrm{H} e^{i(\phi_n \mathrm{N} + \phi_p \mathrm{Z})} \right\rangle$ and $\left\langle e^{i(\phi_n \mathrm{N} + \phi_p \mathrm{Z})} \right\rangle$ are strongly peaked around $\phi_p = \phi_n = 0$ in gauge space, i.e., the neutron- and proton-number distributions of $\left| \Psi \right\rangle$ are strongly peaked around N_0 and Z_0, respectively, one can perform an expansion of the overlaps. The most convenient formulation of this expansion is based on an idea originally proposed by Kamlah [77, 91], resulting in expressions which are equivalent to the *cumulant* or *connected-linked expansion* employed in [72]. In gauge space, the particle-number operators N and Z can be represented as derivatives of the overlaps with respect to the gauge angles; thus, the Kamlah operators defined by

$$\mathcal{N} \equiv \frac{1}{i} \frac{\partial}{\partial \phi_n} - \left\langle \mathrm{N} \right\rangle \tag{3.140}$$

$$\mathcal{Z} \equiv \frac{1}{i} \frac{\partial}{\partial \phi_p} - \left\langle \mathrm{Z} \right\rangle \tag{3.141}$$

describe neutron- and proton-number *deviations*. Using these operators, the Hamiltonian overlap is expanded as

$$\left\langle \mathrm{H} e^{i(\phi_n \mathrm{N} + \phi_p \mathrm{Z})} \right\rangle \simeq \sum_{m_n, m_p}^{M = m_n + m_p} h_{m_n m_p} \mathcal{N}^{m_n} \mathcal{Z}^{m_p} \left\langle e^{i(\phi_n \mathrm{N} + \phi_p \mathrm{Z})} \right\rangle, \qquad (3.142)$$

where M determines the order of the approximation, with $M \to \infty$ obviously corresponding to the exact result. The expansion coefficients $h_{m_n m_p}$ are determined by applying all combinations of the operators (3.140) up to order M to Eq. (3.142) and solving the resulting system of equations in the limit $\phi_n, \phi_p \to 0$:

$$\left\langle \mathrm{H}(\Delta \mathrm{N})^{k_n}(\Delta \mathrm{Z})^{k_p} \right\rangle = \sum_{m_n, m_p}^{M} h_{m_n m_p} \left\langle \Delta \mathrm{N}^{(k_n + m_n)} \right\rangle \left\langle \Delta \mathrm{Z}^{(k_p + m_p)} \right\rangle, \qquad (3.143)$$

where $\Delta \mathrm{A} = \mathrm{A} - \left\langle \mathrm{A} \right\rangle$, $k_n, k_p = 0, \ldots, M$ such that $k_n + k_p \leq M$, and expectation values are taken with respect to $\left| \Psi \right\rangle$. Note that products of the neutron and proton number fluctuation operators factorize:

$$\left\langle \Delta \mathrm{N}^{k_n} \Delta \mathrm{Z}^{k_p} \right\rangle = \left\langle \Delta \mathrm{N}^{k_n} \right\rangle \left\langle \Delta \mathrm{Z}^{k_p} \right\rangle. \qquad (3.144)$$

Plugging the expansion (3.142) into the projected energy (3.54), we obtain the approximate projected energy to order M:

$$E_M^{N_0 Z_0} = \sum_{m_n, m_p}^{M} h_{m_n m_p} (N_0 - \left\langle \mathrm{N} \right\rangle)^{m_n} (Z_0 - \left\langle \mathrm{Z} \right\rangle)^{m_p}. \qquad (3.145)$$

Since the $h_{m_n m_p}$ depend on the quasiparticle vacuum, a fully variational approach to the minimization of $E_M^{N_0 Z_0}$ would also consider the variations in the expansion coefficients [72]. While such a procedure, referred to as the Self-Consistent Kamlah Expansion (SCK), has been studied [73], the variations of the expansion coefficients quickly become very involved, and the overall effort approaches (or even surpasses) that of the full VAP. The actual Lipkin-Nogami approach, on the other hand, is based on the Kamlah expansion of order $M = 2$ and considers the second-order expansion coefficients to be fixed quantities, which are iteratively updated while solving the approximately projected HFB equations. In this sense, the Lipkin-Nogami approach corresponds to a minimization where not just the mean particle number, but also the particle number fluctuation are constrained, similar to the Generator Coordinate Method (GCM) [21] — however, due to the relations (3.143), one does not probe the full potential energy surface as in the GCM.

The Lipkin-Nogami Energy

For $M = 2$, the approximate projected energy reads

$$\begin{aligned} E_2^{N_0 Z_0} =\; & h_{00} + h_{10}(N_0 - \left\langle \mathrm{N} \right\rangle) + h_{01}(Z_0 - \left\langle \mathrm{Z} \right\rangle) + h_{20}(N_0 - \left\langle \mathrm{N} \right\rangle)^2 + h_{02}(Z_0 - \left\langle \mathrm{Z} \right\rangle)^2 \\ & + 2 h_{11}(N_0 - \left\langle \mathrm{N} \right\rangle)(Z_0 - \left\langle \mathrm{Z} \right\rangle), \end{aligned} \qquad (3.146)$$

and the corresponding variation, with h_{20}, h_{02}, and h_{11} held constant, is given by

$$\begin{aligned}\delta E_2^{N_0 Z_0} =&\delta h_{00} + \delta h_{10}(N_0 - \langle\, \mathrm{N}\,\rangle) - h_{10}\delta\,\langle\, \mathrm{N}\,\rangle +\delta h_{01}(Z_0 - \langle\, \mathrm{Z}\,\rangle) - h_{01}\delta\,\langle\, \mathrm{Z}\,\rangle \\ &- 2h_{20}(N_0 - \langle\, \mathrm{N}\,\rangle)\delta\,\langle\, \mathrm{N}\,\rangle -2h_{02}(Z_0 - \langle\, \mathrm{Z}\,\rangle)\delta\,\langle\, \mathrm{Z}\,\rangle \\ &- 2h_{11}\left(\delta\,\langle\, \mathrm{N}\,\rangle(Z_0 - \langle\, \mathrm{Z}\,\rangle) + (N_0 - \langle\, \mathrm{N}\,\rangle)\delta\,\langle\, \mathrm{Z}\,\rangle\right) = 0\,.\end{aligned} \tag{3.147}$$

Obviously, many of the terms in this variational equation will vanish if the usual HFB particle-number conditions

$$\langle\, \mathrm{N}\,\rangle = N_0\,, \quad \langle\, \mathrm{Z}\,\rangle = Z_0\,, \tag{3.148}$$

are satisfied. In fact, one can show that in this case the coefficients h_{10} and h_{01} coincide with the Lagrange multipliers λ_n and λ_p of HFB theory [77], although it is important to note that these coefficients *cannot be simply identified* with the neutron and proton Fermi energies any longer. Satisfying the particle-number conditions is, of course, also a necessary prerequisite for ensuring that the expansion of the projected energy is valid — the particle-number distributions of the quasiparticle vacuum will be centered around the desired particle numbers, and if they are strongly peaked, the higher-order fluctuations $\langle\, \Delta \mathrm{A}^n\,\rangle$ should become increasingly negligible.

Writing out the equations for the coefficients with the additional input of the particle number conditions, we obtain the system of equations

$$\langle\, \mathrm{H}\,\rangle = h_{00} + h_{20}\langle\, \Delta \mathrm{N}^2\,\rangle +h_{02}\langle\, \Delta \mathrm{Z}^2\,\rangle \tag{3.149a}$$

$$\langle\, \mathrm{H}\Delta \mathrm{N}\,\rangle = h_{10}\langle\, \Delta \mathrm{N}^2\,\rangle +h_{20}\langle\, \Delta \mathrm{N}^3\,\rangle \tag{3.149b}$$

$$\langle\, \mathrm{H}\Delta \mathrm{Z}\,\rangle = h_{01}\langle\, \Delta \mathrm{Z}^2\,\rangle +h_{02}\langle\, \Delta \mathrm{Z}^3\,\rangle \tag{3.149c}$$

$$\langle\, \mathrm{H}\Delta \mathrm{N}^2\,\rangle = h_{00}\langle\, \Delta \mathrm{N}^2\,\rangle +h_{10}\langle\, \Delta \mathrm{N}^3\,\rangle +h_{20}\langle\, \Delta \mathrm{N}^4\,\rangle +h_{02}\langle\, \Delta \mathrm{N}^2\,\rangle\langle\, \Delta \mathrm{Z}^2\,\rangle \tag{3.149d}$$

$$\langle\, \mathrm{H}\Delta \mathrm{Z}^2\,\rangle = h_{00}\langle\, \Delta \mathrm{Z}^2\,\rangle +h_{01}\langle\, \Delta \mathrm{Z}^3\,\rangle +h_{20}\langle\, \Delta \mathrm{N}^2\,\rangle\langle\, \Delta \mathrm{Z}^2\,\rangle +h_{02}\langle\, \Delta \mathrm{Z}^4\,\rangle \tag{3.149e}$$

$$\langle\, \mathrm{H}\Delta \mathrm{N}\Delta \mathrm{Z}\,\rangle = h_{11}\langle\, \Delta \mathrm{N}^2\,\rangle\langle\, \Delta \mathrm{Z}^2\,\rangle\,, \tag{3.149f}$$

which is solved by

$$h_{00} = \langle\, \mathrm{H}\,\rangle -h_{20}\langle\, \Delta \mathrm{N}^2\,\rangle -h_{02}\langle\, \Delta \mathrm{Z}^2\,\rangle \tag{3.150}$$

$$h_{10} = \frac{\langle\, \mathrm{H}\Delta \mathrm{N}\,\rangle -h_{20}\langle\, \Delta \mathrm{N}^3\,\rangle}{\langle\, \Delta \mathrm{N}^2\,\rangle} \tag{3.151}$$

$$h_{01} = \frac{\langle\, \mathrm{H}\Delta \mathrm{Z}\,\rangle -h_{02}\langle\, \Delta \mathrm{Z}^3\,\rangle}{\langle\, \Delta \mathrm{Z}^2\,\rangle} \tag{3.152}$$

$$h_{20} = \frac{\langle\,(\mathrm{H} - \langle\, \mathrm{H}\,\rangle)\Delta \mathrm{N}^2\,\rangle -\langle\, \mathrm{H}\Delta \mathrm{N}\,\rangle\langle\, \Delta \mathrm{N}^3\,\rangle / \langle\, \Delta \mathrm{N}^2\,\rangle}{\langle\, \Delta \mathrm{N}^4\,\rangle -\langle\, \Delta \mathrm{N}^2\,\rangle^2 -\langle\, \Delta \mathrm{N}^3\,\rangle^2 / \langle\, \Delta \mathrm{N}^2\,\rangle} \tag{3.153}$$

$$h_{02} = \frac{\langle\,(\mathrm{H} - \langle\, \mathrm{H}\,\rangle)\Delta \mathrm{Z}^2\,\rangle -\langle\, \mathrm{H}\Delta \mathrm{Z}\,\rangle\langle\, \Delta \mathrm{Z}^3\,\rangle / \langle\, \Delta \mathrm{Z}^2\,\rangle}{\langle\, \Delta \mathrm{Z}^4\,\rangle -\langle\, \Delta \mathrm{Z}^2\,\rangle^2 -\langle\, \Delta \mathrm{Z}^3\,\rangle^2 / \langle\, \Delta \mathrm{Z}^2\,\rangle} \tag{3.154}$$

$$h_{11} = \frac{\langle\, \mathrm{H}\Delta \mathrm{N}\Delta \mathrm{Z}\,\rangle}{\langle\, \Delta \mathrm{N}^2\,\rangle\langle\, \Delta \mathrm{Z}^2\,\rangle}\,. \tag{3.155}$$

The coefficients h_{10}, h_{01}, h_{20}, and h_{02} have the same form as for approximate projection with only a single species of particles (cf. [77]). The coefficient h_{11} couples proton- and neutron-number fluctuations, but due to the particle-number conditions it does not contribute to the second-order approximate energy (3.146).

Thus, we finally arrive at the following expression for the Lipkin-Nogami energy,

$$E_{\text{LN}} = \langle\, H \,\rangle - h_2^n \langle\, \Delta N^2 \,\rangle - h_2^p \langle\, \Delta Z^2 \,\rangle, \tag{3.156}$$

where we have introduced $h_2^n = h_{20}$ and $h_2^p = h_{02}$ as a more intuitive notation for the expansion coefficients, which we are going to use from now on.

Evaluation of the Lipkin-Nogami Coefficients

The various contributions to the Lipkin-Nogami coefficients h_2^n and h_2^p can be calculated with the help of the expressions given in Appendix C.2. In terms of the overlaps $H(\phi_n, \phi_p)$ and $x(\phi_n, \phi_p)$ defined in Sect. 3.2.2, the required expectation values are given by

$$\langle\, H\Delta N \,\rangle = \frac{1}{i} \frac{\partial}{\partial\phi_n} H(\phi_n, \phi_p)\Big|_{\{\phi\}=0} \tag{3.157}$$

$$\langle\, (H - \langle\, H \,\rangle)\, \Delta N^2 \,\rangle = \frac{1}{i^2} \frac{\partial^2}{\partial\phi_n^2} H(\phi_n, \phi_p)\Big|_{\{\phi\}=0} \tag{3.158}$$

and

$$\langle\, \Delta N^k \,\rangle = 2\pi \frac{1}{i} \frac{\partial^k}{\partial\phi_n^k} x_n(\phi_n)\Big|_{\{\phi\}=0}, \tag{3.159}$$

with $\{\phi\} = 0$ implying that *both* gauge angles are set to zero, and analogous relations hold for the protons. Defining the auxiliary densities

$$\chi_n \equiv \rho_n(1_n - \rho_n) = \kappa_n \kappa_n^\dagger, \tag{3.160}$$

$$\eta_n \equiv (1_n - 2\rho_n), \tag{3.161}$$

where 1_n denotes the unit matrix in neutron space, we have

$$\langle\, \Delta N^2 \,\rangle = 2\text{tr}\,\chi_n, \tag{3.162}$$

$$\langle\, \Delta N^3 \,\rangle = 4\text{tr}\,\eta_n\chi_n, \tag{3.163}$$

$$\langle\, \Delta N^4 \,\rangle = 12\,(\text{tr}\,\chi_n)^2 + 8\left(\text{tr}\,\chi_n - 6\text{tr}\,\chi_n^2\right). \tag{3.164}$$

The expectation values containing the Hamiltonian can be expressed conveniently if we introduce the auxiliary fields $(\tau = p, n)$

$$\Gamma_{jj'}^n[\chi] \equiv \sum_\tau \sum_{jj'll'} \bar{v}_{jl'j'l}^{n\tau} \chi_{ll'}^\tau \tag{3.165}$$

and

$$\Delta_{ll'}^{n}[\eta\kappa] \equiv \frac{1}{2} \sum_{jj'll'} \bar{v}_{jj'll'}^{nn} \left[\eta^{n}\kappa^{n}\right]_{ll'} , \tag{3.166}$$

which eventually leads to (cf. Sect. C.2)

$$\left\langle \mathrm{H}\Delta\mathrm{N} \right\rangle = 2\mathrm{tr}\,(h_{n}\chi_{n}) - \mathrm{Re}\,\mathrm{tr}\,(\Delta_{n}\kappa_{n}^{*}\eta_{n}) , \tag{3.167}$$

$$\left\langle \left(\mathrm{H} - \left\langle\,\mathrm{H}\,\right\rangle\right)\Delta\mathrm{N}^{2} \right\rangle = 4\mathrm{tr}\,(h_{n}\eta_{n}\chi_{n} + \Gamma_{n}[\chi]\chi_{n}) - \mathrm{tr}\,(\Delta_{n}[\eta\kappa][\eta_{n}\kappa_{n}])$$
$$- \mathrm{Re}\,\mathrm{tr}\,(\Delta_{n}\kappa_{n}^{*}(1 - 8\chi_{n})) . \tag{3.168}$$

The HFB+Lipkin-Nogami Equations

With the derived expressions at hand, we can now carry out the variation of the Lipkin-Nogami energy (3.156) under the particle-number constraints. There is, however, an ambiguity in the variation of the Lipkin-Nogami correction terms, where we have

$$\delta\left\langle \Delta\mathrm{A}_{\tau}^{2} \right\rangle = 2\delta\mathrm{tr}\,\chi_{\tau} . \tag{3.169}$$

Since χ_{τ} can be expressed either in terms of the density matrix or the pairing tensor, it is possible to shift the contribution from the variation of χ_{τ} between the HF and pairing fields, and there are indeed various prescriptions in the literature (see e.g. [72, 92]). For this work, we choose

$$\delta\left\langle \Delta\mathrm{A}_{\tau}^{2} \right\rangle = \delta\,\mathrm{tr}\,\left(\rho_{\tau} - \rho_{\tau}^{2}\right) + \delta\,\mathrm{tr}\,\left(\kappa_{\tau}\kappa_{\tau}^{\dagger}\right) . \tag{3.170}$$

Using

$$\sum_{j} \frac{\partial\chi_{jj}^{\tau}}{\partial\rho_{k'k}^{\tau}} = \sum_{j} \frac{\partial}{\partial\rho_{k'k}^{\tau}}\left(\rho_{jj}^{\tau} - \sum_{l}\rho_{jl}^{\tau}\rho_{lj}^{\tau}\right) = \delta_{kk'} - 2\rho_{kk'}^{\tau} = \eta_{kk'}^{\tau} \tag{3.171}$$

and

$$\sum_{j} \frac{\partial\chi_{jj}^{\tau}}{\partial\kappa_{kk'}^{\tau*}} = \frac{\partial}{\partial\kappa_{kk'}^{\tau*}} \sum_{jl}\kappa_{jl}^{\tau}\kappa_{jl}^{\tau*} = 2\kappa_{kk'}^{\tau}, \quad (k < k') , \tag{3.172}$$

we obtain the HFB+LN equations

$$\begin{pmatrix} h_{\tau} - h_{2}^{\tau}\eta_{\tau} - \lambda_{\tau} & \Delta_{\tau} - 2h_{2}^{\tau}\kappa_{\tau} \\ -\Delta_{\tau}^{*} + 2h_{2}^{\tau}\kappa_{\tau}^{*} & -h_{\tau}^{*} + h_{2}^{\tau}\eta_{\tau}^{*} + \lambda_{\tau} \end{pmatrix} \begin{pmatrix} U_{\tau} \\ V_{\tau} \end{pmatrix} = E_{\tau} \begin{pmatrix} U_{\tau} \\ V_{\tau} \end{pmatrix} . \tag{3.173}$$

3.2.4   Implementation

We end the discussion of exact and approximate PNP with a remark on the implementation. In the exact HFB+VAPNP method, no Lagrange multipliers λ_{τ} enter the variational equations. In principle, there is no need to adjust the mean particle number

— i.e., the norm of the intrinsic state — because the projected energy or other projected expectation values can be obtained from practically any intrinsic state, as long as it has a non-vanishing overlap with the state $\left| \Psi_{N_0 Z_0} \right\rangle$. Numerically, though, we have to discretize the gauge-angle integrals, and the intrinsic state might change strongly from iteration to iteration. As a result, the iterative procedure may converge slowly or become numerically unstable if the overlaps become too small by accident. To avoid these problems, we manually add constraints on the mean particle number, i.e., we solve

$$
\begin{pmatrix} h_\tau^P - \mu_\tau & \Delta_\tau^P \\ -\Delta_\tau^{P*} & -h_\tau^{P*} + \mu_\tau \end{pmatrix} \begin{pmatrix} U_\tau^P \\ V_\tau^P \end{pmatrix} = E_\tau^P \begin{pmatrix} U_\tau^P \\ V_\tau^P \end{pmatrix} .
\tag{3.174}
$$

As the iterations converge, it becomes unnecessary to adjust the Lagrange multipliers, and the μ_τ automatically converge to 0, i.e., the HFB+VAPNP results become independent of μ_τ [81, 88]. This convergence also provides a very stringent test for the numerical accuracy of the method.

Similarly, in the Lipkin-Nogami method the λ_τ are in principle determined by

$$
\lambda_\tau = h_1^\tau
\tag{3.175}
$$

(see Sect. 3.2.3). This relation has to be satisfied automatically during the iterative solution of the HFB+LN equations, where it can be subject to numerical instabilities. Thus, we again introduce an additional constraint on the mean particle numbers and solve

$$
\begin{pmatrix} h_\tau - h_2^\tau \eta_\tau - \lambda_\tau - \mu_\tau & \Delta_\tau - 2h_2^\tau \kappa_\tau \\ -\Delta_\tau^* + 2h_2^\tau \kappa_\tau^* & -h_\tau^* + h_2^\tau \eta_\tau^* + \lambda_\tau + \mu_\tau \end{pmatrix} \begin{pmatrix} U_\tau \\ V_\tau \end{pmatrix} = E_\tau \begin{pmatrix} U_\tau \\ V_\tau \end{pmatrix} ,
\tag{3.176}
$$

where μ_τ again automatically converges to 0 as the iterations reach convergence and the condition (3.175) is satisfied with increasing accuracy.

3.3   Density-Dependent Interactions

3.3.1 $3N$ and Density-Dependent Interactions

The discussion of HFB theory and its particle-number-projected extensions in the previous sections was based on a Hamiltonian consisting of one- and two-body operators e.g. the full or intrinsic kinetic energy and the NN interaction. If a $3N$ interaction is included as well, the application of the Wick theorem yields the following expression for the energy:

$$
\begin{aligned}
E[\rho, \kappa, \kappa^*] =& \frac{\left\langle \Psi \middle| \mathrm{H} \middle| \Psi \right\rangle}{\left\langle \Psi \middle| \Psi \right\rangle} \\
=& \sum_{kk'} t_{kk'} \rho_{k'k} + \frac{1}{2} \sum_{kk'qq'} \bar{v}_{kq'k'q} \rho_{k'k} \rho_{qq'} - \frac{1}{4} \sum_{kk'qq'} \bar{v}_{kk'qq'} \kappa_{k'k}^* \kappa_{qq'} \\
&+ \frac{1}{6} \sum_{kk'qq'rr'} \bar{w}_{kq'r'k'qr} \rho_{k'k} \rho_{qq'} \rho_{rr'} - \frac{1}{4} \sum_{kk'qq'rr'} \bar{w}_{krr'k'qq'} \rho_{k'k} \kappa_{r'r}^* \kappa_{qq'} ,
\end{aligned}
\tag{3.177}
$$

where $\bar{w}$ denotes the antisymmetrized matrix element of the $3N$ interaction. While the variation of this energy with respect to the densities is no more complicated than for the case without the $3N$ interaction, the numerical effort required for handling the new terms is tremendous — in particular, the matrix elements $\bar{w}$ need to be stored, and the two additional indices imply an increase in effort by a factor of n^2 for all summations containing these matrix elements, where n is the configuration space basis size. Matters are made worse by noting that all currently used $3N$ forces comprise more dense matrices than their NN counterparts.

Rearranging Eq. (3.177), the energy can be expressed as

$$
\begin{aligned}
E[\rho, \kappa, \kappa^*] =& \frac{\langle\, \Psi\, |\, \mathrm{H}\, |\, \Psi\, \rangle}{\langle\, \Psi\, |\, \Psi\, \rangle} \\
=& \sum_{kk'} t_{kk'} \rho_{k'k} + \frac{1}{2} \sum_{kk'qq'} \left(\bar{v}_{kq'k'q} + \frac{1}{3} \sum_{rr'} \bar{w}_{kq'r'k'qr} \rho_{rr'} \right) \rho_{k'k} \rho_{qq'} \\
& - \frac{1}{4} \sum_{kk'qq'} \left(\bar{v}_{kk'qq'} + \sum_{rr'} \bar{w}_{r'kk'rqq'} \rho_{rr'} \right) \kappa^*_{k'k} \kappa_{qq'} \,,
\end{aligned}
\tag{3.178}
$$

which suggests that the $3N$ interaction contributes to the energy like a density-dependent force (note, however, the different factors in the particle-hole and particle-particle channels). In a recent coupled-cluster calculation of ^{4}He employing a renormalized chiral N2LO $3N$ interaction along with $V_{\text{low-k}}$, it was shown that the effect of the residual $3N$ interaction on the binding energy is very small even in more advanced many-body methods [93, 94], hence the use of an appropriately constructed density-dependent force may yield most of the effects of the full $3N$ force.

The idea of replacing the $3N$ interaction by a density-dependent NN interaction has been discussed since the work of Skyrme [74] — mean-field approaches based on effective density-dependent interactions like the Skyrme or Gogny forces make use of the equivalence of a simple $3N$ contact interaction of the form

$$
\mathrm{w} = t_3 \delta^{(3)}(\mathbf{r}_1 - \mathbf{r}_2) \delta^{(3)}(\mathbf{r}_2 - \mathbf{r}_3)
\tag{3.179}
$$

with a zero-range two-body force with linear density-dependence

$$
\mathrm{v}[\rho] = \frac{t_3}{6} \left(1 + \mathrm{P}_\sigma\right) \rho \left(\frac{\mathbf{r}_1 + \mathbf{r}_2}{2} \right) \delta^{(3)}(\mathbf{r}_1 - \mathbf{r}_2) \,,
\tag{3.180}
$$

in *systems with time-reversal symmetry*, i.e., even-even nuclei [76, 95]. In Eq. (3.180), P_σ is the spin-exchange operator. The Skyrme and Gogny parameterizations commonly used nowadays further generalize this type of interaction, considering powers of the density and weights for the spin-exchange operator as additional fit parameters (see e.g. [82, 96, 97, 98]):

$$
\mathrm{v}[\rho] = t_0 \left(1 + x_0 \mathrm{P}_\sigma\right) \rho^\alpha \left(\frac{\mathbf{r}_1 + \mathbf{r}_2}{2} \right) \delta^{(3)}(\mathbf{r}_1 - \mathbf{r}_2) \,.
\tag{3.181}
$$

Besides not being founded entirely in a microscopic approach, the integer or rational power-law dependencies on the density introduced in these forces lead to problems in

symmetry-projected HFB theory [79], a subject which we will come back to in Sect. 3.4. While the formulae of this section will be derived for a force of the the general type (3.181) to allow comparisons with the Gogny interaction, we will only use (3.180) in conjunction with V_{UCOM}.

3.3.2 HFB with a Density-Dependent Interaction

For convenience, we consider the energy contribution of the density-dependent interaction in the integral form

$$
\breve{E}[\rho, \kappa, \kappa^*] = \frac{\left\langle \Psi \right| \mathrm{V}[\rho] \left| \Psi \right\rangle}{\left\langle \Psi | \Psi \right\rangle} = \frac{\left\langle \Psi \right| \sum_{i<j} \mathrm{v}_{ij}[\rho] \left| \Psi \right\rangle}{\left\langle \Psi | \Psi \right\rangle}
$$

$$
= t_0 \int d^3r \, \rho^\alpha(\boldsymbol{r}) \frac{1}{2} \left(\left(1 + \frac{x_0}{2}\right) \rho^2(\boldsymbol{r}) - \left(x_0 + \frac{1}{2}\right) \sum_\tau \rho_\tau^2(\boldsymbol{r}) \right.
$$

$$
\left. + \frac{1}{2} \left(1 - x_0\right) \sum_\tau \kappa_\tau^*(\boldsymbol{r}) \kappa_\tau(\boldsymbol{r}) \right), \tag{3.182}
$$

where

$$
\rho(\boldsymbol{r}) = \sum_{\tau k k'} \rho_{kk'}^\tau \psi_{k\tau}^*(\boldsymbol{r}) \psi_{k'\tau}(\boldsymbol{r}), \tag{3.183}
$$

$$
\kappa(\boldsymbol{r}) = \sum_{\tau k \bar{k}'} \kappa_{k\bar{k}'}^\tau \psi_{k\tau}(\boldsymbol{r}) \psi_{\bar{k}'\tau}(\boldsymbol{r}), \tag{3.184}
$$

$\bar{k}$ denotes a time-reversed state, and $\tau = p, n$. We can now carry out the variation of $\breve{E}$ with respect to the densities and obtain

$$
\breve{\Gamma}_{kk'}^\tau = \int d^3r \, \frac{\partial \breve{E}}{\partial \rho_\tau(\boldsymbol{r})} \frac{\partial \rho_\tau(\boldsymbol{r})}{\partial \rho_{k'k}^\tau} = \int d^3r \, \psi_{k'\tau}^*(\boldsymbol{r}) \breve{\Gamma}_\tau(\boldsymbol{r}) \psi_{k\tau}(\boldsymbol{r}), \tag{3.185}
$$

$$
\breve{\Delta}_{kk'}^\tau = \int d^3r \, \frac{\partial \breve{E}}{\partial \kappa_\tau^*(\boldsymbol{r})} \frac{\partial \kappa_\tau^*(\boldsymbol{r})}{\partial \kappa_{k'k}^{\tau*}} = \int d^3r \, \breve{\Delta}_\tau(\boldsymbol{r}) \psi_{k\tau}(\boldsymbol{r}) \psi_{k'\tau}(\boldsymbol{r}), \qquad \text{for } (k < k'), \tag{3.186}
$$

with

$$
\breve{\Gamma}_\tau(\boldsymbol{r}) = t_0 \left[\left(1 + \frac{x_0}{2}\right) \rho^{\alpha+1}(\boldsymbol{r}) - \left(x_0 + \frac{1}{2}\right) \rho^\alpha(\boldsymbol{r}) \rho_\tau(\boldsymbol{r}) \right]
$$

$$
+ \frac{t_0}{4} \alpha \left(1 - x_0\right) \left(\rho^{\alpha+1}(\boldsymbol{r}) + \rho^{\alpha-1}(\boldsymbol{r}) \sum_{\tau'} \kappa_{\tau'}^*(\boldsymbol{r}) \kappa_{\tau'}(\boldsymbol{r}) \right)
$$

$$
+ t_0 \alpha \left(x_0 + \frac{1}{2}\right) \rho^{\alpha-1}(\boldsymbol{r}) \rho_p(\boldsymbol{r}) \rho_n(\boldsymbol{r}) \tag{3.187}
$$

and

$$
\breve{\Delta}_\tau(\boldsymbol{r}) = \frac{1}{2} t_0 \left(1 - x_0\right) \rho^\alpha(\boldsymbol{r}) \kappa_\tau(\boldsymbol{r}). \tag{3.188}
$$

The pairing field (3.188) and the terms in the first bracket of the HF field (3.187) correspond to the usual contractions of the pairing tensor and density matrix with a two-body interaction, just as in Sect. 3.1. Due to the density-dependence of the interaction, however, there is a further contribution to the HF field, i.e., the terms proportional to α, which constitute the so-called *rearrangement term*.

Spherical Symmetry

In the case of spherical symmetry, the densities and fields introduced above only depend on the radial coordinate r. The expressions for the densities are reduced to

$$\rho(r) = \sum_{\tau l j n n'} \frac{2j+1}{4\pi} \rho_{nn'}^{lj\tau} R_{nl}(r) R_{n'l}(r), \qquad (3.189)$$

$$\kappa(r) = \sum_{\tau l j n n'} \frac{2j+1}{4\pi} (-1)^l \kappa_{nn'}^{lj\tau} R_{nl}(r) R_{n'l}(r), \qquad (3.190)$$

where the phase $(-1)^l$ appears due to using the properties of the spherical harmonics under time-reversal (cf. Appendix B.1), and $R_{nl}(r)$ are radial spherical harmonic oscillator wavefunctions. For the fields, we have

$$\breve{\Gamma}_{nn'}^{(lj\tau)} = \int dr\, R_{nl}(r) \breve{\Gamma}_\tau(r) R_{n'l}(r), \qquad (3.191)$$

$$\breve{\Delta}_{nn'}^{(lj\tau)} = \int dr\, R_{nl}(r) \breve{\Delta}_\tau^{(lj)}(r) R_{n'l}(r), \qquad (3.192)$$

with

$$
\begin{aligned}
\breve{\Gamma}_\tau(r) = {}& t_0 \left[\left(1 + \frac{x_0}{2} \right) \rho^{\alpha+1}(r) - \left(x_0 + \frac{1}{2} \right) \rho^\alpha(r) \rho_\tau(r) \right] \\
& + \frac{t_0}{4} \alpha \left(1 - x_0 \right) \left(\rho^{\alpha+1}(r) + \rho^{\alpha-1}(r) \sum_{\tau'} \kappa_{\tau'}^2(r) \right) \\
& + t_0 \alpha \left(x_0 + \frac{1}{2} \right) \rho^{\alpha-1}(r) \rho_p(r) \rho_n(r)
\end{aligned}
\qquad (3.193)
$$

and

$$\breve{\Delta}_\tau^{(lj)}(r) = \frac{1}{2} t_0 \left(1 - x_0 \right) \rho^\alpha(r) (-1)^l \kappa_\tau(r). \qquad (3.194)$$

Since the density matrix and pairing tensor are real matrices (cf. Sect. 3.1.5), the coordinate-space densities and fields are real as well, which further simplifies the formulae.

3.3.3 Exact Particle-Number Projection

The density-dependence of the interaction (3.181) poses a problem as soon as projection techniques are considered, because it is unclear *which* density should be used in the interaction. For this, two prescriptions have been primarily discussed in the literature (see e.g. [78]):

(i) the *projected-density prescription*,

$$\rho^P(\boldsymbol{r}) = \rho_n^P(\boldsymbol{r}) + \rho_p^P(\boldsymbol{r}), \qquad (3.195)$$

$$\rho_\tau^P(\boldsymbol{r}) \equiv \frac{\left\langle \Psi_{N_0 Z_0} \middle| \Psi_\tau^\dagger(\boldsymbol{r}) \Psi_\tau(\boldsymbol{r}) \middle| \Psi_{N_0 Z_0} \right\rangle}{\left\langle \Psi_{N_0 Z_0} \middle| \Psi_{N_0 Z_0} \right\rangle}, \qquad (3.196)$$

(ii) the *mixed-density prescription*,

$$\rho(\phi_n, \phi_p, \boldsymbol{r}) = \rho_n(\phi_n, \boldsymbol{r}) + \rho_p(\phi_p, \boldsymbol{r}) \,, \tag{3.197}$$

$$\rho_\tau(\phi_\tau, \boldsymbol{r}) \equiv \frac{\left\langle \Psi \middle| \Psi_\tau^\dagger(\boldsymbol{r}) \Psi_\tau(\boldsymbol{r}) e^{i\phi_\tau A_\tau} \middle| \Psi \right\rangle}{\left\langle \Psi \middle| e^{i\phi_\tau A_\tau} \middle| \Psi \right\rangle} \,. \tag{3.198}$$

Since we are introducing the density-dependent interaction as an approximation for a $3N$ interaction in the sense of a contraction of the $3N$ matrix element with a single density matrix, i.e.

$$\sum_{rr'} \bar{w}_{kqr'k'q'r} \rho_{rr'} \rightarrow v[\rho]_{kqk'q'} \,, \tag{3.199}$$

the mixed density is the more appropriate description of the two, because the density matrix in (3.199) would be replaced by the transition density matrix[5]$\rho(\phi_n, \phi_p)$. Furthermore, while both prescriptions yield similar results [77, 78] in the case of particle-number projection, only the mixed-density prescription gives sensible results when one deals with the restoration of coordinate-space symmetries in parity or angular-momentum projection [100].

The contribution of the density-dependent interaction to the projected energy is obtained by replacing the densities in (3.182) by the corresponding transition densities, and performing the integration over the gauge angles:

$$\breve{E}^{N_0 Z_0} = \int d\phi_n d\phi_p y_n(\phi_n) y_p(\phi_p) \left(\breve{H}_{\mathrm{ph}}(\phi_n, \phi_p) + \breve{H}_{\mathrm{pp}}(\phi_n, \phi_p) \right) \,, \tag{3.200}$$

with

$$\breve{H}_{\mathrm{ph}}(\phi_n, \phi_p) = \frac{t_0}{2} \int d^3 r \, \rho^\alpha(\phi_n, \phi_p, \boldsymbol{r})$$
$$\times \left(\left(1 + \frac{x_0}{2} \right) \rho^2(\phi_n, \phi_p, \boldsymbol{r}) - \left(x_0 + \frac{1}{2} \right) \sum_\tau \rho_\tau^2(\phi_\tau, \boldsymbol{r}) \right) \,, \tag{3.201}$$

$$\breve{H}_{\mathrm{pp}}(\phi_n, \phi_p) = \frac{t_0}{4} \int d^3 r \, \rho^\alpha(\phi_n, \phi_p, \boldsymbol{r}) (1 - x_0) \left(\sum_\tau \bar{\kappa}_\tau^*(\phi_\tau, \boldsymbol{r}) \kappa_\tau(\phi_\tau, \boldsymbol{r}) \right) \,. \tag{3.202}$$

Analogously, the matrix elements of the transition fields are given by Eqs. (3.185) and (3.186) for

$$\breve{\Gamma}_\tau(\phi_n, \phi_p, \boldsymbol{r})$$
$$= t_0 \left[\left(1 + \frac{x_0}{2} \right) \rho^{\alpha+1}(\phi_n, \phi_p, \boldsymbol{r}) - \left(x_0 + \frac{1}{2} \right) \rho^\alpha(\phi_n, \phi_p, \boldsymbol{r}) \rho_\tau(\phi_\tau, \boldsymbol{r}) \right]$$
$$+ \frac{t_0}{4} \alpha (1 - x_0) \left(\rho^{\alpha+1}(\phi_n, \phi_p, \boldsymbol{r}) + \rho^{\alpha-1}(\phi_n, \phi_p, \boldsymbol{r}) \sum_{\tau'} \bar{\kappa}_{\tau'}^*(\phi_{\tau'}, \boldsymbol{r}) \kappa_{\tau'}(\phi_{\tau'}, \boldsymbol{r}) \right)$$
$$+ t_0 \alpha \left(x_0 + \frac{1}{2} \right) \rho^{\alpha-1}(\phi_n, \phi_p, \boldsymbol{r}) \rho_p(\phi_p, \boldsymbol{r}) \rho_n(\phi_n, \boldsymbol{r}) \tag{3.203}$$

---

[5]There are more examples in GCM-based methods where only the use of the mixed-density prescription yields correct expressions in certain limits, as in the derivation of the RPA equations from the GCM [99, 100], for instance.

and

$$\breve{\Delta}_\tau(\phi_n, \phi_p, \boldsymbol{r}) = \frac{1}{2}t_0 \left(1 - x_0\right) \rho^\alpha(\phi_n, \phi_p, \boldsymbol{r})\kappa_\tau(\phi_\tau, \boldsymbol{r}) \,. \tag{3.204}$$

The projected fields for the density-dependent interaction now become

$$\breve{\Gamma}_\tau^P = \frac{1}{2}\int d\phi_n \int d\phi_p \, y_n(\phi_n)y_p(\phi_p)Y_\tau(\phi_\tau)\breve{H}_{\rm ph}(\phi_n, \phi_p)$$
$$+ \frac{1}{2}\int d\phi_\tau y_\tau(\phi_\tau)e^{-2i\phi_\tau}C_\tau(\phi_\tau)\tilde{\Gamma}_\tau(\phi_\tau)C_\tau(\phi_\tau) + h.c. \,, \tag{3.205}$$

$$\breve{\Lambda}_\tau^P = \frac{1}{2}\int d\phi_n \int \phi_p y_n(\phi_n)y_p(\phi_p)Y_\tau(\phi_\tau)\breve{H}_{\rm pp}(\phi_n, \phi_p)$$
$$+ \frac{i}{2}\int d\phi_\tau y_\tau(\phi_\tau)e^{-i\phi_\tau}\sin\phi_\tau$$
$$\times \left(C_\tau(\phi_\tau)\tilde{\Delta}_\tau(\phi_\tau)\bar{\kappa}_\tau^*(\phi_\tau) + \kappa_\tau(\phi_\tau)\tilde{\bar{\Delta}}_\tau^*(\phi_\tau)C_\tau(\phi_\tau)\right) + h.c. \,, \tag{3.206}$$

and

$$\Delta_\tau^P = \frac{1}{2}\int d\phi_\tau \, y_\tau(\phi_\tau) \left(C_\tau(\phi_\tau)\tilde{\Delta}_\tau(\phi_\tau) - \tilde{\Delta}_\tau^T(\phi_\tau)C_\tau^T(\phi_\tau)\right) \,, \tag{3.207}$$

where we have introduced the modified fields

$$\tilde{\Gamma}_\tau(\phi_\tau) = \int d\phi_{\tau'}y_{\tau'}(\phi_{\tau'})\breve{\Gamma}(\phi_\tau, \phi_\tau'), \quad \tau \neq \tau' \,, \tag{3.208}$$

$$\tilde{\Delta}_\tau(\phi_\tau) = \int d\phi_{\tau'}y_{\tau'}(\phi_{\tau'})\breve{\Delta}(\phi_\tau, \phi_\tau'), \quad \tau \neq \tau' \,, \tag{3.209}$$

by integrating out one of the gauge angles, just as in Sect. 3.2.2.

3.3.4 The Lipkin-Nogami Method

For a density-dependent interaction, the expressions for the Lipkin-Nogami coefficients given in Sect. 3.2.3 are modified by rearrangement-like terms originating from the derivatives of the density-dependent interaction matrix elements with respect to the gauge angles [77]. The system of equations (3.149) now becomes

$$\left\langle \, {\rm H} \, \right\rangle = h_0 + h_2^n \left\langle \, \Delta{\rm N}^2 \, \right\rangle + h_2^p \left\langle \, \Delta{\rm Z}^2 \, \right\rangle \tag{3.210a}$$

$$\left\langle \, {\rm H}\Delta{\rm N} + \frac{1}{i}\frac{\partial{\rm H}}{\partial\phi_n}\bigg|_{\{\phi\}=0} \, \right\rangle = h_1^n \left\langle \, \Delta{\rm N}^2 \, \right\rangle + h_2^n \left\langle \, \Delta{\rm N}^3 \, \right\rangle \tag{3.210b}$$

$$\left\langle \, {\rm H}\Delta{\rm Z} + \frac{1}{i}\frac{\partial{\rm H}}{\partial\phi_p}\bigg|_{\{\phi\}=0} \, \right\rangle = h_1^p \left\langle \, \Delta{\rm Z}^2 \, \right\rangle + h_2^p \left\langle \, \Delta{\rm Z}^3 \, \right\rangle \tag{3.210c}$$

$$\left\langle \, {\rm H}\Delta{\rm N}^2 + 2\Delta{\rm N}\frac{1}{i}\frac{\partial{\rm H}}{\partial\phi_n}\bigg|_{\{\phi\}=0} + \frac{1}{i^2}\frac{\partial^2{\rm H}}{\partial\phi_n^2}\bigg|_{\{\phi\}=0} \, \right\rangle = h_0 \left\langle \, \Delta{\rm N}^2 \, \right\rangle + h_1^n \left\langle \, \Delta{\rm N}^3 \, \right\rangle + h_2^n \left\langle \, \Delta{\rm N}^4 \, \right\rangle$$
$$+ h_2^p \left\langle \, \Delta{\rm N}^2 \, \right\rangle \left\langle \, \Delta{\rm Z}^2 \, \right\rangle \tag{3.210d}$$

$$\left\langle \, {\rm H}\Delta{\rm Z}^2 + 2\Delta{\rm Z}\frac{1}{i}\frac{\partial{\rm H}}{\partial\phi_p}\bigg|_{\{\phi\}=0} + \frac{1}{i^2}\frac{\partial^2{\rm H}}{\partial\phi_p^2}\bigg|_{\{\phi\}=0} \, \right\rangle = h_0 \left\langle \, \Delta{\rm Z}^2 \, \right\rangle + h_1^p \left\langle \, \Delta{\rm Z}^3 \, \right\rangle + h_2^p \left\langle \, \Delta{\rm Z}^4 \, \right\rangle$$
$$+ h_2^n \left\langle \, \Delta{\rm N}^2 \, \right\rangle \left\langle \, \Delta{\rm Z}^2 \, \right\rangle \,, \tag{3.210e}$$

where $\{\phi\} = 0$ indicates that both gauge angles are set to zero after differentiating, and the solutions are given by

$$h_0 = \big\langle\, \mathrm{H} \,\big\rangle - h_2^n \big\langle\, \Delta\mathrm{N}^2 \,\big\rangle - h_2^p \big\langle\, \Delta\mathrm{Z}^2 \,\big\rangle \,, \tag{3.211}$$

$$h_1^n = \frac{\big\langle\, \mathrm{H}\Delta\mathrm{N} + \frac{1}{i}\frac{\partial\mathrm{H}}{\partial\phi_n}\big|_{\{\phi\}=0} \,\big\rangle - h_2^n \big\langle\, \Delta\mathrm{N}^3 \,\big\rangle}{\big\langle\, \Delta\mathrm{N}^2 \,\big\rangle} \,, \tag{3.212}$$

$$h_1^p = \frac{\big\langle\, \mathrm{H}\Delta\mathrm{Z} + \frac{1}{i}\frac{\partial\mathrm{H}}{\partial\phi_p}\big|_{\{\phi\}=0} \,\big\rangle - h_2^p \big\langle\, \Delta\mathrm{Z}^3 \,\big\rangle}{\big\langle\, \Delta\mathrm{Z}^2 \,\big\rangle} \,, \tag{3.213}$$

$$h_2^n = \frac{\big\langle\, (\mathrm{H} - \langle\, \mathrm{H} \,\rangle)\Delta\mathrm{N}^2 + 2\Delta\mathrm{N}\,\frac{1}{i}\frac{\partial\mathrm{H}}{\partial\phi_n}\big|_{\{\phi\}=0} + \frac{1}{i^2}\frac{\partial^2\mathrm{H}}{\partial\phi_n^2}\big|_{\{\phi\}=0} \,\big\rangle - \big\langle\, \mathrm{H}\Delta\mathrm{N} \,\big\rangle \big\langle\, \Delta\mathrm{N}^3 \,\big\rangle / \big\langle\, \Delta\mathrm{N}^2 \,\big\rangle}{\big\langle\, \Delta\mathrm{N}^4 \,\big\rangle - \big\langle\, \Delta\mathrm{N}^2 \,\big\rangle^2 - \big\langle\, \Delta\mathrm{N}^3 \,\big\rangle^2 / \big\langle\, \Delta\mathrm{N}^2 \,\big\rangle} \,, \tag{3.214}$$

$$h_2^p = \frac{\big\langle\, (\mathrm{H} - \langle\, \mathrm{H} \,\rangle)\Delta\mathrm{Z}^2 + 2\Delta\mathrm{Z}\,\frac{1}{i}\frac{\partial\mathrm{H}}{\partial\phi_p}\big|_{\{\phi\}=0} + \frac{1}{i^2}\frac{\partial^2\mathrm{H}}{\partial\phi_p^2}\big|_{\{\phi\}=0} \,\big\rangle - \big\langle\, \mathrm{H}\Delta\mathrm{Z} \,\big\rangle \big\langle\, \Delta\mathrm{Z}^3 \,\big\rangle / \big\langle\, \Delta\mathrm{Z}^2 \,\big\rangle}{\big\langle\, \Delta\mathrm{Z}^4 \,\big\rangle - \big\langle\, \Delta\mathrm{Z}^2 \,\big\rangle^2 - \big\langle\, \Delta\mathrm{Z}^3 \,\big\rangle^2 / \big\langle\, \Delta\mathrm{Z}^2 \,\big\rangle} \,. \tag{3.215}$$

The ϕ_τ-dependence of the Hamiltonian is due to the density-dependent part, so we formally need to evaluate expectation values like

$$\Big\langle\, \frac{1}{i}\frac{\partial\mathrm{V}[\rho(\phi_n,\phi_p,\boldsymbol{r})]}{\partial\phi_\tau}\Big|_{\{\phi\}=0} \,\Big\rangle = \Big\langle\, \frac{\partial\mathrm{V}[\rho(\phi_n,\phi_p,\boldsymbol{r})]}{\partial\rho(\phi_n,\phi_p,\boldsymbol{r})}\,\frac{1}{i}\frac{\partial\rho(\phi_n,\phi_p,\boldsymbol{r})}{\partial\phi_\tau}\Big|_{\{\phi\}=0} \,\Big\rangle \tag{3.216}$$

Fortunately, these are automatically obtained from the derivatives of the density-dependent Hamiltonian overlaps with respect to the gauge angles, just as in the density-independent case presented in Sect. 3.2.3, i.e.

$$\Big\langle\, \mathrm{V}[\rho]\Delta\mathrm{N} + \frac{1}{i}\frac{\partial\mathrm{V}[\rho]}{\partial\phi_n}\Big|_{\{\phi\}=0} \,\Big\rangle = \frac{1}{i}\,\frac{\partial\breve{H}(\phi_n,\phi_p)}{\partial\phi_n}\Big|_{\{\phi\}=0} \,, \tag{3.217}$$

$$\Big\langle\, \mathrm{V}[\rho]\Delta\mathrm{N}^2 + 2\Delta\mathrm{N}\,\frac{1}{i}\frac{\partial\mathrm{V}[\rho]}{\partial\phi_n}\Big|_{\{\phi\}=0} + \frac{1}{i^2}\frac{\partial^2\mathrm{V}[\rho]}{\partial\phi_n^2}\Big|_{\{\phi\}=0} \,\Big\rangle = \frac{1}{i^2}\,\frac{\partial^2\breve{H}(\phi_n,\phi_p)}{\partial\phi_n^2}\Big|_{\{\phi\}=0} \,, \tag{3.218}$$

and likewise for the protons. The evaluated expressions can be found in Appendix C.2.5.

3.4 Poles in Particle-Number Projected HFB Theory

3.4.1 The Definition of Gauge-Rotation Matrices Revisited

In Sect. 3.2.2, we have defined the gauge-rotation matrix as

$$C_\tau(\phi_\tau) = e^{2i\phi_\tau}(1 + \rho_\tau \cdot (e^{2i\phi_\tau} - 1))^{-1} \,, \tag{3.219}$$

which raises the question whether it is always well-defined during the projection procedure. Pulling the exponential factor in the inverse matrix, we can rewrite (3.219) as

$$C_\tau(\phi_\tau) = \left(e^{-2i\phi_\tau} + \rho_\tau \cdot (1 - e^{-2i\phi_\tau}) \right)^{-1} = \left(\rho_\tau + (1 - \rho_\tau)e^{-2i\phi_\tau} \right)^{-1}$$

$$= \left(1 - (1 - \rho_\tau)(1 - e^{-2i\phi_\tau}) \right)^{-1}. \tag{3.220}$$

$C_\tau(\phi_\tau)$ can be expanded as a Neumann series

$$C_\tau(\phi_\tau) = \left(1 - (1 - \rho_\tau)(1 - e^{-2i\phi_\tau}) \right)^{-1} = \sum_{n=0}^{\infty} \left((1 - \rho_\tau)(1 - e^{-2i\phi_\tau}) \right)^n, \tag{3.221}$$

which converges if

$$||(1 - \rho_\tau)(1 - e^{-2i\phi_\tau})||_\infty < 1, \tag{3.222}$$

where $|| \cdot ||_\infty$ is the operator norm [101]. We have

$$||(1 - \rho_\tau)(1 - e^{-2i\phi_\tau})||_\infty = |1 - e^{-2i\phi_\tau}| \cdot ||1 - \rho_\tau||_\infty$$

$$\leq 2||1 - \rho_\tau||_\infty = 2 \max_\mu |1 - v_{\tau\mu}^2| = 2 \max_\mu u_{\tau\mu}^2 < 1, \tag{3.223}$$

where we have used that the operator norm of the Hermitian matrix $1 - \rho_\tau$ is given by its spectral radius (i.e., the largest eigenvalue with the largest modulus), and that the eigenvalues of ρ_τ are the squared (real) canonical coefficients. By the same reasoning, a similar condition can be derived for the $v_{\tau\mu}^2$, and we find that $C_\tau(\phi_\tau)$ is well-defined in the domain

$$D = \left\{ \{u_{\tau\mu}, v_{\tau\mu}\} \in \mathbb{R} : u_{\tau\mu}^2 \neq v_{\tau\mu}^2, u_{\tau\mu}^2 + v_{\tau\mu}^2 = 1 \right\}, \tag{3.224}$$

but not for

$$u_\mu^2 = v_\mu^2 = \frac{1}{2}. \tag{3.225}$$

The reason for the breakdown of the expansion becomes clear when we look at $C_\tau(\phi_\tau)$ in the canonical basis: in the critical case,

$$C_{\mu\nu}^\tau(\phi_\tau) = \frac{e^{2i\phi_\tau}}{u_{\tau\mu}^2 + v_{\tau\mu}^2 e^{2i\phi_\tau}} \delta_{\mu\nu} \tag{3.226}$$

has a singularity at $\phi_\tau = \pm\frac{\pi}{2}$.

3.4.2 Cancellation of Singularities in the Hamiltonian Case

The singularity discussed in the previous section proves to be no problem at all as long as the PNP before or after the variation is based on a *density-independent* Hamiltonian. This becomes clear if we look at the integrands appearing in the projected energy, following the discussion of Anguiano et al. [78]. Introducing the shorthand

$$\left| \bar{\Psi} \right\rangle = e^{i(\phi_n \mathrm{N} + \phi_p \mathrm{Z})} \left| \Psi \right\rangle, \tag{3.227}$$

the single-particle integrand is given by

$$
\begin{aligned}
x(\phi_n,\phi_p)H_{\rm sp}(\phi_n,\phi_p) &= \left\langle\,\Psi\,\middle|\,\bar\Psi\,\right\rangle \sum_\tau \sum_{\mu\mu'} t^\tau_{\mu\mu'}\rho^\tau_{\mu'\mu}(\phi_\tau)\\
&= \left\langle\,\Psi\,\middle|\,\bar\Psi\,\right\rangle \sum_\tau \sum_{\mu,\mu'>0}\left(t^\tau_{\mu\mu'}\rho^\tau_{\mu'\mu}(\phi_\tau)+t^\tau_{\bar\mu\bar\mu'}\rho^\tau_{\bar\mu'\bar\mu}(\phi_\tau)\right)\\
&= \sum_\tau \sum_{\mu>0}\left(t^\tau_{\mu\mu'}+t^\tau_{\bar\mu\bar\mu}\right)\frac{v^2_{\tau\mu}e^{2i\phi_\tau}}{u^2_{\tau\mu}+v^2_{\tau\mu}e^{2i\phi_\tau}}\cdot\prod_{\tau'}\prod_{\nu>0}\left(u^2_{\tau'\nu}+v^2_{\tau'\nu}e^{2i\phi_{\tau'}}\right)\\
&= \sum_\tau \sum_{\mu>0}\left(t^\tau_{\mu\mu'}+t^\tau_{\bar\mu\bar\mu}\right)v^2_{\tau\mu}e^{2i\phi_\tau}\cdot\prod_{\tau'}\prod_{\nu>0,\nu\neq\mu}\left(u^2_{\tau'\nu}+v^2_{\tau'\nu}e^{2i\phi_{\tau'}}\right),\qquad (3.228)
\end{aligned}
$$

i.e., the denominators in the density matrix are cancelled by the overlap and the result is regular. For the particle-hole part,

$$
\begin{aligned}
&x(\phi_n,\phi_p)H_{\rm ph}(\phi_n,\phi_p)\\
&= \left\langle\,\Psi\,\middle|\,\bar\Psi\,\right\rangle \frac{1}{2}\sum_{\tau,\tau'}\sum_{\mu\mu'}\bar{v}^{\tau\tau'}_{\mu\mu'\mu\mu'}\rho^\tau_{\mu\mu}(\phi_\tau)\rho^{\tau'}_{\mu'\mu'}(\phi_{\tau'})\\
&= \left\langle\,\Psi\,\middle|\,\bar\Psi\,\right\rangle \frac{1}{2}\sum_{\substack{\mu,\mu'>0\\\tau,\tau'}}\left(\bar{v}^{\tau\tau'}_{\mu\mu'\mu\mu'}+\bar{v}^{\tau\tau'}_{\bar\mu\mu'\bar\mu\mu'}+\bar{v}^{\tau\tau'}_{\mu\bar\mu'\mu\bar\mu'}+\bar{v}^{\tau\tau'}_{\bar\mu\bar\mu'\bar\mu\bar\mu'}\right)\rho^\tau_{\mu\mu}(\phi_\tau)\rho^{\tau'}_{\mu'\mu'}(\phi_{\tau'}),\quad (3.229)
\end{aligned}
$$

which will have no divergences if $\tau\neq\tau'$ or $\mu=\mu'$, because then each denominator from the density matrices is again cancelled by a corresponding term of the norm overlap. For $\tau=\tau',\mu=\mu'$, however, this cancellation does not occur, and exploiting the antisymmetry of the matrix elements, we have

$$
x(\phi_n,\phi_p)H_{\rm ph}(\phi_n,\phi_p)\Big|_{\rm pole}=\left\langle\,\Psi\,\middle|\,\bar\Psi\,\right\rangle\sum_\tau\sum_{\mu>0}\bar{v}^{\tau\tau}_{\bar\mu\mu\bar\mu\mu}\left(\frac{v^2_{\tau\mu}e^{2i\phi_\tau}}{u^2_{\tau\mu}+v^2_{\tau\mu}e^{2i\phi_\tau}}\right)^2.\qquad (3.230)
$$

The particle-particle part contributes

$$
\begin{aligned}
x(\phi_n,\phi_p)H_{\rm pp}(\phi_n,\phi_p)&=\left\langle\,\Psi\,\middle|\,\bar\Psi\,\right\rangle\frac{1}{4}\sum_\tau\sum_{\mu\mu'}\bar{v}^{\tau\tau}_{\bar\mu\mu\bar\mu'\mu'}\bar\kappa^{\tau*}_{\bar\mu\mu}(\phi_\tau)\kappa^\tau_{\bar\mu'\mu'}(\phi_\tau)\\
&=\left\langle\,\Psi\,\middle|\,\bar\Psi\,\right\rangle\sum_\tau\sum_{\mu,\mu'>0}\bar{v}^{\tau\tau}_{\bar\mu\mu\bar\mu'\mu'}\bar\kappa^{\tau*}_{\bar\mu\mu}(\phi_\tau)\kappa^\tau_{\bar\mu'\mu'}(\phi_\tau),\qquad (3.231)
\end{aligned}
$$

and we can again only have a possible singularity for $\mu=\mu'$, where

$$
x(\phi_n,\phi_p)H_{\rm pp}(\phi_n,\phi_p)\Big|_{\rm pole}=\left\langle\,\Psi\,\middle|\,\bar\Psi\,\right\rangle\sum_\tau\sum_{\mu>0}\bar{v}^{\tau\tau}_{\bar\mu\mu\bar\mu\mu}\frac{u^2_{\tau\mu}v^2_{\tau\mu}e^{2i\phi_\tau}}{\left(u^2_{\tau\mu}+v^2_{\tau\mu}e^{2i\phi_\tau}\right)^2}.\qquad (3.232)
$$

Taking the sum of the particle-hole and particle-particle contributions at the 'pole', we find that

$$
x(\phi_n, \phi_p) \left[H_{\mathrm{ph}}(\phi_n, \phi_p) + H_{\mathrm{pp}}(\phi_n, \phi_p) \right] \Big|_{\mathrm{pole}}
$$

$$
= \left\langle \, \Psi \big| \bar{\Psi} \, \right\rangle \sum_{\tau} \sum_{\mu > 0} \bar{v}^{\tau\tau}_{\bar{\mu}\mu\bar{\mu}\mu} \frac{\left(u^2_{\tau\mu} + v^2_{\tau\mu} e^{2i\phi_\tau} \right) v^2_{\tau\mu} e^{2i\phi_\tau}}{\left(u^2_{\tau\mu} + v^2_{\tau\mu} e^{2i\phi_\tau} \right)^2}
$$

$$
= \left\langle \, \Psi \big| \bar{\Psi} \, \right\rangle \sum_{\tau} \sum_{\mu > 0} \bar{v}^{\tau\tau}_{\bar{\mu}\mu\bar{\mu}\mu} \frac{v^2_{\tau\mu} e^{2i\phi_\tau}}{u^2_{\tau\mu} + v^2_{\tau\mu} e^{2i\phi_\tau}} \, , \tag{3.233}
$$

and the cancellation between the dangerous denominator and the norm overlap takes place again, yielding a completely regular result.

Thus, although the various contributions to the projected energy are singular, *the singularities from the direct, exchange, and pairing parts cancel.* For this cancellation to work, it is *crucial* that all terms of the Hamiltonian are treated on the same footing in the HFB calculations, i.e., one cannot omit kinetic energy or Coulomb contributions to the pairing field, or calculate the exchange and pairing terms for parts of the nucleon-nucleon interaction, as has often been done in past applications. One can also draw the conclusion that a well-defined particle-number projected HFB theory demands the use of the *same interaction in the particle-hole and particle-particle channels*. These demands are obviously automatically satisfied if the theoretical framework is based on a Hamiltonian.

In the past decades, self-consistent mean-field calculations have been almost exclusively performed in the framework of Density Functional Theory, using the Skyrme and Gogny forces as effective interactions. In DFT, the problematic terms discussed above do not cancel properly because the exact density functional is not known[6], and some of the approximations mentioned above — omission of certain interaction terms, etc. — were performed for convenience. As a result, one has spurious contributions to the energy, which are related to self-pairing and self-interactions. In electronic DFT, these problems have been known since the 1980's, and methods exist to correct for these effects [105]. Recently, there have been attempts to transfer these approaches to the nuclear DFT [79, 106].

3.4.3 Density-Dependent Interactions

While an approach using a density-dependent interaction as introduced in Sect. 3.3 is not subject to the spurious energy contributions briefly discussed at the end of the previous section as long as it acts in both the particle-hole and particle-particle channel consistently, it nevertheless has an obvious pathological feature — the interaction itself may become singular due to its explicit density-dependence. We will briefly discuss this problem in this section, following a recent study by Dobaczewski et al. (see [79] and references therein).

---

[6]In fact, extensions of the Hohenberg-Kohn theorem for the existence of an exact intrinsic density functional for a self-bound system have been achieved only recently, see [102, 103, 104].

The particle-number projection operator (cf. Eq. (3.74))

$$\mathrm{P}^{N_0} = \frac{1}{2\pi} \int_0^{2\pi} d\phi_n \, e^{i\phi_n(\mathrm{N}-N_0)} \tag{3.234}$$

is a special realization of the operator-valued integral

$$\mathrm{P}^{N_0} = \frac{1}{2\pi i} \oint_{C_n} dz_n \, z_n^{\mathrm{N}-N_0-1} \,, \tag{3.235}$$

where C is a closed contour around the origin of the complex z_n-plane (and likewise for the protons). The so-called shift operator defined by ($\mathrm{A}_\tau = \mathrm{N}, \mathrm{Z}$)

$$\mathrm{z}_\tau \equiv z_\tau^{\mathrm{A}_\tau} \equiv e^{(\eta_\tau + i\phi_\tau)\mathrm{A}_\tau} \tag{3.236}$$

has the properties (cf. Eq. (3.136))

$$\mathrm{z}_\tau \mathrm{a}_{\tau\mu}^\dagger \mathrm{z}_\tau^{-1} = z_\tau \mathrm{a}_{\tau\mu}^\dagger \,, \tag{3.237}$$

$$\mathrm{z}_\tau \mathrm{a}_{\tau\mu} \mathrm{z}_\tau^{-1} = z_\tau^{-1} \mathrm{a}_{\tau\mu} \,, \tag{3.238}$$

and is therefore seen to be the generalization of the unitary gauge-rotation we have used so far. z_τ shifts the HFB vacuum in the complex z_τ-plane, i.e.,

$$\left| \Psi(z_n, z_p) \right\rangle = \mathrm{z}_n \mathrm{z}_p \left| \Psi \right\rangle = \prod_\tau \prod_{\mu>0} \left(u_{\tau\mu} + z_\tau^2 v_{\tau\mu} \mathrm{a}_{\tau\mu}^\dagger \mathrm{a}_{\tau\bar\mu}^\dagger \right) \left| 0 \right\rangle , \tag{3.239}$$

with $z_n = z_p = 1$ corresponding to the intrinsic state. Noting that the shifted states are analytic in z_τ, one finds that all closed contour integrals in (3.235) yield the same result: the integrand in Eq. (3.235) is a Laurent series in z_τ whose coefficients are given by the particle number components of the intrinsic state, and the component with the desired particle number is the coefficient of $1/z_\tau$, in particular, hence the projected state can be expressed as the residuum[7]

$$\left| \Psi_{N_0 Z_0} \right\rangle = \mathop{\mathrm{res}}_{z_n=0, z_p=0} z_n^{-N_0-1} z_p^{-Z_0-1} \left| \Psi(z_n, z_p) \right\rangle . \tag{3.240}$$

The invariance with respect to the choice of the contour implies that any shifted state can be used to project the particle number. Consider a HFB solution $\left| \Phi \right\rangle$ with given mean particle numbers N_0 and Z_0, and a shifted state $\left| \Phi(z_n', z_p') \right\rangle$. Then

$$\mathrm{P}^{N_0 Z_0} \left| \Psi \right\rangle = \left(\frac{1}{2\pi i} \right)^2 \oint_{C_n} \oint_{C_p} dz_n dz_p \, z_n^{\mathrm{N}-N_0-1} z_p^{\mathrm{Z}-Z_0-1} \left| \Psi \right\rangle$$

$$= \left(\frac{1}{2\pi i} \right)^2 \oint_{C_n} \oint_{C_p} dz_n dz_p \, z_n^{\mathrm{N}-N_0-1} z_p^{\mathrm{Z}-Z_0-1} (z_n')^{\mathrm{N}} (z_p')^{\mathrm{Z}} \left| \Phi \right\rangle$$

$$= \left(\frac{1}{2\pi i} \right)^2 (z_n')^{N_0} (z_p')^{Z_0} \oint_{\bar C_n} \oint_{\bar C_p} d\bar z_n d\bar z_p \, \bar z_n^{\mathrm{N}-N_0-1} \, \bar z_p^{\mathrm{Z}-Z_0-1} \left| \Phi \right\rangle$$

$$= (z_n')^{N_0} (z_p')^{Z_0} \cdot \mathrm{P}^{N_0 Z_0} \left| \Phi \right\rangle , \tag{3.241}$$

---

[7]Similar expressions can be derived for the projected energy and other observables [107, 21].
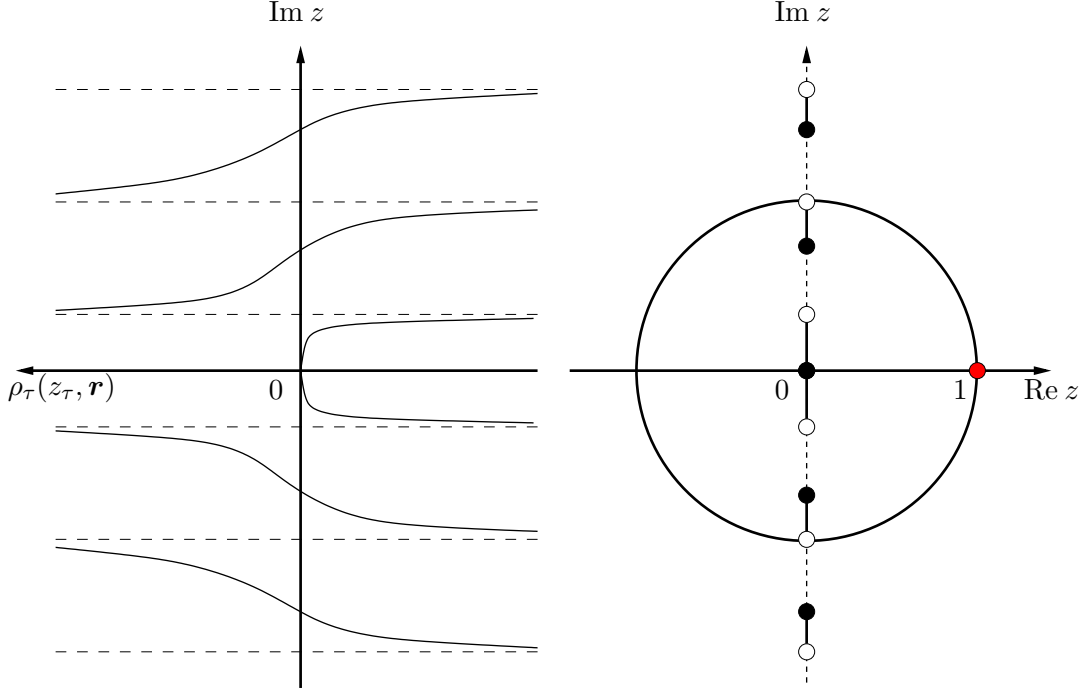
Figure 3.1: Analytic structure of $\rho_\tau(z_\tau, \boldsymbol{r})$ at a fixed point $\boldsymbol{r}$ in space. *Left:* Transition density $\rho_\tau(z_\tau, \boldsymbol{r})$ on the imaginary axis. *Right:* Poles ($\bigcirc$)and zeros ($\bullet$)of $\rho_\tau(z_\tau, \boldsymbol{r})$ in the complex z_τ-plane. The intrinsic HFB density ($z_\tau = 1$) is marked by ($\color{red}\bullet$). Branch cuts on the imaginary axis are indicated by solid black lines. Adapted from [79].

i.e., one obtains the same projected state up to an overall phase and normalization. Furthermore, expectation values calculated with the projected state will not be changed due to the division by the overlap of the projected and intrinsic state. This so-called *shift invariance* can be used to implement variations of the contour in a simple manner, because intrinsic states with different mean particle numbers are special cases of shifted states, and they are easily obtained by readjusting the particle-number constraints during the variation after PNP [108] (cf. Sect. 3.2.4).

As a function of the shifts z_τ, the local transition densities are given by

$$\rho_\tau(z_\tau, \boldsymbol{r}) = \sum_\mu \frac{z_\tau^2 v_{\tau\mu}^2}{u_{\tau\mu}^2 + z_\tau^2 v_{\tau\mu}^2} |\psi_{\tau\mu}(\boldsymbol{r})|^2 \tag{3.242}$$

$$\kappa_\tau(z_\tau, \boldsymbol{r}) = \sum_\mu \frac{z_\tau^2 u_{\tau\mu} v_{\tau\mu}}{u_{\tau\mu}^2 + z_\tau^2 v_{\tau\mu}^2} \psi_{\tau\mu}(\boldsymbol{r})\psi_{\bar{\tau}\mu}(\boldsymbol{r}) \tag{3.243}$$

$$\bar{\kappa}_\tau(z_\tau, \boldsymbol{r}) = \sum_\mu \frac{u_{\tau\mu} v_{\tau\mu}}{u_{\tau\mu}^2 + z_\tau^2 v_{\tau\mu}^2} \psi_{\tau\mu}^*(\boldsymbol{r})\psi_{\bar{\tau}\mu}^*(\boldsymbol{r}) \,, \tag{3.244}$$

with singularities occurring pairwise at

$$z_{\tau\mu} = \pm i \frac{u_{\tau\mu}}{v_{\tau\mu}}. \tag{3.245}$$

The poles of the transition density $\rho_\tau(z_\tau, \boldsymbol{r})$ are shown schematically in Fig. 3.1.

The projected energy of the density-dependent interaction

$$\mathrm{v}[\rho] = t_0 \left(1 + x_0 \mathrm{P}_\sigma\right) \rho^\alpha \left(\frac{\mathbf{r}_1 + \mathbf{r}_2}{2}\right) \delta^3(\mathbf{r}_1 - \mathbf{r}_2),\qquad(3.246)$$

introduced in Sect. 3.3 is now given by

$$\breve{E}^{N_0 Z_0} = \frac{\oint_{C_n} \oint_{C_p} dz_n dz_p\, z_n^{-N_0-1} z_p^{-Z_0-1} \left\langle \Psi \middle| \Psi(z_n, z_p) \right\rangle \breve{H}(z_n, z_p)}{(2\pi i)^2 \operatorname{res}_{z_n = z_p = 0} z_n^{-N_0-1} z_p^{-Z_0-1} \left\langle \Psi \middle| \Psi(z_n, z_p) \right\rangle},\qquad(3.247)$$

where the Hamiltonian overlap $\breve{H}(z_n, z_p)$ is defined analogously to Eq. (3.200), and the representation (3.240) was used for the projected state in the denominator. If the density-dependence of the interaction is linear, i.e. $\alpha = 1$, the integrand in Eq. (3.247) has additional first order poles wherever the density is singular, and therefore the projected energy is no longer independent of the integration contour, since the result of the integral depends on *the residues of all enclosed poles*. This dependence causes jumps in the projected energy whenever the contour crosses a pole. In principle, one should now minimize the energy with respect to the integration contour as well.

For rational α, the integrand of Eq. (3.200) becomes a multivalued function, and one has to introduce branch cuts in the complex plane. The usual procedure for rational power laws places these roots at the negative real axis, so one has to consider where the transition density becomes real negative. Since the canonical coefficients in Eq. (3.242) are real and positive, the transition density can only be real and negative on the imaginary axis. Furthermore, since its poles on the imaginary axis are of first order, the sign of the $\rho_\tau(z_\tau, \boldsymbol{r})$ changes at a pole, so there has to be a zero *between* two adjacent poles, and this zero and the pole itself are the endpoints of a branch cut (see Fig. 3.1). Matters are complicated by noting that the location of the poles is independent of $\boldsymbol{r}$, but the zeros of the transition densities are not — this becomes particularly relevant for calculations with deformed nuclei, either in constrained mean-field or in GCM calculations.

The discussion of this section has shown that a density-dependent interaction can cause significant trouble in numerical PNP calculations if used recklessly. For forces with a linear density-dependence ($\alpha = 1$), like we are going to use with V_{UCOM} as an approximation for a three-nucleon force, one at least has to check whether the results are stable with respect to the chosen integration contour, e.g., by projecting from several neighboring nuclei. In this context, projection after variation is numerically more stable than the full VAPNP, because in the former the canonical coefficients are already fixed, while they are not in the latter. Thus, the VAPNP probes the z_τ-planes during the iterative procedure, which may lead to oscillations with respect to the pole content of the contour. As indicated above, the VAPNP can be controlled to some extent by modifying the mean particle number of the intrinsic state — if one couples this procedure to the detection of possibly singular canonical coefficients, one can avoid some of the trouble, at least in ground state calculations.

For interactions with rational density-dependence ($\alpha = p/q, p, q \in \mathbb{N}$), one has to face the additional problem of the branch cuts. Since the numerical behavior of complex functions at a cut is determined by the compiler, it is unclear whether one actually integrates over a closed contour at all. One can, in principle, model the contour in such

a fashion that one always stays on the same Riemann sheet, but this requires very fine integration meshes, and likely much effort due to the $\boldsymbol{r}$-dependence of the branch cuts in all calculations where the transition density is still changing. In this work, however, we are going to use forces with $\alpha \neq 1$ only for numerical comparison in PNP calculations.

Chapter 4

HFB Results

In order to test the numerical implementation of the HFB and particle-number projection methods, we perform benchmark calculations using the density-dependent Gogny D1 and D1S interactions (cf. Appendix E.4) and compare them to published results of other groups. The discussion of these results offers the opportunity to highlight the importance of a consistent treatment of all terms in the Hamiltonian, including the Coulomb and kinetic energy contributions. Then, after having grasped the more technical aspects as well as the interplay between the various contributions to the HF and pairing fields, we will proceed to perform calculations with V_{UCOM}.

4.1 Benchmark Calculations

4.1.1 HFB Calculations for the $N = 50$ and $Z = 50$ Chains

As a first test, we have performed plain HFB calculations for the Sn isotopic chain using the Gogny D1 interaction for comparison with the results from the original paper by Dechargé and Gogny [82]. In their calculations, they decompose the intrinsic kinetic energy into a one- and a two-body operator,

$$\mathrm{T}_{\mathrm{int}} = \frac{2}{A} \sum_{i<j} \frac{\mathbf{q}_{ij}}{m} = \frac{1}{2A} \sum_{i<j} \frac{(\mathbf{p}_i - \mathbf{p}_j)^2}{m} = \sum_i \frac{\mathbf{p}_i^2}{2m} \left(1 - \frac{1}{A}\right) - \frac{1}{Am} \sum_{i<j} \mathbf{p}_i \cdot \mathbf{p}_j, \quad (4.1)$$

where m denotes the nucleon mass, and subsequently omit the two-body term — we will indicate the same approximation by using the superscript 'ob' in the following. As in the HF case (cf. Chapter 2), we calculate the HFB ground states for a given set of harmonic oscillator constants a_{HO} and take the minimal energy. In the case of basis sizes of $e_{\max} = 10$ or larger, the a_{HO}-dependence is already weak, causing changes of the order of at most $10 - 100$ keV for the ground-state energies in a plateau region from $a_{\mathrm{HO}} = 1.60$ to 2.0 fm. Although the pairing energy is closely related to the spectral properties of the ground states, we have verified that its a_{HO}-dependence is comparably small. It has to be realized, however, that the $e_{\max} = 10$ basis which is used in the comparisons of this chapter due to the availability of published results may not yet be sufficient to obtain converged pairing energies with respect to the basis size. For this reason, we will use at least $e_{\max} = 12$ and $l_{\max} = 10$ in our calculations with V_{UCOM} later on.
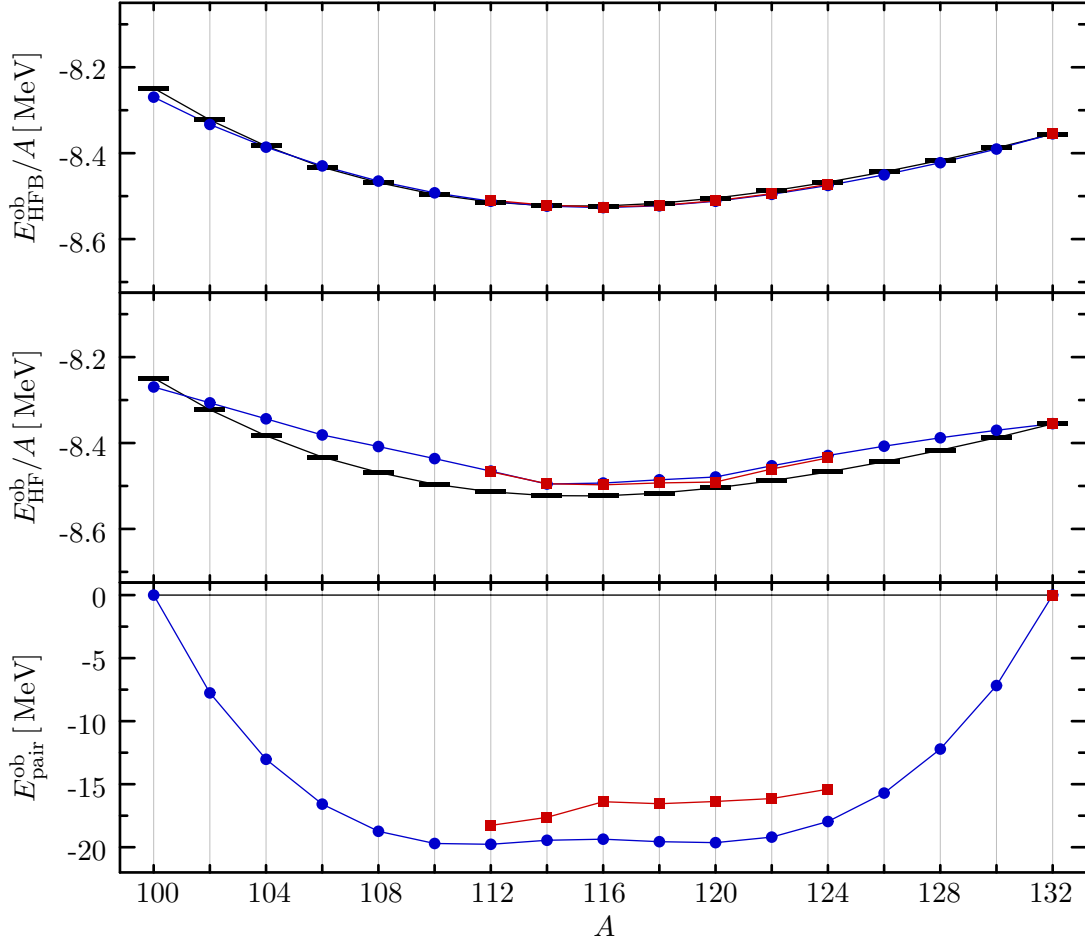
Figure 4.1:   HFB (top) and HF (center) ground-state energies as well as HFB pairing energies (bottom) of the Sn isotopes for the Gogny D1 interaction, calculated with the one-body center-of-mass correction. Comparison of the present implementation (——●——) with results from Ref. [82] (——■——) and experiment (————)($e_{\max} = 10$).

In Fig. 4.1, we compare our Sn ground-state energies from a HFB and a HF calculation with the same code to the results of Ref. [82]; the corresponding numerical values are listed in Tab. 4.1. We obtain a very nice agreement in the HFB case, with a maximum deviation of about 0.3 MeV for ^{124}Sn. In the HF case, the largest deviation is about 1.4 MeV, which still only amounts to a relative difference of about 0.1%. There is, however, a difference in the pairing content of the wavefunctions, as is evident from the pairing energies reported in Fig. 4.1 and Tab. 4.1. After thoroughly checking our HFB code, we can only speculate on the technical reasons for this difference. A likely cause is the tuning of the harmonic oscillator constant in [82] — recall that we are explicitly minimizing the HFB ground-state energy for a fixed set of a_{HO}-values. Other possible differences may be the choice of the integration mesh, or even the numerical accuracy of the employed computers, since the reference is quite dated. Since the pairing energies depend on to the spectral properties of the nucleus around the Fermi energy, it is clear that they are much more sensitive to the details of employed interaction than the binding energy, and therefore to the numerics of the actual implementation. There may also
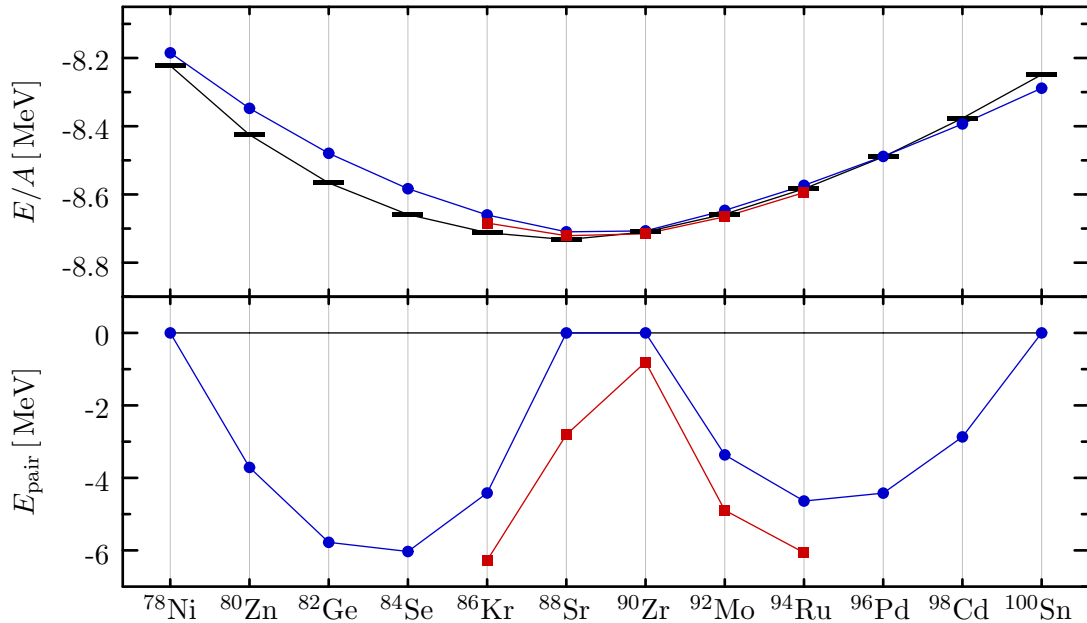
Figure 4.2:   HFB ground-state and pairing energies of $N = 50$ isotones for the Gogny D1S interaction.   Comparison of our present implementation (—●—) with results from Ref. [83] (—■—) and experiment (————)($e_{\max} = 10$).

be a physical component to the deviation, related to the treatment of the center-of-mass motion, as discussed in the next section.

In Fig. 4.2 and Tab. 4.2, we compare HFB results for the $N = 50$ isotones obtained with the Gogny D1S interaction with a more recent publication by Anguiano et al. [83]. As in our approach, the calculations of [83] consistently take *all two-body terms* in the Hamiltonian — NN interaction, intrinsic kinetic energy, and Coulomb interaction — into account when the HF and pairing fields are constructed. While the technical details on the calculation of matrix elements for the interaction and the kinetic energy operators are not specified in the paper, the authors state that they use 11 major oscillator shells (i.e., $e_{\max} = 10$) in a triaxial basis HO expansion whose oscillator lengths are explicitly set to the same values for the calculation of spherical nuclei. Note, however, that this *does not enforce* spherical symmetry throughout every iteration step: spherical nuclei are merely possible results of the energy minimization. Thus, the code used in [83] probes a more complicated energy surface during the iteration, and does not necessarily result in the same energy minimum. Keeping this in mind, we again obtain a very nice agreement of the binding energies, with deviations of 2 MeV or less, i.e., relative differences of 0.25% or better. For the pairing energies, the absolute deviations are of the same size; the largest difference occurs in ^{88}Sr, where the pairing breaks down in our calculation. In light of the aforementioned differences in the codes and the lack of further specifics, we can consider the numerical agreement as well as the reproduction of the systematics satisfactory.

A	E_{exp}	Dechargé & Gogny [82]			this work		
		$E_{\text{HFB}}^{\text{ob}}$	$E_{\text{pair}}^{\text{ob}}$	$E_{\text{HF}}^{\text{ob}}$	$E_{\text{HFB}}^{\text{ob}}$	$E_{\text{pair}}^{\text{ob}}$	$E_{\text{HF}}^{\text{ob}}$
100	−824.879				−826.956	0.00	−826.956
102	−848.905				−849.977	−7.76	−847.261
104	−871.852				−872.142	−13.03	−867.737
106	−893.867				−893.543	−16.58	−888.413
108	−914.588				−914.216	−18.74	−908.087
110	−934.562				−934.155	−19.70	−927.991
112	−953.529	−953.065	−18.27	−948.301	−953.325	−19.77	−948.125
114	−971.571	−971.434	−17.63	−968.403	−971.659	−19.45	−968.489
116	−988.680	−988.939	−16.93	−985.701	−989.101	−19.36	−985.210
118	−1004.951	−1005.553	−16.55	−1002.164	−1005.660	−19.56	−1001.307
120	−1020.544	−1021.310	−16.37	−1018.898	−1021.430	−19.64	−1017.489
122	−1035.528	−1036.295	−16.14	−1032.187	−1036.491	−19.20	−1031.265
124	−1049.962	−1050.605	−15.40	−1045.901	−1050.920	−17.96	−1045.210
126	−1063.888				−1064.764	−15.71	−1059.333
128	−1077.347				−1078.044	−12.21	−1073.644
130	−1090.400				−1090.753	−7.18	−1088.148
132	−1102.917	−1102.772	0.00	−1102.772	−1102.854	0.00	−1102.854

Table 4.1:   HFB ground-state and pairing energies (in MeV) for the Gogny D1 interaction, calculated with the one-body center-of-mass correction. ($e_{\text{max}} = 10$).

Nucleus	E_{exp}	Anguiano et al. [83]		this work	
		E_{HFB}	E_{pair}	E_{HFB}	E_{pair}
^{78}Ni	−641.377			−638.425	0.00
^{80}Zn	−674.012			−667.804	−3.71
^{82}Ge	−702.437			−695.308	−5.78
^{84}Se	−727.341			−720.987	−6.03
^{86}Kr	−749.235	−746.803	−6.28	−744.767	−4.42
^{88}Sr	−768.466	−767.447	−2.81	−766.444	0.00
^{90}Zr	−783.892	−784.373	−0.80	−783.611	0.00
^{92}Mo	−796.508	−797.225	−4.89	−795.494	−3.36
^{94}Ru	−806.849	−807.883	−6.06	−805.896	−4.64
^{96}Pd	−815.034			−814.901	−4.42
^{98}Cd	−820.897			−822.548	−2.87
^{100}Sn	−824.879			−828.853	0.00

Table 4.2:   HFB ground-state and pairing energies (in MeV) of $N = 50$ isotones for the Gogny D1S interaction from fully self-consistent calculations ($e_{\text{max}} = 10$).
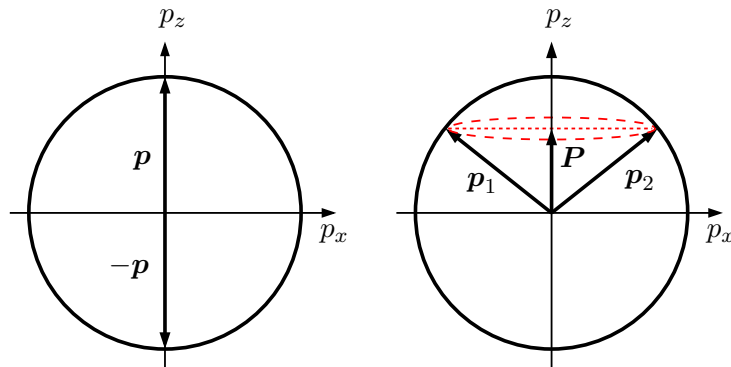
Figure 4.3:   Pairing interaction: phase space for $\boldsymbol{P} = 0$ and $\boldsymbol{P} \neq 0$ (see text).

4.1.2   Intrinsic Kinetic Energy, Coulomb Interaction & Consistency

In the development of the HFB formalism in Chapter 3, we have stressed that a consistent formulation of the HFB approximation starting from a Hamiltonian necessarily means that

(i)   the same interaction is used in the particle-hole and particle-particle channels, and

(ii)   all two-body terms, including the Coulomb interaction and the intrinsic kinetic energy, have to be considered in the construction of the fields.

The latter requirement was found to be particularly important to ensure the cancellation of divergences in projection methods (cf. Sect. 3.4). Setting this technical point aside, it is clear that Coulomb repulsion will counteract the pairing induced by the NN interaction to some extent in a realistic physical situation, and should therefore not be simply omitted.

  The situation is less obvious in the case of the intrinsic kinetic energy. In BCS theory, it is well-known that the formation of Cooper pairs is impeded by a non-vanishing center-of-mass momentum $\boldsymbol{P}$ of the interacting nucleon pair. This can be understood intuitively by considering Fig. 4.3: the pair bound-state results from an infinite number of scattering processes at the Fermi surface of the system, which are mediated by the interaction. For $\boldsymbol{P} = 0$, i.e. $\boldsymbol{p}_1 = -\boldsymbol{p}_2 = \boldsymbol{p}$, the phase space for these processes is the whole Fermi sphere, while only a ring on the sphere, indicated by a red dashed line, is available otherwise[1]. This implies that it is very important to properly separate off the center-of-mass degrees of freedom of the effective or realistic NN interaction already at the two-body level in order to prevent the interaction itself from inducing spurious center-of-mass motion in the many-body state during the scattering processes. In our approach this is achieved by using the intrinsic Hamiltonian H_{int} and carrying out a Talmi transformation for all its components, i.e., intrinsic kinetic energy, Coulomb and NN interaction (cf. Appendix E.1).

---

[1]Note that this means that the pure pairing force explicitly breaks the Galilean invariance of the non-relativistic nuclear Hamiltonian. In nuclear matter, this is of no consequence; in finite nuclei, one would need to project the many-body states on vanishing center-of-mass momentum. In practical applications, the strength of pure pairing forces is usually fit to empirical gaps of the nuclei of interest, which hides the impact of this effect (and other effects) on the pairing properties of the nuclear wavefunction.
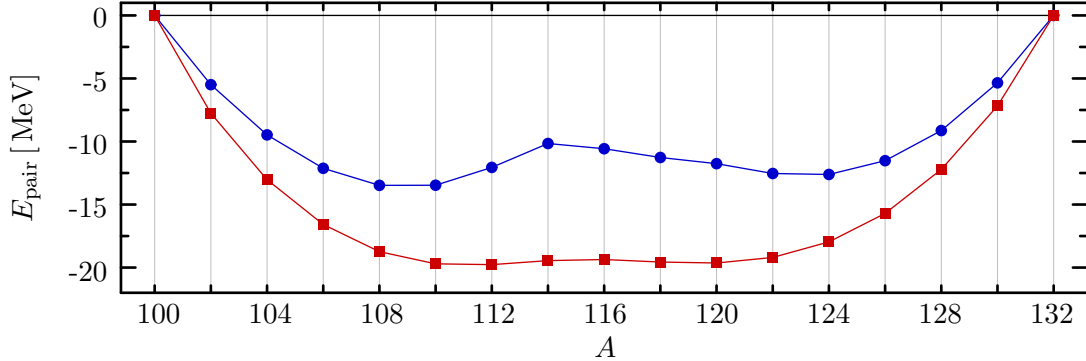
Figure 4.4:   Pairing energies of Sn isotopes for the Gogny D1 interaction and different center-of-mass treatments: full intrinsic kinetic energy (———●———) and one-body approximation (cf. Eq. (4.1) and text) (———■———)($e_{\mathrm{max}} = 10$).

	E^{ob}	E	V^n_{pair}	T^n_{pair}	E^n_{pair}
HFB, one-body approx.	-971.659	-957.213	-19.45	1.62	-17.83
HFB, full kinetic energy	—	-957.793	-11.11	0.95	-10.16
VAP, one-body approx.	-975.622	-963.302	-22.75	1.77	-20.98
VAP, full kinetic energy	—	-963.376	-20.69	1.62	-19.07

Table 4.3:   HFB and VAP ground-state and neutron pairing energies of ^{114}Sn obtained with the one-body approximation and the full intrinsic kinetic energy for Gogny D1 ($e_{\mathrm{max}} = 10$, all values in MeV).

In Fig. 4.4, we demonstrate the impact of the self-consistent inclusion of the intrinsic kinetic energy in the pairing field. Compared to the one-body approximation discussed above, there is a substantial reduction of the pairing energy in the Sn isotopes due to the inclusion of the anti-pairing kinetic energy term in the pairing field, with the strongest effect occurring at the sub-shell closure in ^{114}Sn. As seen more quantitatively in the upper panel of Fig. 4.5, the actual contribution of the kinetic term is of the order of $1 - 2 \, \mathrm{MeV}$, which implies that the reduction of the full pairing energy results from a complex interplay during the iteration procedure.

In Tab. 4.3, we report the ground-state and neutron pairing energies for ^{114}Sn resulting from calculations with the one-body approximation and the full intrinsic kinetic energy. The two datasets can be considered as points on a potential-energy surface emerging from a constrained HFB calculation (see e.g. [21]) with the Hamiltonian

$$\mathrm{H} = \sum_i \frac{\mathbf{p}_i^2}{2m} \left(1 - \frac{1}{A} \right) - \frac{1 - \delta}{Am} \sum_{i<j} \mathbf{p}_i \cdot \mathbf{p}_j + \mathrm{V} \,, \qquad (4.2)$$

for $\delta = 0$ (full intrinsic kinetic energy) and $\delta = 1$ (one-body approximation), respectively. We find that the intrinsic ground-state energies of both states, differ by a mere 580 keV while the corresponding pairing energies differ by more than 7 MeV, i.e., the competition between the particle-hole and particle-particle channels can produce energetically similar ground states with significantly different pairing properties. Keep in mind, however, that the HFB approximation is just the simplest approach to the description of superfluidity in the nucleus — as we can also see in Tab. 4.3, the binding and pairing energies
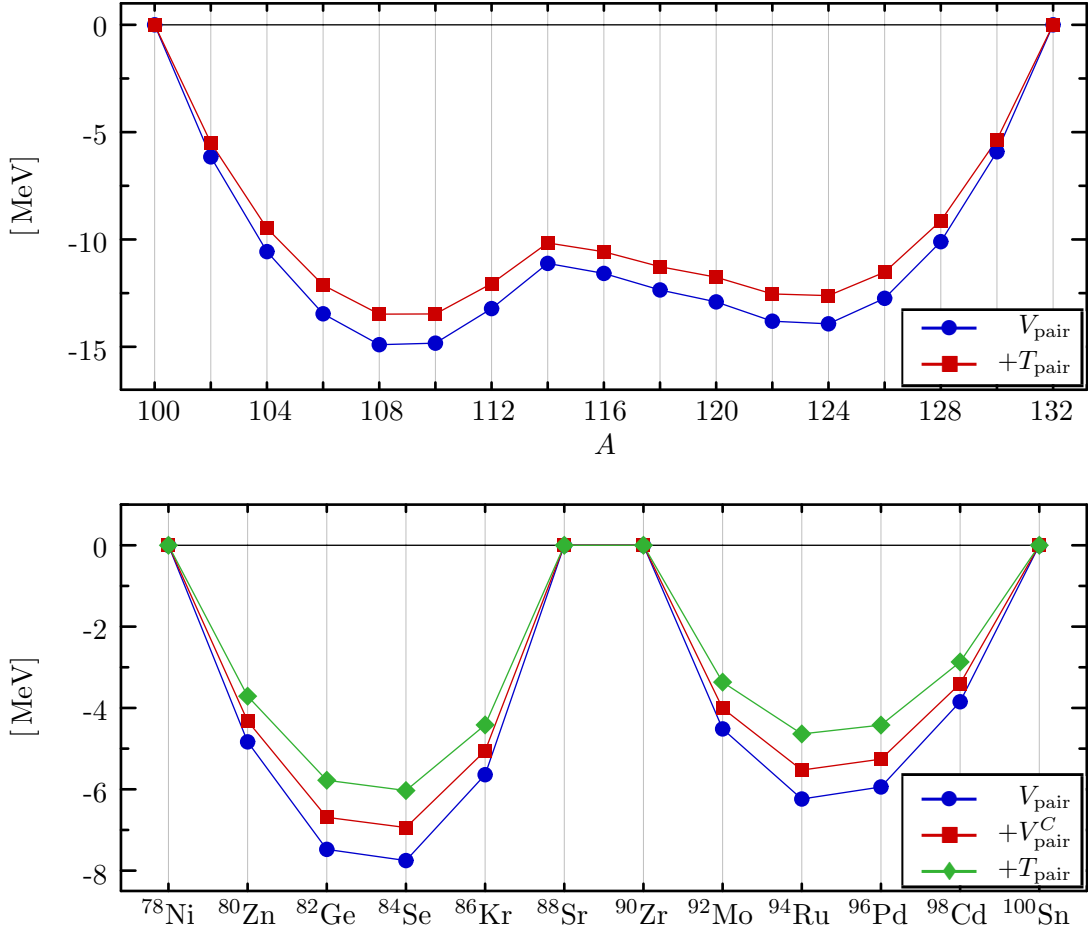
Figure 4.5: Contributions to the pairing energy in Sn isotopes (Gogny D1, top), and $N = 50$ isotones (Gogny D1S, bottom) for $e_{\max} = 10$.

become more similar in a VAP calculation, which takes additional pairing correlations into account, and even then it is not certain whether other physically relevant effects like the coupling of the nucleons to surface vibrations (see e.g. [109]) are taken into account properly by the improved many-body Hilbert space.

For the implementation, the apparent flatness of the potential energy surface of the Hamiltonian (4.2) confirms that the minimization procedure is quite sensitive to the details of the implementation of the kinetic energy, as argued above. Moreover, the calculation shows that the use of the one-body approximation alone neglects a significant repulsive energy contribution: at the very least, the full intrinsic kinetic energy has to be considered perturbatively for the converged results, which has not always been done in past applications of the HFB method (see also the discussion in [83]). From the T_{pair}^{n} values presented in Tab. 4.3, we can see that such a perturbative inclusion is not sufficient to remove the pairing-energy differences in a plain HFB calculation as shown in Fig. 4.4.

Since there is no proton pairing in the Sn isotopes due to the $Z = 50$ major-shell closure, we show the decomposition of E_{pair} for the $N = 50$ isotones in the lower panel
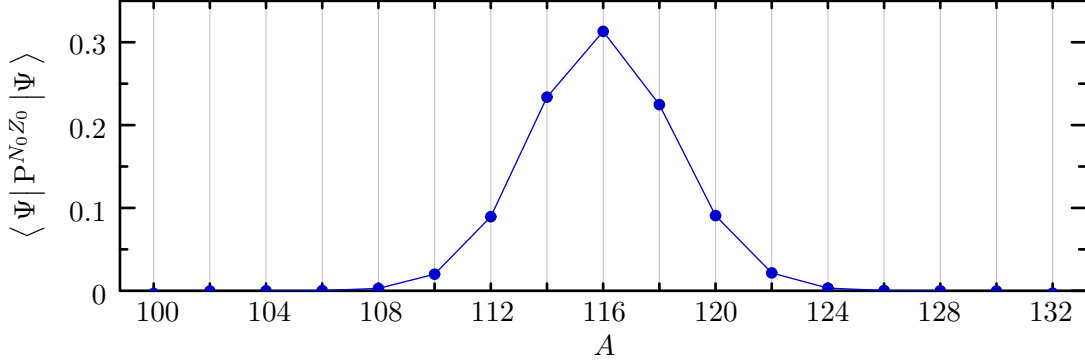
Figure 4.6:   Overlap of ^{116}Sn with other Sn isotopes from a projection after variation with Gogny D1 ($e_{\max} = 10$).

of Fig. 4.5 to assess the size of the anti-pairing effect of the Coulomb interaction. We find contributions of up to 810 keV in ^{84}Se, which are comparable in magnitude to the kinetic energy contributions in these nuclei.

4.1.3   Particle-Number Projection

We now consider the particle-number projection approaches introduced in Chapter 3. A stringent test for the calculation of overlaps is the exhaustion of the HFB sum rules for the overlaps and energies. Since the quasiparticle vacuum can be expanded in states with sharp particle numbers,

$$\left| \Psi \right\rangle = \sum_{N,Z=0}^{\infty} \left| \Psi_{NZ} \right\rangle \left\langle \Psi_{NZ} | \Psi \right\rangle, \tag{4.3}$$

where

$$\left| \Psi_{NZ} \right\rangle \equiv \frac{1}{\sqrt{\left\langle \Psi \right| \mathrm{P}^{NZ} \left| \Psi \right\rangle}} \mathrm{P}^{NZ} \left| \Psi \right\rangle, \quad \left\langle \Psi_{NZ} | \Psi_{N'Z'} \right\rangle = \delta_{NN'} \delta_{ZZ'}, \tag{4.4}$$

we have the conditions

$$\left\langle \Psi | \Psi \right\rangle = \sum_{N,Z} \left\langle \Psi \right| \mathrm{P}^{NZ} \left| \Psi \right\rangle = 1 \tag{4.5}$$

and

$$E = \sum_{N,Z} \left\langle \Psi \right| \mathrm{P}^{NZ} \left| \Psi \right\rangle E^{NZ}, \tag{4.6}$$

where E and E^{NZ} are the unprojected and projected energies, respectively. In Fig. 4.6, we show the overlaps obtained from projection after variation of the HFB ground state of ^{116}Sn (PAV). The HFB ground state contains non-negligible contributions of wavefunctions with up to $\Delta N = \pm 8$, which already exhaust 99.6% of the norm sum rule, and summing over the Sn chain yields near-perfect agreement. The energy sum rule is satisfied equally well.
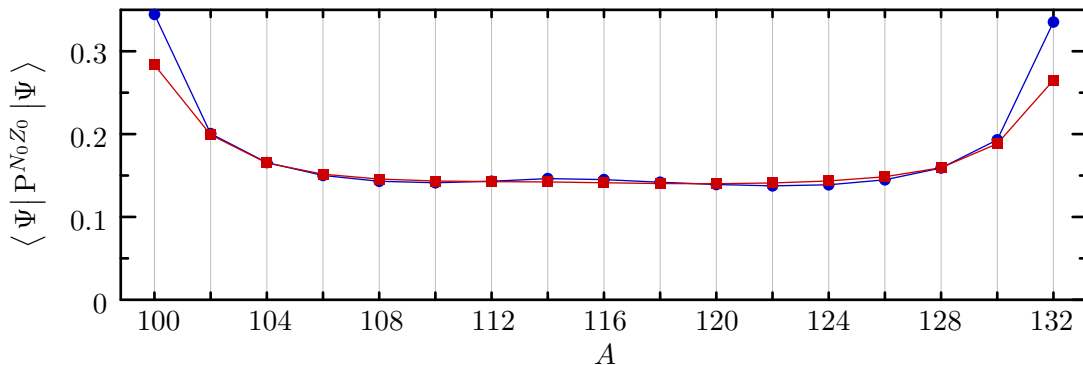
Figure 4.7: Overlaps of Sn isotopes from VAP (——●——) and PLN (——■——) calculations with Gogny D1 ($e_{max} = 10$).

In Fig. 4.7, we show overlaps resulting from full variation after projection (VAP), as well as Lipkin-Nogami with subsequent projection after the variation (PLN). In the full VAP calculation, all but the wavefunction component with the desired particle numbers are discarded, hence we only show the overlap obtained if each nucleus is projected onto its own proton and neutron number. Typically, this is the largest overlap in the particle-number distribution, unless there is near-degeneracy with the $\Delta A = \pm 2$ states. Note that there is both proton and neutron pairing in the PLN and VAP calculations, i.e., the particle-number distribution is spread in the N and Z directions. Thus, the overlap, defined as the product of the neutron and proton overlaps is reduced in size compared to the HFB case shown in Fig. 4.6: in the mid-shell region, typical values for the neutron and proton overlaps are about 0.3 and 0.5, respectively.

The size of the overlap is an indirect measure for the shape of the particle-number distribution: in the mid-shell region, the overlap is about 0.15 for all isotopes, which implies a rather wide distribution with sizable particle-number fluctuations. Near the shell closures, the overlap increases rapidly to about 0.35, and the particle-number distribution becomes narrow, which is in line with the results discussed in [110]. Note, however, that the overlap is not even close to 1 at the shell closure, as would be expected from projection after variation of a plain HFB solution where the pairing breaks down. Since the full VAP procedure is equivalent to diagonalizing the Hamiltonian in a basis of gauge-rotated quasiparticle Slater determinants, the resulting ground state is a superposition of Slater determinants and therefore able to describe pairing correlations beyond the simple independent-quasiparticle approximation of HFB. These types of pairing correlations are referred to as *dynamical pairing correlations*, as opposed to the *static pairing correlations* described by standard HFB.

As far as approximations to the full VAP are concerned, we find that the projected Lipkin-Nogami solution provides overlaps which are very similar to the VAP, aside from a larger discrepancy at the shell closure. This behavior is reflected in the deviations of the ground-state energies obtained in approximate PNP from the VAP results, as shown in Fig. 4.8. The agreement of PLN with the exact VAP is typically better than 1 MeV, except for a slightly larger deviation at the shell closure. Despite being non-variational, the unprojected Lipkin-Nogami approach (LN) gives the next best approximation in the mid-shell range, but produces a sharper increase at the shell closures. If we look at
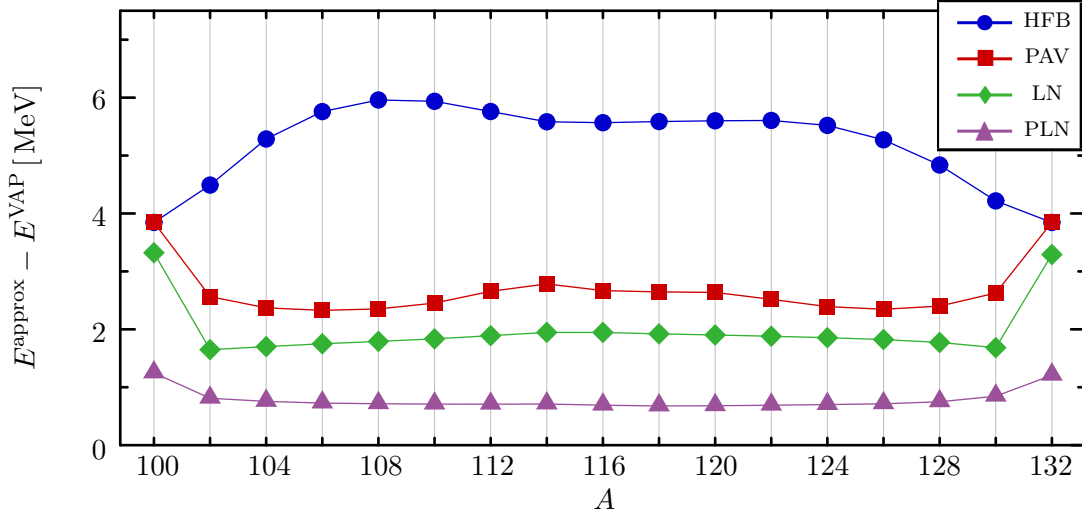
Figure 4.8:   Deviation of ground-state energies of Sn isotopes in various approximate PNP methods from exact VAP results, calculated with the Gogny D1 interaction ($e_{\mathrm{max}} = 10$).

the Lipkin-Nogami coefficients (cf. Sect. 3.2.3)

$$h_2^n = \frac{\langle(\mathrm{H} - \langle\,\mathrm{H}\,\rangle)\Delta\mathrm{N}^2\,\rangle - \langle\,\mathrm{H}\Delta\mathrm{N}\,\rangle\langle\,\Delta\mathrm{N}^3\,\rangle/\langle\,\Delta\mathrm{N}^2\,\rangle}{\langle\,\Delta\mathrm{N}^4\,\rangle - \langle\,\Delta\mathrm{N}^2\,\rangle^2 - \langle\,\Delta\mathrm{N}^3\,\rangle^2/\langle\,\Delta\mathrm{N}^2\,\rangle}, \tag{4.7}$$

and

$$h_2^p = \frac{\langle(\mathrm{H} - \langle\,\mathrm{H}\,\rangle)\Delta\mathrm{Z}^2\,\rangle - \langle\,\mathrm{H}\Delta\mathrm{Z}\,\rangle\langle\,\Delta\mathrm{Z}^3\,\rangle/\langle\,\Delta\mathrm{Z}^2\,\rangle}{\langle\,\Delta\mathrm{Z}^4\,\rangle - \langle\,\Delta\mathrm{Z}^2\,\rangle^2 - \langle\,\Delta\mathrm{Z}^3\,\rangle^2/\langle\,\Delta\mathrm{Z}^2\,\rangle}, \tag{4.8}$$

we can see that the expansion of the projected energy may become ill-defined in the weak-pairing regime, were all of the particle number fluctuation terms become small or even vanish (keep in mind, however, that we are dealing with an approximately projected state, i.e., some of the correlations of the full VAP are taken into account). While it is not fully understood why the Lipkin-Nogami method does not break down completely in these cases (see [72, 73]), the corresponding LN as well PLN results have to be considered unreliable.

The observed deviations of the approximately projected ground-state energies from the VAP energy closely match the results of Anguiano et al. [110], which are shown in Fig. 4.9, both qualitatively and quantitatively. The exception is the plain HFB approximation, where the inflection of the curves in the Figs. 4.8 and 4.9 is just reversed — keep in mind, though, that this is a discrepancy of the order of a few MeV, which is very small compared to the binding energies of the Sn isotopes. As discussed in Sect. 4.1.2, the treatment of the intrinsic kinetic energy can have a notable impact on the pairing content of the many-body wavefunction and the balance of particle-hole and particle-particle contributions to the ground-state energy at the HFB level. While the framework of Ref. [110] included both the one- and two-body terms of the intrinsic kinetic energy, there are explicit differences in the implementation, like the use of triaxial HO states with equal oscillator lengths for the spherical case compared to
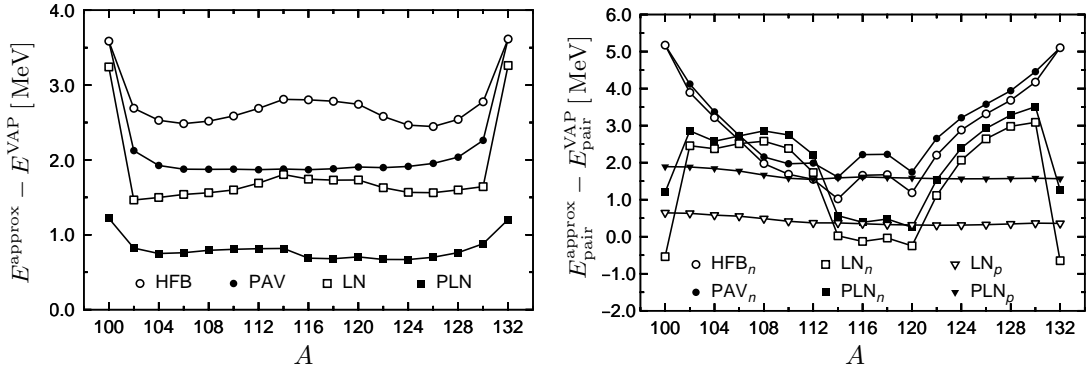
Figure 4.9: Deviation of ground-state (left) and pairing energies (right) of the Sn isotopes for HFB and different approximate PNP methods from VAP results. Calculations were done with the Gogny D1 interaction; figures were taken from [110].

our spherical HO states and the use of the projected-density rather than the mixed-density prescription for the density-dependent interaction term as in our case (see the discussion in Sect. 3.3.3). Since the agreement between both approaches improves with the sophistication of the many-body method, i.e., as the details of the single-particle basis become less important, we conclude that the discrepancy in the HFB results is indeed caused by the choice of single-particle states and/or further calculational details which are not given, and therefore not problematic.

To conclude this section, we show the neutron and proton pairing energies resulting from our calculations in Fig. 4.10; the corresponding results from [110] are displayed in Fig. 4.11. At the HFB level, we observe the discrepancy which was discussed extensively before, but for the (P)LN and VAP approaches, we obtain a satisfactory agreement. In the Lipkin-Nogami approach, the mixed-density prescription yields pairing energies which are about $2-3$ MeV larger than those obtained with the projected-density prescription in the $A = 150$ region (cf. Fig. 7 of [77]). Furthermore, we separate the Lipkin-Nogami corrections to the particle-hole and particle-particle contributions of the energy, while the entire Lipkin-Nogami correction is added to the HF part of the energy in Ref. [110], and therefore not included in Fig. 4.11. This typically *reduces* the LN pairing energy by $1-2$ MeV, and therefore counteracts the effect of using the mixed density prescription. If we also allow for some overestimation of the pairing energy in the LN method, it seems reasonable to expect an additional $1-2$ MeV of pairing energy in our VAP calculations as well.

The HFB pairing energy exhibits a distinctive drop at $N = 64$, which coincides with the closure of the $1d_{5/2}$ sub-shell in a simple single-particle shell-model picture. In Fig. 4.12, we display the coefficients v_μ^2 of the special Bogoliubov transformation (cf. Sect. 3.1.3) which correspond to the (normalized) fractional occupation of the the canonical basis states near the Fermi surface, and we indeed see that the $0g_{7/2}$ and $1d_{5/2}$ states, which dominate the pairing in the lower half of the shell, are almost filled at $N = 64$, and therefore unable to participate any further. In comparison, the phase space offered by the next two levels — $1d_{3/2}$ and $2s_{1/2}$ is rather limited, and pairing with the $0h_{11/2}$ states is not yet favorable. In the Lipkin-Nogami approach, also shown in Fig. 4.12, the filling of the shells occurs more gradually, thereby preventing a sudden limitation of the phase space for pairing as in the plain HFB case. Consequently, the double-peak
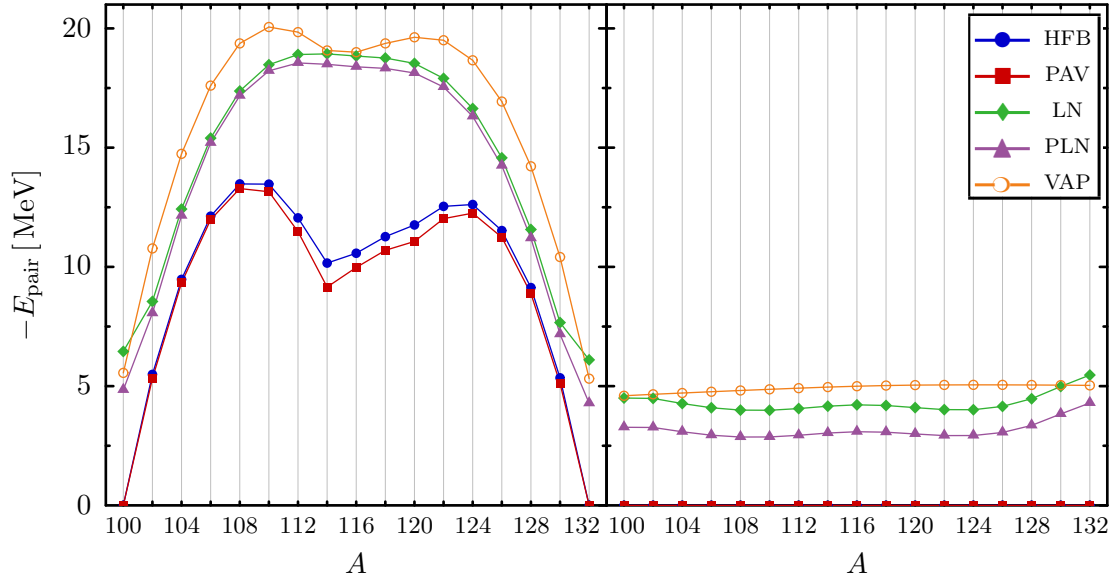
Figure 4.10: Neutron (left) and proton (right) pairing energies of the Sn isotopes for the Gogny D1 interaction ($e_{\max} = 10$).
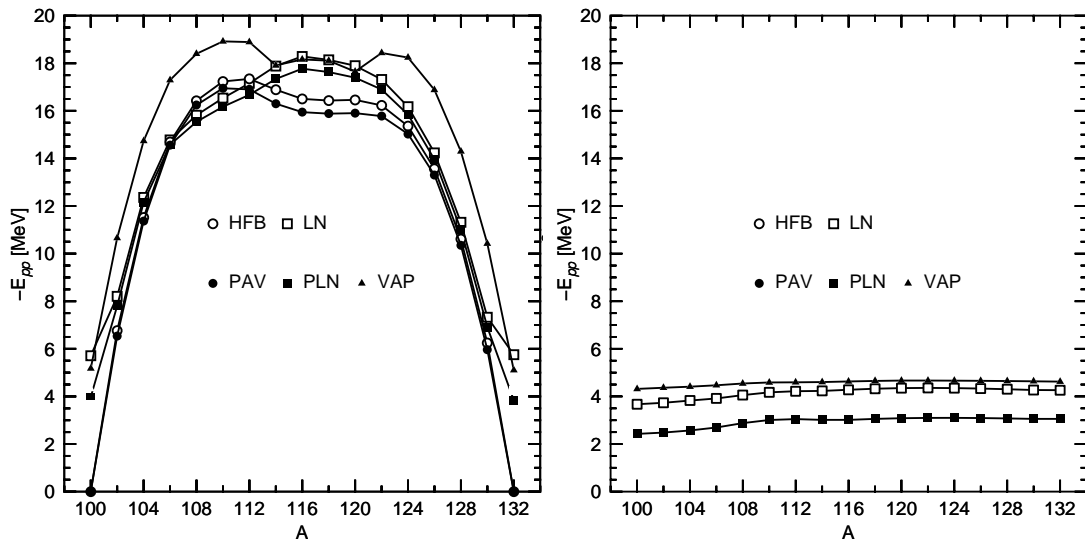

Figure 4.11: Neutron (left) and proton pairing energies (right) of Sn isotopes for the Gogny D1 interaction in various approaches to PNP. Figures taken from [110].
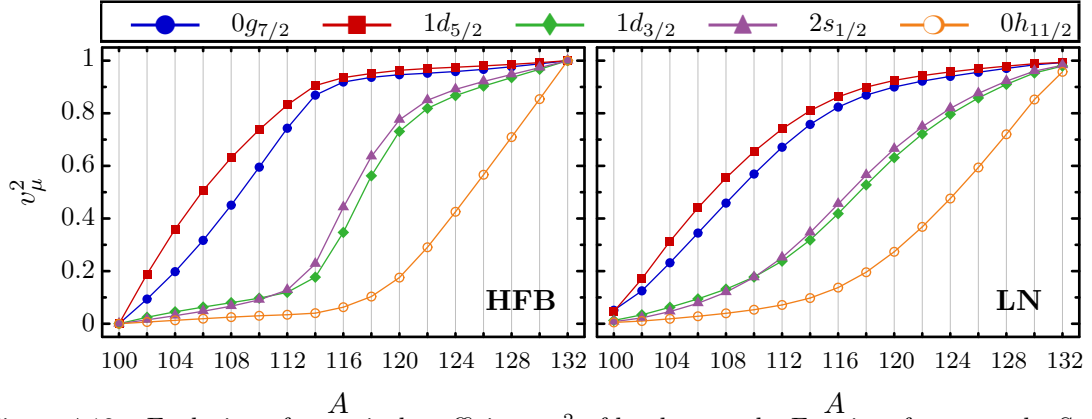
Figure 4.12: Evolution of canonical coefficients v_μ^2 of levels near the Fermi surface over the Sn isotopic chain (Gogny D1, $e_{\max} = 10$).

structure in the pairing energy is replaced by a single peak in the LN approach. For the PAV, PLN, and VAP methods, the invariance of the projected energy and other relevant observables with respect to the choice of the intrinsic state implies that the canonical coefficients of the intrinsic state are merely parameters which cannot yield physically relevant information on the projected ground state (cf. Sect. 3.2.2 and 3.4).

At the major-shell closures, the LN method overestimates the pairing in comparison to the VAP approach. As explained above, this signals a possible breakdown of the Lipkin-Nogami expansion of the energy. Although particle-number fluctuations are not completely suppressed at $N = 64$, it is possible that the increase of the pairing energy in ^{114}Sn is to some extent artificial. This assumption is backed by the full VAP result, where the double-peak shape re-emerges, although the drop in the pairing energy is not as severe as in the plain HFB calculation.

For the projection after variation methods, i.e., PAV and PLN, the pairing energy is slightly lowered. For the PAV approach, the effect is largest in the mid-shell region near $N = 64$. At the major shell closures, the PAV approach cannot increase the pairing energy because it is contingent on the existence of static pairing in the HFB ground state in the first place. This is easily understood by considering the expression for the overlap in the canonical basis that was derived in Sect. 3.2.2:

$$x(\phi_n, \phi_p) = e^{-i(\phi_n N_0 + \phi_p Z_0)} \prod_\tau \prod_{\mu > 0} \left(u_{\tau\mu}^2 + v_{\tau\mu}^2 e^{2i\phi_\tau} \right), \qquad (4.9)$$

where τ labels the isospin of the nucleons. In HFB, the state reduces to the HF limit at the major shell closure, and the coefficients v_μ^2 are either 1 for occupied or 0 for unoccupied levels (see Fig. 4.12), with the corresponding u_μ^2 given by

$$u_\mu^2 = 1 - v_\mu^2 \qquad (4.10)$$

due to the normalization condition. Thus, the overlap contains product terms which are zero and vanishes identically. In contrast, Fig. 4.12 reveals that the LN method yields non-zero v_μ^2 for the $0g_{7/2}$ and $1d_{5/2}$ states at $N = 50$ and the $0h_{11/2}$ state at $N = 82$, respectively, and the PNP overlap does not vanish. The reduction by projection after variation in the PLN approach can then correct for the overestimation of the pairing energy in the standard LN method.

The proton pairing energies shown in Fig. 4.10 nicely support the previous discussion. While the HFB and PAV methods do not yield any proton pairing at all, there is a sizable energy contribution in the (P)LN and VAP approaches from the inclusion of dynamical pairing correlations, despite the $Z = 50$ shell closure. Contrary to the neutron case, the LN proton pairing energy does not overshoot the VAP result, except at $N = 82$. We also note that the LN and PLN methods exhibit a more pronounced N-dependence than the results of Ref. [110] (cf. Fig. 4.10). Since we have not taken pn-pairing into account in our approach, this dependence has to result from small rearrangements of the nucleons due to the particle-hole part of the interaction, leading to small modifications of the coordinate-space density. Due to our use of the mixed-density rather than the projected-density prescription of Ref. [110] for the density-dependent part of the interaction (cf. Sect. 3.3.3), the more pronounced isotopic variations are to be expected.

4.2   Pairing with V_{UCOM}

We now carry out HFB and PNP calculations with V_{UCOM}. From our experience with the HF results of Chapter 2, we can already expect that the spreading of single-particle spectra and the low-level density near the Fermi level will impede the formation of static pairing in the HFB groundstate. Analogous observations have been made by various authors in the study of nuclear matter based on realistic NN interactions. In this setting, a static pairing phase is characterized by the BCS pairing gap Δ_{BCS}. While Δ_{BCS} is well-constrained by the phase shifts of the attractive $^1S_0$ and $^3P_2$ partial waves of the NN interaction, as well as the Fermi momentum at the saturation point [19, 111], more refined treatments of ground-state correlations as in the Self-Consistent Green's Function method [112], lead to a significant reduction of the pairing gaps from realistic NN interactions due to the redistribution of single-particle strength.

As shown in our benchmark calculations, dynamical pairing correlations associated with the finite size of a nucleus have a sizable impact on the pairing properties. The impact of the explicit treatment of short-range correlations on the dynamical pairing correlations included via the PNP approaches is not obvious, and the author is not aware of any existing studies of this subject. The effective forces used to describe pairing in finite nuclei, either in the shell-model or self-consistent mean-field calculations, always contain phenomenological input on the single-particle and pairing strengths to a significant degree, and while this allows for a good description of phenomena associated with nuclear superfluidity, the connection to the underlying 'fundamental' NN interaction is hidden completely.

4.2.1   Optimized Two-Body V_{UCOM}

We start our investigation with the optimized two-body V_{UCOM} interaction ($I_\vartheta^{(1,0)} = 0.09\,\text{fm}^3, I_\vartheta^{(1,1)} = 0\,\text{fm}^3$). As seen in Fig. 4.13, the energy gain of the Sn isotopes by switching from HF to HFB is very small in the case of V_{UCOM} — indeed, apart from the region between $N = 58$ and $N = 70$, the HFB solutions collapse onto the plain HF solutions. PNP methods increase the binding energy by $2 - 3$ MeV by including dynamical pairing correlations, which is about half the size of the results obtained for
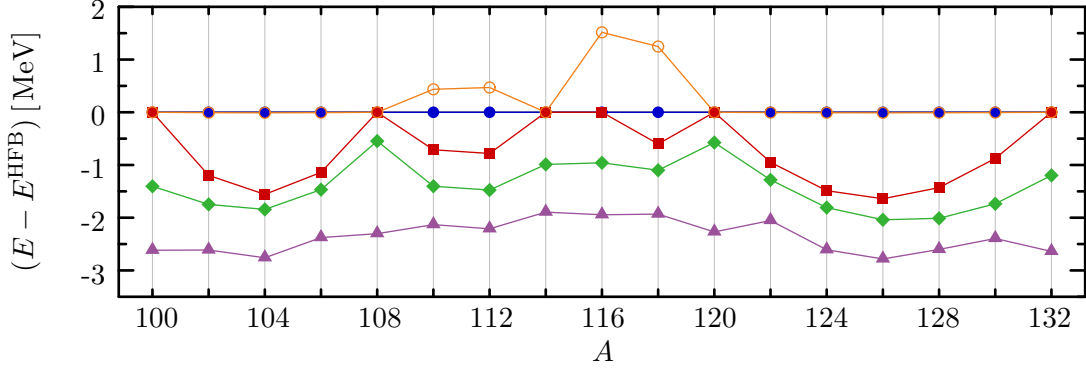
Figure 4.13: Energy gain from PNP (bottom) of the Sn isotopes for V_{UCOM} with $I_\vartheta^{(1,0)} = 0.09\,\mathrm{fm}^3, I_\vartheta^{(1,1)} = 0\,\mathrm{fm}^3$. Comparison of HFB (—●—), PAV (—■—), PLN (—◆—), and VAP (—▲—)($e_{\mathrm{max}} = 12, l_{\mathrm{max}} = 10$). The energy difference of the HF and HFB ground states is included as well (—○—).
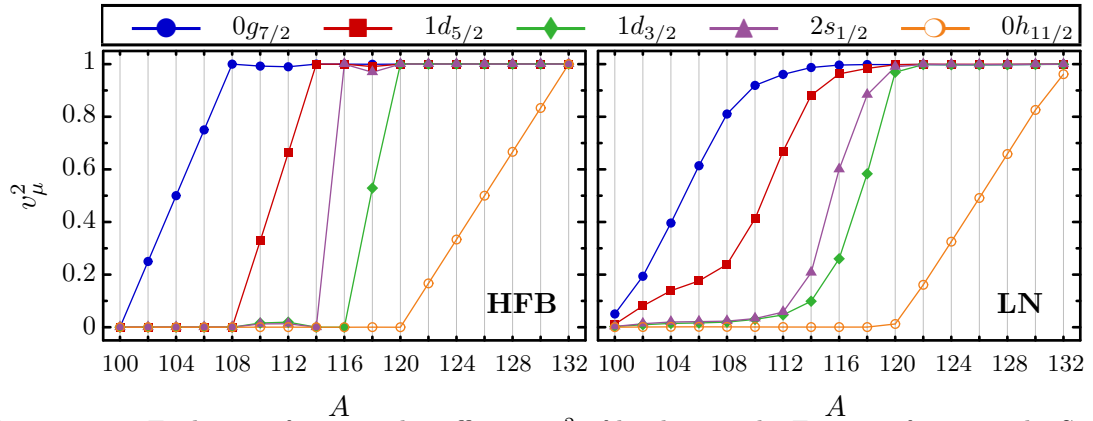
Figure 4.14: Evolution of canonical coefficients v_μ^2 of levels near the Fermi surface over the Sn isotopic chain ($V_{\mathrm{UCOM}}, I_\vartheta^{(1,0)} = 0.09\,\mathrm{fm}^3, I_\vartheta^{(1,1)} = 0\,\mathrm{fm}^3, e_{\mathrm{max}} = 12, l_{\mathrm{max}} = 10$).

Gogny D1 (cf. Fig. 4.8). The hierarchy of the approximations is the same as observed in our benchmark calculations i.e., PAV, PLN, and VAP successively improve the ground-state energy.

The structure of the energy gain from PAV exhibits a very distinctive structure, which matches the closure of sub-shells in the major shell from $N = 50$ to $N = 82$. The canonical coefficients v_μ^2 which are shown in Fig. 4.14 confirm this observation. Rather than a smooth, gradual filling of the shells, the occupation of the shells increases abruptly with every added neutron over the isotopic chain, as in the HF case. Only the $1d_{3/2}$ and $2s_{1/2}$ shells show small indications of pairing in the regions where the HFB solution gains a few MeV of additional binding compared to the HF case. As noted in Sect. 4.1.3, the Lipkin-Nogami approximation slightly smoothens the filling and allows for some pairing, which can then be enhanced by the projection after variation in the PLN approach.

In our HF calculations in Chapter 2, we have observed that V_{UCOM} single-particle spectra exhibit a low level density, which serves as an impediment for pairing. Nevertheless, the complete lack of pairing contributions from the $0g_{7/2}$ and $0h_{11/2}$ shells is surprising, because the spreading of the spectra does not prevent the nucleons *within* the
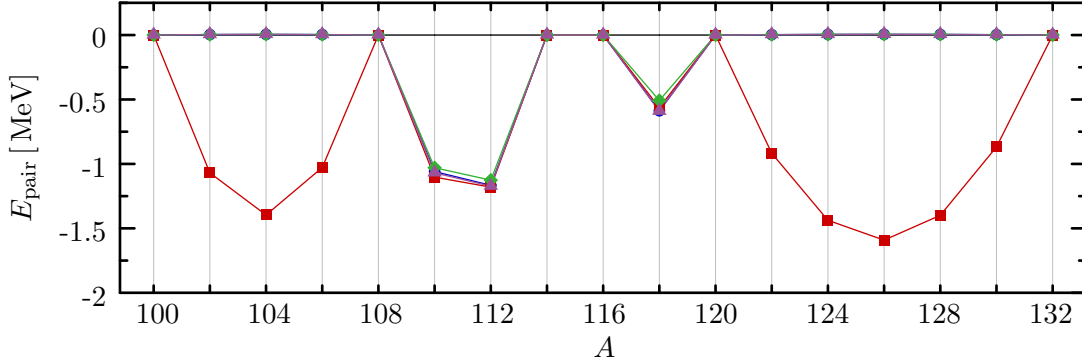
Figure 4.15:   HFB pairing energies of the Sn isotopes for V_{UCOM} with $I_\vartheta^{(1,0)} = 0.09$ fm^3, $I_\vartheta^{(1,1)} = 0$ fm^3. The curves indicate the partial waves of the interaction used in the pairing channel: all (——●——), (S) (——■——), (S,P) (——◆——), and (S,P,D) (——▲——).

same j-sub-shell from pairing, as proven even in simple calculations with a schematic single-j-shell Hamiltonian and a pure pairing force (see e.g. [71]). It is interesting to note, however, that only the sub-shells with the *highest* possible angular momenta seem to be affected, which suggests that an angular momentum-dependent component of the interaction causes the pairing breakdown.

To test this hypothesis, we have performed HFB calculations where all but the lowest partial waves of V_{UCOM} were discarded in the pairing channel. The pairing energies resulting from these calculations are shown in Fig. 4.15. If we only include the relative S-waves (of which only $^1S_0$ contributes in like-particle pairing), we indeed obtain pairing in every subshell. As soon as the relative P-waves are present, the pairing breaks down in the $0g_{7/2}$ and $0h_{11/2}$ shells. This is somewhat contrary to expectations, since the attractive $^3P_2$ partial wave (cf. Sect. 1.3) should actually provide *additional* pairing from naive considerations (see [19]). The further inclusion of the D-waves has a negligible effect, as is evident from the similarity with the results obtained with the unrestricted V_{UCOM}.

Referring to the operators appearing in the correlated interaction (cf. Sect. 1.1.4),

$$\Big\{ \mathbb{1},\ \boldsymbol{\sigma}_1 \cdot \boldsymbol{\sigma}_2,\ \mathrm{q}_r^2,\ \mathrm{q}_r^2 \boldsymbol{\sigma}_1 \cdot \boldsymbol{\sigma}_2,\ \mathbf{l}^2,\ \mathbf{l}^2 \boldsymbol{\sigma}_1 \cdot \boldsymbol{\sigma}_2, \mathbf{l} \cdot \mathbf{s},\ \mathrm{s}_{12}(\hat{\mathbf{r}}, \hat{\mathbf{r}}),\ \mathrm{s}_{12}(\mathbf{l}, \mathbf{l}), $$
$$\bar{\mathrm{s}}_{12}(\mathbf{q}_\Omega, \mathbf{q}_\Omega),\ \mathbf{l}^2 \mathbf{l} \cdot \mathbf{s},\ \mathrm{q}_r \mathrm{s}_{12}(\mathbf{r}, \mathbf{q}_\Omega),\ \mathbf{l}^2 \bar{\mathrm{s}}_{12}(\mathbf{q}_\Omega, \mathbf{q}_\Omega), \ldots \Big\} \otimes \{1,\ \boldsymbol{\tau}_1 \cdot \boldsymbol{\tau}_2\}\ , \qquad (4.11)$$

there are only a few possible sources for this effect: the non-local tensor operators like $\bar{\mathrm{s}}_{12}(\mathbf{q}_\Omega, \mathbf{q}_\Omega)$ are off-diagonal in the relative angular momentum and therefore unable to contribute to the energy in mean-field type calculations, which leaves $\mathbf{l}^2, \mathbf{l} \cdot \mathbf{s}, \mathbf{l}^2 \mathbf{l} \cdot \mathbf{s}, \mathrm{s}_{12}(\hat{\mathbf{r}}, \hat{\mathbf{r}})$ and $\mathrm{s}_{12}(\mathbf{l}, \mathbf{l})$ (corresponding to a $(\mathbf{l} \cdot \mathbf{s})^2$-type interaction, see Appendix A.3). Since all of these operators except $\mathbf{l}^2$ affect the spin-orbit splittings and we found no significant defects in the spin-orbit structure of the correlated interaction in our HF calculations (see [10] and Chapter 2) the $\mathbf{l}^2$ component of V_{UCOM} appears to be the main cause for the breakdown of the pairing, especially since this particular type of angular momentum-dependent interaction is not included in the usual Gogny or Skyrme-type interactions.

The angular momentum-dependent suppression of the pairing is *not caused* by the well-known Coriolis anti-pairing effect leading to the breaking of pairs in a collective rotor model for deformed nuclei (see [21]), because our calculations are strictly spherically
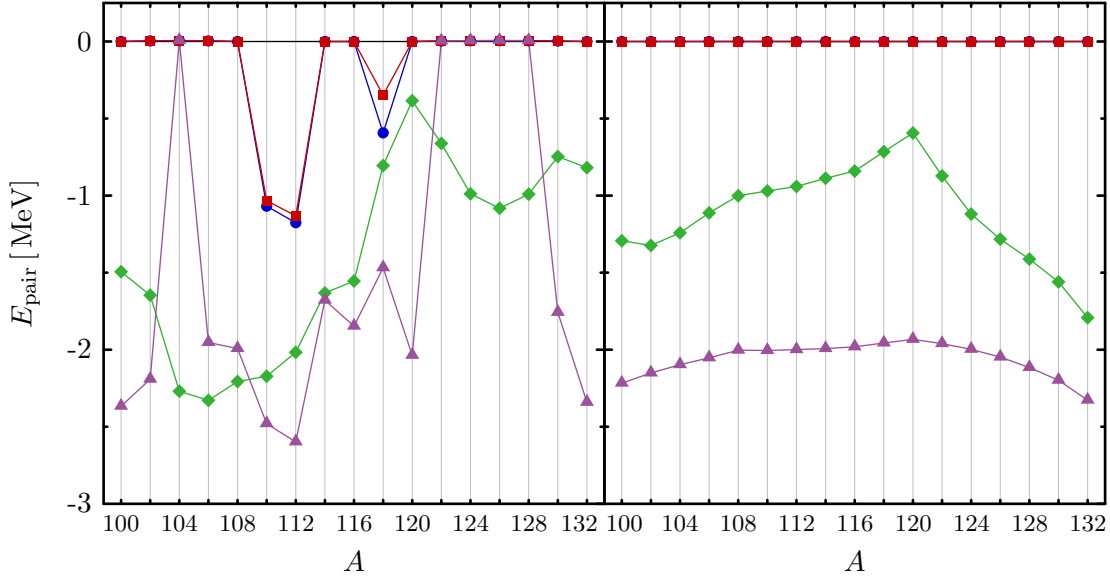
Figure 4.16: Neutron (left) and proton pairing energies (right) of the Sn isotopes for V_{UCOM} with $I_\vartheta^{(1,0)} = 0.09$ fm^3, $I_\vartheta^{(1,1)} = 0$ fm^3. Comparison of HFB (——●——), PAV (——■——), PLN (——◆——), and VAP (——▲——) ($e_{\max} = 12, l_{\max} = 10$).

symmetric. We also stress that the restriction of V_{UCOM} to the relative $^1S_0$ wave in the particle-particle channel is *not a viable prescription* for future calculations, because the inconsistency in the treatment of the interaction makes the projection techniques discussed in 3.2.2 ill-defined.

In Fig. 4.16, we illustrate the effect of the various PNP methods on the pairing energies. Compared to the results for the Gogny interaction, the neutron pairing energies are significantly smaller — keep in mind, however, that the pairing energies are not observable, and a wide range of about $10 - 20$ MeV is quoted in the literature for (spherical) HFB calculations with different effective interactions, see e.g. [113]. The results from plain HFB are in line with our observations for the ground-state energies. There is a complete breakdown of static pairing except in the mid-shell region, and the bounds of vanishing pairing energy coincide with sub-shell closures. PAV is unable to significantly increase the pairing energy, but PLN and VAP yield a notable improvement from the inclusion of dynamical pairing correlations. As discussed in Sects. 2.1.4 and 2.1.5, the shift of the $\nu 0h_{11/2}$ sub-shell caused by V_{UCOM} leads to an unrealistic major-shell closure at $N = 70$, whose signature is still visible in the PLN results.

For the proton pairing energies, V_{UCOM} yields about half the size of the Gogny results. While the PLN pairing energy shows a distinct isotopic dependence, in particular at the additional $N = 70$ major-shell closure, the VAP pairing energy curve is rather flat over the Sn chain.

The breakdown of neutron pairing in the VAP approach for $N = 54$ and $N = 72 - 78$ is a strong indication in favor of our hypothesis regarding an angular momentum-related suppression from above, because our benchmark calculations with Gogny D1 have always led to non-vanishing VAP pairing energies, regardless of shell closures. To rule out a numerical reason, we have checked the convergence with basis size, as well as carried out the projection with varying number of mesh points for the gauge-angle integration,
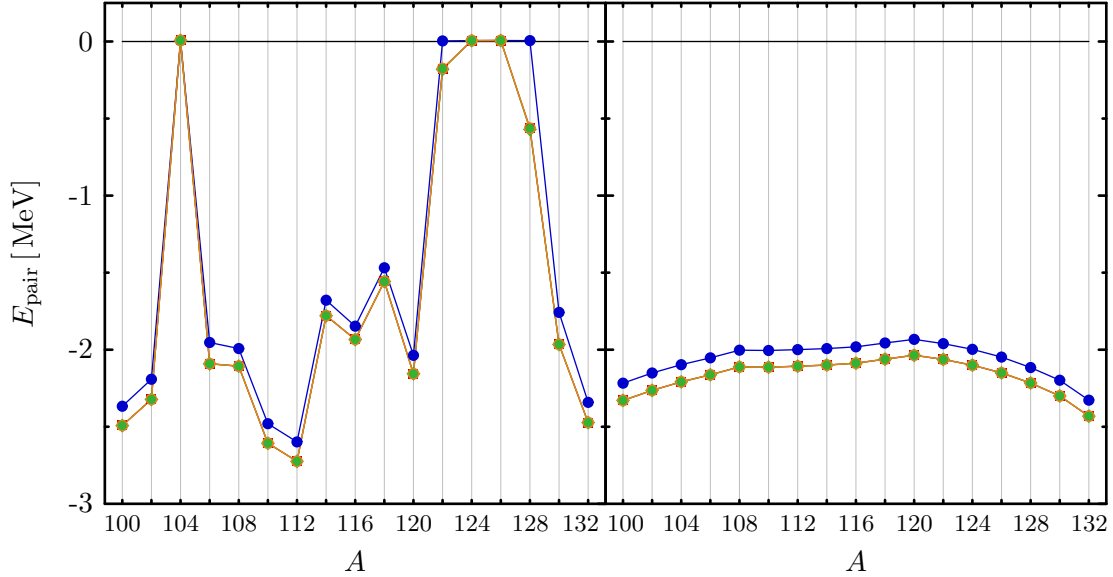
Figure 4.17:   Neutron (left) and proton (right) pairing energies of the Sn isotopes for V_{UCOM} with $I_\vartheta^{(1,0)} = 0.09$ fm^3, $I_\vartheta^{(1,1)} = 0$ fm^3. Comparison of $e_{\max} = 12, l_{\max} = 10$ (———●———), and various calculations with $e_{\max} = 14, l_{\max} = 10$: projection from $N + 2$ (———◆———), projection with 10 (———▲———), 12 (———■———), and 14 angles (———○———).

and from different intrinsic states, as discussed in Sect. 3.4. The results are in very close agreement, as shown in Fig. 4.17. Since the Hamiltonian-based PNP framework is free of spurious singularities (cf. Sect. 3.2.2), we conclude that the angular momentum-dependent effect also affects the dynamical pairing correlations.

4.2.2   Variation of the Tensor Correlator Ranges

Let us now consider the effect of the tensor-correlator range constraints on the pairing properties of the HFB ground state. Due to the comparably weak pairing obtained with V_{UCOM}, the effect of such variations on the HFB ground-state energies of the Sn isotopes is very similar to the HF case studied in Chapter 2, and therefore not shown again. In Fig. 4.18, we consider the additional ground-state energy gained by performing a VAP rather than a HFB calculation. The variation of the triplet-even tensor correlator constraint $I_\vartheta^{(1,0)}$ has a very small effect because the $(S,T) = (1,0)$ interaction affects the like-particle $T = 1$ pairing only indirectly by modifying the underlying particle-hole mean-field. In contrast, $I_\vartheta^{(1,1)}$ directly shifts strength between the interaction components which contribute to the particle-particle matrix elements, and we observe a notable effect on the energy for the tin isotopes below mass $A = 114$.

In Figs. 4.19 and 4.20, we show the corresponding neutron pairing energies of the Sn isotopes from the HFB and VAP approaches. The HFB pairing energies are suppressed by an increase of $I_\vartheta^{(1,0)}$, which coincides with the systematic reduction of the single-particle level density observed in the HF calculations in Chapter 2. While the VAP pairing energies follow the same general trend with the exception of the nuclei at the sub-shell closures, where the differences for various correlator ranges are tiny, we observe a sensitivity to the triplet-even tensor correlator range which is evocative of
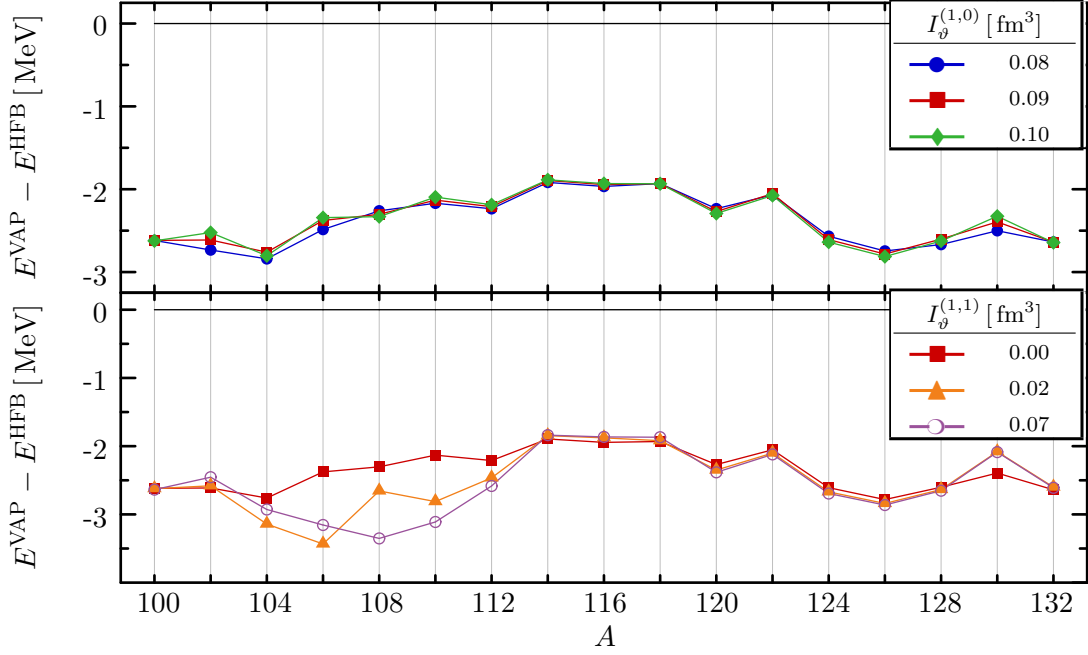
Figure 4.18: Energy gain from VAP of the Sn isotopes for V_{UCOM} with various tensor correlator constraints. *Top:* $I_\vartheta^{(1,1)} = 0$ fm^3 varying $I_\vartheta^{(1,0)}$ ($e_{\max} = 12, l_{\max} = 10$). *Bottom:* $I_\vartheta^{(1,0)} = 0.09$ fm^3 various $I_\vartheta^{(1,1)}$ ($e_{\max} = 12, l_{\max} = 10$).

non-continuity, although one has to keep in mind that we are not varying the parameter smoothly. The breakdown of pairing in the shells with high angular momentum is closely related to the value of $I_\vartheta^{(1,0)}$, and therefore to the amount of strength shifted from the mixed partial waves of the even-channel tensor interaction to the non-tensorial interaction terms. In the $0h_{11/2}$, we already have a pronounced signature of the breakdown for $I_\vartheta^{(1,0)} = 0.08$ fm^3, while the $0g_{7/2}$ still appears to be largely unaffected. As the triplet-even tensor correlator becomes longer-ranged, the pairing breakdown spreads to the boundaries of the shell, which seems to indicate a connection to the number of possible particle-hole versus particle-particle and hole-hole configurations. Furthermore, the breakdown also commences in $0g_{7/2}$ for $I_\vartheta^{(1,0)} = 0.0$ fm^3.

For $N \geq 70$, the variation of the triplet-odd tensor correlator range has similar effects as the variation of the triplet-even parameter $I_\vartheta^{(1,0)}$. In isotopes with $N \leq 58$, however, the HFB ground state exhibits neutron pairing for $I_\vartheta^{(1,1)} \neq 0$ fm^3. For $I_\vartheta^{(1,1)} = 0.02$ fm^3, the active $0g_{7/2}$ shell contributes up to 3 MeV of pairing energy, and the contribution of the $1d_{5/2}$ shell is slightly enhanced. Increasing $I_\vartheta^{(1,1)}$ to as much as 0.07 fm^3 ultimately starts to have a detrimental effect again — recall, however, that the triplet-odd tensor correlations are then almost exclusively described by the correlation operator (cf. Chapter 2), and no further effect is expected if we keep on increasing $I_\vartheta^{(1,1)}$. The VAP calculations exhibit much smoother trends as $I_\vartheta^{(1,1)}$ is increased. In the light Sn isotopes, the pairing energy is enhanced significantly, in particular for ^{108}Sn.

Finally, we show the VAP proton pairing energies in Fig. 4.21, which exhibit only tiny variations with either tensor correlator range. This behavior is consistent with the
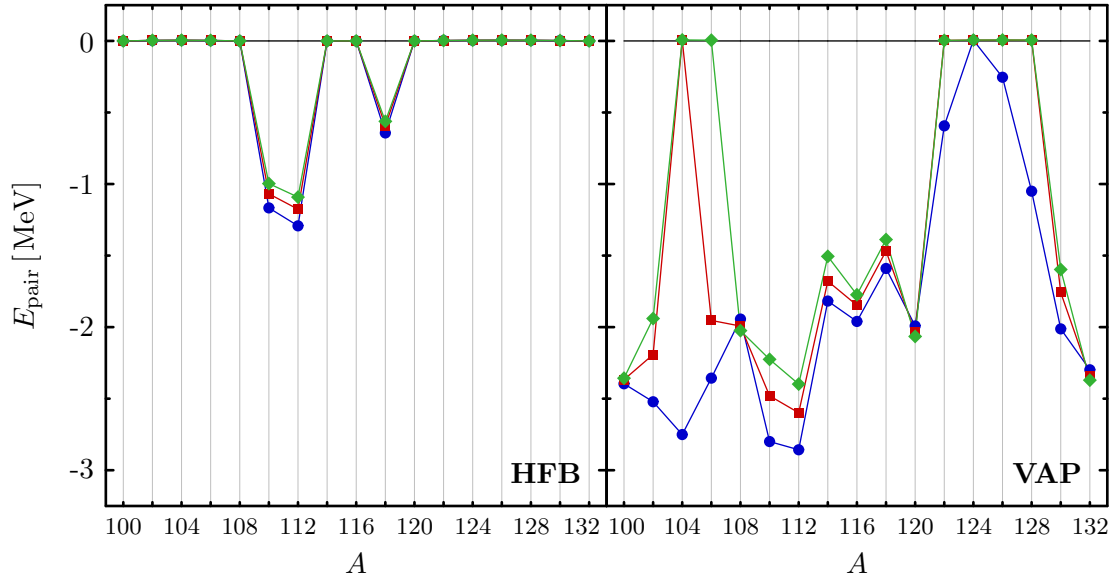
Figure 4.19:   HFB (left) and VAP (right) neutron pairing energies of the Sn isotopes for V_{UCOM} with $I_\vartheta^{(1,1)} = 0$ fm^3 and $I_\vartheta^{(1,0)} = 0.08$ fm^3 (——●——), 0.09 fm^3 (——■——), and 0.10 fm^3 (——◆——)($e_{\max} = 12, l_{\max} = 10$).
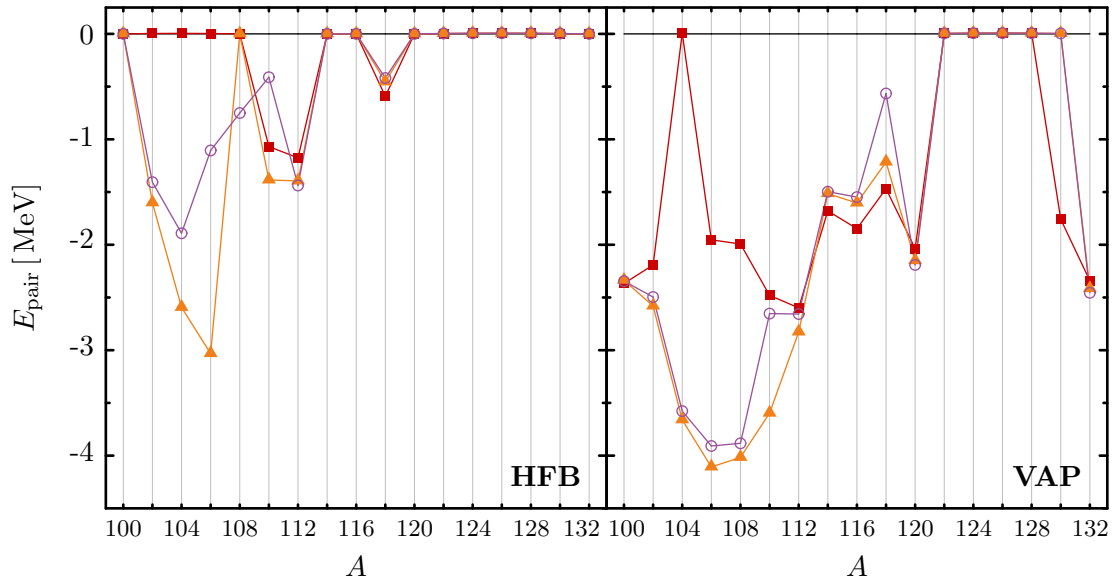
Figure 4.20:   HFB (left) and VAP (right) neutron pairing energies of the Sn isotopes for V_{UCOM} with $I_\vartheta^{(1,0)} = 0.09$ fm^3 and $I_\vartheta^{(1,1)} = 0$ fm^3 (——■——), 0.02 fm^3 (——▲——), and 0.07 fm^3 (——○——)($e_{\max} = 12, l_{\max} = 8$).
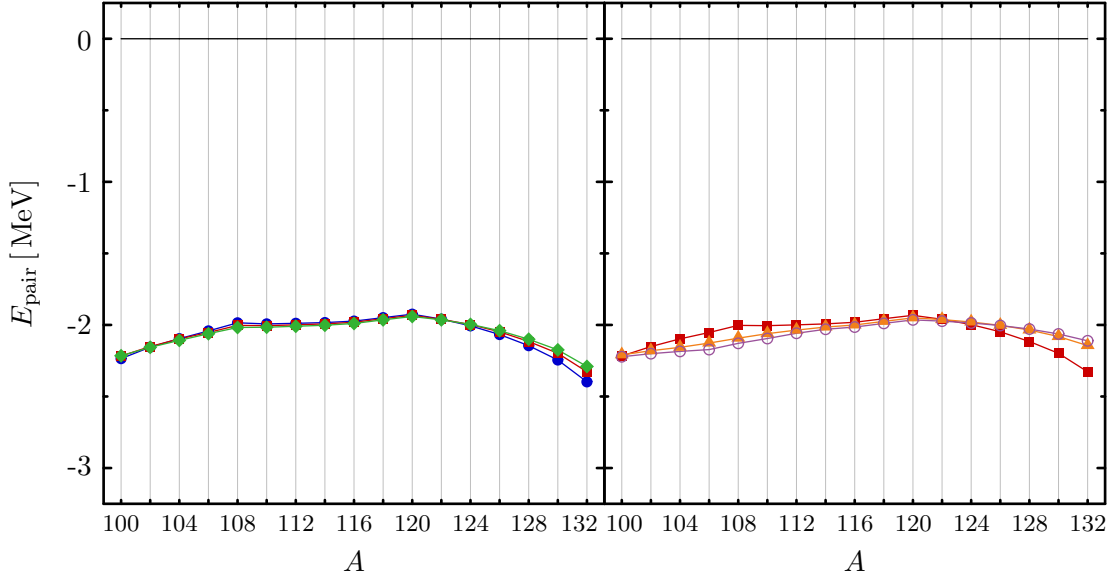
Figure 4.21: Proton pairing energies in the VAP approach. *Left:* V_{UCOM} with $I_\vartheta^{(1,1)} = 0$ fm^3 and $I_\vartheta^{(1,0)} = 0.08$ fm^3 ($\bullet$), 0.09 fm^3 ($\blacksquare$), and 0.10 fm^3 ($\blacklozenge$) ($e_{\max} = 12, l_{\max} = 10$). *Right:* V_{UCOM} with $I_\vartheta^{(1,0)} = 0.09$ fm^3 and $I_\vartheta^{(1,1)} = 0$ fm^3 ($\blacksquare$), 0.02 fm^3 ($\blacktriangle$), and 0.07 fm^3 ($\bigcirc$) ($e_{\max} = 12, l_{\max} = 08$).

insensitivity of the VAP neutron pairing energies to the tensor correlator range at the major neutron-shell closures in ^{100}Sn and ^{132}Sn.

The strong influence of the short-range correlations treated by the UCOM on the pairing properties is supported qualitatively by the Self-Consistent Green's Function (SCGF) results of Müther and Dickhoff [112] mentioned at the beginning of Sect. 4.2. While the approach to the treatment of short-range correlations is conceptually different, the observation of a suppression of pairing due to redistributed single-particle strength is the same. In the SCGF, the calculation is entirely based on a two-body interaction, and the strength redistribution is caused by the inclusion of more complex configurations in the intermediate states. In the UCOM, on the other hand, this redistribution is also manifestly connected to induced many-nucleon forces, which can in turn affect the single-particle strength by modifying the particle-hole channel, and one has to see how the proper inclusion of these terms will affect our present results.

4.2.3 Inclusion of $3N$ Effects via Density-Dependence

Although pairing is clearly a two-body correlation effect, the $3N$ force has an indirect effect on the pairing properties of a HF or HFB many-body state because it affects the underlying single-particle spectra. In Sect. 2.3, in particular, we have seen that the inclusion of a repulsive $3N$ contact force of the type

$$w = t_3 \delta^{(3)}(\mathbf{r}_1 - \mathbf{r}_2)\delta^{(3)}(\mathbf{r}_2 - \mathbf{r}_3) \tag{4.12}$$

can counter the spreading of the single-particle spectra which results from using V_{UCOM} in such calculations. Since the numerical effort of including such an interaction in HFB calculations is almost prohibitive because all off-diagonal matrix elements of the $3N$
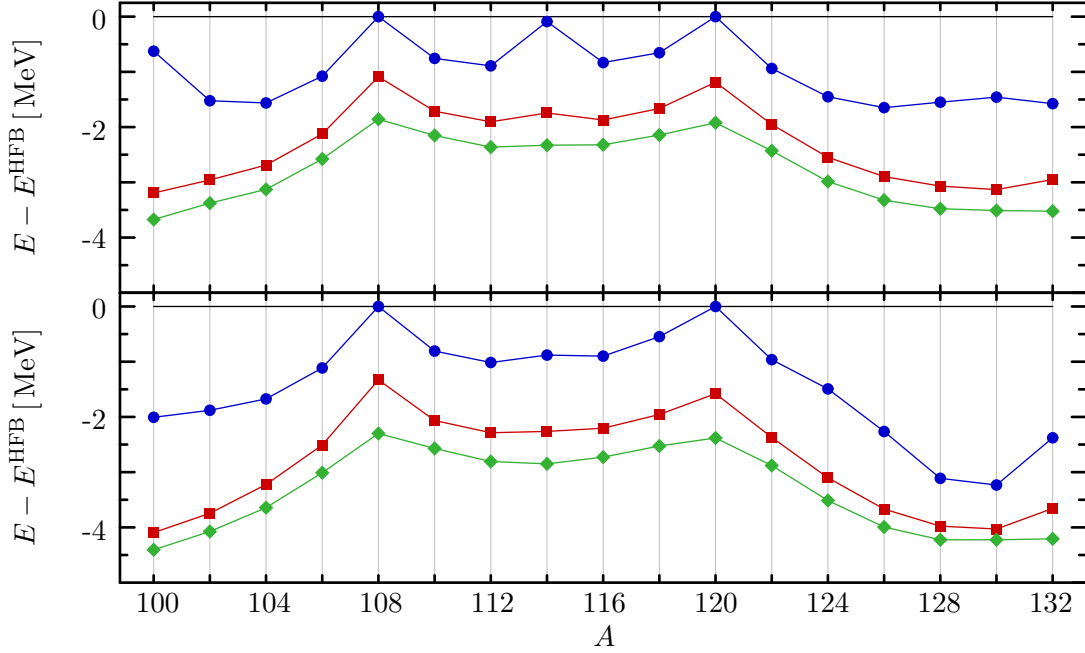
Figure 4.22: Energy gain from approximate and exact PNP methods for V_{UCOM} with $I_{\vartheta}^{(1,0)} = 0.2 \, \mathrm{fm}^3$, $I_{\vartheta}^{(1,1)} = 0.1 \, \mathrm{fm}^3$ and density-dependent interactions with $t_0 = 250 \, \mathrm{MeV \, fm}^6$ (top) and $416.67 \, \mathrm{MeV \, fm}^6$. Compared are PAV ($\bullet$), PLN ($\blacksquare$), and VAP ($\blacklozenge$) ($e_{\max} = 12$, $l_{\max} = 10$)

interaction are required as input, we have performed calculations with the corresponding approximate density-dependent two-body interaction

$$\mathrm{v}[\rho] = t_0 \left(1 + \mathrm{P}_\sigma\right) \rho \left(\frac{\mathbf{r}_1 + \mathbf{r}_2}{2}\right) \delta^{(3)}(\mathbf{r}_1 - \mathbf{r}_2) \tag{4.13}$$

as described in Sect. 3.3, being aware of the possible problems this may cause in the PNP methods. As in the HF case, we use longer-ranged tensor correlators for the two-body V_{UCOM} in these calculations, i.e. $I_{\vartheta}^{(1,0)} = 0.2 \, \mathrm{fm}^3$ and $I_{\vartheta}^{(1,1)} = 0.1 \, \mathrm{fm}^3$. For the density-dependent interaction, we use $t_0 = 250$ and $416.67 \, \mathrm{MeV \, fm}^6$, which correspond to the $3N$ contact interactions with $t_3 = 1.5$ and $2.5 \, \mathrm{GeV \, fm}^6$ adopted from [22] and discussed in Chapter 2.

In Fig. 4.22, we display the PNP binding-energy gain for the tin isotopes. For $t_0 = 250 \, \mathrm{MeV \, fm}^6$, the PAV result still shows distinct signatures of each sub-shell closure in the Sn isotopes, which become less pronounced as the PNP techniques become more sophisticated and the description of dynamical pairing correlations improves. The stronger density-dependent interaction with $t_0 = 416.67 \, \mathrm{MeV \, fm}^6$ leads to a larger binding energy gain, which indicates a stronger pairing content in the many-body state — one should keep in mind, however, that the latter also reduces the total ground-state energy, while the $t_0 = 250 \, \mathrm{MeV \, fm}^4$ interaction, just like its $3N$ contact counterpart, more or less leaves the ground-state energies invariant (cf. Sect. 2.3).

In Figs. 4.23 and 4.24, we show the corresponding pairing energies for the Sn isotopes, which reflect the behavior of the total ground-state energies, i.e., the weaker density-dependent interaction has vanishing neutron pairing for all sub-shell closures

Figure 4.23:   Neutron (left) and proton (right) pairing energies of the Sn isotopes in HFB and various approaches to PNP for V_{UCOM} with $I_{\vartheta}^{(1,0)} = 0.2$ fm^3, $I_{\vartheta}^{(1,1)} = 0.1$ fm^3 and a density-dependent interaction with $t_0 = 250$ MeV fm^6 ($e_{\max} = 12, l_{\max} = 10$).

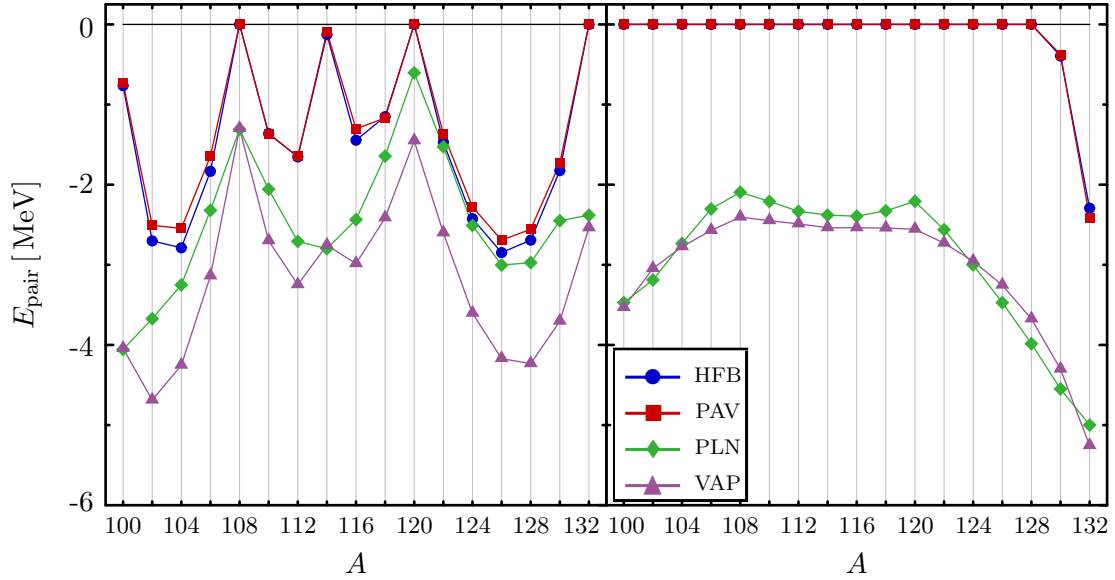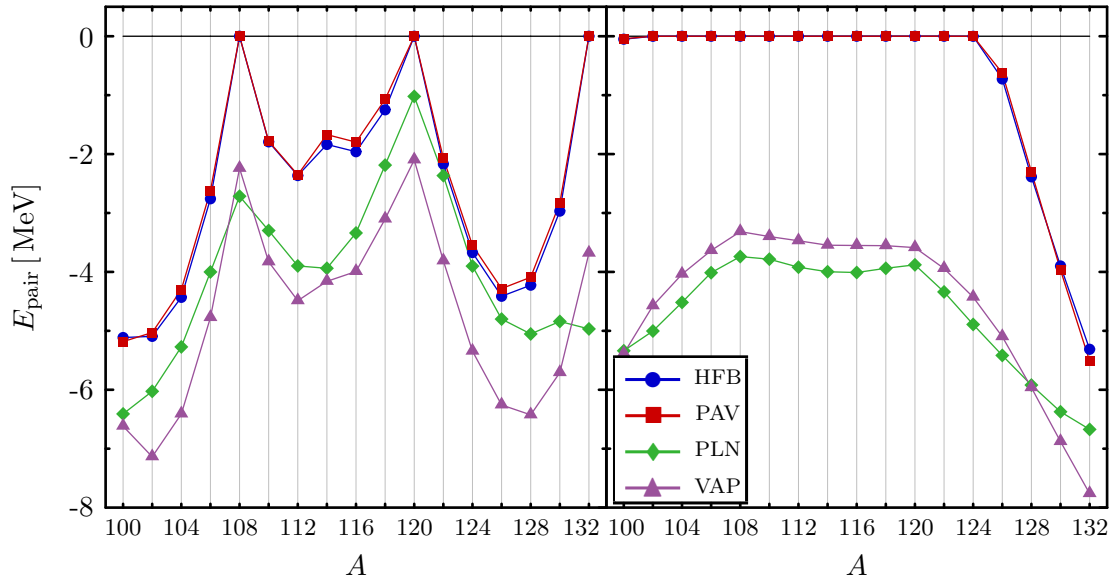Figure 4.24:   Neutron (left) and proton (right) pairing energies of the Sn isotopes in HFB and various approaches to PNP for V_{UCOM} with $I_{\vartheta}^{(1,0)} = 0.2$ fm^3, $I_{\vartheta}^{(1,1)} = 0.1$ fm^3 and a density-dependent interaction with $t_0 = 416.67$ MeV fm^6 ($e_{\max} = 12, l_{\max} = 10$).

in the HFB and PAV approaches. Note that just as in our benchmark calculations with the Gogny D1 interaction, the exact VAP shows a slight dip at $N = 64$, which is not properly reproduced by the approximate PNP in the projected Lipkin-Nogami approach. The stronger compression of the single-particle spectra by the stronger of the two density-dependent interactions manifests in somewhat higher pairing energies than for the standard two-body V_{UCOM}

For both density-dependent interactions, however, we observe pathologies in the systematics of the pairing energies: in particular, there is no longer a complete breakdown of the HFB pairing at $N = 50$, which indicates a significant alteration in the underlying single-particle level structure of ^{100}Sn. HF calculations with both $3N$ contact forces as well as the corresponding density-dependent interactions reveal the significant reduction of the $\nu 0g_{7/2} - \nu 0g_{9/2}$ level splitting in ^{100}Sn as the likely cause. Similarly, we have non-vanishing proton pairing energies near $N = 82$, which is caused by the simultaneous influence of the reduced proton $\pi 0g_{7/2} - \pi 0g_{9/2}$ level splitting and the evolution of the level structure due to the proton-neutron interaction in the particle-hole channel and the filling of neutron shells. As discussed in Sect. 2.3, this is a strong indication that at least a spin- and/or spin-orbit dependence in the $3N$ force is necessary to achieve agreement with experimental data.

4.2.4   Separation Energies

As pointed out repeatedly, the HF single-particle energies are only approximately related to nucleon removal energies. In HFB, the corresponding quantities are the quasiparticle energies, the eigenvalues of the HFB Hamiltonian. Since the quasiparticles, however, are in general superpositions of particles and holes, these energies cannot be directly related to experimentally observed removal energies any longer. Some authors define so-called 'equivalent single-particle energies' via the diagonal matrix elements of the HFB Hamiltonian in the *canonical basis*, usually in conjunction with the renormalization of a zero-range pairing interaction (see e.g. [113]). While their definition superficially resembles the BCS expressions, the HFB fields are not diagonal in the canonical basis like their BCS counterparts. Moreover, the definition of equivalent energies is rendered meaningless in the context of projection methods, where the quasiparticle energies become mere parameters (cf. Sect. 4.1.3). For this reason, we prefer to extract spectral information from experimentally verifiable quantities instead, and the simplest of these are the $2n$ separation energies

$$S_{2n} = E(Z, N) - E(Z, N - 2) \,. \tag{4.14}$$

In Fig. 4.25, we show separation energies for the Sn isotopes, obtained from calculations with the optimized two-body V_{UCOM}. In the upper panel, we first compare the results from HF and plain HFB calculations. We immediately notice the distinct increases in S_{2n} at the sub-shell closures, as well as the dramatic rise at $N = 70$, which corresponds to the unrealistic major-shell closure we have noticed repeatedly in our results. In ^{122}Sn and ^{124}Sn, the separation energies are actually positive, which indicates that these nuclei are unstable with respect to di-neutron emission. Rather than the experimentally observed smooth increase of S_{2n} over the isotopic chain, we notice that
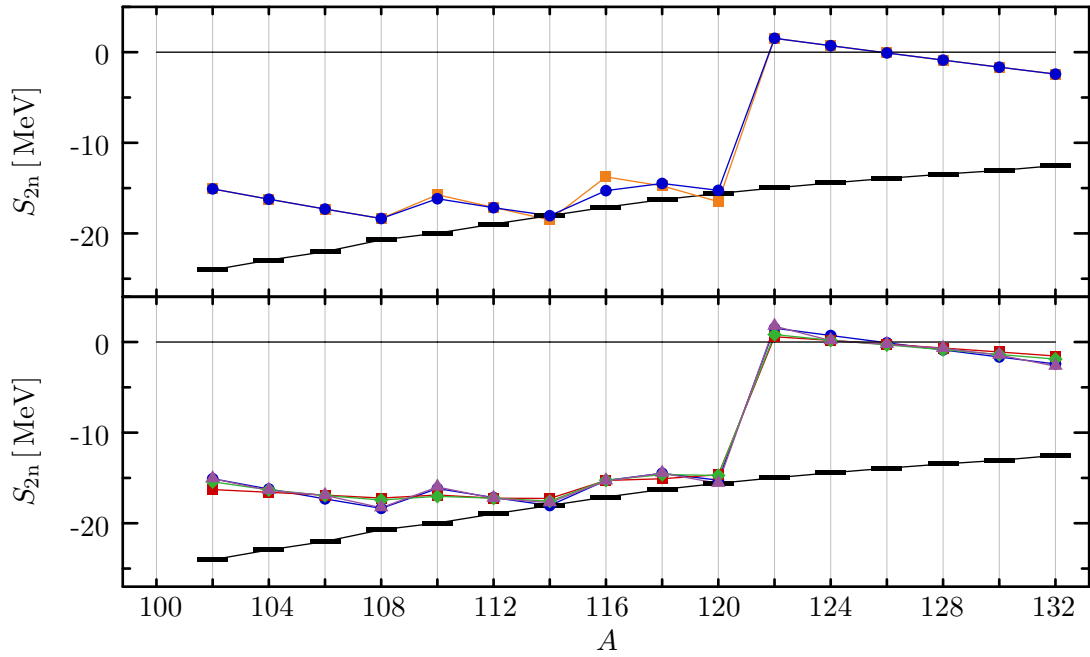
Figure 4.25: Two-neutron separation energies for V_{UCOM} with $I_{\vartheta}^{(1,0)} = 0.09\ \mathrm{fm}^3, I_{\vartheta}^{(1,1)} = 0\ \mathrm{fm}^3$ ($e_{\max} = 12, l_{\max} = 10$). *Top:* HFB ($\bullet$) and HF ($\blacksquare$). *Bottom:* HFB, PAV ($\blacksquare$), PLN ($\blacklozenge$), and VAP ($\blacktriangle$). Experimental data are indicated by (———).
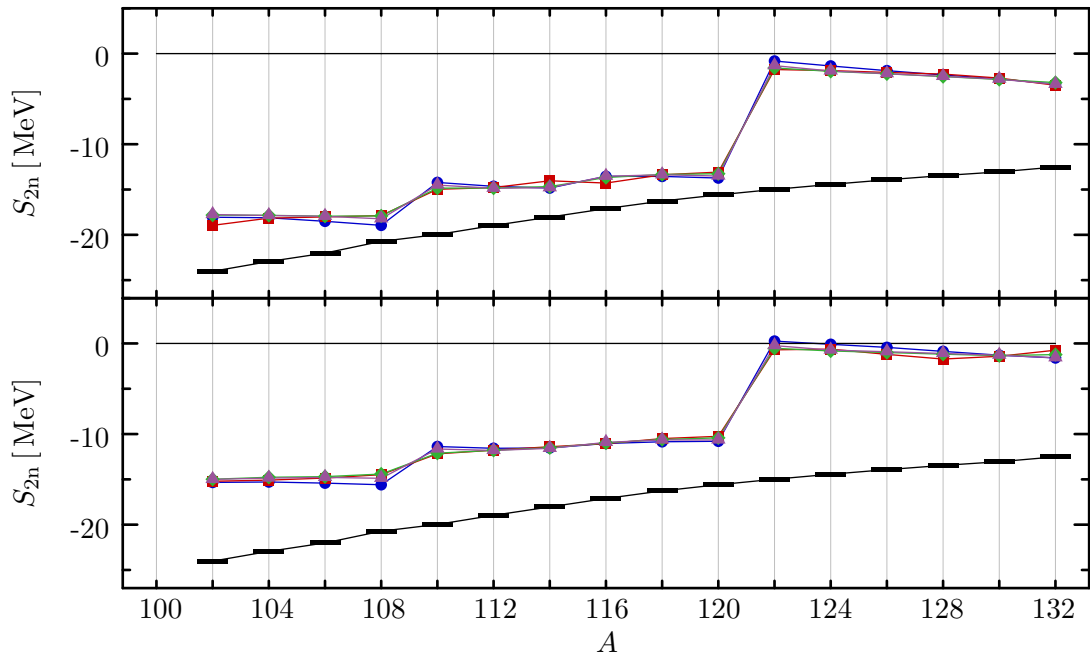
Figure 4.26: Two-neutron separation energies for V_{UCOM} with $I_{\vartheta}^{(1,0)} = 0.2\ \mathrm{fm}^3, I_{\vartheta}^{(1,1)} = 0.1\ \mathrm{fm}^3$ and density-dependent interactions with $t_0 = 250\ \mathrm{MeV\,fm}^6$ (top) and $416.67\ \mathrm{MeV\,fm}^6$ (bottom). HFB ($\bullet$), PAV ($\blacksquare$), PLN ($\blacklozenge$), and VAP ($\blacktriangle$) compared to experimental data (———) ($e_{\max} = 12, l_{\max} = 10$).

V_{UCOM} causes a decrease of the separation energies as neutrons are added to a particular sub-shell.

In the mid-shell region from $N = 62$ to $N = 70$, HF yields reasonable agreement with experiment. The inclusion of pairing correlations in HFB has no significant impact with the exception of a slightly lowered separation energy in ^{116}Sn, leading to an improvement of the systematic trend between ^{116}Sn and ^{120}Sn. The influence of PNP on the two-neutron separation energies is almost negligible, which is in part due to the weak pairing content of the ground states in the various methods. Interestingly, the projection after variation methods PAV and PLN seem to produce slightly smoother trends, although these have to be deemed less reliable than the full VAP results.

Finally, we show the S_{2n} obtained with the density-dependent interactions in Fig. 4.26. The additional repulsion is sufficient to stabilize the trends in the separation energies with respect to the addition of neutrons in the sub-shells, although we do not yet recover the experimentally observed reduction of S_{2n} as neutrons are added. The $N = 70$ major-shell closure is still evident — however, the density-dependent interaction with $t_0 = 250$ MeV fm^6 does no longer cause a positive S_{2n} past the shell closure. For $t_0 = 416.67$ MeV fm^6, the overall reduction of the separation energy goes along with the reappearance of the di-neutron instability in the plain HFB calculations. With the enhanced pairing content of the ground state in these calculations, we also obtain a somewhat more visible effect of the PNP methods.

Chapter 5

Pairing & Collective Excitations

Excitation spectra provide an excellent test for the validity of nuclear structure models, because electromagnetic or weak transitions are far more sensitive to the details of the nuclear wavefunctions than bulk properties like the binding energy. The Random Phase Approximation (RPA), starting from a HF ground-state wavefunction, is the simplest theory of nuclear excitations which allows for correlations in the ground state as well as the excited states, therefore going beyond the simple independent-particle picture. Such correlations are of crucial importance for a proper description of collective excitations in the nucleus. The proper generalization of RPA to systems with pairing is the Quasiparticle RPA, which combines the treatment of ground-state and pairing correlations in a unified framework.

5.1 The Quasiparticle Random Phase Approximation

This section is dedicated to the derivation of the Quasiparticle Random Phase Approximation for like-particle and charge-exchange transitions. Contrary to other recent approaches (see [114, 115, 116], for example), our formulation is entirely based on a Hamiltonian, hence the particle-hole and particle-particle channel matrix elements of the QRPA matrices are consistently derived from the *same* interaction, both in the like-particle and the charge-exchange cases used to study electromagnetic and weak transitions, respectively.

5.1.1 The QRPA Equations

A very elegant derivation of the QRPA can be carried out in the equations-of-motion method (EOM) [117, 118], although there are a number of other approaches like considering time-dependent HFB for small amplitude oscillations. In the EOM, one postulates that an excited state of the nucleus can be obtained from the ground state $\left| \Psi \right\rangle$ by applying a creation operator

$$\left| k \right\rangle = \mathrm{O}_k^\dagger \left| 0 \right\rangle, \quad \left| 0 \right\rangle \equiv \left| \Psi \right\rangle. \tag{5.1}$$

The corresponding annihilation operator O_k is required to annihilate $\left| \Psi \right\rangle$, which can then be interpreted as the vacuum state for the excitations:

$$\mathrm{O}_k \left| 0 \right\rangle = 0. \tag{5.2}$$

If the excited state $|k\rangle$ is assumed to satisfy the Schrödinger equation

$$\mathrm{H}|k\rangle = E_k|k\rangle,\tag{5.3}$$

we can use the properties of $\mathrm{O}_k^\dagger$ and obtain the system of equations

$$[\mathrm{H},\mathrm{O}_k^\dagger]|0\rangle = (E_k - E_0)|0\rangle \equiv \hbar\omega_k\mathrm{O}_k^\dagger|0\rangle,\tag{5.4}$$
$$[\mathrm{H},\mathrm{O}_k]|0\rangle = 0,\tag{5.5}$$

where E_0 is the ground-state energy of H.

The conditions (5.1) and (5.2) do *not* define $\mathrm{O}_k^\dagger$ uniquely: while

$$\mathrm{O}_k^\dagger = |k\rangle\langle 0|\tag{5.6}$$

is an obvious solution, any operator of the form

$$\mathrm{O}_k^\dagger + \delta\mathrm{O}_k^\dagger = |k\rangle\langle 0| + \sum_{i,j\neq 0,k} C_{ij}|i\rangle\langle j|\tag{5.7}$$

will have the same properties as long as the excited states are orthogonal. The amplitudes C_{ij} can be determined by taking the overlap of $\delta\mathrm{O}_k^\dagger|0\rangle$ with Eq. (5.4), which yields the equation of motion

$$\langle\Psi|[\delta\mathrm{O}_k,[\mathrm{H},\mathrm{O}_k^\dagger]]|\Psi\rangle = \hbar\omega_k\langle\Psi|[\delta\mathrm{O}_k,\mathrm{O}_k^\dagger]|\Psi\rangle.\tag{5.8}$$

Up to this point, the discussion of the EOM method was completely general. Depending on the choice of O_k, one can derive HF, HFB, RPA, etc. In QRPA, we want to treat two-quasiparticle ($2qp$) excitations, which encompass the particle-hole, particle-particle, and hole-hole cases in a unified manner. In the canonical basis introduced in Sect. 3.1.3, the excitation operator is then defined as

$$\mathrm{O}_k^\dagger = \sum_{\mu<\mu'}\left(X_{\mu\mu'}^k\alpha_\mu^\dagger\alpha_{\mu'}^\dagger - Y_{\mu\mu'}^k\alpha_\mu\alpha_{\mu'}\right),\tag{5.9}$$

where $\mu < \mu'$ prevents the double counting of pairs of canonical states, and the forward and backward going amplitudes are defined as

$$X_{\mu\mu'}^k = \langle\Psi|\alpha_\mu\alpha_{\mu'}|k\rangle\tag{5.10}$$

and

$$Y_{\mu\mu'}^k = \langle\Psi|\alpha_\mu^\dagger\alpha_{\mu'}^\dagger|k\rangle,\tag{5.11}$$

respectively. As discussed above, the creation operator $\mathrm{O}_k^\dagger$ now has to be applied to the ground state of the quasiparticle Hamiltonian, which can be expressed as

$$\mathrm{H} = \mathrm{H}_0 + \mathrm{V}_{\mathrm{res}},\tag{5.12}$$

where H_0 contains the groundstate energy and the quasiparticle-quasihole excitations obtained from solving the HFB equations (cf. Eq. (3.22) of Section 3.1.2), and

$$V_{\text{res}} = \frac{1}{4} \sum_{\mu\mu'\nu\nu'} \bar{V}_{\mu\nu\mu'\nu'} : a_\mu^\dagger a_\nu^\dagger a_{\nu'} a_{\mu'} : \tag{5.13}$$

is the residual interaction in normal ordering with respect to the quasiparticle vacuum. To avoid confusion with the canonical coefficient v, we use the capital $\bar{V}$ for antisymmetrized matrix elements of the interaction in the remainder of this chapter. Analogous to Eq. (5.2), the QRPA groundstate is defined as

$$O_k \left| \text{QRPA} \right\rangle = 0 \,. \tag{5.14}$$

Since we do not know $\left| \text{QRPA} \right\rangle$ a priori, we resort to the usual *quasi-boson approximation* [21, 118], and replace it by the HFB ground state in the equation of motion[1]:

$$\left\langle \text{HFB} \right| \left[\delta O_k, \left[H, O_k^\dagger \right] \right] \left| \text{HFB} \right\rangle = \hbar\omega_k \left\langle \text{HFB} \right| \left[\delta O_k, O_k^\dagger \right] \left| \text{HFB} \right\rangle \,. \tag{5.15}$$

Plugging (5.1) into Eq. (5.15) we obtain the QRPA equations

$$\begin{pmatrix} A & B \\ -B^* & -A^* \end{pmatrix} \begin{pmatrix} X^k \\ Y^k \end{pmatrix} = \hbar\omega_k \begin{pmatrix} X^k \\ Y^k \end{pmatrix} \,, \tag{5.16}$$

where A is Hermitian and B is symmetric. In the canonical basis (cf. Sect. 3.1.3), the matrices A and B are given by

$$A_{\mu\mu'\nu\nu'} = \left\langle \Psi \right| \left[\alpha_{\mu'}\alpha_\mu, \left[H, \alpha_\nu^\dagger \alpha_{\nu'}^\dagger \right] \right] \left| \Psi \right\rangle \tag{5.17}$$

$$B_{\mu\mu'\nu\nu'} = \left\langle \Psi \right| \left[\alpha_{\mu'}\alpha_\mu, \left[H, \alpha_\nu^\dagger \alpha_{\nu'}^\dagger \right] \right] \left| \Psi \right\rangle \,. \tag{5.18}$$

Inserting the quasiparticle Hamiltonian given in Appendix D.1 into Eq. (5.17), we obtain

$$\begin{aligned} A_{\mu\mu'\nu\nu'} = {} & H_{\mu\nu}^{11}\delta_{\mu'\nu'} + H_{\mu'\nu'}^{11}\delta_{\mu\nu} - H_{\mu'\nu}^{11}\delta_{\mu\nu'} - H_{\mu\nu'}^{11}\delta_{\mu'\nu} \\ & + \bar{V}_{\mu\bar{\nu}'\bar{\mu}'\nu} \left(u_\mu v_{\mu'} u_\nu v_{\nu'} + v_\mu u_{\mu'} v_\nu u_{\nu'} \right) \\ & - \bar{V}_{\mu\bar{\nu}\bar{\mu}'\nu'} \left(u_\mu v_{\mu'} v_\nu u_{\nu'} + v_\mu u_{\mu'} u_\nu v_{\nu'} \right) \\ & + \bar{V}_{\mu\mu'\nu\nu'} \left(u_\mu u_{\mu'} u_\nu u_{\nu'} + v_\mu v_{\mu'} v_\nu v_{\nu'} \right) \end{aligned} \tag{5.19}$$

and

$$\begin{aligned} B_{\mu\mu'\nu\nu'} = {} & \bar{V}_{\mu\nu\bar{\mu}'\bar{\nu}'} \left(v_\mu u_{\mu'} v_\nu u_{\nu'} + u_\mu v_{\mu'} u_\nu v_{\nu'} \right) \\ & - \bar{V}_{\mu\nu'\bar{\mu}'\bar{\nu}} \left(u_\mu v_{\mu'} v_\nu u_{\nu'} + v_\mu u_{\mu'} u_\nu v_{\nu'} \right) \\ & - \bar{V}_{\mu\mu'\bar{\nu}\bar{\nu}'} \left(v_\mu v_{\mu'} u_\nu u_{\nu'} + u_\mu u_{\mu'} v_\nu v_{\nu'} \right) \,, \end{aligned} \tag{5.20}$$

---

[1]By considering the 2*qp* excitations as bosons, we neglect terms in the commutator which arise from the fermionic anti-commutation relations, which means that (i) potentially important groundstate correlations are missing, and (ii) the QRPA may break down in certain situations. To improve the description, one can construct the full QRPA by solving Eq. (5.15) iteratively [21]. The use of such an iterative *extended RPA* scheme with V_{UCOM} does not lead to dramatic changes compared to standard RPA with the quasi-boson approximation [12].

where $\bar{\mu}$ denotes the canonical conjugate partner state of μ. The quasiparticle-quasihole terms in A are given by

$$H_{\mu\nu}^{11} = (u_\mu u_\nu - v_\mu v_\nu)(h_{\mu\nu} - \lambda \delta_{\mu\nu}) - (u_\mu v_\nu + v_\mu u_\nu)\Delta_{\mu\nu} \,, \tag{5.21}$$

where $h_{\mu\nu}$ and $\Delta_{\mu\nu}$ are the Hartree-Fock and pairing fields in the canonical basis, respectively, and λ is the Fermi energy.

5.1.2   Angular-Momentum Coupled Representation

In practical applications, the QRPA equations (5.16) are usually solved in an angular-momentum coupled representation, because one is primarily interested in the response of nuclei to excitations of a given multipolarity.

In a spherical canonical basis, the single-particle states are characterized by

$$\left| \mu m_\mu \right\rangle = \left| n_\mu l_\mu j_\mu m_\mu \right\rangle , \tag{5.22}$$

and we have

$$\left| \overline{\mu m_\mu} \right\rangle = (-1)^{l_\mu + j_\mu - m_\mu} \left| n_\mu l_\mu j_\mu m_\mu \right\rangle . \tag{5.23}$$

For convenience, we will absorb the phase factor $(-1)_\mu^l$ in the definition of the canonical coefficient v_μ in the following,

$$v_\mu \to (-1)^{l_\mu} v_\mu \tag{5.24}$$

to avoid too much cluttering in the formulae for the matrix elements.

The excitation with coupled angular momentum J is now created by

$$\mathrm{O}_{kJM}^\dagger = \sum_{\mu \le \mu'} \left(X_{[\mu\mu']JM}^k \mathrm{A}_{[\mu\mu']JM}^\dagger - Y_{[\mu\mu']JM}^k \tilde{\mathrm{A}}_{[\mu\mu']JM} \right) , \tag{5.25}$$

where the restriction of the sum is changed compared to Eq. (5.9) because μ is explicitly independent of m_μ. The coupled quasiparticle-pair creation operator is defined as

$$\mathrm{A}_{[\mu\mu']JM}^\dagger \equiv \frac{1}{\sqrt{1 + \delta_{\mu\mu'}}} \sum_{m_\mu, m_{\mu'}} \left\langle j_\mu m_\mu j_{\mu'} m_{\mu'} \middle| JM \right\rangle \alpha_\mu^\dagger \alpha_{\mu'} \tag{5.26}$$

and $\tilde{\mathrm{A}}_{[\mu\mu']JM}$ is its spherical adjoint (cf. Appendix B.2).

If we assume that the HFB ground state is spherically symmetric, the canonical coefficients are independent of m_μ as well, and we can explicitly sum over the single-particle m_μ's, and further reduce the QRPA equations to the M-independent form (cf. [114])

$$\sum_{\nu \le \nu'} \begin{pmatrix} A_{[\mu\mu']J,[\nu\nu']J} & B_{[\mu\mu']J,[\bar{\nu}\bar{\nu}']J} \\ -B_{[\mu\mu']J,[\bar{\nu}\bar{\nu}']J}^* & -A_{[\mu\mu']J,[\nu\nu']J}^* \end{pmatrix} \begin{pmatrix} X_{[\nu\nu']J}^k \\ Y_{[\nu\nu']J}^k \end{pmatrix} = \hbar\omega_k \begin{pmatrix} X_{[\nu\nu']J}^k \\ Y_{[\nu\nu']J}^k \end{pmatrix} , \quad \mu \le \mu' . \tag{5.27}$$

The reduced matrix elements of A and B are given by

$$
\begin{aligned}
A_{[\mu\mu']J,[\nu\nu']J} = {} & \frac{1}{\sqrt{1+\delta_{\mu\mu'}}} \frac{1}{\sqrt{1+\delta_{\nu\nu'}}} \\
& \times \Bigg\{ H^{11}_{\mu\nu}\delta_{\mu'\nu'} + H^{11}_{\mu'\nu'}\delta_{\mu\nu} - (-1)^{j_\mu+j_{\mu'}-J} \left(H^{11}_{\mu'\nu}\delta_{\mu\nu'} + H^{11}_{\mu\nu'}\delta_{\mu'\nu} \right) \\
& \quad + F(\mu\mu'\nu\nu';J) \left(u_\mu v_{\mu'} u_\nu v_{\nu'} + v_\mu u_{\mu'} v_\nu u_{\nu'} \right) \\
& \quad - (-1)^{j_\nu+j_{\nu'}-J} F(\mu\mu'\nu'\nu;J) \left(u_\mu v_{\mu'} v_\nu u_{\nu'} + v_\mu u_{\mu'} u_\nu v_{\nu'} \right) \\
& \quad + G(\mu\mu'\nu\nu';J) \left(u_\mu u_{\mu'} u_\nu u_{\nu'} + v_\mu v_{\mu'} v_\nu v_{\nu'} \right) \Bigg\}
\end{aligned}
\tag{5.28}
$$

and

$$
\begin{aligned}
B_{[\mu\mu']J,[\nu\nu']J} = {} & \frac{1}{\sqrt{1+\delta_{\mu\mu'}}} \frac{1}{\sqrt{1+\delta_{\nu\nu'}}} \\
& \times \Bigg\{ F(\mu\mu'\nu\nu';J) \left(v_\mu u_{\mu'} u_\nu v_{\nu'} + u_\mu v_{\mu'} v_\nu u_{\nu'} \right) \\
& \quad - (-1)^{j_\nu+j_{\nu'}-J} F(\mu\mu'\nu'\nu;J) \left(u_\mu v_{\mu'} u_\nu v_{\nu'} + v_\mu u_{\mu'} v_\nu u_{\nu'} \right) \\
& \quad - G(\mu\mu'\nu\nu';J) \left(u_\mu u_{\mu'} v_\nu v_{\nu'} + v_\mu v_{\mu'} u_\nu u_{\nu'} \right) \Bigg\} .
\end{aligned}
\tag{5.29}
$$

The single-quasiparticle term $H^{11}_{\mu\mu'}$ has the same form as in (5.21), but μ and μ' are now manifestly independent of magnetic quantum numbers, and the HF and pairing fields are replaced by their reduced versions defined in Sect. 3.1.5. The particle-hole and particle-particle channel matrix elements are given by

$$
F(\mu\mu'\nu\nu';J) = \sum_{J'} (-1)^{j_{\mu'}+j_\nu+J'} (2J'+1) \begin{Bmatrix} j_\mu & j_{\mu'} & J \\ j_\nu & j_{\nu'} & J' \end{Bmatrix} \left\langle [\mu\nu']J \middle| \bar{V} \middle| [\mu'\nu]J \right\rangle
\tag{5.30}
$$

and

$$
G(\mu\mu'\nu\nu';J) = \left\langle [\mu\mu']J \middle| \bar{V} \middle| [\nu\nu']J \right\rangle ,
\tag{5.31}
$$

where $\left\langle [\mu\nu']J \middle| \bar{V} \middle| [\mu'\nu]J \right\rangle$ are just the antisymmetrized interaction matrix elements defined in Appendix E.1 in the canonical basis.

5.1.3 Charge-Exchange QRPA

The QRPA matrix elements required for the description of charge-exchange processes are special cases of the expressions derived in the previous section, where no isospin quantum numbers were considered at all. Denoting neutron and proton canonical states by ν, ν' and π, π', respectively, the QRPA phonon creation operator for quasiproton-quasineutron excitations is given by [119]

$$
O^\dagger_k = \sum_{\pi\nu} \left(X^k_{\pi\nu} \alpha^\dagger_\pi \alpha^\dagger_\nu - Y^k_{\pi\nu} \alpha_\pi \alpha_\nu \right) .
\tag{5.32}
$$

The matrices A and B are simpler than in the like-particle case, because matrix elements of the type $\bar{V}_{\pi\pi'\nu\nu'}$ vanish due to isospin conservation. Thus, we obtain

$$
\begin{aligned}
A_{\pi\nu\pi'\nu'} = {} & H_{\pi\pi'}^{11}\delta_{\nu\nu'} + H_{\nu\nu'}^{11}\delta_{\pi\pi'} \\
& + \bar{V}_{\pi\nu\pi'\nu'}\left(u_\pi u_\nu u_{\pi'} u_{\nu'} + v_\pi v_\nu v_{\pi'} v_{\nu'}\right) \\
& - \bar{V}_{\pi\bar{\nu}'\pi'\bar{\nu}}\left(u_\pi v_\nu u_{\pi'} v_{\nu'} + v_\pi u_\nu v_{\pi'} u_{\nu'}\right)
\end{aligned}
\tag{5.33}
$$

and

$$
\begin{aligned}
B_{\pi\nu\pi'\nu'} = {} & \bar{V}_{\pi\nu'\pi'\nu}\left(u_\pi v_\nu v_{\pi'} u_{\nu'} + v_\pi u_\nu u_{\pi'} v_{\nu'}\right) \\
& - \bar{V}_{\pi\nu\bar{\pi}'\bar{\nu}'}\left(v_\pi v_\nu u_{\pi'} u_{\nu'} + u_\pi u_\nu v_{\pi'} v_{\nu'}\right) .
\end{aligned}
\tag{5.34}
$$

Likewise, the angular momentum-coupled phonon creation operator is given by

$$
O_{kJM}^\dagger = \sum_{\pi\nu}\left(X_{[\pi\nu]JM}^k A_{[\pi\nu]JM}^\dagger - Y_{[\pi\nu]JM}^k \tilde{A}_{[\pi\nu]JM}\right) ,
\tag{5.35}
$$

and plugging (5.35) into Eq. (5.15) yields

$$
\begin{aligned}
A_{[\pi\nu]J,[\pi'\nu']J} = {} & H_{\pi\pi'}^{11}\delta_{\nu\nu'} + H_{\nu\nu'}^{11}\delta_{\pi\pi'} \\
& + G(\pi\nu\pi'\nu'; J)\left(u_\pi u_\nu u_{\pi'} u_{\nu'} + v_\pi v_\nu v_{\pi'} v_{\nu'}\right) \\
& + F(\pi\nu\pi'\nu'; J)\left(u_\pi v_\nu u_{\pi'} v_{\nu'} + v_\pi u_\nu v_{\pi'} u_{\nu'}\right)
\end{aligned}
\tag{5.36}
$$

and

$$
\begin{aligned}
B_{\pi\nu\pi'\nu'} = {} & F(\pi\nu\pi'\nu'; J)\left(u_\pi v_\nu v_{\pi'} u_{\nu'} + v_\pi u_\nu u_{\pi'} v_{\nu'}\right) \\
& - G\pi\nu\pi'\nu'; J\left(v_\pi v_\nu u_{\pi'} u_{\nu'} + u_\pi u_\nu v_{\pi'} v_{\nu'}\right) ,
\end{aligned}
\tag{5.37}
$$

where F and G are given by the same expressions as before (cf. [119, 120]).

5.1.4 Properties of the QRPA Equations

Similar to the HFB equations discussed in Sect. 3.1, the QRPA equations (5.16) have adjoint pairs of solutions. This can easily be seen by rearranging rows and columns and taking the complex conjugate:

$$
\begin{pmatrix} A & B \\ -B^* & -A^* \end{pmatrix}\begin{pmatrix} Y^* \\ X^* \end{pmatrix} = -\hbar\omega^*\begin{pmatrix} Y^* \\ X^* \end{pmatrix} ,
\tag{5.38}
$$

i.e., to any solution $(X, Y)^T$ with energy $\hbar\omega$, there is an adjoint solution $(Y^*, X^*)^T$ with energy $-\hbar\omega^*$, with the exception of spurious solutions with vanishing energy, which will be discussed below. In practice, the appearance of an imaginary eigenvalue signals the breakdown of the QRPA due to the use of an unstable HFB ground state as a basis for the calculation (see e.g. [118]), and therefore the energies should occur in pairs of $\pm\hbar\omega$.

Equation (5.16) can be rewritten as

$$
S\begin{pmatrix} X^k \\ Y^k \end{pmatrix} = \hbar\omega M\begin{pmatrix} X^k \\ Y^k \end{pmatrix} ,
\tag{5.39}
$$

with

$$S = \begin{pmatrix} A & B \\ B^* & A^* \end{pmatrix}, \qquad M = \begin{pmatrix} 1 & \\ & -1 \end{pmatrix}. \tag{5.40}$$

The matrix S is sometimes referred to as the Hamiltonian or the stability matrix. The latter designation is due to the appearance of S as the quadratic term in the expression for the HFB energy in the quasiparticle expression (cf. [21]), which means that S corresponds to the Hessian matrix of the variational problem. Thus, the HFB solution used as input for the QRPA is only a stable minimum if S is positive definite, as mentioned above.

The metric matrix M leads to a modification of the usual orthonormalization condition of Hermitian eigenvalue problems, which reads

$$\sum_{\mu < \mu'} X_{\mu\mu'}^{k*} X_{\mu\mu'}^{l} - Y_{\mu\mu'}^{k*} Y_{\mu\mu'}^{l} = \pm\delta_{kl}, \tag{5.41}$$

where QRPA states with positive energy are normalized to 1, and solutions with negative energy to -1.

Spurious Modes

From the structure of the equation of motion (5.15), it is evident that we can expect to obtain a zero-energy solution for any operator that commutes with the Hamiltonian, like the center-of-mass momentum $\mathbf{P}$ generating the translational symmetry of H:

$$\langle \Psi | \left[\delta\mathbf{P}, \left[\mathrm{H}, \mathbf{P} \right] \right] | \Psi \rangle = 0. \tag{5.42}$$

Upon analyzing the situation in more detail, it turns out that the actual appearance of the spurious mode in the QRPA excitation spectrum is contingent on the violation of the associated symmetry by the ground-state wavefunction [21]. In the case of translational invariance, this is obviously the case due to the inevitable localization of the many-body wavefunction in space resulting from the use of an independent-particle picture.

Spurious modes are associated with the generators of every symmetry of H, e.g. rotational invariance, number conservation, etc., and they occur in the (J^π, T)-channels corresponding to the quantum numbers of the symmetry generators, i.e., in $(J^\pi = 0^+, T = 0)$ for particle number conservation, $(J^\pi = 1^-, T = 0)$ for the center-of-mass momentum, and so on. In these channels, the spurious mode can mix with the non-spurious states because numerical inaccuracies and the truncation of the configuration space usually prevent an exact separation at zero energy [118].

5.1.5 Intrinsic Kinetic Energy in QRPA

For the sake of simplicity, we have not explicitly considered the intrinsic kinetic energy contributions to the QRPA matrix elements derived in the previous sections. Similar to the HF and HFB cases, one simply has to make the replacement

$$\bar{V}_{\mu\mu'\nu\nu'} \to \bar{V}_{\mu\mu'\nu\nu'} + \frac{2}{A}\bar{t}_{\mathrm{int},\mu\mu'\nu\nu'} \tag{5.43}$$

in the formulae for the matrices A and B, where $\bar{t}_{\text{int}}$ are the antisymmetrized matrix elements of the relative kinetic energy operator.

In conjunction with the Talmi transformation used in the calculation of two-body matrix elements (see Appendix E.1), the use of the intrinsic kinetic energy leads to a well-realized decoupling of the spurious mode associated with the center-of-mass motion, as discussed in detail in Ref. [11].

5.2   Transitions

5.2.1   Transition Operators

In this section, we introduce the transition operators associated with the electromagnetic and weak transitions, which are obtained by considering the coupling of the nucleon to the electromagnetic field or the weak gauge-boson fields in time-dependent perturbation theory. In addition, one usually uses further approximations to obtain simple one-body forms for convenience (see e.g. [121, 119]). In first order, the transition probabilities from the initial state $\left| i J_i \right\rangle$ to the final state $\left| f J_f \right\rangle$ is given by Fermi's golden rule

$$
\begin{aligned}
\mathcal{T}_J(i J_i \to f J_f) &= p_J(E) B(J; i J_i \to f J_f) \\
&= p_J(E) \frac{1}{2J_i + 1} \left| \left\langle f J_f \right| \left| Q_J \right| \left| i J_i \right\rangle \right|^2 ,
\end{aligned}
\tag{5.44}
$$

where we have assumed that the transition operator is a spherical tensor (cf. Appendix B) of rank J, and $p_J(E)$ is a phase space factor. The reduced transition probability $B(J; i J_i \to f J_f)$, defined as the reduced matrix element of the transition operator, contains the contribution of nuclear structure details on the transition.

Electric Multipole Transitions

For electric multipole transitions, the reduced transition probabilities are given by

$$
B^T(EJ, J_i \to J_f) = \frac{1}{2J_i + 1} \left| \left\langle f J_f \right| \left| Q_J^T \right| \left| i J_i \right\rangle \right|^2 ,
\tag{5.45}
$$

where J_i and J_f denote the angular momenta of the initial and final states, $T = 0, 1$ is the isospin, and J denotes the multipolarity of the transition, which is determined by the transition operator Q_J^T. In the simplest case, the isoscalar ($T = 0$) and isovector ($T = 1$) electromagnetic transition operators are defined as

$$
Q_{JM}^0 = e \sum_{i=1}^{A} x_i^J Y_{JM}(\hat{\mathbf{x}}_i)
\tag{5.46}
$$

and

$$
Q_{JM}^1 = e \sum_{i=1}^{A} \tau_3^{(i)} x_i^J Y_{JM}(\hat{\mathbf{x}}_i) ,
\tag{5.47}
$$

where $\mathbf{x}_i$ are the single-particle position operators, and $\tau_3(i)$ is the isospin projection. There are, however, a few exceptions. The definition of the isoscalar monopole operator

contains an additional factor x^2:

$$Q_{00}^0 = e \sum_{i=1}^{A} x_i^2 Y_{00}(\hat{\mathbf{x}}_i). \tag{5.48}$$

Since the dipole response is affected by the spurious mode associated with the center-of-mass momentum, it is customary to use the corrected dipole operators [21]

$$Q_{JM}^0 = e \sum_{i=1}^{A} \left(x_i^3 - \frac{5}{3} \left\langle R_{ms} \right\rangle x_i \right) Y_{1M}(\hat{\mathbf{x}}_i) \tag{5.49}$$

and

$$Q_{JM}^1 = e \frac{N}{A} \sum_{p=1}^{Z} x_p Y_{1M}(\hat{\mathbf{x}}_p) - e \frac{Z}{A} \sum_{n=1}^{A} x_n Y_{1M}(\hat{\mathbf{x}}_n), \tag{5.50}$$

where R_{ms} is the intrinsic mean-square radius operator defined in Sect. 2.1.3. As discussed in [11], the spurious mode associated with the center-of-mass motion is already well-separated from the non-spurious states when the uncorrected dipole operators are used, which are given by Eqs. (5.46) and (5.47) for $J = 1$. This is a result of using the intrinsic kinetic energy and the explicit separation of center-of-mass and relative contributions via a Talmi transformation in the matrix elements of the residual interaction. The use of the corrected dipole transition operators (5.49) and (5.50) merely removes the strength associated with the spurious state from the spectrum altogether.

In QRPA, the transition matrix elements needed for the calculation of $B(EJ)$ values are given by [118, 119]

$$\langle kJ || Q_J^T || 0 \rangle =$$
$$\sum_{\mu \leq \mu'} \left(X_{[\mu\mu']J}^{k*} \langle \mu || Q_J^T || \mu' \rangle + (-1)^J Y_{[\mu\mu']J}^{k*} \langle \mu || Q_J^T || \mu' \rangle^* \right) \left(u_\mu v_{\mu'} + (-1)^J v_\mu u_{\mu'} \right),$$
$$\tag{5.51}$$

where the reduced matrix elements of Q_J^T in the canonical single-particle basis are given in Appendix D.2.

Weak Transitions

The simplest weak transitions we can study in the charge-exchange QRPA approach occur between the $J^\pi = 0^+$ ground state of an even-even reference nucleus and excited 0^+ or 1^+ states in a neighboring odd-odd nucleus. The former are called *isobaric analog states*, while the latter are referred to as *Gamow-Teller states*. Accordingly, the transitions are described by the Fermi and Gamow-Teller operators

$$Q_{\beta\pm}^F = \sum_{i=1}^{A} \tau_\pm^{(i)} \tag{5.52}$$

and

$$Q_{\beta\pm}^{GT} = \sum_{i=1}^{A} \boldsymbol{\sigma}_i \tau_{\pm}^{(i)}, \tag{5.53}$$

where $\boldsymbol{\sigma}_i$ are the spin vector operators up to a constant, and $\tau_{\pm}^{(i)}$ are the isospin raising and lowering operators. The corresponding reduced transition probabilities are given by

$$B_{\beta\pm}^{F}(E_k) = \frac{1}{2J_i + 1} |\langle k || Q_{\beta\pm}^{F} ||0\rangle|^2 \tag{5.54}$$

and

$$B_{\beta\pm}^{(GT)}(E_k) = \frac{1}{2J_i + 1} |\langle k || Q_{\beta\pm}^{GT} ||0\rangle|^2, \tag{5.55}$$

where $E_k = \hbar\omega_k$ is the energy of the excited state. The required reduced matrix elements are given by

$$\langle k || Q_{\beta\pm}^{(F/GT)} ||0\rangle = \sum_{\pi\nu} \langle \pi || Q^{(F/GT)\beta\pm} ||\nu\rangle \left(X_{\pi\nu}^{k} u_\pi v_\nu + V_{\pi\nu}^{k} v_\pi u_\nu \right), \tag{5.56}$$

and the reduced single-particle matrix elements can be found in Appendix D.2.

Correlated Transition Operators

In the UCOM, all observables need to be correlated consistently (cf. Sect. 1.1), hence we actually have to consider effective transition operators. To this end, the transition operators are first explicitly rewritten in terms of relative and center-of-mass position operators $\mathbf{r}_{ij}$ and $\mathbf{X}_{ij}$, respectively. For the isoscalar quadrupole operator, one obtains

$$Q_{2M}^{0} = e \sum_{i=1}^{A} x_i^2 Y_{2M}(\hat{\mathbf{x}}_i) = \frac{e}{2(A-1)} \sum_{i<j}^{A} r_{ij}^2 Y_{2M}(\hat{\mathbf{r}}_{ij}) + 4 X_{ij}^2 Y_{2M}(\hat{\mathbf{X}}_{ij}), \tag{5.57}$$

which can be transformed with C_r and C_Ω, just like the Hamiltonian. Since we are working with angular-momentum eigenstates, it is convenient to apply the tensor correlator C_Ω to the states rather than the operator itself (cf. Sect. 1.1 and Appendix A). Details on the calculation of $\widetilde{Q}_{2M}^{0}$ can be found in Ref. [11]. Numerically, one finds that the difference between the correlated and uncorrelated operators is small, at least if the cluster expansion of $\widetilde{Q}_{2M}^{0}$ is truncated at the two-body level. This results from the insensitivity of the long-ranged transition operators to short-range correlations and is analogous to our observations for the radii, as mentioned in Chapter 2. For this reason, we content ourselves with the uncorrelated transition operators in the following.

5.2.2 Sum Rules

The transition operators discussed in the previous section satisfy sum rules which are a useful tool for the discussion of collective excitations. For the electromagnetic transitions, the energy-weighted sum rule (EWSR)

$$S = \sum_{k>0} \hbar\omega_k |\langle k| Q |0\rangle|^2 = \frac{1}{2} \langle 0| [Q, [H, Q]] |0\rangle \tag{5.58}$$

is of particular importance. Generally, the transition operator matrix elements can be expressed in terms of the QRPA amplitudes as [117, 119]

$$\left\langle 0\right| \mathrm{Q}\left|k\right\rangle = \begin{pmatrix} Q^\dagger & Q^T \end{pmatrix} \begin{pmatrix} X_k \\ Y_k \end{pmatrix}, \qquad Q_{\mu\nu} = \left\langle \mu\right| \mathrm{Q}\left|\nu\right\rangle. \tag{5.59}$$

Using these expressions as well as the QRPA eigenenergies to evaluate the left-hand side, Thouless has shown that Eq. (5.58) holds exactly if the *HFB vacuum* is used as $\left|0\right\rangle$ on the right-hand side [122].

Electric Multipole Transitions & Non-Locality in the Interaction

For the electric multipole transitions, the EWSR is given by

$$S^T(EJ) = \sum_{k>0} \hbar\omega_k B^T(EJ, \omega_k), \tag{5.60}$$

where we have indicated the final state by its excitation energy in $B^T(EJ, \omega_k)$, and the initial state is always the even-even HFB ground state with $J^\pi = 0^+$.

There are several approximate classical sum rules which may be used for comparison. They are derived under the assumption of a completely local interaction in the Hamiltonian H, so that the only contributions to the commutator are due to the kinetic energy. Evaluating the resulting matrix elements (see e.g. [21]), one obtains

$$S^{T=0}(E0) = \frac{2\hbar^2 e^2}{m} \left(N\left\langle \mathrm{R}^n_{\mathrm{ms}} \right\rangle + Z\left\langle \mathrm{R}^p_{\mathrm{ms}} \right\rangle \right), \tag{5.61}$$

for the isoscalar monopole operator, where $\mathrm{R}^{(n/p)}_{\mathrm{ms}}$ are the intrinsic neutron and proton mean-square radii. For the isovector dipole operator, one has the well-known Thomas-Reiche-Kuhn (TRK) sum rule

$$S^{T=1}(E1) = \frac{\hbar^2 e^2}{2m} \frac{9}{4\pi} \frac{NZ}{A}, \tag{5.62}$$

and for the isoscalar quadrupole response,

$$S^{T=0}(E0) = \frac{25\hbar^2 e^2}{4\pi m} \left(N\left\langle \mathrm{R}^n_{\mathrm{ms}} \right\rangle + Z\left\langle \mathrm{R}^p_{\mathrm{ms}} \right\rangle \right). \tag{5.63}$$

In practical calculations, non-local interaction terms will lead to an enhancement of the EWSR compared to the classical sum rules (5.61) to (5.63), and the size of this enhancement is a measure for the non-locality of a particular NN potential in the corresponding (J^π, T)-channel. This is particularly true for the completely model-independent TRK sum rule.

Weak Transitions

The non-energy weighted sum of the Fermi and Gamow-Teller transitions is given by

$$S^{(F/GT)}_{\beta\pm} = \sum_k B^{(F/GT)}_{\beta\pm}(E_k), \tag{5.64}$$

with the reduced transition probabilities defined in Sect. 5.2.1. These strengths satisfy the model-independent *Ikeda sum rules* [123]

$$S^F_{\beta-} - S^F_{\beta+} = N - Z \tag{5.65}$$

and

$$S^{GT}_{\beta-} - S^{GT}_{\beta+} = 3(N - Z) \,, \tag{5.66}$$

respectively. The β^+-decay contribution to (5.65) can often be neglected because the neutron isobaric analog states are occupied, and the transition is suppressed by Pauli blocking. The same reasoning does not hold for the Gamow-Teller transition because of the possible spin-flip.

5.3 Results

In this section, we present results from the application of our QRPA implementation to a few select resonances in the tin isotopes as well as ^{90}Zr. A more systematic study based on V_{UCOM} is in progress, and will include the treatment of $3N$ effects by means of density-dependent interactions.

5.3.1 Monopole Strength in the Tin Isotopes

Giant Monopole Resonances and the Incompressibility of Nuclear Matter

The systematics of the isoscalar giant monopole resonance (ISGMR) in the tin isotopes has recently drawn attention due to a puzzling discrepancy between theoretical results and experimentally measured energies. By its nature as a compressional mode, the ISGMR energy is closely related to the incompressibility of nuclear matter K_∞. From a sum rule for the nuclear mean-square radius, one can derive the relation [124]

$$E_{\mathrm{ISGMR}} = \hbar\sqrt{A\frac{K_A}{m\left\langle \mathrm{R_{ms}} \right\rangle}} \,, \tag{5.67}$$

where m is the nucleon mass, $\left\langle \mathrm{R_{ms}} \right\rangle$ the mean-square mass radius, and the incompressibility of the nucleus is related to K_∞ by the expansion

$$K_A = K_\infty(1 + cA^{-1/3}) + K_\tau((N - Z)/A)^2 + K_{\mathrm{Coul}}Z^2A^{-4/3} + \dots. \tag{5.68}$$

K_τ and K_{Coul} parameterize the effects of the nuclear asymmetry and the Coulomb interaction, similar to the Liquid Drop Model. In practice, K_∞ is determined by calculating the ISGMR with various effective interactions like the Skyrme forces or the relativistic mean field (RMF) models, and adopting the incompressibility of the interaction which provides the closest match for the experimental ISGMR energy. Unfortunately, the incompressibility $K_\infty \sim 210 - 230$ MeV extracted from non-relativistic calculations systematically disagrees from the RMF approaches, which yield $K_\infty \sim 250 - 270$ MeV [16, 125]. Since the effective interactions used in these calculations are fit to nuclear bulk properties and therefore inherently contain beyond-mean field effects, one cannot easily
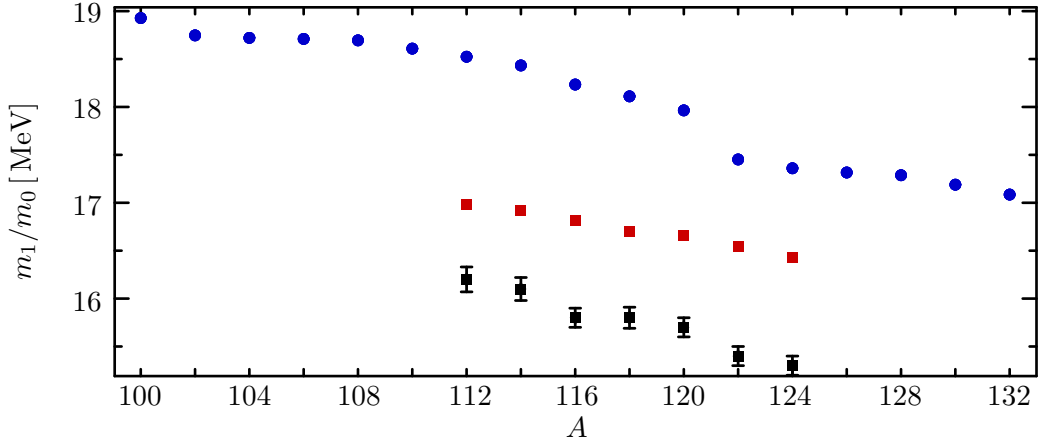
Figure 5.1: Centroid energies of the isoscalar monopole strength function in Sn isotopes. Comparison of the standard V_{UCOM} ($e_{\max} = 14$) (●) and a relativistic RPA calculation with the NL3 (■) interaction (cf. [126]). Black boxes with error bars indicate experimental data [127].

discern the cause of this discrepancy. Hence, it is worthwile to consider the problem from a more consistent ab-initio approach like UCOM.

The use of the standard V_{UCOM} interaction with $I_\vartheta^{(1,0)} = 0.09$ fm^3, $I_\vartheta^{(1,1)} = 0$ fm^3 was found to yield reasonable results for the isoscalar monopole response of various closed shell nuclei in Ref. [11]. Compared to experiment, the centroid energies of the strength distributions appear to be slightly overestimated in heavier systems like ^{90}Zr and ^{208}Pb. Using the QRPA formulated in the previous sections, we can now extend this study to the open-shell tin isotopes.

In Fig. 5.1, we compare the centroids of the ISM strength distribution obtained with V_{UCOM} to experimental data from inelastic α-scattering experiments at the RCNP facility in Osaka [127]. Results from a relativistic RPA calculation with the NL3 interaction are shown for comparison [126]. Compared to the experimental data, V_{UCOM} overestimates the centroid energies by roughly $2 - 2.5$ MeV. Judging from the relation (5.67), it stands to reason that this is directly tied to the underestimation of the nuclear radii. Both the inclusion of additional correlations in Second RPA [128] as well as the inclusion of $3N$ forces in standard RPA [22] have been confirmed to cause shifts of the strength distribution, and a combination of both will likely improve the agreement with experiment.

Looking in more detail, we observe that the centroids obtained with V_{UCOM} reflect the sub-shell structure of the tin isotopes — in particular, there is a very distinct kink at ^{120}Sn, where the spreading of the spectra caused by V_{UCOM} has lead to a new major shell closure for $N = 70$. The same kink is observed in the experimental data, although the change in the centroid energies from ^{120}Sn to ^{122}Sn is just about half the size of the V_{UCOM} result. Furthermore, the experimental data exhibits a second kink at the $N = 64$ sub-shell closure in ^{114}Sn, which is much less distinct for V_{UCOM}. The relativistic calculation does not conclusively reproduce these features of the experimental systematics, and the deviation from experiment grows worse with increasing neutron number — keep in mind, however, that the relativistic RPA does not include pairing effects.
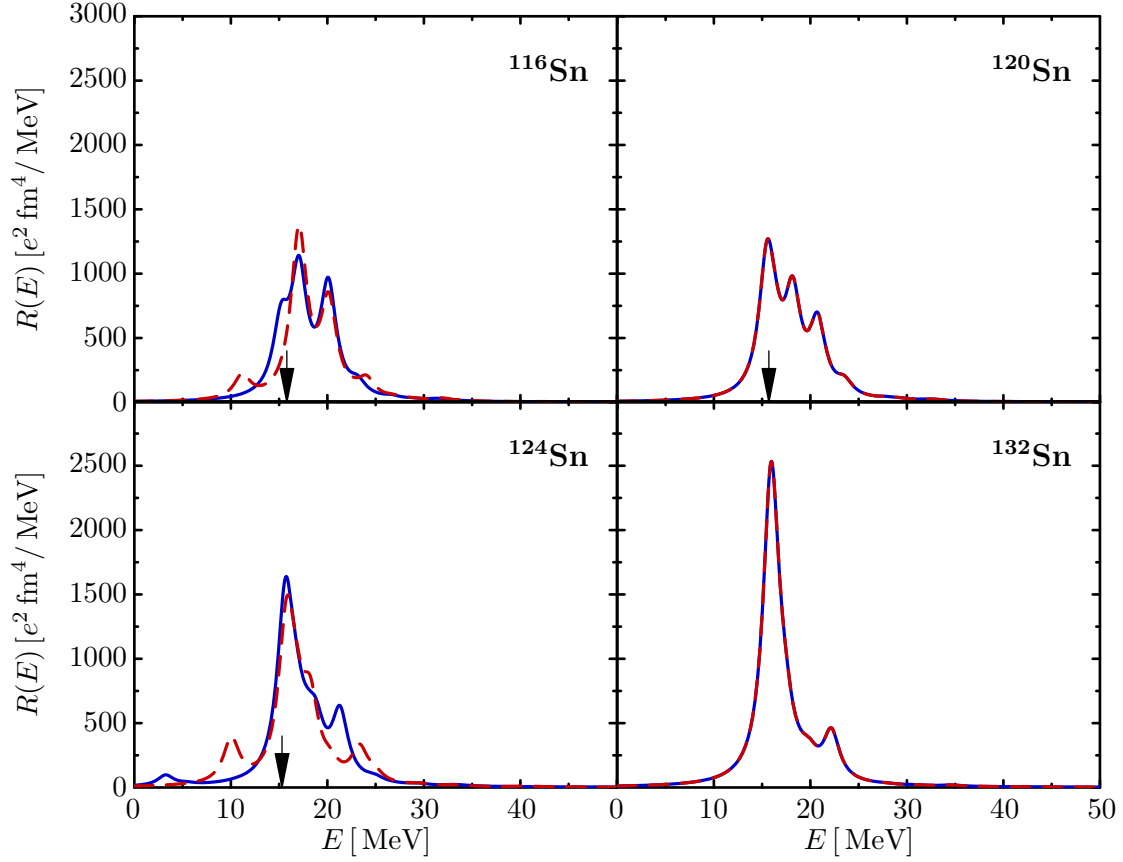
Figure 5.2:   Comparison of QRPA (———) and standard RPA (— — —) isoscalar monopole strength functions in selected Sn isotopes ($e_{\mathrm{max}} = 14$). Black arrows indicate experimental centroids [127].

Pairing Effects on the Monopole Strength

In our HFB calculations in Chapter 4, we found that the two-body V_{UCOM} produced at most a weak static pairing in the ground states of the tin isotopes, and it took the inclusion of dynamical pairing correlations via particle number projection to enhance their pairing properties. QRPA accounts for certain dynamical pairing correlations as well, and therefore we can expect to see pairing effects on the strength distributions even if we start from a HFB solution without static pairing. To this end, we compare QRPA calculations for ^{116}Sn,^{120}Sn,^{124}Sn and ^{132}Sn to results from RPA calculations which properly account for the partial filling in the open-shell nuclei. The resulting isoscalar monopole (ISM) strength distributions are shown in Fig. 5.2. The discrete (Q)RPA energies were folded with a Lorentzian function with arbitrarily chosen width $\Gamma = 2$ MeV.

As pointed out before, the spreading of the single-particle strength caused by V_{UCOM} results in a new major-shell closure for ^{120}Sn in addition to the regular one in ^{132}Sn. In these nuclei, we obtain perfect agreement of the QRPA and RPA strength distributions. This implies that the VAPNP method, which yields non-vanishing pairing energies in these nuclei (cf. Sect. 4.2), takes *different* dynamical pairing correlations into account than the QRPA, which is an interesting prospect for future work on a particle-number
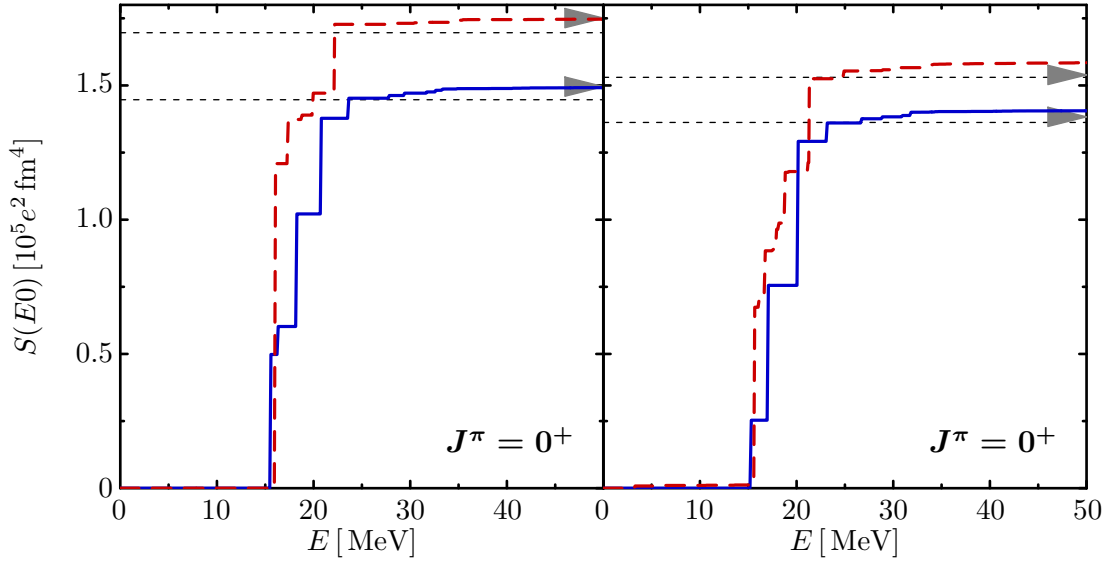
Figure 5.3:   Exhaustion of the isoscalar monopole sum rule. *Left:* ^{120}Sn (———) and ^{132}Sn (— — —). *Right:* ^{116}Sn (———) and ^{124}Sn (— — —). Results from corresponding RPA calculations (bold arrows) and classical sum rules (·······) are included as well.

projected QRPA.

In ^{116}Sn and ^{124}Sn, on the other hand, the bulk of the ISM strength resides in a somewhat smaller interval compared to the RPA result, with a slightly higher centroid energy. The pairing correlations enhance the collectivity of the resonance due to the inclusion of dynamical particle-particle and hole-hole excitations, which are not present in standard RPA. This result is in qualitative agreement with the findings from phenomenological QRPA calculations in Ref. [129].

The energy-weighted ISM response shown in Fig. 5.3 reflects the observations from the strength distributions. Whereas the values from QRPA and RPA agree for ^{120}Sn and ^{132}Sn, the summed ISM strength is notably larger for ^{116}Sn and ^{124}Sn if dynamical pairing correlations are included. Since the NN interaction is not considered in the derivation of the approximate classical monopole sum rule (cf. Sect. 5.2.2), our results are enhanced by a few percent compared to the values obtained by Eq. (5.61), which are included in Fig. 5.3 for comparison. This is in agreement with the UCOM-RPA results for closed-shell nuclei published in [11].

5.3.2   Isovector Dipole Response & Pygmy Resonances

The study of the isovector dipole response has become an active field of research since the prediction of the Pygmy dipole resonance (PDR) in nuclei with strong proton-neutron asymmetry. The dipole response of neutron-rich Sn isotopes has recently been investigated at GSI [130]. In the case of ^{130}Sn and ^{132}Sn, the obtained experimental data exhibit distinct peaks in the low-energy region around 10 MeV, which can be attributed to a PDR, although there is no definite proof for their collectivity as of yet.

In Fig. 5.4, we show the dipole response of ^{130}Sn and ^{132}Sn obtained from QRPA and open-shell RPA calculations with the standard two-body V_{UCOM}. The centroid energy of the giant dipole resonance (GDR), which contributes the bulk of the dipole
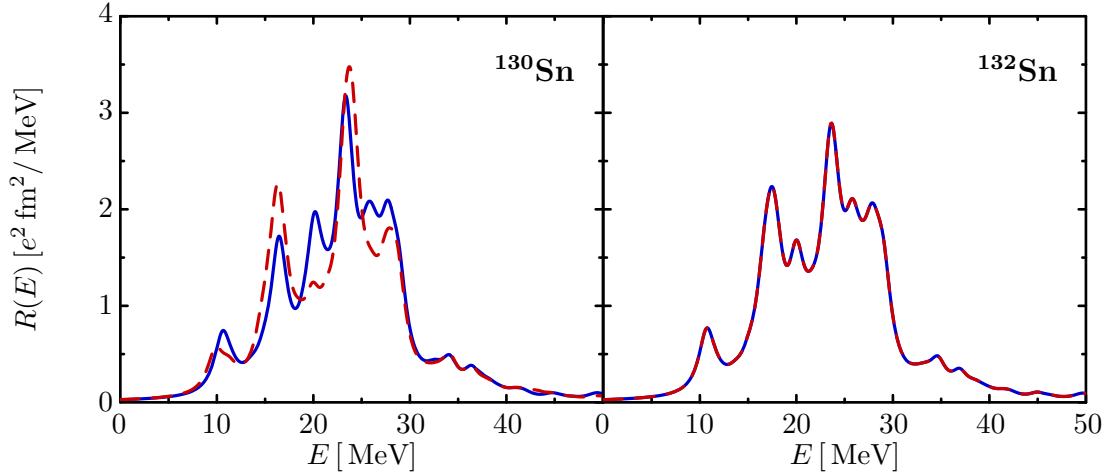
Figure 5.4:   QRPA (———) and standard RPA (– – –) isovector dipole strength distributions in ^{130}Sn and ^{132}Sn ($e_{\max} = 14$).

$E\,[\mathrm{MeV}]$	EWSR [%]	N_{neut} [%]	N_{prot} [%]	$N_{ph} > 1\%$	dominant $p-h$ config.
10.59	2.2	93.1	6.1	11	$\nu 0g_{9/2} \to \nu 0h_{11/2}$ (48.2%)
23.31	19.2	51.8	48.2	14	$\nu 0g_{7/2} \to \nu 0h_{9/2}$ (34.5%)
					$\pi 0f_{7/2} \to \pi 0g_{9/2}$ (24.1%)

Table 5.1:   Structure of the Pygmy dipole resonance and the strongest giant dipole resonance peak in ^{130}Sn. EWSR refers to the exhaustion of the energy-weighted IVD sum rule, N_{neut} and N_{prot} are the contributions from neutron and proton particle-hole (ph) configurations, respectively. We also list the number of ph configurations which contribute more than 1% to the state, as well as the dominant configurations. All N are evaluated with respect to the norm of the QRPA state.

strength, lies at about 23 MeV and therefore overestimates experimental data by about 6 MeV [11]. The cause for this behavior is the spreading of the single-particle strength in calculations with V_{UCOM}, which also manifests in the distinct fragmentation of the GDR. In the low-lying strength region, however, we indeed find peaks at excitation energies 10.6 and 10.7 MeV in ^{130}Sn and ^{132}Sn, respectively. While the QRPA and RPA IVD strength distributions match perfectly in the case of ^{132}Sn, just as in the monopole case, the inclusion of pairing effects has a distinct effect in ^{130}Sn, and particularly enhances the PDR peak.

The structure of the low-lying PDR peak in ^{130}Sn is analyzed in more detail in Tab. 5.1, and put in relation to the center peak of the GDR. While the GDR peak is made up almost evenly of proton and neutron particle-hole configurations, the PDR is strongly dominated by neutron ph-configurations, with a ratio of about 15:1, in accordance with theoretical predictions (see the recent review [131], for instance). While the PDR is dominated by the $\nu 0g_{9/2} \to \nu 0h_{11/2}$ transition, there is a significant number of other configurations with contributions in the $1 - 10\%$ range, which proves the collectivity of the state in our calculations.

Compared to the experimental centroids, which lie at 10.1 and 9.8 MeV in ^{130}Sn
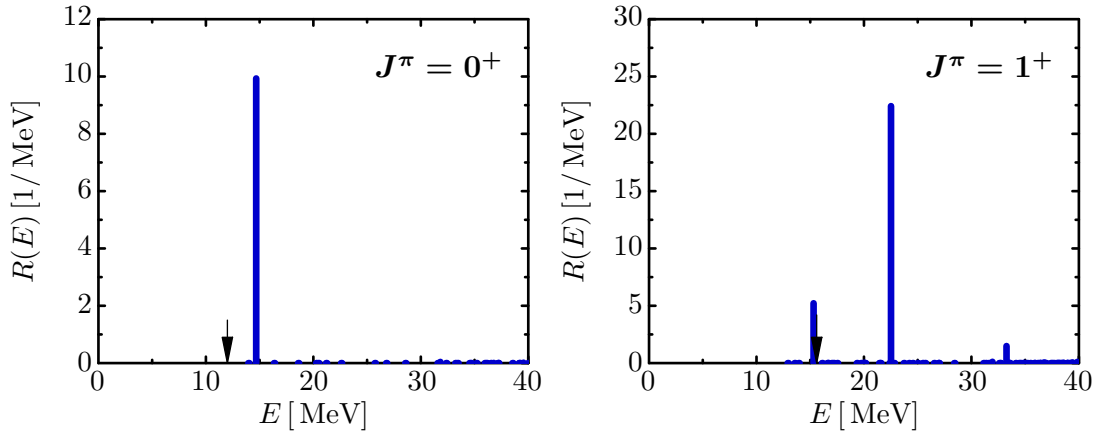
Figure 5.5: Response of ^{90}Zr in the $J^\pi = 0^+$ and $J^\pi = 1^+$ channels from a QRPA calculation with V_{UCOM} ($e_{\max} = 12$). Experimental energies of the isobaric analog and Gamow-Teller energies extracted from Ref. [133] (see text) are indicated by black arrows.

and ^{132}Sn, respectively, we slightly overestimate the PDR energy. Contrary to the GDR case, however, our results provide a much closer match to experiment, which is surprising given the increased splitting of the single-particle levels (cf. Chapter 2). We conclude our discussion by comparing the exhaustion of the Thomas-Reiche-Kuhn sum rule (5.62) to the experimental values of $7 \pm 3\%$ and $4 \pm 3\%$ in ^{130}Sn and ^{132}Sn, respectively. In our calculation, the PDR exhausts 2.2% of the energy-weighted dipole sum rule in ^{130}Sn (see Tab. 5.1) and 2.4% in ^{132}Sn, which corresponds to about $4 - 4.5\%$ of the TRK sum rule due to the significant enhancement of the summed dipole strength in calculations with V_{UCOM}. The latter is most likely caused by the non-locality of the interaction, which is neglected in the derivation of (5.62) (cf. Sect. 5.2.2).

5.3.3 Charge Exchange Transitions in ^{90}Zr

The understanding and correct description of β-decay processes is important for a wide range of theoretical subjects, from nucleosynthesis in stellar environments to the properties of exotic nuclei towards the drip line which become accessible with the advent of radioactive beam facilities (see [131] and references therein). Moreover, the study of neutrinoless double beta decay provides a test for the Standard Model of particle physics, because it may clarify whether neutrinos are Dirac or Majorana particles [132].

In Fig. 5.5, we show the response of ^{90}Zr to the Fermi and Gamow-Teller transition operators introduced in Sect. 5.2.1. We choose the closed-shell nucleus ^{90}Zr because the energies of the isobaric analog (associated with the Fermi operator) and Gamow-Teller resonances are experimentally well-established [133]. Note, however, that the energies in [133], as in most of the experimental literature on charge-exchange processes, are given with respect to the daughter nucleus, i.e. ^{90}Nb. Hence we have to add the mass differences of the nuclei as well as the proton-neutron mass difference to the measured energy to compare with our calculations [116].

We obtain a practically unfragmented isobaric analog resonance (IAR) at $E = 14.68$ MeV, which is somewhat above the experimental resonance at 12 ± 0.2 MeV. The sum rule

$$S_{\beta^-}^F - S_{\beta^+}^F = N - Z = 10 \tag{5.69}$$

is exhausted by more than 99%, in accordance with experiment. For the Gamow-Teller resonance, on the other hand, we obtain three peaks, with the lowest at $E = 15.31$ MeV lying close to the experimental resonance energy at 15.6 MeV. Experimentally, the GTR exhausts $90 \pm 5\%$ percent of the Ikeda sum rule

$$S_{\beta-}^{GT} - S_{\beta+}^{GT} = 3(N - Z) = 30 \,, \tag{5.70}$$

whereas the lowest peak contributes merely about 11% of the summed GT strength in our calculation. The bulk of the calculated GT strength, amounting to about 72%, resides in the peak at $E = 22.5$ MeV. Inspecting the *ph*-configurations contributing to the lowest peaks, we find that *both* are exclusively made up of the transitions $\nu 0g_{9/2} \rightarrow \pi 0g_{9/2}$ and $\nu 0g_{9/2} \rightarrow \pi 0g_{7/2}$. Since the sum of the former's quasiparticle energies is lower, it dominates the first peak, while the situation is reversed for the second peak. From our experience with the single-particle spectra generated by V_{UCOM}, it would appear as if the fragmentation of the Gamow-Teller strength is produced by this effect, and that at least the lowest two fragments should actually fall on a single, collective resonance, which would then contain about 80% (or more) of the summed Gamow-Teller strength. The remainder of the GT strength in our calculation is contained in the third peak, which is governed by the $\nu 0g_{9/2} \rightarrow \pi 1g_{9/2}$ and $\nu 0g_{9/2} \rightarrow \pi 1g_{7/2}$ transitions.

Chapter 6

Conclusions

The Unitary Correlation Operator Method (UCOM) and the Similarity Renormalization Group (SRG) allow the derivation of 'tamed' phase-shift equivalent interactions which are a suitable starting point for a wide array of many-body methods. In particular, they are applicable in mean-field approaches like Hartree-Fock and Hartree-Fock-Bogoliubov which cannot be used in conjunction with realistic NN interactions like the Argonne V18 or Nijmegen potentials.

While the UCOM and the SRG are conceptually very different, the similarity of the resulting effective interactions in momentum space reveals that both approaches treat the same kind of physics, i.e., the short-range central and tensor correlations. By examining the SRG flow equation at the initial point, we were able to explicitly show that the SRG generator, which dynamically drives the interaction towards band-diagonality in momentum space, has same structure as the explicit generators used in the UCOM. In higher partial waves, we observe differences between the matrix elements of the UCOM and SRG interactions, which are most likely caused by the independent running of the SRG flow, whereas different UCOM transformations are only allowed in the four possible (S, T) channels.

The new effective interactions exhibit a dramatically improved convergence behaviour in few-body calculations with the No-Core Shell Model (NCSM) [6], which results from the decoupling of low- and high-momentum matrix elements. Compared to the parent interaction, the V_{UCOM} gives a lower ground-state energy, which serves as a direct measure for omitted higher-order many-nucleon interactions, which are automatically generated by the UCOM. The balancing of induced terms with genuine 'realistic' interactions via the Tjon line allows for the definition of an optimized two-body V_{UCOM}, characterized by a specific value of the tensor correlator range in the $(S, T) = (1, 0)$ channel, which reproduces the experimental ^{3}H and ^{4}He binding energies without a $3N$ force. NCSM calculations of p-shell nuclei with this optimized V_{UCOM} demonstrate impressively that features like the correct ordering of the ground state and first excited state in ^{10}B, which were believed to be fingerprints of $3N$ forces, can be obtained with a pure two-body interaction [69]. This observation shows that the net $3N$ force can be minimized explicitly by unitary transformations due to the existence of infinitely many unitarily equivalent representations of the strong interaction in the low-energy regime, which opens the possibility to shift interaction strength between the on- and off-shell parts of the NN interaction as well as higher many-nucleon forces.

Applying a UCOM and a SRG interaction optimized with the help of the Tjon line, we find that the less pronounced band-diagonalization of V_{UCOM} proves to be of merit in such mean-field based calculations. While the SRG-evolved interaction overbinds heavier nuclei due to a significant shift of repulsive interaction strength to high momenta and higher many-nucleon forces, V_{UCOM} avoids this pathology and yields a good reproduction of the systematics of experimental binding energies [10]. The radii, on the other hand, turn out to be too small. This is the first manifestation of a problematic feature of V_{UCOM} which can be traced back to the non-locality of the interaction, resulting from the shift of the repulsive core of the parent AV18 interaction to momentum-dependent terms and induced repulsive higher many-nucleon forces. In the single-particle spectra, this non-locality is responsible for the existence of deeply-bound single-particle states, and an overall reduction of the single-particle level density. As expected, the SRG-evolved interaction exhibits the same trends in a more pronounced fashion.

Since V_{UCOM} explicitly deals with short-range correlations only, residual long-range correlations have to be described by the many-body state, and they can give significant contributions to the binding energy, as evident from the NCSM results in Chapter 1. In mean-field based approaches, second-order many-body perturbation theory (MBPT) is able to treat such correlations well, and the small size of the third-order correction indicates convergence of the perturbation series. Perturbative corrections to radii, however, are not sufficient to reproduce experimental values [10].

Our fully consistent HFB framework with and without particle-number projection is benchmarked by using the Gogny interactions, and subsequently applied in calculations with V_{UCOM}. As a consequence of the low level density, we find that the formation of static pairing is severely impeded in standard HFB calculations, and it takes the inclusion of dynamical pairing correlations by means of particle-number projection to improve the situation. In general, we observe a systematic variation of the pairing energy with the range of the tensor correlators in the triplet-even and triplet-odd channels, which indicates that the pairing energy is highly sensitive to the treatment of short-range correlations. This is in qualitative agreement with the results of other authors, which encounter a reduction of the BCS pairing gap due to the redistribution of single-particle strength caused by short-range calculations [19]. Compared to results obtained with phenomenological forces [82, 113, 110], our pairing energies are significantly smaller. Since the former are at least numerically close to experimental values, this indicates that important effects are cumulatively absorbed in the fit parameters of these forces, and the details of the underlying physics is lost. Moreover, there are considerable discrepancies in the size and systematics of the gaps for different phenomenological pairing forces, and different predictions on whether the pairing is a volume or surface effect [113].

From the theoretical point of view, we also have to account for the many-nucleon forces induced by the treatment of short-range correlations in the UCOM. To explore this issue, we have also performed HFB and HFB+PNP calculations including a repulsive density-dependent interaction as an approximation for the $3N$ contact force discussed in [22]. The improvement of the level density near the Fermi surface has the expected effect of leading to an increase of the pairing energy, which is then found to be at least comparable in magnitude to phenomenological results.

Finally, we have derived the fully self-consistent Quasiparticle Random Phase Ap-

proximation on the basis of our HFB framework, and applied it to the study of select electromagnetic and charge-exchange transitions in the tin isotopes and ^{90}Zr, respectively. In these calculations, the optimized two-body V_{UCOM} is consistently used as the residual interaction in the all channels. For closed-shell nuclei, the QRPA results are in qualitative and quantitative agreement with standard RPA calculations.

In the open-shell Sn isotopes, we observe signatures of dynamical pairing correlations in the calculations of the isoscalar monopole and isovector dipole strength distributions. The centroid energies in these channels are typically shifted to higher energies as a result of the spreading of the spectra. By the nature of the transitions, the effect is more pronounced in the dipole response, where the experimental centroid energy in ^{130}Sn and ^{132}Sn is overestimated by $6-7$ MeV. Interestingly, we were able to obtain a low-lying dipole resonance peak with much smaller deviation of the order of $1-2$ MeV from recent experimental measurements at GSI [130]. A detailed analysis of our result indicates that these peaks correspond to pygmy dipole resonances, although experimental evidence is not yet conclusive.

In the charge-exchange calculation, the distortion of the single-particle spectrum obtained with V_{UCOM} causes significant problems. While the isobaric analog resonance in the β^- decay channel of ^{90}Zr is reproduced at about 2.7 MeV above the experimental value, the Gamow-Teller resonance is strongly fragmented, in contrast to experimental predictions.

The main agenda for future work is the inclusion of $3N$ forces, ideally in a fully consistent approach were two- and three-body V_{UCOM} are derived from chiral interactions. Technically, however, such a procedure is highly non-trivial. In principle, the SRG offers a simpler way for a consistent evolution of the $NN + 3N$ interaction, hence it may be useful to seek out a hybrid approach to the construction of the effective interaction. The optimization of UCOM correlators by means of the SRG is an interesting concept in general, and presently being pursued.

The aim of the research on V_{UCOM} is to overcome the inter-connected problems of too-small radii and the spreading of the single-particle strength. Once these issues are solved, an obvious subject for further study are calculations for odd nuclei, using either the simple blocking approximation [21], or the more sophisticated approach of Duguet et al. [134, 135]. Aside from this, there are many possible avenues which can be explored in the future. In the HFB and QRPA codes developed for this work, the details of the calculational routines and the underlying single-particle basis structure are separated from one another, i.e., the single-particle basis can be exchanged quite easily to allow for deformations. The complicated operator structure of the V_{UCOM} in coordinate space makes it virtually impossible to perform coordinate space calculations for nuclei near the driplines, where the coupling to continuum states becomes very important and weakly bound single-nucleon states are encountered. A useful method to treat these effects in a configuration space picture employs transformed harmonic oscillator states ([136, 92]). The adaptation of these states to the UCOM framework will be of great interest.

In conjunction with the continuing improvement of the available many-body methods, the use of modern effective interactions derived in the UCOM and SRG approaches holds the promise of a truly unified description of the nuclear few- and many-body problem in the domain of nuclear structure, preserving a stringent connection to QCD which is obscured in phenomenological approaches.

Appendix A

UCOM Relations & Parameters

This appendix collects UCOM formulas and operator relations from the original publications [7, 8, 6], including some minor corrections.

A.1   Momentum Operators

The central correlator (Sect. 1.1.1) used to shift particles in their relative coordinate $\boldsymbol{r}$ is constructed from the *radial momentum operator* q_r

$$\mathrm{q}_r = \frac{1}{2}\left(\mathbf{q}\cdot\hat{\mathbf{r}} + \hat{\mathbf{r}}\cdot\mathbf{q}\right). \tag{A.1}$$

Its coordinate-space representation is

$$\langle\,\boldsymbol{r}\,|\,\mathrm{q}_r\,|\psi\,\rangle = -\left(\frac{i}{r} + \frac{\partial}{\partial r}\right)\langle\,\boldsymbol{r}\,|\psi\,\rangle = -i\frac{1}{r}\frac{\partial}{\partial r}r\,\langle\,\boldsymbol{r}\,|\psi\,\rangle, \tag{A.2}$$

yielding

$$\langle\,\boldsymbol{r}\,|\,\mathrm{q}_r^2\,|\psi\,\rangle = -\frac{1}{r}\frac{\partial}{\partial r}\left(r\frac{1}{r}\frac{\partial}{\partial r}r\,\langle\,\boldsymbol{r}\,|\psi\,\rangle\right) = -\frac{1}{r}\frac{\partial^2}{\partial r^2}r\,\langle\,\boldsymbol{r}\,|\psi\,\rangle. \tag{A.3}$$

The relative momentum operator $\mathbf{q}$ can be decomposed into a radial and an orbital part,

$$\mathbf{q} = \mathbf{q}_r + \mathbf{q}_\Omega. \tag{A.4}$$

The operators

$$\mathbf{q}_r \equiv \hat{\mathbf{r}}\,\mathrm{q}_r \quad\text{and}\quad \mathbf{q}_\Omega \equiv \frac{1}{2\mathrm{r}}(\mathbf{l}\times\hat{\mathbf{r}} - \hat{\mathbf{r}}\times\mathbf{l}) \tag{A.5}$$

do not commute; using the elementary commutation relation of position and momentum we find

$$\left[\mathrm{q}_r, \mathbf{q}_\Omega\right] = \frac{i}{\mathrm{r}}\mathbf{q}_\Omega \tag{A.6}$$

and

$$\mathbf{q}_r\cdot\mathbf{q}_\Omega - \mathbf{q}_\Omega\cdot\mathbf{q}_r = i\left(\mathrm{q}_r\frac{1}{\mathrm{r}} + \frac{1}{\mathrm{r}}\mathrm{q}_r\right) = -\frac{1}{\mathrm{r}^2} + \frac{2i}{\mathrm{r}}\mathrm{q}_r. \tag{A.7}$$

$\mathbf{q}_\Omega$ commutes with functions of the *relative distance* operator,

$$\left[\mathbf{q}_\Omega, f(\mathrm{r})\right] = 0, \tag{A.8}$$

but the orbital momentum operator does not commute with the relative position vector operator:

$$\left[q_{\Omega k}, r_l \right] = i \left(\frac{r_k r_l}{r^2} - \delta_{kl} \right) . \tag{A.9}$$

By setting $k = l$ and summing in Eq. (A.9), we obtain

$$\mathbf{r} \cdot \mathbf{q}_\Omega - \mathbf{q}_\Omega \cdot \mathbf{r} = 2i . \tag{A.10}$$

Some additional helpful identities are

$$\mathbf{q}_r \cdot \mathbf{q}_\Omega + \mathbf{q}_\Omega \cdot \mathbf{q}_r = -\frac{1}{r^2} , \tag{A.11}$$

$$\mathbf{q}_\Omega^2 = \frac{1}{r^2} \left(l^2 + 1 \right) . \tag{A.12}$$

A.2   Correlated Matrix Elements

In this section, we list the matrix elements of V_{UCOM} between relative two-body states with coupled angular momenta and isospins $\left| \phi(LS)JT \right\rangle$; corresponding expressions for a potential in partial-wave representation can be found in [6]. For a spherically symmetric, charge-independent potential, there is no explicit M- and M_T-dependence in the matrix element.

Recall that the fully correlated Hamiltonian in two-body space can be rewritten as

$$c_r^\dagger c_\Omega^\dagger h c_\Omega c_r = \left(c_r^\dagger c_\Omega^\dagger c_r \right) \left(c_r^\dagger h c_r \right) \left(c_r^\dagger c_\Omega c_r \right)$$

$$= \left(c_r^\dagger c_\Omega c_r \right)^\dagger \left(c_r^\dagger h c_r \right) \left(c_r^\dagger c_\Omega c_r \right) , \tag{A.13}$$

and we can let the *central correlated* tensor correlation operator $\widetilde{c}_\Omega$ act on the two-body wavefunction:

$$\widetilde{c}_\Omega \left| \phi(J \pm 1, 1)JT \right\rangle = \cos \widetilde{\theta}_J(r) \left| \phi(J \pm 1, 1)J \right\rangle \mp \sin \widetilde{\theta}_J(r) \left| \phi(J \mp 1, 1)J \right\rangle , \tag{A.14}$$

with

$$\widetilde{\theta}_J(r) = 3\sqrt{J(J+1)} \vartheta(R_+(r)) . \tag{A.15}$$

Local Interactions

For local interactions of the type $v(r)o$, where o is independent of the radial coordinate, the diagonal matrix elements $L = L' = J$ are not affected by the tensor correlator, and we have

$$\left\langle n(JS)JT \right| c_r^\dagger c_\Omega^\dagger v(r)o\, c_\Omega c_r \left| n'(JS)JT \right\rangle$$

$$= \int dr\, u_{n,J}^*(r)\, \widetilde{v}(r)\, u_{n',J}(r) \left\langle (JS)JT \right| o \left| (JS)JT \right\rangle , \tag{A.16}$$

where $\widetilde{v}(r) = v(R_+(r))$ is the transformed radial dependence. The $u_{n,L}(r) = r\phi_{n,L}(r)$ are the radial relative wavefunctions, depending on a radial quantum number n and the

orbital angular momentum L. The diagonal matrix elements with $L = L' = J \mp 1$ are given by

$$
\left\langle\, n(J \mp 1, 1)JT \,\middle|\, c_r^\dagger c_\Omega^\dagger\, v(\mathrm{r})\mathrm{o}\, c_\Omega c_r \,\middle|\, n'(J \mp 1, 1)JT \,\right\rangle
$$

$$
= \int dr\, u_{n,J\mp1}^*(r)\, \widetilde{v}(r)\, u_{n',J\mp1}(r)
$$

$$
\times \Big\{\quad \left\langle (J \mp 1, 1)JT \middle| \mathrm{o} \middle| (J \mp 1, 1)JT \right\rangle \cos^2 \widetilde{\theta}_J(r)
$$

$$
+\ \left\langle (J \pm 1, 1)JT \middle| \mathrm{o} \middle| (J \pm 1, 1)JT \right\rangle \sin^2 \widetilde{\theta}_J(r)
$$

$$
\pm\ \left\langle (J \mp 1, 1)JT \middle| \mathrm{o} \middle| (J \pm 1, 1)JT \right\rangle 2\cos\widetilde{\theta}_J(r)\sin\widetilde{\theta}_J(r)\Big\}\ ,\quad \text{(A.17)}
$$

and the off-diagonal matrix elements for $L = J \mp 1, L' = J \pm 1$ are

$$
\left\langle\, n(J \mp 1, 1)JT \,\middle|\, c_r^\dagger c_\Omega^\dagger\, v(\mathrm{r})\mathrm{o}\, c_\Omega c_r \,\middle|\, n'(J \pm 1, 1)JT \,\right\rangle
$$

$$
= \int dr\, u_{n,J\mp1}^*(r)\, \widetilde{v}(r)\, u_{n',J\pm1}(r)
$$

$$
\times \Big\{\quad \left\langle (J \mp 1, 1)JT \middle| \mathrm{o} \middle| (J \pm 1, 1)JT \right\rangle \cos^2 \widetilde{\theta}_J(\mathrm{r})
$$

$$
-\ \left\langle (J \pm 1, 1)JT \middle| \mathrm{o} \middle| (J \mp 1, 1)JT \right\rangle \sin^2 \widetilde{\theta}_J(\mathrm{r})
$$

$$
\mp\ \left\langle (J \mp 1, 1)JT \middle| \mathrm{o} \middle| (J \mp 1, 1)JT \right\rangle \cos\widetilde{\theta}_J(\mathrm{r})\sin\widetilde{\theta}_J(\mathrm{r})
$$

$$
\pm\ \left\langle (J \pm 1, 1)JT \middle| \mathrm{o} \middle| (J \pm 1, 1)JT \right\rangle \sin\widetilde{\theta}_J(\mathrm{r})\cos\widetilde{\theta}_J(\mathrm{r})\Big\}\ .\quad \text{(A.18)}
$$

The tensor correlator is responsible for the mixing of states whose orbital angular momenta differ by $\Delta L = 2$, which is evident in the structure of the matrix elements (A.17) and (A.18). Note also that due to the linear combinations of diagonal matrix elements occurring in Eq. (A.18), even operators like $\mathbf{l}^2$ and $\mathbf{l}\cdot\mathbf{s}$ have non-vanishing off-diagonal *correlated* matrix elements. If we were using an operator representation of V_{UCOM}, these matrix elements would occur due to the higher order tensor terms (see Sect. A.3).

Momentum-Dependent Interactions

For a momentum-dependent interaction, Eqs. (A.38) and (A.39) can be used to obtain

$$
\frac{1}{2}c_r^\dagger c_\Omega^\dagger \left[v_q(\mathrm{r})\mathrm{q}_r^2 + \mathrm{q}_r^2 v_q(\mathrm{r}) \right] c_\Omega c_r = \frac{1}{2}c_r^\dagger \left[v_q(\mathrm{r})\mathrm{q}_r^2 + \mathrm{q}_r^2 v_q(\mathrm{r}) \right] c_r + \widetilde{v}_q(\mathrm{r}) \left[\widetilde{\vartheta}'(\mathrm{r})\mathrm{s}_{12}(\mathbf{r}, \mathbf{q}_\Omega) \right]^2
$$

$$
- c_r^\dagger \left[v_q(\mathrm{r})\vartheta'(\mathrm{r})\mathrm{q}_r + \mathrm{q}_r\vartheta'(\mathrm{r})v_q(\mathrm{r}) \right] c_r\, \mathrm{s}_{12}(\mathbf{r}, \mathbf{q}_\Omega)\,,\quad \text{(A.19)}
$$

with $\widetilde{\vartheta}'(\mathrm{r}) = \vartheta'(R_+(\mathrm{r}))$, the central correlated q_r^2-term given by Eq. (A.32), and

$$
c_r^\dagger \left[v_q(\mathrm{r})\vartheta'(\mathrm{r})\mathrm{q}_r + \mathrm{q}_r\vartheta'(\mathrm{r})v_q(\mathrm{r}) \right] c_r = \frac{\widetilde{v}_q(\mathrm{r})}{R_+(\mathrm{r})}\widetilde{\vartheta}'(\mathrm{r})\mathrm{q}_r + \mathrm{q}_r\widetilde{\vartheta}'(\mathrm{r})\frac{\widetilde{v}_q(\mathrm{r})}{R_+(\mathrm{r})}\,.\quad \text{(A.20)}
$$

The diagonal matrix elements with $L = L' = J$ read

$$\left\langle n(JS)JT \right| c_r^\dagger c_\Omega^\dagger v_q c_\Omega c_r \left| n'(JS)JT \right\rangle \tag{A.21}$$

$$= \int dr \left\{ u_{n,J}^*(r)\, u_{n',J}(r) \left[\widetilde{v}_q(\mathrm{r})\, w(\mathrm{r}) - \widetilde{v}_q'(\mathrm{r}) \frac{R_+''(r)}{[R_+'(r)]^2} \right] \right.$$

$$\left. - \frac{1}{2} \left[u_{n,J}^*(r)\, u_{n',J}''(r) + u_{n,J}''^*(r)\, u_{n',J}(r) \right] \frac{\widetilde{v}_q(r)}{[R_+'(r)]^2} \right\} , \tag{A.22}$$

where $\widetilde{v}_q'(\mathrm{r}) = v_q'(R_+(\mathrm{r}))$, and $w(r)$ is defined in Eq. (A.29). For $L = L' = J \mp 1$, we obtain

$$\left\langle n(J \mp 1, 1)JT \right| c_r^\dagger c_\Omega^\dagger v_q c_\Omega c_r \left| n'(J \mp 1, 1)JT \right\rangle$$

$$= \int dr \left\{ u_{n,J\mp1}^*(r)\, u_{n',J\mp1}(r) \left[\widetilde{v}_q(\mathrm{r})\, w(\mathrm{r}) + \widetilde{v}_q(\mathrm{r})\, \widetilde{\theta}_J'(r)^2 - \widetilde{v}_q'(\mathrm{r}) \frac{R_+''(r)}{[R_+'(r)]^2} \right] \right.$$

$$\left. - \frac{1}{2} \left[u_{n,J\mp1}^*(r)\, u_{n',J\mp1}''(r) + u_{n,J\mp1}''^*(r)\, u_{n',J\mp1}(r) \right] \frac{\widetilde{v}_q(r)}{[R_+'(r)]^2} \right\} \tag{A.23}$$

with $\widetilde{\theta}'(\mathrm{r}) = \theta'(R_+(\mathrm{r}))$. Finally, the off-diagonal matrix elements are

$$\left\langle n(J \mp 1, 1)JT \right| c_r^\dagger c_\Omega^\dagger v_q c_\Omega c_r \left| n'(J \pm 1, 1)JT \right\rangle$$

$$= \pm \int dr \left[u_{n,J\mp1}^*(r)\, u_{n',J\pm1}'(r) - u_{n,J\mp1}'^*(r)\, u_{n',J\pm1}(r) \right] \times \frac{\widetilde{v}_q(r)\, \widetilde{\theta}'_J(r)}{R_+'(r)} . \tag{A.24}$$

Kinetic Energy

The matrix elements of the correlated angular and radial kinetic energies are special cases of Eqs. (A.16) to (A.18) and Eqs. (A.21) to (A.24), respectively, and can be obtained by using $1/(2\mu \mathrm{r}^2)$ and $1/2\mu$ as radial dependencies in the corresponding matrix elements for l^2 or q_r^2 interactions.

A.3 Correlated Operators

A.3.1 Central Correlated Operators

For the basic operators appearing in the NN interaction, the effect of the central correlator is given by

$$c_r^\dagger \mathbf{r}\, c_r = R_+(\mathrm{r})\hat{\mathbf{r}} , \qquad\qquad c_r^\dagger \mathrm{r}\, c_r = R_+(\mathrm{r}) , \tag{A.25a}$$

$$c_r^\dagger \hat{\mathbf{r}}\, c_r = \hat{\mathbf{r}} , \tag{A.25b}$$

$$c_r^\dagger \mathrm{q}_r c_r = \frac{1}{\sqrt{R_+(\mathrm{r})}} \mathrm{q}_r \frac{1}{\sqrt{R_+(\mathrm{r})}} , \qquad\qquad c_r^\dagger \mathrm{q}_{\Omega k} c_r = \frac{\mathrm{r}}{R_+(\mathrm{r})} \mathrm{q}_{\Omega k} , \tag{A.25c}$$

$$c_r^\dagger \mathbf{l}\, c_r = \mathbf{l} , \qquad\qquad c_r^\dagger \boldsymbol{\sigma}\, c_r = \boldsymbol{\sigma} . \tag{A.25d}$$

Spin and isospin operators are obviously not affected.

Starting from a two-body Hamiltonian containing the NN interaction as well as the kinetic energy, separated into center-of-mass and relative contributions, we obtain the central correlated Hamiltonian

$$c_r^\dagger h c_r = t_{\text{cm}} + t_r + t_\Omega + \widetilde{t}_r^{[2]} + \widetilde{t}_\Omega^{[2]} + \widetilde{v}^{[2]} \,, \tag{A.26}$$

The correlated radial kinetic energy is given by

$$\widetilde{t}_r^{[2]} = c_r^\dagger t_r c_r - t_r = \frac{1}{2} \left(q_r^2 \frac{1}{2\widetilde{\mu}_r(\text{r})} + \frac{1}{2\widetilde{\mu}_r(\text{r})} q_r^2 \right) + \widetilde{w}(\text{r}) \tag{A.27}$$

with the r-dependent effective mass

$$\frac{1}{2\widetilde{\mu}_r(\text{r})} = \frac{1}{2\mu} \left(\frac{1}{[R'_+(\text{r})]^2} - 1 \right) \tag{A.28}$$

and the additional local potential

$$w(\text{r}) = \frac{1}{2\mu} \left(\frac{7 R''_+(\text{r})^2}{4 R'_+(\text{r})^4} - \frac{R'''_+(\text{r})}{2 R'_+(\text{r})^3} \right) \,. \tag{A.29}$$

Applying the correlator to the angular part of the correlated kinetic energy yields

$$\widetilde{t}_\Omega^{[2]} = c_r^\dagger t_\Omega c_r - t_\Omega = \frac{1}{2\widetilde{\mu}_\Omega(\text{r})} \frac{\mathbf{l}^2}{\text{r}^2} \,, \tag{A.30}$$

with another distance-dependent mass term

$$\frac{1}{2\widetilde{\mu}_\Omega(\text{r})} = \frac{1}{2\mu} \left(\frac{\text{r}^2}{R_+^2(\text{r})} - 1 \right) \,. \tag{A.31}$$

Analogously, the momentum-dependent potential becomes

$$\widetilde{v}_q = c_r^\dagger v_q c_r = \frac{1}{2} \left(q_r^2 \frac{v_q(R_+(\text{r}))}{[R'_+(\text{r})]^2} + \frac{v_q(R_+(\text{r}))}{[R'_+(\text{r})]^2} q_r^2 \right)$$
$$+ v_q(R_+(\text{r})) w(\text{r}) - v_q(R_+(\text{r})) \frac{R''_+(\text{r})}{[R'_+(\text{r})]^2} \,. \tag{A.32}$$

Since all other operators in the NN interaction commute with r and q_r, only the radial dependencies are affected by the correlator, and using the unitarity of c_r we obtain

$$c_r^\dagger v_p(\text{r}) o_p c_r = v_p(R_+(\text{r})) o_p \,. \tag{A.33}$$

Tensor Correlated Operators

Using

$$\widetilde{c}_\Omega = c_r^\dagger c_\Omega c_r = \vartheta(R_+(\text{r})) s_{12}(\mathbf{r}, \mathbf{q}_\Omega) \,, \tag{A.34}$$

the fully correlated Hamiltonian

$$\widetilde{c}_\Omega^\dagger \left(c_r^\dagger h c_r \right) \widetilde{c}_\Omega = e^{i\widetilde{g}_\Omega} \left(c_r^\dagger h c_r \right) e^{-i\widetilde{g}_\Omega} \tag{A.35}$$

can be calculated by using the Baker-Campbell-Hausdorff formula,

$$e^{i\widetilde{g}_\Omega}\left(c_r^\dagger hc_r\right)e^{-i\widetilde{g}_\Omega} = \left(c_r^\dagger hc_r\right) + i\left[g_\Omega, \left(c_r^\dagger hc_r\right)\right] + \frac{i^2}{2}\left[g_\Omega, \left[g_\Omega, \left(c_r^\dagger hc_r\right)\right]\right] + \ldots. \quad (A.36)$$

For r, q_r, and q_r^2, the BCH series terminates,

$$c_\Omega^\dagger r c_\Omega = r, \quad (A.37)$$

$$c_\Omega^\dagger q_r c_\Omega = q_r - \vartheta'(r)s_{12}(\mathbf{r}, \mathbf{q}_\Omega), \quad (A.38)$$

$$c_\Omega^\dagger q_r^2 c_\Omega = q_r^2 - \left(q_r\vartheta'(r) + \vartheta'(r)q_r\right)s_{12}(\mathbf{r}, \mathbf{p}_\Omega) + \vartheta'(r)^2 s_{12}(\mathbf{r}, \mathbf{q}_\Omega)^2, \quad (A.39)$$

but for all other operators, the commutators with $s_{12}(\mathbf{r}, \mathbf{q}_\Omega)$ generate increasing powers of angular momentum and non-local tensor operators, and the series needs to be truncated in practical applications. The following sections list the algebraic relations required to evaluate the BCH series up to third order, which reproduces the exact correlated matrix elements of Sect. A.2 sufficiently well [8, 9].

A.3.2 Decomposition Formulae for Reducible Tensor Operators

In this section we list decomposition formulas for reducible tensor operators occurring in the correlated and uncorrelated NN interactions. The derivation was performed in [18], using the irreducible spherical tensor representation of the operators.

$$(\mathbf{l}\cdot\mathbf{s})^2 = \frac{2}{3}\mathbf{l}^2\Pi_{S=1} - \frac{1}{2}\mathbf{l}\cdot\mathbf{s} + \frac{1}{6}s_{12}(\mathbf{l}, \mathbf{l}) \quad (A.40)$$

$$\bar{s}_{12}(\mathbf{q}_\Omega, \mathbf{q}_\Omega) = 2r^2 s_{12}(\mathbf{q}_\Omega, \mathbf{q}_\Omega)12 + s_{12}(\mathbf{l}, \mathbf{l}) - \frac{1}{2}s_{12}(\hat{\mathbf{r}}, \hat{\mathbf{r}}) \quad (A.41)$$

$$s_{12}(\mathbf{r}, \mathbf{q}_\Omega)^2 = 6(\mathbf{l}^2 + 3)\Pi_{S=1} + \frac{45}{2}\mathbf{l}\cdot\mathbf{s} + \frac{3}{2}s_{12}(\mathbf{l}, \mathbf{l}) \quad (A.42)$$

The explicit dependencies of the tensor operators on the *radial coordinate* are cancelled by corresponding factors of $\mathbf{q}_\Omega$ (see (A.5) or (A.52)), hence they only act on directional variables in coordinate space.

A.3.3 Algebra of Tensor Operators

This section lists the algebraic relations needed to calculate tensor-correlated interactions up to next-to-next-to-leading order in angular momentum, as derived in Ref. [18].

$$\left[s_{12}(\mathbf{r}, \mathbf{q}_\Omega), s_{12}(\hat{\mathbf{r}}, \hat{\mathbf{r}})\right] = -24i\,\Pi_{S=1} - 18i\,\mathbf{l}\cdot\mathbf{s} + 3i\,s_{12}(\hat{\mathbf{r}}, \hat{\mathbf{r}}) \quad (A.43)$$

$$\left[s_{12}(\mathbf{r}, \mathbf{q}_\Omega), \mathbf{l}\cdot\mathbf{s}\right] = -i\,\bar{s}_{12}(\mathbf{q}_\Omega, \mathbf{q}_\Omega) \quad (A.44)$$

$$\left[s_{12}(\mathbf{r}, \mathbf{q}_\Omega), \mathbf{l}^2\right] = 2i\,\bar{s}_{12}(\mathbf{q}_\Omega, \mathbf{q}_\Omega) \quad (A.45)$$

$$\left[s_{12}(\mathbf{r}, \mathbf{q}_\Omega), s_{12}(\mathbf{l}, \mathbf{l})\right] = 7i\,\bar{s}_{12}(\mathbf{q}_\Omega, \mathbf{q}_\Omega) \quad (A.46)$$

$$\left[s_{12}(\mathbf{r}, \mathbf{q}_\Omega), \bar{s}_{12}(\mathbf{q}_\Omega, \mathbf{q}_\Omega)\right] = i(96\mathbf{l}^2 + 108)\Pi_{S=1} + i(36\mathbf{l}^2 + 153)\mathbf{l}\cdot\mathbf{s}$$
$$+ 15i\,s_{12}(\mathbf{l}, \mathbf{l}) \quad (A.47)$$

$$
\big[s_{12}(\mathbf{r}, \mathbf{q}_\Omega), \mathbf{l}^2 \mathbf{l} \cdot \mathbf{s}\big] = -3i\bar{s}_{12}(\mathbf{q}_\Omega, \mathbf{q}_\Omega)
$$

$$
- \frac{i}{2}\big(\mathbf{l}^2 \bar{s}_{12}(\mathbf{q}_\Omega, \mathbf{q}_\Omega) + \bar{s}_{12}(\mathbf{q}_\Omega, \mathbf{q}_\Omega)\mathbf{l}^2\big) \tag{A.48}
$$

$$
\big[s_{12}(\mathbf{r}, \mathbf{q}_\Omega), \mathbf{l}^2 \bar{s}_{12}(\mathbf{q}_\Omega, \mathbf{q}_\Omega)\big] = i(144\,\mathbf{l}^4 + 600\,\mathbf{l}^2 + 324)\Pi_{S=1}
$$

$$
+ i(36\,\mathbf{l}^4 + 477\,\mathbf{l}^2 + 477)\mathbf{l} \cdot \mathbf{s} + i(27\,\mathbf{l}^2 + 51)s_{12}(\mathbf{l}, \mathbf{l}) \tag{A.49}
$$

A.3.4   Reduced Matrix Elements

The Wigner-Eckart Theorem

In the conventions of the Particle Data Group [137], the *Wigner-Eckart theorem* reads

$$
\big\langle\, n'j'm'\,\big|\, t_q^{(k)}\,\big|\, njm\,\big\rangle = (-1)^{2k}\,\big\langle\, jmkq\big|j'm'\,\big\rangle \frac{\big\langle\, n'j'\big|\big|\, t^{(k)}\,\big|\big|nj\,\big\rangle}{\sqrt{2j'+1}} \tag{A.50}
$$

where $t_q^{(k)}$ is an irreducible spherical tensor operator of rank k. The factor $\frac{1}{\sqrt{2j'+1}}$ is sometimes included in the definition of the reduced matrix element in the literature.

Coordinate Space Operators

The reduced matrix elements of the basic operators $\mathbf{r}$, $\mathbf{q}_\Omega$, and $\mathbf{l}$ in angular momentum eigenstates are needed to calculate the matrix elements of the various tensor operators. All of the above operators are vector operators, hence they only connect states with $\Delta l = \pm 1$, while all other matrix elements vanish.

$$
\big\langle\, l'\,\big|\big|\, r_q^{(1)}\,\big|\big|\, l\,\big\rangle = (\sqrt{l+1}\,\delta_{l',l+1} - \sqrt{l}\,\delta_{l',l-1})r\,, \tag{A.51}
$$

$$
\big\langle\, l'\,\big|\big|\, q_{\Omega,q}^{(1)}\,\big|\big|\, l\,\big\rangle = \Big((l+1)^{3/2}\delta_{l',l+1} + l^{3/2}\delta_{l',l-1}\Big)\frac{i}{r} \tag{A.52}
$$

and

$$
\big\langle\, l'\,\big|\big|\, l_q^{(1)}\,\big|\big|\, l\,\big\rangle = \sqrt{l(l+1)(2l+1)}\,\delta_{ll'}\,. \tag{A.53}
$$

Spin Operators

In spin space, we need the matrix elements of the total spin operator

$$
s^{(1)} = \frac{1}{2}\Big(\sigma^{(1)} \otimes \mathbb{1} + \mathbb{1} \otimes \sigma^{(1)}\Big)\,, \tag{A.54}
$$

and the rank 2 tensor operator which is needed to construct cartesian tensor operators $s_{12}(\mathbf{a}, \mathbf{b})$:

$$
s^{(2)} = \Big\{s^{(1)}s^{(1)}\Big\}^{(2)}\,. \tag{A.55}
$$

The only non-vanishing matrix elements are between $s = 1$ states:

$$
\big\langle\, 1\,\big|\big|\, s^{(1)}\,\big|\big|\, 1\,\big\rangle = \sqrt{6} \tag{A.56}
$$

and

$$
\big\langle\, 1\,\big|\big|\, s^{(2)}\,\big|\big|\, 1\,\big\rangle = 2\sqrt{5}\,. \tag{A.57}
$$

Coupling Formulae

In general, two irreducible spherical tensor operators of ranks k_1 and k_2 which act on the same Hilbert space can be coupled to an irreducible tensor operator of rank k by using the Clebsch-Gordan coefficients:

$$\left\{ a^{(k_1)} b^{(k_2)} \right\}_q^{(k)} = \sum_{q_1, q_2} \left\langle k_1 q_1, k_2 q_2 \middle| k q \right\rangle a_{q_1}^{(k_1)} b_{q_2}^{(k_2)} . \tag{A.58}$$

In some cases, we will need a hermitized coupled product, which will be denoted by the shorthand expression

$$(ab)_q^{(k)} = \frac{1}{2} \left(\left\{ a^{(k_1)} b^{(k_2)} \right\}_q^{(k)} + \left\{ b^{(k_2)} a^{(k_1)} \right\}_q^{(k)} \right) \tag{A.59}$$

For two spherical tensor operators of rank 1 which act on different Hilbert spaces, Eq. (A.58) defines a scalar product by

$$a^{(1)} \cdot t^{(1)} = -\sqrt{3} \left\{ a^{(1)} \otimes t^1 \right\}^{(0)} , \tag{A.60}$$

and for rank 2 tensor operators one finds

$$a^{(2)} \cdot t^{(2)} = -\sqrt{5} \left\{ a^{(2)} \otimes t^2 \right\}^{(0)} . \tag{A.61}$$

(The tensor product sign indicates that the operators act on different spaces.) Examples are the spin-orbit and tensor operators: For the former, the scalar product reads

$$\mathbf{l} \cdot \mathbf{s} = l^{(1)} \cdot s^{(1)} = -\sqrt{3} \left\{ l^{(1)} \otimes s^{(1)} \right\}^{(0)} , \tag{A.62}$$

and the latter is given by

$$\begin{aligned} s_{12}(\mathbf{a}, \mathbf{b}) &= \frac{3}{2} \left[(\boldsymbol{\sigma}_1 \cdot \mathbf{a})(\boldsymbol{\sigma}_2 \cdot \mathbf{b}) - (\boldsymbol{\sigma}_1 \cdot \boldsymbol{\sigma}_2)(\mathbf{a} \cdot \mathbf{b}) + \mathbf{a} \leftrightarrow \mathbf{b} \right] \\ &= 3 \left\{ a^{(1)} b^{(1)} \right\}^{(2)} \cdot s^{(2)} = 3\sqrt{5} \left\{ (ab)^{(2)} \otimes s^{(2)} \right\}^{(0)} , \end{aligned} \tag{A.63}$$

where the operators $s^{(1)}$ and $s^{(2)}$ act on spin space.

The reduced matrix element of a product of coordinate space operators can be calculated with the help of the Wigner $6j$-symbols [138]:

$$\begin{aligned} &\left\langle l' \middle| \middle| \{ a^{(k_1)} b^{(k_2)} \}^{(k)} \middle| \middle| l \right\rangle = \\ &(-1)^{l'+l-k} \sqrt{2k+1} \sum_{l''} \begin{Bmatrix} k_1 & k_2 & k \\ l & l' & l'' \end{Bmatrix} \left\langle l' \middle| \middle| a^{(k_1)} \middle| \middle| l'' \right\rangle \left\langle l'' \middle| \middle| b^{(k_2)} \middle| \middle| l \right\rangle . \end{aligned} \tag{A.64}$$

The reduced matrix element of a scalar product between two rank-k tensor operators $a^{(k)}$ in coordinate and $s^{(k)}$ in spin space can be calculated using [138]

$$\begin{aligned} &\left\langle (l'1)j \middle| \middle| r^{(k)} \cdot s^{(k)} \middle| \middle| (l1)j \right\rangle = \\ &(-1)^{j+l+1} \sqrt{2j+1} \begin{Bmatrix} l' & l & k \\ 1 & 1 & j \end{Bmatrix} \left\langle l' \middle| \middle| r^{(k)} \middle| \middle| l \right\rangle \left\langle 1 \middle| \middle| s^{(k)} \middle| \middle| 1 \right\rangle . \end{aligned} \tag{A.65}$$

The $6j$-symbol enters due to the switching from the uncoupled (l, s)-basis of the respective matrix elements to the $(ls)j$-coupled basis spanning the appropriate irreducible representation of the rotation group for such scalar products.

Example: $s_{12}(\mathbf{r}, \mathbf{q}_\Omega)$

As a sample application of the coupling formulae presented in the previous subsection, we derive the matrix elements of $s_{12}(\mathbf{r}, \mathbf{q}_\Omega)$, which is used to construct the generator of tensor correlations g_Ω. In coordinate space, the reduced matrix elements of $(rq_\Omega)^{(2)}$ need to be evaluated:

$$
\begin{aligned}
\langle\, l'\,||\, \{rq_\Omega\}^{(2)}\,||\,l\,\rangle &= (-1)^{l'+l-2}\sqrt{5}\sum_{l''}\begin{Bmatrix} 1 & 1 & 2 \\ l & l' & l'' \end{Bmatrix}\langle\, l'\,||\, \mathrm{r}^{(1)}\,||\,l''\,\rangle\langle\, l''\,||\, \mathrm{q}_\Omega^{(1)}\,||\,l\,\rangle \\
&= (-1)^{l'+l-2}\sqrt{5}\sum_{l''}\begin{Bmatrix} 1 & 1 & 2 \\ l & l' & l'' \end{Bmatrix}\left(\sqrt{l''+1}\,\delta_{l',l''+1} - \sqrt{l''}\,\delta_{l',l''-1}\right)r \\
&\qquad\times \frac{i}{r}\left((l+1)^{3/2}\delta_{l'',l+1} - (l)^{3/2}\delta_{l'',l-1}\right) \\
&= i\sqrt{5}\left(\begin{Bmatrix} 1 & 1 & 2 \\ l & l' & l+1 \end{Bmatrix}\left(\sqrt{l+2}(l+1)^{3/2}\delta_{l',l+2} - (l+1)^2\delta_{ll'}\right)\right. \\
&\qquad\left.+ \begin{Bmatrix} 1 & 1 & 2 \\ l & l' & l-1 \end{Bmatrix}\left(l^2\delta_{ll'} - \sqrt{l-1}\,l^{3/2}\delta_{l',l-2}\right)\right),
\end{aligned}
\tag{A.66}
$$

where the exponent $(-1)^{l'+l-2}$ is always even due to the Kronecker deltas, i.e., the factor is always 1. A similar calculation yields

$$
\begin{aligned}
\langle\, l'\,||\, \{q_\Omega r\}^{(2)}\,||\,l\,\rangle = i\sqrt{5}\left(\begin{Bmatrix} 1 & 1 & 2 \\ l & l' & l+1 \end{Bmatrix}\left(\sqrt{l+1}(l+2)^{3/2}\delta_{l',l+2} + (l+1)^2\delta_{ll'}\right)\right. \\
\left.- \begin{Bmatrix} 1 & 1 & 2 \\ l & l' & l-1 \end{Bmatrix}\left(l^2\delta_{ll'} + \sqrt{l}(l-1)^{3/2}\delta_{l',l-2}\right)\right),
\end{aligned}
\tag{A.67}
$$

and using

$$
\begin{Bmatrix} 1 & 1 & 2 \\ l & l+2 & l+1 \end{Bmatrix} = \frac{1}{\sqrt{5}}\frac{1}{\sqrt{2l+3}},\quad \begin{Bmatrix} 1 & 1 & 2 \\ l & l-2 & l-1 \end{Bmatrix} = \frac{1}{\sqrt{5}}\frac{1}{\sqrt{2l-1}},
\tag{A.68}
$$

we finally obtain

$$
\begin{aligned}
\langle\, l'\,||\,& (rq_\Omega)^{(2)}\,||\,l\,\rangle \\
&= \frac{i}{2}\left(\sqrt{(l+1)(l+2)(2l+3)}\,\delta_{l',l+2} - \sqrt{(l-1)l(2l-1)}\,\delta_{l',l-2}\right).
\end{aligned}
\tag{A.69}
$$

With

$$
\begin{Bmatrix} j+1 & j-1 & 2 \\ 1 & 1 & j \end{Bmatrix} = \begin{Bmatrix} j-1 & j+1 & 2 \\ 1 & 1 & j \end{Bmatrix} = \frac{1}{\sqrt{5}}\frac{(-1)^{2j}}{\sqrt{2j+1}}
\tag{A.70}
$$

Eq. (A.65) now yields

$$
\langle\, (j\pm 1,1)j\,||\, s_{12}(\mathbf{r},\mathbf{q}_\Omega)\,||\,(j\mp 1,1)j\,\rangle = \pm 3i\sqrt{j(j+1)(2j+1)}.
\tag{A.71}
$$

$l = l'$	$s_{12}(\hat{\mathbf{r}}, \hat{\mathbf{r}})$	$s_{12}(\mathbf{l}, \mathbf{l})$	$s_{12}(\mathbf{q}_\Omega, \mathbf{q}_\Omega)$
$j-1$	$-2\dfrac{j-1}{\sqrt{2j+1}}$	$\sqrt{2j+1}(j-1)(2j-3)$	$-\dfrac{1}{r^2}\dfrac{j-1}{\sqrt{2j+1}}(2j^2-(2j+1))$
j	$2\sqrt{2j+1}$	$-\sqrt{2j+1}(2j-1)(2j+3)$	$-\dfrac{1}{r^2}\sqrt{2j+1}(2j^2+2j-1)$
$j+1$	$-2\dfrac{j+2}{\sqrt{2j+1}}$	$\sqrt{2j+1}(j+2)(2j+3)$	$-\dfrac{1}{r^2}\dfrac{j+2}{\sqrt{2j+1}}(2j^2+3(2j+1))$

Table A.1: Non-vanishing diagonal reduced matrix elements $\left\langle (l1)j \middle\| \mathrm{o} \middle\| (l'1)j \right\rangle$.

(l, l')	$(j \mp 1, j \pm 1)$
$s_{12}(\hat{\mathbf{r}}, \hat{\mathbf{r}})$	$6\sqrt{\dfrac{j(j+1)}{(2j+1)}}$
$s_{12}(\mathbf{r}, \mathbf{q}_\Omega)$	$\mp 3i\sqrt{j(j+1)(2j+1)}$
$s_{12}(\mathbf{q}_\Omega, \mathbf{q}_\Omega)$	$-\dfrac{6}{r^2}\sqrt{\dfrac{(j(j+1))^3}{2j+1}}$
$\bar{s}_{12}(\mathbf{q}_\Omega, \mathbf{q}_\Omega)$	$-3\sqrt{j(j+1)(2j+1)^3}$
$(\mathbf{l}^2\bar{s}_{12}(\mathbf{q}_\Omega, \mathbf{q}_\Omega))_h$	$-3(j(j+1)+1)\sqrt{j(j+1)(2j+1)^3}$

Table A.2: Non-vanishing off-diagonal reduced matrix elements $\left\langle (l1)j \middle\| \mathrm{o} \middle\| (l'1)j \right\rangle$.

Tables of Reduced Matrix Elements

The non-vanishing reduced matrix elements of $s_{12}(\hat{\mathbf{r}}, \hat{\mathbf{r}})$ and the various UCOM tensor operators are listed in tables A.1 and A.2. The subscript h indicates that the operator

$$\left(\mathbf{l}^2\,\bar{s}_{12}(\mathbf{q}_\Omega, \mathbf{q}_\Omega)\right)_h \equiv \frac{1}{2}(\mathbf{l}^2\,\bar{s}_{12}(\mathbf{q}_\Omega, \mathbf{q}_\Omega) + \bar{s}_{12}(\mathbf{q}_\Omega, \mathbf{q}_\Omega)\,\mathbf{l}^2), \tag{A.72}$$

is hermitized, which is necessary since $\mathbf{l}^2$ and $\bar{s}_{12}(\mathbf{q}_\Omega, \mathbf{q}_\Omega)$ do not commute.

A.4 Correlator Parameters

This section lists the parameters of the correlation functions employed in this work. Details on their determination can be found in Ref. [6].

$$R_+^{\mathrm{I}}(r) = r + \alpha\,(r/\beta)^\eta \exp[-\exp(r/\beta)] \tag{A.73}$$

$$R_+^{\mathrm{II}}(r) = r + \alpha\,[1 - \exp(-r/\gamma)]\exp[-\exp(r/\beta)] \tag{A.74}$$

$$\vartheta(r) = \alpha\,[1 - \exp(-r/\gamma)]\exp[-\exp(r/\beta)] \tag{A.75}$$

S	T	Param.	α [fm]	β [fm]	γ [fm]	η
0	0	II	0.7971	1.2638	0.4621	—
0	1	I	1.3793	0.8853	—	0.3724
1	0	I	1.3265	0.8342	—	0.4471
1	1	II	0.5665	1.3888	0.1786	—

Table A.3: Parameters of the central correlation functions $R_+(r)$ for the AV18 potential, obtained from energy minimization in the NN system (see text). Taken from [6].

T	I_ϑ [fm^3]	α [fm]	β [fm]	γ [fm]
0	0.03	491.32	0.9793	1000.0
0	0.04	521.60	1.0367	1000.0
0	0.05	539.86	1.0868	1000.0
0	0.06	542.79	1.1360	1000.0
0	0.07	543.21	1.1804	1000.0
0	0.08	541.29	1.2215	1000.0
0	0.09	536.67	1.2608	1000.0
0	0.10	531.03	1.2978	1000.0
0	0.11	524.46	1.3333	1000.0
0	0.12	517.40	1.3672	1000.0
1	0.01	-0.1036	1.5869	3.4426
1	0.02	-0.0815	1.9057	2.4204
1	0.03	-0.0569	2.1874	1.4761
1	0.04	-0.0528	2.3876	1.2610
1	0.05	-0.0463	2.6004	0.9983
1	0.06	-0.0420	2.7984	0.8141
1	0.07	-0.0389	2.9840	0.6643
1	0.08	-0.0377	3.1414	0.6115
1	0.09	-0.0364	3.2925	0.5473
1	0.10	-0.0353	3.4349	0.4997

Table A.4: Parameters of the tensor correlation functions $\vartheta(r)$ for the AV18 potential with different values I_ϑ for the range constraint obtained from energy minimization in the NN system. Taken from [6].

Appendix B

Hartree-Fock-Bogoliubov Theory and Spherical Symmetry

B.1 Time Reversal

Let us consider a spherical harmonic oscillator state $\left| nljm \right\rangle$, which is an eigenstate of the angular momentum and parity operators. Its wavefunction is given by

$$\psi_{n(l\frac{1}{2})jm}(r,\Omega) = R_{nl}(r) \cdot \sum_{m_l,m_s} \left\langle lm_l \tfrac{1}{2}m_s \big| jm \right\rangle Y_{lm_l}(\Omega)\chi_{\frac{1}{2}m_s} \,. \tag{B.1}$$

In the Condon-Shortley phase convention [139], the time reversal operation is defined by demanding that

$$\mathrm{PD}(0,\pi,0)\Theta \left| nljm \right\rangle = \left| nljm \right\rangle \,,$$

where P and Θ are the parity and time inversion operators, respectively, and $\mathrm{D}(0,\pi,0)$ is a unitary rotation by π around the y-axis. The invariance of the ket under this transformation implies that

$$\Theta \left| nljm \right\rangle = (-1)^{l+j-m} \left| nlj-m \right\rangle \,.$$

B.2 Irreducible Spherical Tensor Operators

B.2.1 Irreducible Spherical Tensor Operators

Let us start by introducing the notion of the *irreducible spherical tensor operator* (see e.g. [139, 140]).

Definition B.2.1 (Irreducible Spherical Tensor Operator)**.** An *irreducible spherical tensor operator of rank* k, $\mathrm{T}_q^{(k)}$, is a $2k+1$-component operator which transforms as

$$\mathrm{D}(R)\mathrm{T}_q^{(k)}\mathrm{D}^\dagger(R) = \sum_{q'=-k}^{k} \mathrm{T}_{q'}^{(k)} D_{q'q}^{(k)}(R) \,, \tag{B.2}$$

or, equivalently, as

$$D^\dagger(R) T_q^{(k)} D(R) = \sum_{q'=-k}^{k} D_{qq'}^{(k)*}(R) T_{q'}^{(k)} \tag{B.3}$$

under rotations. Here, $R \in SU(2)$ is a given rotation, $D(R)$ the unitary rotation operator representing R on configuration space, and $D_{qq'}^{(k)}(R)$ a Wigner D-Function.

Remark B.2.2. The above definition of irreducible spherical tensor operators is equivalent to the relation

$$\left[j_\mu, T_q^{(k)} \right] = \sqrt{j(j+1)} \left\langle kq1\mu \middle| k\mu+q \right\rangle T_{\mu+q}^{(k)}, \tag{B.4}$$

where j_μ denotes the spherical components of the angular momentum operator.

Proof. This can easily be shown by expanding Eq. (B.2) in the case of an infinitesimal rotation. $\square$

The situation is more complicated for the Hermitian adjoint $T_q^{(k)\dagger}$, because Eq. (B.2) implies that

$$D(R) T_q^{(k)\dagger} D^\dagger(R) = \sum_{q'=-k}^{k} T_{q'}^{(k)\dagger} D_{q'q}^{(k)*}(R), \tag{B.5}$$

which is incompatible with Eq. (B.2). A generalization of the Hermitian adjoint is necessary to preserve the $SU(2)$ tensor structure of the operator $T_q^{(k)}$.

Definition B.2.3 (Generalized Hermitian Adjoint). Let $T_q^{(k)}$ be an irreducible spherical tensor operator of rank k. The operator

$$\left[T^\dagger \right]_q^{(k)} \equiv (-1)^{k+q} \left(T_{-q}^{(k)} \right)^\dagger \tag{B.6}$$

is the *generalized Hermitian adjoint* of $T_q^{(k)}$.

Lemma B.2.4. *The generalized Hermitian adjoint $\left[T^\dagger \right]_q^{(k)}$ of $T_q^{(k)}$ is an irreducible spherical tensor operator of rank k.*

Proof. Starting from Eq. (B.5), we use the symmetry properties of the D-Function [138] to obtain

$$D(R) T_q^{(k)\dagger} D^\dagger(R) = \sum_{q'=-k}^{k} T_{q'}^{(k)\dagger} (-1)^{q-q'} D_{-q'-q}^{(k)}(R),$$

and subsequently

$$D(R)(-1)^{-q} T_q^{(k)\dagger} D^\dagger(R) = \sum_{q'} (-1)^{-q'} T_{q'}^{(k)\dagger} D_{-q'-q}^{(k)}(R)$$

$$= \sum_{q'} (-1)^{q'} T_{-q'}^{(k)\dagger} D_{q'-q}^{(k)}(R).$$

where we have exploited the freedom to change the summation variable from q' to $-q'$ because the sum runs over all possible spherical components. Exchanging $-q$ by q, we find that the operator $(-1)^q T_{-q}^{(k)\dagger}$ transforms like $T_q^{(k)}$, and this behavior is obviously not changed if we multiply both sides of the equation by a factor $(-1)^k$. $\square$

In the proof of Lemma B.2.4, we have seen that we are free to introduce a q-independent phase in the definition of the generalized Hermitian adjoint, because only the factor $(-1)^q$ is required to obtain the correct transformation behavior under rotations. As pointed out in [139], another factor $(-1)^k$ is necessary to properly transfer the structure of Definition B.2.3 to tensor products of irreducible spherical tensor operators. This specific choice of phase originates in the properties of the Clebsch-Gordan coefficients, as we will see in the proof of the following proposition:

Proposition B.2.5. *Let* $\mathrm{R}_q^{(k)}, \mathrm{S}_{q'}^{(k')}$ *be commuting irreducible spherical tensor operators, and*

$$\mathrm{T}_Q^{(K)} = \sum_{qq'} \langle\, kqk'q'\,|\,KQ\,\rangle\, \mathrm{R}_q^{(k)} \mathrm{S}_{q'}^{(k')}$$

their tensor product of rank K. Then

$$\big[\mathrm{T}^\dagger\big]_Q^{(K)} = \sum_{qq'} \langle\, kqk'q'\,|\,KQ\,\rangle\, \big[\mathrm{R}^\dagger\big]_q^{(k)} \big[\mathrm{S}^\dagger\big]_{q'}^{(k')} .$$

Proof. Starting from the LHS, we find

$$
\begin{aligned}
\big[\mathrm{T}^\dagger\big]_Q^{(K)} &= (-1)^{K+Q} \mathrm{T}_{-Q}^{(K)\dagger} \\
&= (-1)^{K+Q} \sum_{qq'} \langle\, kqk'q'\,|\,K-Q\,\rangle\, \mathrm{R}_q^{(k)\dagger} \mathrm{S}_{q'}^{(k')\dagger} \\
&= (-1)^{K+Q} \sum_{qq'} (-1)^{k+k'-K} \langle\, k-qk'-q'\,|\,KQ\,\rangle\, \mathrm{R}_q^{(k)\dagger} \mathrm{S}_{q'}^{(k')\dagger} \\
&= \sum_{qq'} (-1)^{k+k'+(-q-q')} \langle\, k-qk'-q'\,|\,KQ\,\rangle\, \mathrm{R}_q^{(k)\dagger} \mathrm{S}_{q'}^{(k')\dagger} \\
&= \sum_{qq'} (-1)^{k+k'+q+q'} \langle\, kqk'q'\,|\,KQ\,\rangle\, \mathrm{R}_{-q}^{(k)\dagger} \mathrm{S}_{-q'}^{(k')\dagger} \\
&= \sum_{qq'} \langle\, kqk'q'\,|\,KQ\,\rangle\, \big[\mathrm{R}^\dagger\big]_q^{(k)} \big[\mathrm{S}^\dagger\big]_{q'}^{(k')} .
\end{aligned}
$$

$\square$

B.2.2 Particle Creation and Annihilation Operators

We now consider fermionic creation and annihilation operators corresponding to a basis of j and j_z eigenstates, $|\,\alpha j m\,\rangle$. Suppressing other quantum numbers for the time being, these operators satisfy the canonical anti-commutation relations

$$\big\{\mathrm{c}_{jm}, \mathrm{c}_{j'm'}^\dagger\big\} = \delta_{jj'}\delta_{mm'} , \tag{B.7}$$

$$\big\{\mathrm{c}_{jm}, \mathrm{c}_{j'm'}\big\} = \big\{\mathrm{c}_{jm}^\dagger, \mathrm{c}_{j'm'}^\dagger\big\} = 0 . \tag{B.8}$$

Proposition B.2.6. *The creation operator* $\mathrm{c}_{jm}^\dagger$ *is an irreducible spherical tensor operator of rank j:*

$$\big[\mathrm{j}_q, \mathrm{c}_{jm}^\dagger\big] = \langle\, jm1q\,|\,jm+q\,\rangle\, \sqrt{j(j+1)}\, \mathrm{c}_{jm+q}^\dagger . \tag{B.9}$$

Proof. Using Eq. (B.2), we find:

$$[\mathrm{j}_q, \mathrm{c}_{jm}^{\dagger}] = \sum_{j'j''m'm''} \langle j'm'|\,\mathrm{j}_q\,|j''m''\rangle\,[\mathrm{c}_{j'm'}^{\dagger}\mathrm{c}_{j''m''}, \mathrm{c}_{jm}^{\dagger}]$$

$$= \sum_{j'j''m'm''} \langle j'm'|\,\mathrm{j}_q\,|j''m''\rangle\,\left\{\mathrm{c}_{j'm'}^{\dagger}\mathrm{c}_{j''m''}\mathrm{c}_{jm}^{\dagger} - \mathrm{c}_{jm}^{\dagger}\mathrm{c}_{j'm'}^{\dagger}\mathrm{c}_{j''m''}\right\}$$

$$= \sum_{j'j''m'm''} \langle j'm'|\,\mathrm{j}_q\,|j''m''\rangle\,\delta_{jj''}\delta_{mm''}\mathrm{c}_{j'm'}^{\dagger} \qquad\qquad \text{(CAC)}$$

$$= \sum_{j'm'} \langle jm1q|j'm'\rangle\,\frac{\langle j'||\mathrm{j}||j\rangle}{\sqrt{2j'+1}}\mathrm{c}_{j'm'}^{\dagger} \qquad\qquad \text{(W-E)}$$

$$= \sum_{j'm'} \langle jm1q|j'm'\rangle\,\delta_{jj'}\sqrt{j(j+1)}\mathrm{c}_{j'm'}^{\dagger}$$

$$= \langle jm1q|jm+q\rangle\,\sqrt{j(j+1)}\mathrm{c}_{jm+q}^{\dagger}.$$

In lines 3 and 4, we have used the anticommutation rules and the Wigner-Eckart Theorem, respectively. $\qquad\square$

Corollary B.2.7. *Under a rotation* $R \in SU(2)$*,* $\mathrm{c}_{jm}^{\dagger}$ *transforms as*

$$\mathrm{D}(R)\mathrm{c}_{jm}^{\dagger}\mathrm{D}^{\dagger}(R) = \sum_{m'=-j}^{j} \mathrm{c}_{jm'}^{\dagger}D_{m'm}^{(j)}(R)\,. \qquad\qquad (\text{B.10})$$

Proof. This is a direct consequence of Prop. B.2.6 and Def. B.2.1. $\qquad\square$

Corollary B.2.8. *The operator*

$$\widetilde{\mathrm{c}}_{jm} \equiv (-1)^{j+m}\mathrm{c}_{j-m} \qquad\qquad (\text{B.11})$$

is an irreducible spherical tensor operator.

Proof. This follows from $\mathrm{c}_{jm}^{\dagger}$ being an irreducible spherical tensor operator and Lemma B.2.4. $\qquad\square$

The results of the present section are not surprising. $\mathrm{c}_{jm}^{\dagger}$ obviously transforms like the ket $|jm\rangle$ it creates from the vacuum, which constitutes an irreducible spherical tensor in its own right. Likewise, c_{jm} can be understood as a creation operator for the bra $\langle jm|$ when acting to the left, but it is necessary to consider $\widetilde{\mathrm{c}}_{jm}$ to achieve compatibility between the adjoint operation and the spherical tensor structure.

Corollary B.2.9. *Up to a phase, the operator* $\widetilde{\mathrm{c}}_{jm}^{\dagger}$ *corresponds to the time-reversed creation operator* $\mathrm{c}_{jm}^{\dagger}$*,*

$$\Theta\mathrm{c}_{jm}^{\dagger}\Theta^{-1} = -\widetilde{\mathrm{c}}_{jm}^{\dagger}\,,$$

i.e., it creates particles in the state $|j-m\rangle$*.*

Proof. This immediately follows from Sect. B.1 and $(-1)^{2m} = -1$ for half-integer m. $\qquad\square$

B.3 HFB Theory

B.3.1 The Spherical Bogoliubov Transformation

Let us now study how the Bogoliubov transformation is reduced in the case of explicit rotational symmetry. For this, we assume that the particle operators create a basis of single-particle angular momentum eigenstates as in Sect. B.2.2 (other quantum numbers are suppressed), and prove the following theorem:

Theorem B.3.1. *Let* $c_{jm}^\dagger, c_{jm}$ *be creation and annihilation operators of* j^2 *and* j_z *eigenstates, and* $\beta_{jm}^\dagger$ *a quasi-particle creation operator.* $\beta_{jm}^\dagger$ *is an irreducible spherical tensor operator iff*

$$U_{j'm',jm} = u_j \delta_{jj'}\delta_{mm'}, \qquad V_{j'm',jm} = (-1)^{j'-m'}v_j\delta_{jj'}\delta_{m,-m'}. \qquad \text{(B.12)}$$

Proof. "$\Rightarrow$": Let $\beta_{jm}^\dagger$ be an irreducible spherical tensor operator. Then, for any $R \in SU(2)$,

$$D(R)\beta_{jm}^\dagger D^\dagger(R)$$

$$= D(R)\sum_{j'm'}\left(U_{j'm',jm}c_{j'm'}^\dagger + V_{j'-m',jm}(-1)^{j'-m'}(-1)^{j'+m'}c_{j'+m'}\right)D^\dagger(R)$$

$$= \sum_{j'm'}U_{j'm',jm}D(R)c_{j'm'}^\dagger D^\dagger(R) + V_{j'-m',jm}(-1)^{j'+m'}D(R)\widetilde{c}_{j'm'}D^\dagger(R)$$

$$= \sum_{j'm'm''}U_{j'm',jm}D_{m''m'}^{(j')}(R)c_{j'm''}^\dagger + V_{j'-m',jm}(-1)^{j'-m'}D_{m''m'}^{(j')}(R)\widetilde{c}_{j'm''} \qquad (*)$$

$$\stackrel{!}{=} \sum_{j'm'm''}D_{m''m}^{(j)}(R)\left(U_{j'm',jm''}c_{j'm'}^\dagger + (-1)^{j'+m'}V_{j'-m',jm''}\widetilde{c}_{j'm'}\right). \quad \text{(Def. B.2.1)}$$

Again, we made use of our trick from previous sections and changed the summation from m' to $-m'$. We now exchange m' and m'' in Eq. (*) and subtract the final line. Since the $c_{j'm'}^\dagger$ and $\widetilde{c}_{j'm'}$ have to be linearly independent, each of their coefficients has to vanish separately. We obtain the following set of equations:

$$\sum_{m''}\left(D_{m'm''}^{(j')}(R)U_{j'm'',jm} - U_{j'm',jm''}D_{m''m}^{(j)}(R)\right) = 0 \qquad \text{(I)}$$

$$\sum_{m''}\left((-1)^{j'+m''}D_{m'm''}^{(j')}(R)V_{j'-m'',jm} - (-1)^{j'+m'}V_{j'-m',jm''}D_{m''m}^{(j)}(R)\right) = 0, \qquad \text{(II)}$$

or, in matrix notation,

$$D^{(j')}(R)U_{j'j} - U_{j'j}D^{(j)}(R) = 0 \qquad \text{(I)}$$

$$D^{(j')}(R)\widehat{V}_{j'j} - \widehat{V}_{j'j}D^{(j)}(R) = 0, \qquad \text{(II)}$$

where we have defined

$$\widehat{V}_{j'm',jm} \equiv (-1)^{j'+m'}V_{j'-m',jm}.$$

We now note that the particle Hilbert space $\mathcal{H}$ can be written as the direct sum of subspaces with a given value of j,

$$\mathcal{H} = \bigoplus_j \mathcal{H}^{(j)} \, .$$

The $D^{(j)}(R)$ constitute the irreducible spin-j representation of $SU(2)$ on the carrier space $\mathcal{H}^{(j)}$, and $U_{j'j}, \widehat{V}_{j'j}$ are linear mappings acting between the j- and j'-subspaces. Realizing this, we can invoke Schur's Lemma (see e.g. [101]), which immediately tells us that $j = j'$ and both U_{jj} and $\widehat{V}_{jj}$ are proportional to the unit matrix, i.e.,

$$U_{j'm',jm} = u_j \delta_{jj'} \delta_{mm'}$$

as well as

$$\widehat{V}_{j'm',jm} = (-1)^{j'+m'} V_{j'-m',jm} \overset{!}{=} v_j \delta_{jj'} \delta_{mm'}$$
$$\Rightarrow V_{j'-m',jm} = (-1)^{j'+m'} v_j \delta_{jj'} \delta_{mm'} \, .$$

"$\Leftarrow$": Plugging U and V into the Bogoliubov transformation, we have

$$\begin{aligned}
\beta_{jm}^\dagger &= \sum_{j'm'} U_{j'm',jm} c_{j'm'}^\dagger + V_{j'm',jm} c_{j'm'} \\
&= \sum_{j'm'} u_j \delta_{jj'} \delta_{mm'} c_{j'm'}^\dagger + (-1)^{j+m} v_j \delta_{jj'} \delta_{m,-m'} c_{j'm'} \\
&= u_j c_{jm}^\dagger + (-1)^{j+m} v_j c_{j-m} \\
&= u_j c_{jm}^\dagger + v_j \widetilde{c}_{jm} \, .
\end{aligned}$$

Since u_j and v_j are manifestly independent of m, and $c_{jm}^\dagger$ as well as $\widetilde{c}_{jm}$ are irreducible spherical tensor operators as per the results of Sect. B.2.2, $\beta_{jm}^\dagger$ is also an irreducible spherical tensor operator. This concludes our proof. $\square$

Definition B.3.2 (Spherical Bogoliubov Transformation). Let $c_{jm}^\dagger, c_{jm}$ be fermionic creation and annihilation operators of j^2 and j_z eigenstates. The *spherical Bogoliubov transformation* is then defined by

$$\begin{aligned}
\beta_{jm}^\dagger &= u_j c_{jm}^\dagger + (-1)^{j+m} v_j c_{j-m} \\
\beta_{jm} &= u_j^* c_{jm} + (-1)^{j+m} v_j^* c_{j-m}^\dagger \, .
\end{aligned} \tag{B.13}$$

Keep in mind that the generalized Hermitian adjoint $\widetilde{\beta}_{jm}$ rather than the quasiparticle annihilation operator β_{jm} constitutes an irreducible spherical tensor, for the same reasons as discussed for the particle annihilation operator c_{jm} in Sect. B.2.2.

Corollary B.3.3 (Inverse Spherical Bogoliubov Transformation). *The inverse of the spherical Bogoliubov transformation in Def. B.3.2 is given by*

$$\begin{aligned}
c_{jm}^\dagger &= u_j^* \beta_{jm}^\dagger + (-1)^{j-m} v_j \beta_{j-m} \, , \\
c_{jm} &= u_j \beta_{jm} + (-1)^{j-m} v_j^* \beta_{j-m}^\dagger \, .
\end{aligned} \tag{B.14}$$

Proof. The transformation (B.13) is diagonal in j, but it can mix states with $\pm m$, i.e., *time-reversed states*. Thus, it acts on the four-dimensional particle operator space spanned by $c_{jm}^\dagger, c_{j-m}^\dagger, c_{jm}, c_{j-m}$, and the quasi-particle operator space is necessarily four-dimensional as well. Writing Eq. (B.13) in matrix form, we have

$$
\begin{pmatrix} \beta_{jm}^\dagger \\ \beta_{j-m}^\dagger \\ \beta_{jm} \\ \beta_{j-m} \end{pmatrix} = \begin{pmatrix} u_j & & & (-1)^{j+m}v_j \\ & u_j & (-1)^{j-m}v_j & \\ & (-1)^{j+m}v_j^* & u_j^* & \\ (-1)^{j-m}v_j^* & & & u_j^* \end{pmatrix} \begin{pmatrix} c_{jm}^\dagger \\ c_{j-m}^\dagger \\ c_{jm} \\ c_{j-m} \end{pmatrix},
$$

and, using the unitarity of the transformation matrix,

$$
\begin{pmatrix} c_{jm}^\dagger \\ c_{j-m}^\dagger \\ c_{jm} \\ c_{j-m} \end{pmatrix} = \begin{pmatrix} u_j^* & & & (-1)^{j-m}v_j \\ & u_j^* & (-1)^{j+m}v_j & \\ & (-1)^{j-m}v_j^* & u_j & \\ (-1)^{j+m}v_j^* & & & u_j \end{pmatrix} \begin{pmatrix} \beta_{jm}^\dagger \\ \beta_{j-m}^\dagger \\ \beta_{jm} \\ \beta_{j-m} \end{pmatrix}.
$$

$\square$

B.3.2 Density Matrix and Pairing Tensor

For a spherical HO basis, the Bogoliubov transformation reads

$$
U_{nljm,n'l'j'm'} = U_{nn'}^{(lj)}\delta_{jj'}\delta_{ll'}\delta_{mm'} \tag{B.15}
$$

$$
V_{nljm,n'l'j'm'} = (-1)^{j-m}V_{nn'}^{(lj)}\delta_{jj'}\delta_{ll'}\delta_{m-m'}. \tag{B.16}
$$

Plugging this into Eqs. (3.10) and (3.11), we obtain

$$
\begin{aligned}
\rho_{nljm,n'l'j'm'} &= \sum_{n''l''j''m''} V_{nljm,n''l''j''m''}V_{n''l''j''m'',n'l'j'm'}^T \\
&= \sum_{n''l''j''m''} (-1)^{j+m}(-1)^{j'+m'}V_{nn''}^{(lj)}V_{n''n'}^{(l'j')T}\delta_{jj''}\delta_{j'j''}\delta_{ll''}\delta_{l'l''}\delta_{m,-m''}\delta_{m'',-m'} \\
&= \sum_{n''} (-1)^{j-m}(-1)^{j'-m'}V_{nn''}^{(lj)}V_{n''n'}^{(l'j')T}\delta_{jj'}\delta_{ll'}\delta_{m,m'} \\
&= \sum_{n''} V_{nn''}^{(lj)}V_{n''n'}^{(lj)T}\delta_{jj'}\delta_{ll'}\delta_{m,m'}
\end{aligned}
$$

and

$$
\begin{aligned}
\kappa_{nljm,n'l'j'm'} &= \sum_{n''l''j''m''} V_{nljm,n''l''j''m''}U_{n''l''j''m'',n'l'j'm'}^T \\
&= \sum_{n''l''j''m''} (-1)^{j-m}V_{nn''}^{(lj)}U_{n''n'}^{(l'j')T}\delta_{jj''}\delta_{j'j''}\delta_{ll''}\delta_{l'l''}\delta_{m,-m''}\delta_{m'',m'} \\
&= \sum_{n''} (-1)^{j-m}V_{nn''}^{(lj)}U_{n''n'}^{(l'j')T}\delta_{jj'}\delta_{ll'}\delta_{m,-m'}.
\end{aligned}
$$

We can now define the matrices $\rho_{nn'}^{(lj)}$ and $\kappa_{nn'}^{(lj)}$:

$$\rho_{nljm,n'l'j'm'} = \left[VV^T\right]_{nn'}^{(lj)}\delta_{jj'}\delta_{ll'}\delta_{mm'} \equiv \rho_{nn'}^{(lj)}\delta_{jj'}\delta_{ll'}\delta_{mm'}\,, \tag{B.17}$$

$$\kappa_{nljm,n'l'j'm'} = (-1)^{j-m}\left[VU^T\right]_{nn'}^{(lj)}\delta_{jj'}\delta_{ll'}\delta_{m-m'} \equiv (-1)^{j-m}\kappa_{nn'}^{(lj)}\delta_{jj'}\delta_{ll'}\delta_{m-m'}\,, \tag{B.18}$$

which are both symmetric and real. While the symmetry is quite obvious for $\rho_{nn'}^{(lj)}$, it might come as a surprise in the case of $\kappa_{nn'}^{(lj)}$, since $\kappa_{nljm,n'l'j'm'}$ is antisymmetric. However,

$$\kappa_{n'l'j'm',nljm} = (-1)\kappa_{nljm,n'l'j'm'}$$

$$\Leftrightarrow \qquad (-1)^{j-m'}\kappa_{n'n}^{(lj)}\delta_{m,-m'} = -(-1)^{j-m}\kappa_{nn'}^{(lj)}\delta_{m,-m'}$$

$$\Leftrightarrow \qquad (-1)^{j+m}\kappa_{n'n}^{(lj)} = -(-1)^{j-m}\kappa_{nn'}^{(lj)}$$

$$\Leftrightarrow \qquad \kappa_{nn'}^{(lj)} = -(-1)^{2j}\kappa_{n'n}^{(lj)}.$$

Now note that j is always half-integer, hence $2j$ is always odd and

$$\kappa_{nn'}^{(lj)} = \kappa_{n'n}^{(lj)}\,. \tag{B.19}$$

B.3.3   The Hartree-Fock Field Γ

The Hartree-Fock field defining the particle-hole interaction is obtained by contracting the two-body interaction matrix elements with a single density matrix. In our spherical HO basis, we have

$$\Gamma_{n_1l_1j_1m_1,n_1'l_1'j_1'm_1'} \equiv \sum_{\substack{n_2l_2j_2m_2\\n_2'l_2'j_2'm_2'}} \bar{v}_{n_1l_1j_1m_1n_2l_2j_2m_2,n_1'l_1'j_1'm_1'n_2'l_2'j_2'm_2'}\rho_{n_2'l_2'j_2'm_2',n_2l_2j_2m_2}\,, \tag{B.20}$$

where $\bar{v}$ is the antisymmetrized interaction matrix element. Using Eq. (B.17), we can eliminate the sums over the primed indices save the n_2'-summation, and obtain

$$\Gamma_{n_1l_1j_1m_1,n_1'l_1'j_1'm_1'} = \sum_{\substack{l_2j_2m_2\\n_2n_2'}} \bar{v}_{n_1l_1j_1m_1n_2l_2j_2m_2,n_1'l_1'j_1'm_1'n_2'l_2j_2m_2}\rho_{n_2'n_2}^{(l_2j_2)}$$

$$= \sum_{\substack{l_2j_2m_2\\n_2n_2'}} \sum_{JM,J'M'} \left\langle j_1m_1j_2m_2\middle|JM\right\rangle\left\langle J'M'\middle|j_1'm_1'j_2m_2\right\rangle$$

$$\times\left\langle n_1l_1j_1n_2l_2j_2JM\middle|\bar{v}\middle|n_1'l_1'j_1'n_2'l_2j_2J'M'\right\rangle\rho_{n_2'n_2}^{(l_2j_2)}\,.$$

Since $\bar{v}$ is a scalar operator, the Wigner-Eckart theorem implies that

$$\left\langle n_1l_1j_1n_2l_2j_2JM\middle|\bar{v}\middle|n_1'l_1'j_1'n_2'l_2j_2J'M'\right\rangle = \delta_{JJ'}\delta_{MM'}$$

$$\times\frac{\left\langle n_1l_1j_1n_2l_2j_2J\middle|\middle|\bar{v}\middle|\middle|n_1'l_1'j_1'n_2'l_2j_2J\right\rangle}{\sqrt{2J+1}}\,,$$

and the sums over J' and M' collapse. Using [138]

$$\sum_{m_2M} \left\langle j_1m_1j_2m_2\middle|JM\right\rangle\left\langle JM\middle|j_1'm_1'j_2m_2\right\rangle = \frac{2J+1}{2j_1+1}\delta_{j_1j_1'}\delta_{m_1m_1'}\,,$$

we finally obtain

$$
\Gamma_{n_1 l_1 j_1 m_1, n_1' l_1' j_1' m_1'} = \delta_{j_1 j_1'} \delta_{m_1 m_1'} \sum_{\substack{l_2 j_2 J \\ n_2 n_2'}} \frac{2J+1}{2j_1+1} \frac{\left\langle n_1 l_1 j_1 n_2 l_2 j_2 J \left|\right| \bar{v} \left|\right| n_1' l_1 j_1 n_2' l_2 j_2 J \right\rangle}{\sqrt{2J+1}} \rho_{n_2' n_2}^{(l_2 j_2)}
$$

$$
\equiv \delta_{j_1 j_1'} \delta_{l_1 l_1'} \delta_{m_1 m_1'} \Gamma_{n_1 n_1'}^{(l_1 j_1)}, \tag{B.21}
$$

where the symmetric matrix $\Gamma_{nn'}^{(lj)}$ is also diagonal in l due to parity conservation by $\bar{v}$ (i.e., $(-1)^{l_1} = (-1)^{l_1'}$ for $j_1 = j_1'$).

The use of the intrinsic kinetic energy rather than the total kinetic energy (cf. Sect. 3.1.4) corresponds to the replacement

$$
\bar{v} \longrightarrow \bar{v} + \frac{2}{A} \bar{t}_{\text{int}}
$$

in the equations above.

B.3.4   The Pairing Field Δ

In this section, we repeat the analysis of the Sect. B.3.3 for the pairing field Δ:

$$
\Delta_{n_1 l_1 j_1 m_1, n_1' l_1' j_1' m_1'} \equiv \frac{1}{2} \sum_{\substack{n_2 l_2 j_2 m_2 \\ n_2' l_2' j_2' m_2'}} \bar{v}_{n_1 l_1 j_1 m_1 n_1' l_1' j_1' m_1', n_2 l_2 j_2 m_2 n_2' l_2' j_2' m_2'} \kappa_{n_2 l_2 j_2 m_2, n_2' l_2' j_2' m_2'} .
$$
$$\tag{B.22}$$

Plugging in Eq. (B.18), sums over most of the primed indices collapse, and we have

$$
\Delta_{n_1 l_1 j_1 m_1, n_1' l_1' j_1' m_1'} = \frac{1}{2} \sum_{\substack{l_2 j_2 m_2 \\ n_2 n_2'}} \bar{v}_{n_1 l_1 j_1 m_1 n_1' l_1' j_1' m_1', n_2 l_2 j_2 m_2 n_2' l_2 j_2 -m_2} (-1)^{j_2 - m_2} \kappa_{n_2 n_2'}^{(l_2 j_2)} .
$$

Now

$$
\left\langle n_1 l_1 j_1 m_1 n_1' l_1' j_1' m_1' \right| \bar{v} \left| n_2 l_2 j_2 m_2 n_2' l_2 j_2 - m_2 \right\rangle
$$
$$
= \sum_{JM} \left\langle j_1 m_1 j_1' m_1' \middle| JM \right\rangle \left\langle JM \middle| j_2 m_2 j_2 - m_2 \right\rangle \frac{\left\langle n_1 l_1 j_1 n_1' l_1' j_1' J \left|\right| \bar{v} \left|\right| n_2 l_2 j_2 n_2' l_2 j_2 J \right\rangle}{\sqrt{2J+1}}
$$
$$
= \sum_{J} \left\langle j_1 m_1 j_1' m_1' \middle| J0 \right\rangle \left\langle J0 \middle| j_2 m_2 j_2 - m_2 \right\rangle \frac{\left\langle n_1 l_1 j_1 n_1' l_1' j_1' J \left|\right| \bar{v} \left|\right| n_2 l_2 j_2 n_2' l_2 j_2 J \right\rangle}{\sqrt{2J+1}} ,
$$

which implies $m_1' = -m_1$, and therefore

$$
\begin{aligned}
&\Delta_{n_1 l_1 j_1 m_1, n_1' l_1' j_1' m_1'} \\
&= \delta_{m_1, -m_1'} \frac{1}{2} \sum_{\substack{l_2 j_2 m_2 J \\ n_2 n_2'}} \big\langle j_1 m_1 j_1' - m_1 \big| J0 \big\rangle \big\langle J0 \big| j_2 m_2 j_2 - m_2 \big\rangle (-1)^{j_2 - m_2} \kappa_{n_2 n_2'}^{(l_2 j_2)} \\
&\qquad\qquad \times \frac{\big\langle n_1 l_1 j_1 n_1' l_1' j_1' J \big| \big| \, \bar{v} \, \big| \big| n_2 l_2 j_2 n_2' l_2 j_2 J \big\rangle}{\sqrt{2J+1}} \\
&= \delta_{m_1, -m_1'} \frac{1}{2} \sum_{\substack{l_2 j_2 J \\ n_2 n_2'}} \left(\sum_{m_2} (-1)^{j_2 - m_2} \big\langle J0 \big| j_2 m_2 j_2 - m_2 \big\rangle \right) \big\langle j_1 m_1 j_1' - m_1 \big| J0 \big\rangle \kappa_{n_2 n_2'}^{(l_2 j_2)} \\
&\qquad\qquad \times \frac{\big\langle n_1 l_1 j_1 n_1' l_1' j_1' J \big| \big| \, \bar{v} \, \big| \big| n_2 l_2 j_2 n_2' l_2 j_2 J \big\rangle}{\sqrt{2J+1}} \\
&= \delta_{m_1, -m_1'} \frac{1}{2} \sum_{\substack{l_2 j_2 J \\ n_2 n_2'}} \sqrt{2j_1 + 1} \, \delta_{J0} \big\langle j_1 m_1 j_1' - m_1 \big| J0 \big\rangle \kappa_{n_2 n_2'}^{(l_2 j_2)} \\
&\qquad\qquad \times \frac{\big\langle n_1 l_1 j_1 n_1' l_1' j_1' J \big| \big| \, \bar{v} \, \big| \big| n_2 l_2 j_2 n_2' l_2 j_2 J \big\rangle}{\sqrt{2J+1}} \\
&= \delta_{m_1, -m_1'} \frac{1}{2} \sum_{l_2 j_2 n_2 n_2'} \sqrt{2j_2 + 1} \big\langle j_1 m_1 j_1' - m_1 \big| 00 \big\rangle \kappa_{n_2 n_2'}^{(l_2 j_2)} \\
&\qquad\qquad \times \big\langle n_1 l_1 j_1 n_1' l_1' j_1' 0 \big| \big| \, \bar{v} \, \big| \big| n_2 l_2 j_2 n_2' l_2 j_2 0 \big\rangle \\
&= \delta_{m_1, -m_1'} \frac{1}{2} \sum_{l_2 j_2 n_2 n_2'} (-1)^{j_1 - m_1} \delta_{j_1 j_1'} \sqrt{\frac{2j_2 + 1}{2j_1 + 1}} \big\langle n_1 l_1 j_1 n_1' l_1' j_1 0 \big| \big| \, \bar{v} \, \big| \big| n_2 l_2 j_2 n_2' l_2 j_2 0 \big\rangle \kappa_{n_2 n_2'}^{(l_2 j_2)} \\
&= \delta_{j_1 j_1'} \delta_{l_1 l_1'} \delta_{m_1, -m_1'} \\
&\qquad\qquad \times (-1)^{j_1 - m_1} \frac{1}{2} \sum_{l_2 j_2 n_2 n_2'} \sqrt{\frac{2j_2 + 1}{2j_1 + 1}} \big\langle n_1 l_1 j_1 n_1' l_1 j_1 0 \big| \big| \, \bar{v} \, \big| \big| n_2 l_2 j_2 n_2' l_2 j_2 0 \big\rangle \kappa_{n_2 n_2'}^{(l_2 j_2)}.
\end{aligned}
$$

The pairing field is diagonal in l due to parity conservation by $\bar{v}$: the parity of the bra in the reduced matrix element is $(-1)^{l_1 + l_1'}$, and has to match the parity of the ket $(-1)^{2l_2}$, which is always even since l_2 is integer. Hence, $l_1 + l_1'$ must be even, and since both l_1 and l_1' need to couple with spin $s = \frac{1}{2}$ to j_1, this implies that they are equal.

We can now define a symmetric field $\Delta_{nn'}^{(lj)}$,

$$
\begin{aligned}
&\Delta_{n_1 l_1 j_1 m_1, n_1' l_1' j_1' m_1'} \\
&= \delta_{j_1 j_1'} \delta_{l_1 l_1'} \delta_{m_1, -m_1'} \\
&\qquad\qquad \times (-1)^{j_1 - m_1} \frac{1}{2} \sum_{l_2 j_2 n_2 n_2'} \sqrt{\frac{2j_2 + 1}{2j_1 + 1}} \big\langle n_1 l_1 j_1 n_1' l_1 j_1 0 \big| \big| \, \bar{v} \, \big| \big| n_2 l_2 j_2 n_2' l_2 j_2 0 \big\rangle \kappa_{n_2 n_2'}^{(l_2 j_2)} \\
&\equiv \delta_{j_1 j_1'} \delta_{l_1 l_1'} \delta_{m_1, -m_1'} (-1)^{j_1 - m_1} \Delta_{n_1 n_1'}^{(l_1 j_1)}.
\end{aligned} \tag{B.23}
$$

If the intrinsic kinetic energy (cf. Sect. 3.1.4) is used in the Hamiltonian, it will contribute to the pairing energy, and analogous to Sect. B.3.3, $\bar{v}$ will be replaced by

$$\bar{v} + \frac{2}{A}\bar{t}_{\mathrm{int}}$$

in the equations above.

B.4 Expectation Values

B.4.1 The Ground-State Energy

Generally, the ground-state energy can be written as a functional of ρ and κ:

$$E[\rho, \kappa] \equiv \frac{\langle\,\Psi\,|\,\mathrm{H}\,|\,\Psi\,\rangle}{\langle\,\Psi\,|\,\Psi\,\rangle} = \mathrm{tr}\left(\left(t + \frac{1}{2}\Gamma\right)\rho - \frac{1}{2}\Delta\kappa^*\right). \tag{B.24}$$

We evaluate the HF and pairing contributions separately, starting with E_{HF}. HF contributions can arise from one-body and two-body parts of the Hamiltonian, which will also be distinguished. For the *total kinetic energy* T we find

$$
\begin{aligned}
E_{\mathrm{HF}}^{[1]} = T &= \mathrm{tr}\, t\rho \\
&= \sum_{l_1 j_1} \sum_{\substack{m_1 n_1 \\ m_1' n_1'}} t_{n_1 n_1'}^{(l_1 j_1)} \delta_{m_1 m_1'} \rho_{n_1' n_1}^{(l_1 j_1)} \delta_{m_1 m_1'} \\
&= \sum_{l_1 j_1} \sum_{m_1 n_1 n_1'} \delta_{m_1 m_1} t_{n_1 n_1'}^{(l_1 j_1)} \rho_{n_1' n_1}^{(l_1 j_1)} \\
&= \sum_{l_1 j_1} \sum_{n_1 n_1'} (2j_1 + 1) t_{n_1 n_1'}^{(l_1 j_1)} \rho_{n_1' n_1}^{(l_1 j_1)}.
\end{aligned}
\tag{B.25}
$$

The contribution of the two-body part is given by

$$
\begin{aligned}
E_{\mathrm{HF}}^{[2]} &= \frac{1}{2}\mathrm{tr}\,\Gamma\rho \\
&= \frac{1}{2}\sum_{l_1 j_1} \sum_{\substack{m_1 n_1 \\ m_1' n_1'}} \Gamma_{n_1 n_1'}^{(l_1 j_1)} \rho_{n_1' n_1}^{(l_1 j_1)} \delta_{m_1 m_1'} \delta_{m_1 m_1'} \\
&= \frac{1}{2}\sum_{l_1 j_1} \sum_{m_1 n_1 n_1'} \delta_{m_1 m_1} \Gamma_{n_1 n_1'}^{(l_1 j_1)} \rho_{n_1' n_1}^{(l_1 j_1)} \\
&= \frac{1}{2}\sum_{l_1 j_1} \sum_{n_1 n_1'} (2j_1 + 1) \Gamma_{n_1 n_1'}^{(l_1 j_1)} \rho_{n_1' n_1}^{(l_1 j_1)}.
\end{aligned}
\tag{B.26}
$$

Separate expectation values of the two-body energy contributions are easily obtained by plugging in Eq. (B.21). For the intrinsic kinetic energy, we get

$$T_{\mathrm{int}}^{\mathrm{HF}} = \frac{1}{A} \sum_{\substack{l_1 j_1 n_1 n_1' \\ l_2 j_2 n_2 n_2'}} \sum_J \sqrt{2J+1}\,\langle\, n_1 l_1 j_1 n_2 l_2 j_2 J\,||\,\bar{\mathrm{t}}_{\mathrm{int}}\,||\,n_1' l_1 j_1 n_2' l_2 j_2 J\,\rangle\,\rho_{n_1' n_1}^{(l_1 j_1)} \rho_{n_2' n_2}^{(l_2 j_2)}$$

$$\tag{B.27}$$

and for a two-body interaction, we have

$$V^{\mathrm{HF}} = \frac{1}{2} \sum_{\substack{l_1 j_1 n_1 n_1' \\ l_2 j_2 n_2 n_2'}} \sum_J \sqrt{2J+1} \left\langle n_1 l_1 j_1 n_2 l_2 j_2 J \right| \left| \bar{\mathrm{v}} \right| \left| n_1' l_1 j_1 n_2' l_2 j_2 J \right\rangle \rho_{n_1' n_1}^{(l_1 j_1)} \rho_{n_2' n_2}^{(l_2 j_2)}, \quad \text{(B.28)}$$

where it is understood that the sum runs over all nucleons in V_{NN}^{HF}, and over protons only in the Coulomb energy V_C^{HF}.

For the pairing energy, we have

$$\begin{aligned}
E_{\mathrm{pair}} &= -\frac{1}{2} \mathrm{tr}\, \Delta \kappa^* = -\frac{1}{2} \mathrm{tr}\, \Delta \kappa \\
&= -\frac{1}{2} \sum_{l_1 j_1} \sum_{\substack{m_1 n_1 \\ m_1' n_1'}} (-1)^{j_1 - m_1} \Delta_{n_1 n_1'}^{(l_1 j_1)} (-1)^{j_1 - m_1'} \kappa_{n_1' n_1}^{(l_1 j_1)} \delta_{m_1, -m_1'} \delta_{m_1, -m_1'} \\
&= -\frac{1}{2} \sum_{l_1 j_1} \sum_{m_1 n_1 n_1'} (-1)^{j_1 - m_1} \Delta_{n_1 n_1'}^{(l_1 j_1)} (-1)^{j_1 + m_1} \kappa_{n_1' n_1}^{(l_1 j_1)} \delta_{m_1 m_1} \\
&= -\frac{1}{2} \sum_{l_1 j_1} \sum_{n_1 n_1'} (-1)^{2 j_1} (2 j_1 + 1) \Delta_{n_1 n_1'}^{(l_1 j_1)} \kappa_{n_1' n_1}^{(l_1 j_1)} \\
&= \frac{1}{2} \sum_{l_1 j_1} \sum_{n_1 n_1'} (2 j_1 + 1) \Delta_{n_1 n_1'}^{(l_1 j_1)} \kappa_{n_1' n_1}^{(l_1 j_1)}, \quad \text{(B.29)}
\end{aligned}$$

where we have used that j_1 is always half-integer, and consequentially $(-1)^{2j_1} = -1$. Evaluating this further by using Eq. (B.23) and separating the various contributions, we obtain

$$T_{\mathrm{int}}^{\mathrm{pair}} = \frac{1}{2A} \sum_{\substack{l_1 j_1 n_1 n_1' \\ l_2 j_2 n_2 n_2'}} \sqrt{(2 j_1 + 1)(2 j_2 + 1)} \left\langle n_1 l_1 j_1 n_1' l_1 j_1 0 \right| \left| \bar{\mathrm{t}}_{\mathrm{int}} \right| \left| n_2 l_2 j_2 n_2' l_2 j_2 0 \right\rangle \kappa_{n_2 n_2'}^{(l_2 j_2)} \kappa_{n_1' n_1}^{(l_1 j_1)}$$

$$\text{(B.30)}$$

and

$$V^{\mathrm{pair}} = \frac{1}{4} \sum_{\substack{l_1 j_1 n_1 n_1' \\ l_2 j_2 n_2 n_2'}} \sqrt{(2 j_1 + 1)(2 j_2 + 1)} \left\langle n_1 l_1 j_1 n_1' l_1 j_1 0 \right| \left| \bar{\mathrm{v}} \right| \left| n_2 l_2 j_2 n_2' l_2 j_2 0 \right\rangle \kappa_{n_2 n_2'}^{(l_2 j_2)} \kappa_{n_1' n_1}^{(l_1 j_1)},$$

$$\text{(B.31)}$$

where the sum again runs over all nucleons for V_{NN}^{pair} and over protons only for V_C^{pair}.

The ground state energy is then given by

$$E = T + V_{NN}^{\mathrm{HF}} + V_C^{\mathrm{HF}} + V_{NN}^{\mathrm{pair}} + V_C^{\mathrm{pair}} \quad \text{(B.32)}$$

or

$$E_{\mathrm{int}} = T_{\mathrm{int}} + V_{NN}^{\mathrm{HF}} + V_C^{\mathrm{HF}} + T_{\mathrm{int}}^{\mathrm{pair}} + V_{NN}^{\mathrm{pair}} + V_C^{\mathrm{pair}}, \quad \text{(B.33)}$$

depending on the center-of-mass treatment.

B.4.2   Radii

The calculation of mean-square and charge radii is closely analogous to the calculation of the energy expectation values. To simplify matters, we split up the calculation in several parts, starting from the two-body operator forms introduced in Sect. 2.1.3:

$$R_{\text{ms}} = \frac{1}{2A^2} \sum_{ij} \mathbf{r}_{ij}^2 \,, \tag{B.34}$$

$$R_{\text{ms}}^p = \frac{1}{AZ} \sum_{ij}^{\tau_i = +\frac{1}{2}} \mathbf{r}_{ij}^2 - \frac{1}{2A^2} \sum_{ij} \mathbf{r}_{ij}^2 \,, \tag{B.35}$$

$$R_{\text{ms}}^n = \frac{1}{AN} \sum_{ij}^{\tau_i = -\frac{1}{2}} \mathbf{r}_{ij}^2 - \frac{1}{2A^2} \sum_{ij} \mathbf{r}_{ij}^2 \,, \tag{B.36}$$

where i, j run over the nucleons, and τ_i is the isospin projection of nucleon i. As in Sect. B.4.1, the expectation values have HF and pairing contributions. Since $\mathbf{r}_{ij}^2$ can be thought of as a potential matrix element, we need not repeat all the steps of the energy calculation here, but give the results directly. Since the operators have a more complicated isospin structure, we will explicitly denote the τ quantum numbers.

The HF contribution to the total mean-square radius is

$$R_{\text{ms}}^{\text{HF}} = \frac{1}{2A^2} \sum_{\substack{l_1 j_1 n_1 n_1' \tau_1 \\ l_2 j_2 n_2 n_2' \tau_2}} \sum_{J,T} \left\langle \tfrac{1}{2}\tau_1 \tfrac{1}{2}\tau_2 \big| T\tau_1 + \tau_2 \right\rangle^2 \sqrt{2J+1}\, \rho_{n_1' n_1}^{(l_1 j_1 \tau_1)} \rho_{n_2' n_2}^{(l_2 j_2 \tau_2)}$$
$$\times \left\langle n_1 l_1 j_1 n_2 l_2 j_2 JT \big|\big| \bar{\mathbf{r}}^2 \big|\big| n_1' l_1 j_1 n_2' l_2 j_2 JT \right\rangle \,. \tag{B.37}$$

For like-particle pairing, $T = 1$ and the Clebsch-Gordan coefficients for isospin coupling are always equal to 1. Furthermore, since $\mathbf{r}^2$ is an isoscalar operator, the isospin projections cannot change either. Analogous to Eqs. (B.30) and (B.31), we then obtain the pairing contribution

$$R_{\text{ms}}^{\text{pair}} = \frac{1}{4A^2} \sum_{\substack{l_1 j_1 n_1 n_1' \\ l_2 j_2 n_2 n_2'}} \sum_{\tau} \sqrt{(2j_1+1)(2j_2+1)}\, \kappa_{n_2 n_2'}^{(l_2 j_2 \tau)} \kappa_{n_1' n_1}^{(l_1 j_1 \tau)}$$
$$\times \left\langle n_1 l_1 j_1 n_1' l_1 j_1, J = 0, T = 1 \big|\big| \bar{\mathbf{r}}^2 \big|\big| n_2 l_2 j_2 n_2' l_2 j_2, J = 0, T = 1 \right\rangle \,. \tag{B.38}$$

Let us now introduce the auxiliaries $X_{p,\text{ms}}$ and $X_{n,\text{ms}}$ as shorthands for the first sums in the proton and neutron mean-square radii (cf. Eqs. (B.35) and (B.36)):

$$R_{p,\text{ms}} = X_{p,\text{ms}} - R_{\text{ms}} \,, \tag{B.39}$$
$$R_{n,\text{ms}} = X_{n,\text{ms}} - R_{\text{ms}} \,. \tag{B.40}$$

Their HF contributions are

$$X_{p,\text{ms}}^{\text{HF}} = \frac{1}{AZ} \sum_{\substack{l_1 j_1 n_1 n_1' \\ l_2 j_2 n_2 n_2' \tau_2}} \sum_{J,T} \left\langle \tfrac{1}{2} \tfrac{1}{2} \tfrac{1}{2} \tau_2 \middle| T \tau_2 + \tfrac{1}{2} \right\rangle^2 \sqrt{2J+1} \rho_{n_1' n_1}^{(l_1 j_1 \frac{1}{2})} \rho_{n_2' n_2}^{(l_2 j_2 \tau_2)}$$

$$\times \left\langle n_1 l_1 j_1 n_2 l_2 j_2 JT \middle|\middle| \bar{\mathbf{r}}^2 \middle|\middle| n_1' l_1 j_1 n_2' l_2 j_2 JT \right\rangle, \tag{B.41}$$

$$X_{n,\text{ms}}^{\text{HF}} = \frac{1}{AN} \sum_{\substack{l_1 j_1 n_1 n_1' \\ l_2 j_2 n_2 n_2' \tau_2}} \sum_{J,T} \left\langle \tfrac{1}{2} - \tfrac{1}{2} \tfrac{1}{2} \tau_2 \middle| T \tau_2 - \tfrac{1}{2} \right\rangle^2 \sqrt{2J+1} \rho_{n_1' n_1}^{(l_1 j_1 - \frac{1}{2})} \rho_{n_2' n_2}^{(l_2 j_2 \tau_2)}$$

$$\times \left\langle n_1 l_1 j_1 n_2 l_2 j_2 JT \middle|\middle| \bar{\mathbf{r}}^2 \middle|\middle| n_1' l_1 j_1 n_2' l_2 j_2 JT \right\rangle, \tag{B.42}$$

and their pairing contributions

$$X_{p,\text{ms}}^{\text{pair}} = \frac{1}{2AZ} \sum_{\substack{l_1 j_1 n_1 n_1' \\ l_2 j_2 n_2 n_2'}} \sqrt{(2j_1+1)(2j_2+1)} \kappa_{n_2 n_2'}^{(l_2 j_2 \frac{1}{2})} \kappa_{n_1' n_1}^{(l_1 j_1 \frac{1}{2})}$$

$$\times \left\langle n_1 l_1 j_1 n_1' l_1 j_1, J = 0, T = 1 \middle|\middle| \bar{\mathbf{r}}^2 \middle|\middle| n_2 l_2 j_2 n_2' l_2 j_2, J = 0, T = 1 \right\rangle, \tag{B.43}$$

$$X_{n,\text{ms}}^{\text{pair}} = \frac{1}{2AN} \sum_{\substack{l_1 j_1 n_1 n_1' \\ l_2 j_2 n_2 n_2'}} \sqrt{(2j_1+1)(2j_2+1)} \kappa_{n_2 n_2'}^{(l_2 j_2 - \frac{1}{2})} \kappa_{n_1' n_1}^{(l_1 j_1 - \frac{1}{2})}$$

$$\times \left\langle n_1 l_1 j_1 n_1' l_1 j_1, J = 0, T = 1 \middle|\middle| \bar{\mathbf{r}}^2 \middle|\middle| n_2 l_2 j_2 n_2' l_2 j_2, J = 0, T = 1 \right\rangle. \tag{B.44}$$

The expectation values for $R_{p,\text{ms}}$ and $R_{n,\text{ms}}$ are now easily obtained from Eqs. (B.39) and (B.40).

Appendix C

Particle-Number Projection

C.1 Derivatives for Exact Projection

In the formulae of this section, $\tau = p, n$.

C.1.1 Gauge-Rotation Matrices

The derivative of the gauge-rotation matrices $C_\tau(\phi_\tau)$ with respect to the density matrix ρ_τ can be calculated with the help of the formula

$$\frac{d}{dx}A^{-1} = -A^{-1}\frac{dA}{dx}A^{-1} \, , \tag{C.1}$$

where $A(x)$ is a matrix. Applying this relation, we obtain

$$
\begin{aligned}
\frac{\partial C_{jj'}^\tau(\phi_\tau)}{\partial \rho_{k'k}^{\tau'}} &= -e^{2i\phi_\tau} \sum_{ll'} \left(1 + \rho_\tau(e^{2i\phi_\tau} - 1)\right)_{jl}^{-1} \left[\frac{\partial}{\partial \rho_{k'k}^{\tau'}} \left(1 + \rho_\tau(e^{2i\phi_\tau} - 1)\right)_{ll'}\right] \\
&\quad \times \left(1 + \rho_\tau(e^{2i\phi_\tau} - 1)\right)_{l'j'}^{-1} \\
&= -e^{2i\phi_\tau} \sum_{ll'} \left(1 + \rho_\tau(e^{2i\phi_\tau} - 1)\right)_{jl}^{-1} (e^{2i\phi_\tau} - 1)\delta_{lk'}\delta_{kl'}\delta_{\tau\tau'} \\
&\quad \times \left(1 + \rho_\tau(e^{2i\phi_\tau} - 1)\right)_{l'j'}^{-1} \\
&= -e^{2i\phi_\tau} e^{-2i\phi_\tau} C_{jk'}^\tau(\phi_\tau) \left(e^{2i\phi_\tau} - 1\right) C_{kj'}^\tau(\phi_\tau)e^{-2i\phi_\tau}\delta_{\tau\tau'} \\
&= \left(e^{-2i\phi_\tau} - 1\right) C_{jk'}^\tau(\phi_\tau)C_{kj'}^\tau(\phi_\tau)\delta_{\tau\tau'} \, . \tag{C.2}
\end{aligned}
$$

C.1.2 Norm Overlap

The derivative of the determinant of a matrix $A(x)$ is given by

$$\frac{d}{dx}\det A^{-1} = -\det A^{-1} \operatorname{tr}\left(A^{-1}\frac{dA}{dx}\right) \, , \tag{C.3}$$

which is used in the calculation of the derivative of the overlap:

$$
\begin{aligned}
\frac{\partial x_\tau(\phi_\tau)}{\partial \rho_{k'k}^{\tau'}} &= \frac{\partial}{\partial \rho_{k'k}^{\tau'}} \left(\frac{1}{2\pi} \frac{e^{i\phi_\tau(M-A_\tau)}}{\sqrt{\det C_\tau(\phi_\tau)}} \right) \\
&= \frac{1}{2\pi} e^{i\phi_\tau(M-A_\tau)} \frac{\partial}{\partial \rho_{k'k}^{\tau'}} \sqrt{\det C_\tau^{-1}(\phi_\tau)} \\
&= -\frac{1}{2\pi} e^{i\phi_\tau(M-A_\tau)} \frac{(-\det C_\tau^{-1}(\phi_\tau))}{2\sqrt{\det C_\tau^{-1}(\phi_\tau)}} \mathrm{tr} \left(C_\tau(\phi_\tau) \frac{\partial}{\partial \rho_{k'k}^{\tau'}} C_\tau^{-1}(\phi_\tau) \right) \\
&= \frac{1}{2} x_\tau(\phi_\tau) \mathrm{tr} \left(C_\tau(\phi_\tau) \frac{\partial}{\partial \rho_{k'k}^{\tau'}} C_\tau^{-1}(\phi_\tau) \right) \\
&= \frac{1}{2} x_\tau(\phi_\tau)(1 - e^{-2i\phi_\tau}) C_{kk'}^\tau(\phi_\tau) \delta_{\tau\tau'} \\
&= x_\tau(\phi_\tau) X_{kk'}^\tau(\phi_\tau) \delta_{\tau\tau'} \,,
\end{aligned}
\tag{C.4}
$$

with $A_p = Z, A_n = N$.

C.1.3   Transition Densities

The derivatives of the transition densities $\rho_\tau(\phi_\tau)$ and $\kappa_\tau(\phi_\tau)$ are the building blocks for the projected fields. Using Eq. (C.2), we obtain

$$
\frac{\partial \rho_{jj'}^\tau(\phi_\tau)}{\partial \rho_{k'k}^{\tau'}} = e^{-2i\phi_\tau} C_{jk'}^\tau(\phi_\tau) C_{kj'}^\tau(\phi_\tau) \delta_{\tau\tau'} \,,
\tag{C.5}
$$

$$
\frac{\partial \kappa_{jj'}^\tau(\phi_\tau)}{\partial \rho_{k'k}^{\tau'}} = \sum_l \frac{\partial C_{jl}^\tau(\phi_\tau)}{\partial \rho_{k'k}^{\tau'}} \kappa_{lj'}^\tau = \left(e^{-2i\phi_\tau} - 1 \right) C_{jk'}^\tau(\phi_\tau) \kappa_{kj'}^\tau(\phi_\tau) \delta_{\tau\tau'} \,,
\tag{C.6}
$$

and

$$
\frac{\partial \bar{\kappa}_{jj'}^{\tau*}(\phi_\tau)}{\partial \rho_{k'k}^{\tau'}} = e^{-2i\phi_\tau} \sum_l \kappa_{jl}^{\tau*} \frac{\partial C_{lj'}^\tau(\phi_\tau)}{\partial \rho_{k'k}^{\tau'}} = \left(e^{-2i\phi_\tau} - 1 \right) \bar{\kappa}_{jk'}^{\tau*}(\phi_\tau) C_{kj'}^\tau(\phi_\tau) \delta_{\tau\tau'}
\tag{C.7}
$$

for variations with respect to $\rho_\tau(\phi_\tau)$. Variations with respect to $\kappa_\tau(\phi_\tau)$ require somewhat more attention due to its antisymmetry — for standard HFB, it is sufficient to include an additional factor $\frac{1}{2}$ (cf. Eq. (3.17)), while in the projected case, we obtain

$$
\begin{aligned}
\frac{\partial \kappa_{jj'}^\tau(\phi_\tau)}{\partial \kappa_{k'k}^{\tau'}} &= \sum_l C_{jl}^\tau(\phi_\tau) \frac{\partial \kappa_{lj'}^\tau}{\partial \kappa_{k'k}^{\tau'}} = \sum_l^{l<j'} C_{jl}^\tau(\phi_\tau) \frac{\partial \kappa_{lj'}^\tau}{\partial \kappa_{k'k}^{\tau'}} + \sum_l^{l>j'} C_{jl}^\tau(\phi_\tau) \frac{\partial \kappa_{lj'}^\tau}{\partial \kappa_{k'k}^{\tau'}} \\
&= \sum_l^{l<j'} C_{jl}^\tau(\phi_\tau) \frac{\partial \kappa_{lj'}^\tau}{\partial \kappa_{k'k}^{\tau'}} - \sum_l^{l>j'} C_{jl}^\tau(\phi_\tau) \frac{\partial \kappa_{j'l}^\tau}{\partial \kappa_{k'k}^{\tau'}} \\
&= \left(C_{jk'}^\tau(\phi_\tau) \delta_{kj'} - C_{jk}^\tau(\phi_\tau) \delta_{j'k'} \right) \delta_{\tau\tau'} \,, \qquad \text{for } (k < k') \,,
\end{aligned}
\tag{C.8}
$$

and, analogously,

$$
\begin{aligned}
\frac{\partial \bar{\kappa}_{jj'}^{\tau*}(\phi_\tau)}{\partial \kappa_{k'k}^{*\tau'}} &= e^{-2i\phi_\tau} \sum_l \frac{\partial \kappa_{jl}^{\tau*}}{\partial \kappa_{k'k}^{\tau'*}} C_{lj'}^{\tau}(\phi_\tau) \\
&= e^{-2i\phi_\tau} \left(C_{kj'}^{\tau}(\phi_\tau)\delta_{jk'} - C_{k'j'}^{\tau}(\phi_\tau)\delta_{jk} \right) \delta_{\tau\tau'}, \qquad \text{for } (k < k'). \qquad \text{(C.9)}
\end{aligned}
$$

C.1.4   Hamiltonian Overlaps

Using the relations of the previous section, we can calculate the partial derivatives of the Hamiltonian overlaps defined in Sect. 3.2.2. For the Hartree-Fock field, i.e. variation with respect to $\rho_\tau(\phi_\tau)$, we need the partial derivatives

$$
\begin{aligned}
\frac{\partial}{\partial \rho_{k'k}^{\tau''}} H_{\mathrm{ph}}(\phi_n, \phi_p) &= \frac{\partial}{\partial \rho_{k'k}^{\tau''}} \frac{1}{2} \left(\sum_{\tau\tau'} \sum_{jj'll'} \bar{v}_{jl'j'l}^{\tau\tau'} \rho_{j'j}^{\tau}(\phi_\tau)\rho_{ll'}^{\tau'}(\phi_{\tau'}) \right) \\
&= \frac{1}{2} \sum_{\tau\tau'} \sum_{ll'jj'} \bar{v}_{jl'j'l}^{\tau\tau'} \left(e^{-2i\phi_{\tau''}} C_{j'k'}^{\tau''}(\phi_{\tau''})C_{kj}^{\tau''}(\phi_{\tau''})\rho_{ll'}^{\tau'}(\phi_{\tau'})\delta_{\tau\tau''} \right. \\
&\qquad\qquad\qquad \left. + e^{-2i\phi_{\tau''}} \rho_{j'j}^{\tau}(\phi_\tau) C_{lk'}^{\tau''}(\phi_{\tau''})C_{kl'}^{\tau''}(\phi_{\tau''})\delta_{\tau'\tau''} \right) \\
&= \frac{1}{2} \sum_{\tau'} \sum_{ll'jj'} \bar{v}_{jl'j'l}^{\tau\tau'} e^{-2i\phi_{\tau''}} C_{j'k'}^{\tau''}(\phi_{\tau''})C_{kj}^{\tau''}(\phi_{\tau''})\rho_{ll'}^{\tau'}(\phi_{\tau'}) \\
&\quad + \frac{1}{2} \sum_{\tau} \sum_{ll'jj'} \bar{v}_{l'jlj'}^{\tau'\tau} e^{-2i\phi_{\tau''}} \rho_{j'j}^{\tau}(\phi_\tau) C_{lk'}^{\tau''}(\phi_{\tau''})C_{kl'}^{\tau''}(\phi_{\tau''}) \\
&= e^{-2i\phi_{\tau''}} \sum_{jj'} C_{kj}^{\tau''}(\phi_{\tau''})\Gamma_{jj'}^{\tau''}(\phi_n, \phi_p)C_{j'k'}^{\tau''}(\phi_{\tau''}) \qquad \text{(C.10)}
\end{aligned}
$$

and

$$
\begin{aligned}
\frac{\partial}{\partial \rho_{k'k}^{\tau}} H_{\mathrm{pp}}(\phi_n, \phi_p) &= \frac{\partial}{\partial \rho_{k'k}^{\tau}} \frac{1}{4} \left(\sum_{jj'll'} \bar{v}_{jj'll'} \bar{\kappa}_{jj'}^{\tau*}(\phi_\tau)\kappa_{ll'}^{\tau}(\phi_\tau) \right) \\
&= \frac{1}{4} \left(e^{-2i\phi_\tau} - 1 \right) \sum_{jj'll'} \bar{v}_{jj'll'} \left(\bar{\kappa}_{jk'}^{\tau*}(\phi_\tau)C_{kj'}^{\tau}(\phi_\tau)\kappa_{ll'}^{\tau}(\phi_\tau) + \bar{\kappa}_{jj'}^{\tau*}(\phi_\tau)C_{lk'}^{\tau}(\phi_\tau)\kappa_{kl'}^{\tau}(\phi_\tau) \right) \\
&= \frac{1}{2} \left(e^{-2i\phi_\tau} - 1 \right) \sum_{jj'} \left(\bar{\kappa}_{jk'}^{\tau*}(\phi_\tau)C_{kj'}^{\tau}(\phi_\tau)\Delta_{jj'}^{\tau}(\phi_\tau) + \bar{\Delta}_{jk'}^{\tau*}(\phi_\tau)C_{jk'}^{\tau}(\phi_\tau)\kappa_{kj'}^{\tau}(\phi_\tau) \right) \\
&= \frac{1}{2} \left(1 - e^{-2i\phi_\tau} \right) \sum_{jj'} \left(\bar{\kappa}_{jk'}^{\tau*}(\phi_\tau)C_{kj'}^{\tau}(\phi_\tau)\Delta_{j'j}^{\tau}(\phi_\tau) + \bar{\Delta}_{j'j}^{\tau*}(\phi_\tau)C_{jk'}^{\tau}(\phi_\tau)\kappa_{kj'}^{\tau}(\phi_\tau) \right) \\
&= ie^{-i\phi_\tau} \sin\phi_\tau \sum_{jj'} \left(C_{kj'}^{\tau}(\phi_\tau)\Delta_{j'j}^{\tau}(\phi_\tau)\bar{\kappa}_{jk'}^{\tau*}(\phi_\tau) + \kappa_{kj'}^{\tau}(\phi_\tau)\bar{\Delta}_{j'j}^{\tau*}(\phi_\tau)C_{jk'}^{\tau}(\phi_\tau) \right).
\end{aligned}
$$

$$\text{(C.11)}$$

For the pairing field, we need

$$
\begin{aligned}
\frac{\partial}{\partial \kappa_{k'k}^{\tau*}} H_{\mathrm{pp}}(\phi_n, \phi_p) &= \frac{1}{4} \sum_{jj'll'} \bar{v}_{jj'll'} \frac{\partial \bar{\kappa}_{jj'}^{\tau*}(\phi_\tau)}{\partial \kappa_{k'k}^{\tau*}} \kappa_{ll'}^{\tau}(\phi_\tau) \\
&= \frac{1}{4} \sum_{jj'll'} \bar{v}_{jj'll'} \left(C_{kj'}^{\tau}(\phi_\tau)\delta_{jk'} - C_{k'j'}^{\tau}(\phi_\tau)\delta_{jk} \right) \kappa_{ll'}^{\tau}(\phi_\tau) \\
&= \frac{1}{2} \sum_{jj'} e^{-2i\phi_\tau} \left(C_{kj'}^{\tau}(\phi_\tau)\delta_{jk'} - C_{k'j'}^{\tau}(\phi_\tau)\delta_{jk} \right) \Delta_{jj'}^{\tau}(\phi_\tau) \\
&= -\frac{1}{2} \sum_{j'} e^{-2i\phi_\tau} \left(C_{kj'}^{\tau}(\phi_\tau)\Delta_{j'k'}^{\tau}(\phi_\tau) - C_{k'j'}^{\tau}\Delta_{j'k}^{\tau}(\phi_\tau) \right) .
\end{aligned} \tag{C.12}
$$

C.2   Derivatives for Approximate Projection

For the Lipkin-Nogami method, we need derivatives of the transition densities and fields with respect to the gauge angles. The resulting formulae are conveniently written in terms of the auxiliary densities originally defined in Sect. 3.2.3,

$$
\chi_\tau = \rho_\tau(1_\tau - \rho_\tau), \qquad \eta_\tau = (1_\tau - 2\rho_\tau), \tag{C.13}
$$

where 1_τ is the unit matrix in the subspace of nucleons with $q = n, p$

C.2.1   Gauge Rotation Matrices

With the help of relation (C.1), we find

$$
\frac{\partial C_\tau(\phi_\tau)}{\partial \phi_\tau} = \frac{\partial}{\partial \phi_\tau} \left(e^{2i\phi_\tau}(1_\tau + \rho_\tau(e^{2i\phi_\tau} - 1_\tau))^{-1} \right) = 2i \left[1_\tau - C_\tau(\phi_\tau)\rho_\tau \right] C_\tau(\phi_\tau) \tag{C.14}
$$

$$
\frac{\partial^2 C_\tau(\phi_\tau}{\partial \phi_\tau^2} = 4i^2 \left[C_\tau(\phi_\tau) - 3C_\tau(\phi_\tau)\rho_\tau C_\tau(\phi_\tau) + 2C_\tau(\phi_\tau)\rho_\tau C_\tau(\phi_\tau)\rho_\tau C_\tau(\phi_\tau) \right], \tag{C.15}
$$

and

$$
\begin{aligned}
\frac{\partial^3 C_\tau(\phi_\tau}{\partial \phi_\tau^3} = 8i^3 & \left[C_\tau(\phi_\tau) - 7C_\tau(\phi_\tau)\rho_\tau C_\tau(\phi_\tau) + 12C_\tau(\phi_\tau)\rho_\tau C_\tau(\phi_\tau)\rho_\tau C_\tau(\phi_\tau) \right. \\
& \left. -6C_\tau(\phi_\tau)\rho_\tau C_\tau(\phi_\tau)\rho_\tau C_\tau(\phi_\tau)\rho_\tau C_\tau(\phi_\tau) \right],
\end{aligned} \tag{C.16}
$$

With $C_\tau(0) = 1_\tau$, we have

$$
\left. \frac{1}{i} \frac{\partial C_\tau(\phi_\tau)}{\partial \phi_\tau} \right|_{\phi_\tau=0} = 2(1_\tau - \rho_\tau), \tag{C.17}
$$

$$
\left. \frac{1}{i^2} \frac{\partial^2 C_\tau(\phi_\tau)}{\partial \phi_\tau^2} \right|_{\phi_\tau=0} = 4 \left(1_\tau - 3\rho_\tau + 2\rho_\tau^2 \right), \tag{C.18}
$$

$$
\left. \frac{1}{i^3} \frac{\partial^3 C_\tau(\phi_\tau)}{\partial \phi_\tau^3} \right|_{\phi_\tau=0} = 8 \left(1_\tau - 7\rho_\tau + 12\rho_\tau^2 - 6\rho_\tau^3 \right). \tag{C.19}
$$

C.2.2   Densities

Density Matrices

$$\frac{1}{i}\frac{\partial \rho_\tau(\phi_\tau)}{\partial \phi_\tau}\bigg|_{\phi_\tau=0} = \frac{1}{i}\frac{\partial C_\tau(\phi_\tau)}{\partial \phi_\tau}\rho_\tau\bigg|_{\phi_\tau=0} = 2(1_\tau - \rho_\tau)\rho_\tau = 2\chi_\tau \tag{C.20}$$

$$\frac{1}{i^2}\frac{\partial^2 \rho_\tau(\phi_\tau)}{\partial \phi_\tau^2}\bigg|_{\phi_\tau=0} = \frac{1}{i^2}\frac{\partial^2 C_\tau(\phi_\tau)}{\partial \phi_\tau^2}\rho_\tau\bigg|_{\phi_\tau=0} = 4(1_\tau - 2\rho_\tau)(1_\tau - \rho_\tau)\rho_\tau = 4\eta_\tau\chi_\tau \tag{C.21}$$

Pairing Tensors

$$\frac{1}{i}\frac{\partial \kappa_\tau(\phi_\tau)}{\partial \phi_\tau}\bigg|_{\phi_\tau=0} = 2(1_\tau - \rho_\tau)\kappa_\tau \tag{C.22}$$

$$\frac{1}{i^2}\frac{\partial^2 \kappa_\tau(\phi_\tau)}{\partial \phi_\tau^2}\bigg|_{\phi_\tau=0} = 4\eta_\tau(1 - \rho_\tau)\kappa_\tau \tag{C.23}$$

Adjoint Pairing Tensors

$$\frac{1}{i}\frac{\partial \bar{\kappa}_\tau^*(\phi_\tau)}{\partial \phi_\tau}\bigg|_{\phi_\tau=0} = \frac{1}{i}\left(-2i\bar{\kappa}_\tau^*(\phi_\tau) + e^{-2i\phi_\tau}\kappa_\tau^*\frac{\partial C_\tau(\phi_\tau)}{\partial \phi_\tau}\right)\bigg|_{\phi_\tau=0}$$

$$= (-2\kappa_\tau^* + 2\kappa_\tau^*(1_\tau - \rho_\tau))$$

$$= -2\kappa_\tau^*\rho_\tau \tag{C.24}$$

$$\frac{1}{i^2}\frac{\partial^2 \bar{\kappa}_\tau^*(\phi_\tau)}{\partial \phi_\tau^2}\bigg|_{\phi_\tau=0} = \frac{1}{i^2}\left(4i^2\bar{\kappa}_\tau^*(\phi_\tau) - 4ie^{-2i\phi_\tau}\kappa_\tau^*\frac{\partial C_\tau(\phi_\tau)}{\partial \phi_\tau} + e^{-2i\phi_\tau}\kappa_\tau^*\frac{1}{i^2}\frac{\partial^2 C_\tau(\phi_\tau)}{\partial \phi_\tau^2}\right)\bigg|_{\phi_\tau=0}$$

$$= \left(4\kappa_\tau^* - 8\kappa_\tau^*(1_\tau - \rho_\tau) + 4\kappa_\tau^*(1_\tau - 3\rho_\tau + 2\rho_\tau^2)\right)$$

$$= -4\kappa_\tau^*\rho_\tau\eta_\tau \tag{C.25}$$

C.2.3   Norm Overlap

Using Eq. (C.3), we have

$$\frac{1}{i}\frac{\partial x_\tau(\phi_\tau)}{\partial \phi_\tau}\bigg|_{\phi_\tau=0} = \frac{1}{i}\frac{\partial}{\partial \phi_\tau}\left(\frac{1}{2\pi}\frac{e^{i\phi_\tau(M-A_\tau)}}{\sqrt{\det C_\tau(\phi_\tau)}}\right)\bigg|_{\phi_\tau=0}$$

$$= x_\tau(\phi_\tau)\left[M - A_\tau - \mathrm{tr}\,(1_\tau - \rho_\tau(\phi_\tau))\right]\big|_{\phi_\tau=0}$$

$$= x_\tau(\phi_\tau)\left[M - A_\tau - M + \mathrm{tr}\,\rho_\tau(\phi_\tau)\right]\big|_{\phi_\tau=0}$$

$$= x_\tau(\phi_\tau)\left[\mathrm{tr}\,\rho_\tau(\phi_\tau) - A_\tau\right]\big|_{\phi_\tau=0}$$

$$= 0\,, \tag{C.26}$$

where we have used that $\operatorname{tr} 1_\tau = M$ for a single particle space of dimension M (cf. Sect. 3.2.2) and the HFB particle number condition $\operatorname{tr} \rho_\tau = A_\tau$ is satisfied. Higher-order derivatives are

$$
\frac{1}{i^2} \frac{\partial^2 x_\tau(\phi_\tau)}{\partial \phi_\tau^2}\bigg|_{\phi_\tau} = \frac{1}{i} \frac{\partial x_\tau(\phi_\tau)}{\partial \phi_\tau} \left(\operatorname{tr} \rho_\tau(\phi_\tau) - A_\tau\right)\bigg|_{\phi_\tau=0} + \frac{1}{i} x_\tau(\phi_\tau) \operatorname{tr} \frac{\partial \rho_\tau(\phi_\tau)}{\partial \phi_\tau}\bigg|_{\phi_\tau=0}
$$

$$
= 2\operatorname{tr} \chi_\tau \,, \tag{C.27}
$$

$$
\frac{1}{i^3} \frac{\partial^3 x_\tau(\phi_\tau)}{\partial \phi_\tau^3}\bigg|_{\phi_\tau=0} = \frac{1}{i^2} \frac{\partial^2 x_\tau(\phi_\tau)}{\partial \phi_\tau^2} \left(\operatorname{tr} \rho_\tau(\phi_\tau) - A_\tau\right)\bigg|_{\phi_\tau=0} + \frac{2}{i^2} \frac{\partial x_\tau(\phi_\tau)}{\partial \phi_\tau} \operatorname{tr} \frac{\partial \rho_\tau(\phi_\tau)}{\partial \phi_\tau}\bigg|_{\phi_\tau=0}
$$

$$
+ \frac{1}{i^2} x_\tau(\phi_\tau) \operatorname{tr} \frac{\partial^2 \rho_\tau(\phi_\tau)}{\partial \phi_\tau^2}\bigg|_{\phi_\tau=0}
$$

$$
= 4\operatorname{tr} \left(\eta_\tau \chi_\tau\right) \,, \tag{C.28}
$$

$$
\frac{1}{i^4} \frac{\partial^4 x_\tau(\phi_\tau)}{\partial \phi_\tau^4}\bigg|_{\phi_\tau=0} = \frac{1}{i^3} \frac{\partial^3 x_\tau(\phi_\tau)}{\partial \phi_\tau^3} \left(\operatorname{tr} \rho_\tau(\phi_\tau) - A_\tau\right)\bigg|_{\phi_\tau=0} + \frac{3}{i^3} \frac{\partial^2 x_\tau(\phi_\tau)}{\partial \phi_\tau^2} \operatorname{tr} \frac{\partial \rho_\tau(\phi_\tau)}{\partial \phi_\tau}\bigg|_{\phi_\tau=0}
$$

$$
+ \frac{3}{i^3} \frac{\partial x_\tau(\phi_\tau)}{\partial \phi_\tau} \operatorname{tr} \frac{\partial^2 \rho_\tau(\phi_\tau)}{\partial \phi_\tau^2}\bigg|_{\phi_\tau=0} + \frac{1}{i^3} x_\tau(\phi_\tau) \operatorname{tr} \frac{\partial^3 \rho_\tau(\phi_\tau)}{\partial \phi_\tau^3}\bigg|_{\phi_\tau=0}
$$

$$
= 12 \left(\operatorname{tr} \chi_\tau\right)^2 + 8 \left(\operatorname{tr} \chi_\tau - 6\operatorname{tr} \chi_\tau^2\right) \,. \tag{C.29}
$$

C.2.4   Hamiltonian Overlaps

Single-Particle Hamiltonian Overlap

$$
\frac{1}{i} \frac{\partial}{\partial \phi_{\tau'}} H_{\mathrm{sp}}(\phi_n, \phi_p)\bigg|_{\phi_n=\phi_p=0} = \sum_\tau \sum_{kk'} t_{kk'}^\tau \frac{1}{i} \frac{\partial}{\partial \phi_{\tau'}} \rho_{k'k}^\tau(\phi_\tau)\bigg|_{\phi_{\tau'}=0} = 2 \sum_{kk'} t_{kk'}^{\tau'} \chi_{k'k}^{\tau'}
$$

$$
= 2\operatorname{tr} \left[t_{\tau'} \chi_{\tau'}\right] \tag{C.30}
$$

$$
\frac{1}{i^2} \frac{\partial^2}{\partial \phi_{\tau'}^2} H_{\mathrm{sp}}(\phi_n, \phi_p)\bigg|_{\phi_n=\phi_p=0} = \sum_\tau \sum_{kk'} t_{kk'}^\tau \frac{1}{i^2} \frac{\partial^2}{\partial \phi_{\tau'}^2} \rho_{k'k}^\tau(\phi_\tau)\bigg|_{\phi_{\tau'}=0} = 4 \sum_{kk'} t_{kk'}^{\tau'} \left[\eta^{\tau'} \chi^{\tau'}\right]_{k'k}
$$

$$
= 4\operatorname{tr} \left[t_{\tau'} \eta_{\tau'} \chi_{\tau'}\right] \tag{C.31}
$$

Particle-Hole Overlap

$$\frac{1}{i}\frac{\partial}{\partial\phi_{\tau''}}H_{\text{ph}}(\phi_n,\phi_p)\Bigg|_{\phi_n=\phi_p=0} = \frac{1}{2}\sum_{\tau\tau'}\sum_{jj'll'}\bar{v}_{jl'j'l}^{\tau\tau'}\frac{1}{i}\frac{\partial}{\partial\phi_{\tau''}}\left(\rho_{j'j}^{\tau}(\phi_\tau)\rho_{ll'}^{\tau'}(\phi_{\tau'})\right)\Bigg|_{\phi_n=\phi_p=0}$$

$$= 2\sum_\tau\sum_{jj'll'}\bar{v}_{jl'j'l}^{\tau''\tau}\chi_{j'j}^{\tau''}\rho_{ll'}^{\tau}$$

$$= 2\text{tr}\left[\Gamma_{\tau''}\chi_{\tau''}\right] \tag{C.32}$$

$$\frac{1}{i^2}\frac{\partial^2}{\partial\phi_{\tau''}^2}H_{\text{ph}}(\phi_n,\phi_p)\Bigg|_{\phi_n=\phi_p=0} = \frac{1}{2}\sum_{\tau\tau'}\sum_{jj'll'}\bar{v}_{jl'j'l}^{\tau\tau'}\frac{1}{i^2}\frac{\partial^2}{\partial\phi_{\tau''}^2}\left(\rho_{j'j}^{\tau}(\phi_\tau)\rho_{ll'}^{\tau'}(\phi_{\tau'})\right)\Bigg|_{\phi_n=\phi_p=0}$$

$$= \frac{1}{2}\sum_{\tau\tau'}\sum_{jj'll'}\bar{v}_{jl'j'l}^{\tau\tau'}\left(4\left[\eta^\tau\chi^\tau\right]_{j'j}\rho_{ll'}^{\tau'}\delta_{\tau\tau''} + 8\chi_{j'j}^\tau\chi_{ll'}^{\tau'}\delta_{\tau\tau''}\delta_{\tau'\tau''}\right.$$

$$\left. + 4\rho_{j'j}^\tau\left[\eta^{\tau'}\chi^{\tau'}\right]_{ll'}\delta_{\tau'\tau''}\right)$$

$$= 4\text{tr}\left(\Gamma_{\tau''}\eta_{\tau''}\chi_{\tau''} + \Gamma_{\tau''}[\chi]\chi_{\tau''}\right) \tag{C.33}$$

Here, the auxiliary field $\Gamma_\tau[\chi]$ is defined by (cf. Sect. 3.2.3)

$$\Gamma_{jj'}^\tau[\chi] \equiv \sum_{\tau'}\sum_{jj'll'}\bar{v}_{jl'j'l}^{\tau\tau'}\chi_{ll'}^{\tau'}. \tag{C.34}$$

Particle-Particle Overlap

For the particle-particle Hamiltonian overlap the situation is slightly more complicated. For the first derivative, we have

$$\frac{1}{i}\frac{\partial}{\partial\phi_\tau}H_{\text{pp}}(\phi_n,\phi_p)\Bigg|_{\phi_n=\phi_p=0} = \frac{1}{4}\sum_{\tau'}\sum_{jj'll'}\bar{v}_{jj'll'}^{\tau'\tau'}\frac{1}{i}\frac{\partial}{\partial\phi_\tau}\left(\bar{\kappa}_{jj'}^{\tau'*}(\phi_\tau')\kappa_{ll'}^{\tau'}(\phi_{\tau'})\right)\Bigg|_{\phi_n=\phi_p=0}$$

$$= \frac{1}{4}\sum_{jj'll'}\bar{v}_{jj'll'}^{\tau\tau}\left(-2\left[\kappa^{\tau*}\rho^\tau\right]_{jj'}\kappa_{ll'}^\tau + 2\kappa_{jj'}^{\tau*}\kappa_{ll'}^\tau - 2\kappa_{jj'}^{\tau*}\left[\rho^\tau\kappa^\tau\right]_{ll'}\right)$$

$$= \frac{1}{2}\sum_{jj'll'}\bar{v}_{jj'll'}^{\tau\tau}\left(-\left[\kappa^{\tau*}\rho^\tau\right]_{jj'}\kappa_{ll'}^\tau + \kappa_{jj'}^{\tau*}\kappa_{ll'}^\tau - \kappa_{jj'}^{\tau*}\left[\kappa^\tau\rho^{\tau*}\right]_{ll'}\right)$$

$$= \frac{1}{2}\sum_{jj'll'}\left(\bar{v}_{jj'll'}^{\tau\tau}\kappa_{jj'}^{\tau*}\kappa_{ll'}^\tau - \bar{v}_{jj'll'}^{\tau\tau}\left[\kappa^{\tau*}\rho^\tau\right]_{jj'}\kappa_{ll'}^\tau\right.$$

$$\left. - \bar{v}_{ll'jj'}^{\tau\tau*}\left[\kappa^\tau\rho^{\tau*}\right]_{ll'}\kappa_{jj'}^{\tau*}\right)$$

$$= \frac{1}{2} \sum_{jj'll'} \left(\bar{v}^{\tau\tau}_{jj'll'} \kappa^{\tau*}_{jj'} \kappa^{\tau}_{ll'} - 2\mathrm{Re}\left(\bar{v}^{\tau\tau}_{jj'll'} \left[\kappa^{\tau*}\rho^{\tau}\right]_{jj'} \kappa^{\tau}_{ll'} \right) \right)$$

$$= \frac{1}{2} \sum_{jj'll'} \mathrm{Re}\left(\bar{v}^{\tau\tau}_{jj'll'} \left[\kappa^{\tau*}\eta^{\tau}\right]_{jj'} \kappa^{\tau}_{ll'} \right)$$

$$= -\mathrm{Re}\,\mathrm{tr}\left[\Delta_{\tau}\kappa^{*}_{\tau}\eta_{\tau}\right] , \tag{C.35}$$

where we have used the property (cf. Sect. 3.1)

$$\rho\kappa = \kappa\rho^{*} \tag{C.36}$$

in the third line, and the reality of the pairing energy in the last line to obtain a more compact expression.

For the second derivative, we obtain

$$\frac{1}{i^2}\frac{\partial^2}{\partial\phi_{\tau}^2} H_{\mathrm{pp}}(\phi_n, \phi_p)\Big|_{\phi_n=\phi_p=0} = \frac{1}{4}\sum_{\tau'}\sum_{jj'll'} \bar{v}^{\tau'\tau'}_{jj'll'} \frac{1}{i}\frac{\partial^2}{\partial\phi_{\tau}^2}\left(\bar{\kappa}^{\tau'*}_{jj'}(\phi'_{\tau})\kappa^{\tau'}_{ll'}(\phi_{\tau'})\right)\Big|_{\phi_n=\phi_p=0}$$

$$= \frac{1}{4}\sum_{jj'll'} \bar{v}^{\tau\tau}_{jj'll'}\left(-4\left[\kappa^{\tau*}\rho^{\tau}\eta^{\tau}\right]_{jj'}\kappa^{\tau}_{ll'} - 8\left[\kappa^{\tau*}\rho^{\tau}\right]_{jj'}\kappa^{\tau}_{ll'} - 8\left[\kappa^{\tau*}\rho^{\tau}\right]_{jj'}\left[\rho^{\tau}\kappa^{\tau}\right]_{ll'} \right.$$

$$\left. + 4\kappa^{\tau*}_{jj'}\left[\eta^{\tau}\kappa^{\tau}\right]_{ll'} - 4\kappa^{\tau*}\left[\eta^{\tau}\rho^{\tau}\kappa^{\tau}\right]_{ll'}\right)$$

$$= \frac{1}{4}\sum_{jj'll'} \bar{v}^{\tau\tau}_{jj'll'}\left(8\left[\kappa^{\tau*}\left(\rho^{\tau2}-\rho^{\tau}\right)\right]_{jj'}\kappa^{\tau}_{ll'} + 8\kappa^{\tau*}_{jj'}\left[\left(\rho^{\tau2}-\rho^{\tau}\right)\kappa^{\tau}\right]_{ll'} + 4\kappa^{\tau*}_{jj'}\kappa^{\tau}_{ll'} \right.$$

$$\left. - 4\left[\kappa^{\tau*}\rho^{\tau}\right]_{jj'}\kappa^{\tau}_{ll'} - 4\kappa^{\tau*}_{jj'}\left[\rho^{\tau}\kappa^{\tau}\right]_{ll'} + 8\left[\rho^{\tau*}\kappa^{\tau*}\right]_{jj'}\left[\rho^{\tau}\kappa^{\tau}\right]_{ll'}\right)$$

$$= \frac{1}{4}\sum_{jj'll'} \bar{v}^{\tau\tau}_{jj'll'}\left(-8\left[\kappa^{\tau*}\chi^{\tau}\right]_{jj'}\kappa^{\tau}_{ll'} - 8\kappa^{\tau*}_{jj'}\left[\kappa^{\tau}\chi^{\tau*}\right]_{ll'} + 2\kappa^{\tau*}_{jj'}\kappa^{\tau}_{ll'} \right.$$

$$\left. + 2\left[\eta^{\tau}\kappa^{\tau}\right]^{*}_{jj'}\left[\eta^{\tau}\kappa^{\tau}\right]_{ll'}\right)$$

$$= \frac{1}{2}\sum_{jj'll'} \left(\bar{v}^{\tau\tau}_{jj'll'}\kappa^{\tau*}_{jj'}\kappa^{\tau}_{ll'} - 8\,\mathrm{Re}\left(\bar{v}^{\tau\tau}_{jj'll'}\left[\kappa^{\tau*}\chi^{\tau}\right]_{jj'}\kappa^{\tau}_{ll'}\right) + \bar{v}^{\tau\tau}_{jj'll'}\left[\eta^{\tau}\kappa^{\tau}\right]^{*}_{jj'}\left[\eta^{\tau}\kappa^{\tau}\right]_{ll'}\right)$$

$$= -\mathrm{Re}\,\mathrm{tr}\left(\Delta_{\tau}\kappa^{*}_{\tau}(1-8\chi_{\tau})\right) - \mathrm{tr}\left(\Delta_{\tau}[\eta\kappa][\eta_{\tau}\kappa_{\tau}]^{*}\right) , \tag{C.37}$$

where we have again rewritten some of the terms as an explicit real part, and made use of

$$\chi_{\tau}\kappa_{\tau} = \kappa_{\tau}\chi^{*}_{\tau} , \tag{C.38}$$

which is a direct consequence of Eq. (C.36). Furthermore, we have defined the auxiliary pairing field

$$\Delta^{\tau}_{ll'}[\eta\kappa] \equiv \frac{1}{2}\sum_{jj'll'} \bar{v}^{\tau\tau}_{jj'll'}\left[\eta^{\tau}\kappa^{\tau}\right]_{ll'} . \tag{C.39}$$

C.2.5 Density-Dependent Hamiltonian Overlaps

The particle-hole and particle-particle Hamiltonian overlaps for the density-dependent interaction (3.181) were defined in Sect. 3.3.3 as

$$
\breve{H}_{\mathrm{ph}}(\phi_n, \phi_p) = \frac{t_0}{2} \int d^3r\, \rho^\alpha(\phi_n, \phi_p, \boldsymbol{r})
$$
$$
\times \left(\left(1 + \frac{x_0}{2}\right) \rho^2(\phi_n, \phi_p, \boldsymbol{r}) - \left(x_0 + \frac{1}{2}\right) \sum_\tau \rho_\tau^2(\phi_\tau, \boldsymbol{r}) \right) \qquad \text{(C.40)}
$$

and

$$
\breve{H}_{\mathrm{pp}}(\phi_n, \phi_p) = \frac{t_0}{4} \int d^3r\, \rho^\alpha(\phi_n, \phi_p, \boldsymbol{r}) \left(1 - x_0\right) \left(\sum_\tau \bar{\kappa}_\tau^*(\phi_\tau, \boldsymbol{r}) \kappa_\tau(\phi_\tau, \boldsymbol{r}) \right). \qquad \text{(C.41)}
$$

The derivatives of the local coordinate space densities with respect to the gauge angles are easily obtained from the relations given in Appendix C.2.2, e.g.

$$
\frac{1}{i} \frac{\partial \rho_\tau(\phi_\tau, \boldsymbol{r})}{\partial \phi_\tau}\bigg|_{\{\phi\}=0} = \sum_{kk'} \frac{1}{i} \frac{\partial \rho_{kk'}^\tau}{\partial \phi_\tau}\bigg|_{\{\phi\}=0} \psi_{\tau k}^*(\boldsymbol{r}) \psi_{\tau k'}(\boldsymbol{r}) = 2\chi_\tau(\boldsymbol{r}). \qquad \text{(C.42)}
$$

Rearrangement-like terms can be readily identified by preceding factors of α, the power of the zero-range density-dependent interaction; terms which do not contain α correspond to the expectation values $\langle\, \mathrm{V}[\rho]\Delta \mathrm{A}_\tau \,\rangle$ and $\langle\, \left(\mathrm{V}[\rho] - \langle\, \mathrm{V}[\rho] \,\rangle\right) \Delta \mathrm{A}_\tau^2 \,\rangle$, and can also be computed by replacing the two-body matrix elements $\bar{v}_{jj'kk'}$ with their density-dependent counterparts in the formulae of the previous section.

Particle-Hole Overlap

$$
\frac{1}{i} \frac{\partial \breve{H}_{\mathrm{ph}}(\phi_n, \phi_p)}{\partial \phi_\tau}\bigg|_{\{\phi\}=0}
$$
$$
= t_0 \int d^3r \left\{ \alpha \rho^{\alpha-1}(\boldsymbol{r}) \left(\left(1 + \frac{x_0}{2}\right) \rho^2(\boldsymbol{r}) - \left(x_0 + \frac{1}{2}\right) \sum_{\tau'} \rho_{\tau'}^2(\boldsymbol{r}) \right) \right.
$$
$$
\left. + 2\rho^\alpha(\boldsymbol{r}) \left(\left(1 + \frac{x_0}{2}\right) \rho(\boldsymbol{r}) - \left(x_0 + \frac{1}{2}\right) \rho_\tau(\boldsymbol{r}) \right) \right\} \chi_\tau(\boldsymbol{r}) \qquad \text{(C.43)}
$$

$$
\frac{1}{i^2} \left. \frac{\partial^2 \breve{H}_{\mathrm{ph}}(\phi_n, \phi_p)}{\partial \phi_\tau^2} \right|_{\{\phi\}=0}
$$

$$
= 2t_0 \int d^3r \left\{ \alpha(\alpha-1)\rho^{\alpha-2}(\boldsymbol{r}) \left(\left(1 + \frac{x_0}{2}\right)\rho^2(\boldsymbol{r}) - \left(x_0 + \frac{1}{2}\right)\sum_{\tau'}\rho_{\tau'}^2(\boldsymbol{r}) \right) \right.
$$

$$
+ 4\alpha\rho^{\alpha-1}(\boldsymbol{r}) \left(\left(1 + \frac{x_0}{2}\right)\rho(\boldsymbol{r}) - \left(x_0 + \frac{1}{2}\right)\rho_\tau(\boldsymbol{r}) \right)
$$

$$
\left. + \rho^\alpha(\boldsymbol{r})\left(1 - x_0\right) \right\} \chi_\tau^2(\boldsymbol{r})
$$

$$
+ \left\{ \alpha\rho^{\alpha-1}(\boldsymbol{r}) \left(\left(1 + \frac{x_0}{2}\right)\rho^2(\boldsymbol{r}) - \left(x_0 + \frac{1}{2}\right)\sum_{\tau'}\rho_{\tau'}^2(\boldsymbol{r}) \right) \right.
$$

$$
\left. + 2\rho^\alpha(\boldsymbol{r}) \left(\left(1 + \frac{x_0}{2}\right)\rho(\boldsymbol{r}) - \left(x_0 + \frac{1}{2}\right)\rho_\tau(\boldsymbol{r}) \right) \right\} \left[\eta_\tau\chi_\tau\right](\boldsymbol{r}) \quad \text{(C.44)}
$$

Particle-Particle Overlap

$$
\frac{1}{i} \left. \frac{\partial \breve{H}_{\mathrm{pp}}(\phi_n, \phi_p)}{\partial \phi_\tau} \right|_{\{\phi\}=0} = \frac{t_0}{2}\left(1 - x_0\right)\int d^3r \left\{ \alpha\rho^{\alpha-1}(\boldsymbol{r}) \left(\sum_{\tau'}\kappa_{\tau'}^*(\boldsymbol{r})\kappa_{\tau'}(\boldsymbol{r}) \right) \chi_\tau(\boldsymbol{r}) \right.
$$

$$
\left. + \rho^\alpha(\boldsymbol{r})\mathrm{Re}\left(\left[\kappa_\tau^*\eta_\tau\right](\boldsymbol{r})\kappa_\tau(\boldsymbol{r})\right) \right\} \quad \text{(C.45)}
$$

$$
\frac{1}{i^2} \left. \frac{\partial^2 \breve{H}_{\mathrm{pp}}(\phi_n, \phi_p)}{\partial \phi_\tau^2} \right|_{\{\phi\}=0}
$$

$$
= t_0\left(1 - x_0\right)\int d^3r \left\{ \alpha(\alpha-1)\rho^{\alpha-2}(\boldsymbol{r}) \left(\sum_{\tau'}\kappa_{\tau'}^*(\boldsymbol{r})\kappa_{\tau'}(\boldsymbol{r}) \right) \chi_\tau^2(\boldsymbol{r}) \right.
$$

$$
+ \alpha\rho^{\alpha-1}(\boldsymbol{r})\mathrm{Re}\left(\left[\kappa_\tau^*\eta_\tau\right](\boldsymbol{r})\kappa_\tau(\boldsymbol{r})\right)\chi_\tau(\boldsymbol{r})
$$

$$
+ \alpha\rho^{\alpha-1}(\boldsymbol{r}) \left(\sum_{\tau'}\kappa_{\tau'}^*(\boldsymbol{r})\kappa_{\tau'}(\boldsymbol{r}) \right)\left[\eta_\tau\chi_\tau\right](\boldsymbol{r})
$$

$$
\left. + \frac{1}{2}\rho^\alpha(\boldsymbol{r})\left\{\mathrm{Re}\left(\left[\kappa_\tau^*(1 - 8\chi_\tau)\right](\boldsymbol{r})\kappa_\tau(\boldsymbol{r})\right) + \left[\eta_\tau\kappa_\tau\right]^*(\boldsymbol{r})\left[\eta_\tau\kappa_\tau\right](\boldsymbol{r})\right\} \right\}
$$

$$
\text{(C.46)}
$$

Appendix D

QRPA Formulas

D.1 The Hamiltonian in Quasiparticle Space

Plugging the general Bogoliubov transformation into the nuclear many-body Hamiltonian

$$\mathrm{H} = \sum_{kk'} t_{kk'} \mathrm{c}_k^\dagger \mathrm{c}_{k'} + \frac{1}{4} \sum_{kk'qq'} \bar{v}_{kk'qq'} \mathrm{c}_k^\dagger \mathrm{c}_{k'}^\dagger \mathrm{c}_{q'} \mathrm{c}_q \,, \tag{D.1}$$

we obtain

$$\mathrm{H} = \mathrm{H}^0 + \mathrm{H}^{11} + \mathrm{H}^{20} + \mathrm{H}^{02} + \mathrm{H}^{40} + \mathrm{H}^{04} + \mathrm{H}^{31} + \mathrm{H}^{13} + \mathrm{H}^{22} \tag{D.2}$$

$$= H^0 + \sum_{kk'} H_{kk'}^{11} \beta_k^\dagger \beta_{k'}$$

$$+ \frac{1}{2} \sum_{kk'} \left(H_{kk'}^{20} \beta_k^\dagger \beta_{k'}^\dagger + h.c. \right) + \sum_{kk'qq'} \left(H_{kk'qq'}^{40} \beta_k^\dagger \beta_{k'}^\dagger \beta_q \beta_{q'}^\dagger + h.c. \right)$$

$$+ \sum_{kk'qq'} \left(H_{kk'qq'}^{31} \beta_k^\dagger \beta_{k'}^\dagger \beta_q^\dagger \beta_{q'} + h.c. \right) + \frac{1}{4} \sum_{kk'qq'} H_{kk'qq'}^{22} \beta_k^\dagger \beta_{k'}^\dagger \beta_{q'} \beta_q \,, \tag{D.3}$$

where

$$H^0 = \mathrm{tr} \left(t\rho + \frac{1}{2} \Gamma \rho - \frac{1}{2} \Delta \kappa^* \right) = E_{\mathrm{HFB}} \,, \tag{D.4}$$

$$H^{11} = U^\dagger h U - V^\dagger h^T V + U^\dagger \Delta V - V^\dagger \Delta^* U \,, \tag{D.5}$$

$$H^{20} = U^\dagger h V^* - V^\dagger h^T U^* + U^\dagger \Delta U^* - V^\dagger \Delta^* V^* \,, \tag{D.6}$$

and

$$H_{kk'qq'}^{40} = \frac{1}{4} \sum_{ll'pp'} \bar{v}_{ll'pp'} U_{lk}^* U_{l'k'}^* V_{p'q}^* V_{pq'}^* \,, \tag{D.7}$$

$$H_{kk'qq'}^{31} = \frac{1}{2} \sum_{ll'pp'} \bar{v}_{ll'pp'} \left(U_{lk}^* V_{p'k'}^* V_{pq}^* V_{l'q'} + V_{pk}^* U_{l'k'}^* U_{lq}^* U_{p'q'} \right) \,, \tag{D.8}$$

$$H^{22}_{kk'qq'} = \sum_{ll'pp'} \bar{v}_{ll'pp'} \left(U^*_{lk} V^*_{p'k'} V_{l'q} U_{pq'} - U^*_{lk} V^*_{p'k} V_{l'q} U_{pq'} \right.$$
$$- U^*_{lk} V^*_{p'k'} V_{l'q'} U_{pq} + U^*_{lk'} V^*_{p'k} V_{l'q'} U_{pq}$$
$$\left. + U^*_{lk} U^*_{l'k'} U_{pq} U_{p'q'} + V^*_{pk} V^*_{p'k} V_{lq} V_{l'q'} \right) \qquad (D.9)$$

(cf. [21]). The matrix elements in the canonical basis are easily obtained by setting $C = 1$ in Eq. (3.28)

$$U_{kk'} = \sum_{\mu} D_{k\mu} u_\mu \delta_{\mu k'} \,, \qquad V_{kk'} = \sum_{\mu,\mu'} D^*_{k\mu} v_\mu \delta_{\mu \bar{\mu}'} \delta_{\mu' k'} \,. \qquad (D.10)$$

In quasiparticle space, the HFB equations (3.20) are equivalent to

$$H^{20}_{kk'} = H^{02*}_{k'k} = 0 \,, \qquad (D.11)$$

and the Hamiltonian (D.3) can be written as

$$H = H^0 + \sum_k E_k \beta^\dagger_k \beta_k + H^{40} + H^{04} + H^{31} + H^{13} + H^{22} \,, \qquad (D.12)$$

where E_k denotes the energy of the quasiparticle state k and k runs over the selected quasi-particle solutions (cf. Sect. 3.1).

D.2   Transition Operator Matrix Elements

In this section, we provide the reduced matrix elements of the electric and weak transition operators introduced in Sect. 5.2.1, including the basic building blocks. The matrix elements are evaluated with respect to a spherical harmonic oscillator basis $\left| n(l\frac{1}{2})jm \right\rangle$ — to obtain the matrix elements in the canonical basis, one merely has to carry out the corresponding unitary transformation. Note that many authors interchange the order of the spin- and orbital angular momentum quantum numbers in the single-particle state, which leads to a change of phase due to the properties of the Clebsch-Gordan coefficients (see [21, 119], for example).

In the following formulae, we use

$$\hat{j} = \sqrt{2j+1} \,. \qquad (D.13)$$

D.2.1   Basic Reduced Matrix Elements

Radial Integral

$$\left\langle nl \left| r^\lambda \right| n'l' \right\rangle = \int dr \, r^{2+\lambda} R_{nl}(r) R_{n'l'}(r) \qquad (D.14)$$

Spherical Harmonics, No Spin-Flip

$$\left\langle (l\tfrac{1}{2})j \left|\left| Y_0(\hat{\mathbf{r}}) \right|\right| (l'\tfrac{1}{2})j' \right\rangle = \delta_{ll'} \delta_{jj'} \sqrt{\frac{2j+1}{4\pi}} \qquad (D.15)$$

$$\left\langle (l\tfrac{1}{2})j \left|\left| Y_J(\hat{\mathbf{r}}) \right|\right| (l'\tfrac{1}{2})j' \right\rangle = \frac{1+(-1)^{l+l'+J}}{2} \sqrt{\frac{\hat{j}\hat{j}'\hat{J}}{4\pi}} (-1)^{j'+l+l'-\frac{1}{2}} \begin{pmatrix} j & J & j' \\ -\frac{1}{2} & 0 & \frac{1}{2} \end{pmatrix} \quad (D.16)$$

Spherical Harmonics, Spin-Flip

$$\left\langle (l\tfrac{1}{2})j \middle|\middle| \left[Y_1(\hat{\mathbf{r}}) \otimes \sigma\right]_0 \middle|\middle| (l'\tfrac{1}{2})j' \right\rangle = \delta_{jj'} \frac{(-1)^{l-l'} - 1}{2} \sqrt{\frac{2j+1}{4\pi}} \tag{D.17}$$

$$\left\langle (l\tfrac{1}{2})j \middle|\middle| \left[Y_L(\hat{\mathbf{r}}) \otimes \sigma\right]_J \middle|\middle| (l'\tfrac{1}{2})j' \right\rangle = \frac{1 + (-1)^{l+l'+L}}{2} \sqrt{\frac{\hat{j}\hat{j}'\hat{L}\hat{J}}{4\pi}} (-1)^{l'+J-j-j'}$$
$$\times \left[(-1)^{l'+j'+\frac{1}{2}} \begin{pmatrix} L & 1 & J \\ 0 & 0 & 0 \end{pmatrix} \begin{pmatrix} j & J & j' \\ \frac{1}{2} & 0 & -\frac{1}{2} \end{pmatrix} \right.$$
$$\left. -\sqrt{2} \begin{pmatrix} L & 1 & J \\ 0 & -1 & 1 \end{pmatrix} \begin{pmatrix} j & J & j' \\ \frac{1}{2} & -1 & \frac{1}{2} \end{pmatrix} \right] \tag{D.18}$$

D.2.2 Electric Transition Operators

Monopole Operator

$$\left\langle n(l\tfrac{1}{2})j \middle|\middle| Q_0 \middle|\middle| n'(l'\tfrac{1}{2})j' \right\rangle = \delta_{ll'}\delta_{jj'}e\sqrt{\frac{2j+1}{4\pi}} \left\langle nl \middle| r^2 \middle| n'l' \right\rangle \tag{D.19}$$

General Multipole Operator

$$\left\langle n(l\tfrac{1}{2})j \middle|\middle| Q_J \middle|\middle| n'(l'\tfrac{1}{2})j' \right\rangle = e\left\langle nl \middle| r^J \middle| n'l' \right\rangle \left\langle (l\tfrac{1}{2})j \middle|\middle| Y_J(\hat{\mathbf{r}}) \middle|\middle| (l'\tfrac{1}{2})j' \right\rangle \tag{D.20}$$

D.2.3 Weak Transition Operators

Fermi Operator

$$\left\langle n(l\tfrac{1}{2})j\tau \middle|\middle| \tau_\pm \middle|\middle| n'(l'\tfrac{1}{2})j'\tau' \right\rangle = \delta_{nn'}\delta_{ll'}\delta_{jj'}\sqrt{\frac{2j+1}{4\pi}} \left\langle \tau \middle| \tau_\pm \middle| \tau' \right\rangle \tag{D.21}$$

Gamow-Teller Operator

$$\left\langle n(l\tfrac{1}{2})j\tau \middle|\middle| \left[Y_0(\hat{\mathbf{r}}) \otimes \sigma\right]_1 \tau_\pm \middle|\middle| n'(l'\tfrac{1}{2})j'\tau' \right\rangle$$
$$= \delta_{nn'}\delta_{ll'} \left\langle (l\tfrac{1}{2})j \middle|\middle| \left[Y_0(\hat{\mathbf{r}}) \otimes \sigma\right]_1 \middle|\middle| (l\tfrac{1}{2})j' \right\rangle \left\langle \tau \middle| \tau_\pm \middle| \tau' \right\rangle \tag{D.22}$$

Appendix E

Interactions

E.1   Calculation of Two-Body Matrix Elements

The two-body matrix elements of the NN interaction, as well as the intrinsic kinetic energy and mean-square radii (see Sects. 2.1.2 and 2.1.3) depend only on relative coordinates, and are most conveniently calculated in a relative LS-coupled basis. HF, HFB, and (Q)RPA, on the other hand, rely on the underlying single-particle basis of the many-body state, hence we need to transform the $(LS)J$-coupled states to antisymmetrized jj-coupled two-body states $\left| n_1 l_1 j_1, n_2 l_2 j_2; JT \right\rangle$.

This is achieved by the so-called Talmi-Moshinsky transformation [141, 142], which explicitly separates the center-of-mass and relative coordinates of the spherical harmonic oscillator basis in which the single-particle states are expanded. Including angular momentum recoupling as well, one then obtains

$$
\left\langle n_1 l_1 j_1, n_2 l_2 j_2; JT \right| \mathrm{o} \left| n'_1 l'_1 j'_1, n'_2 l'_2 j'_2; JT \right\rangle
$$

$$
= \sqrt{\hat{j}_1 \hat{j}_2 \hat{j}'_1 \hat{j}'_2} \sum_{L,L',S} \sum_{N,\Lambda} \sum_{\nu,\lambda} \sum_{\nu',\lambda'} \sum_{j}
$$

$$
\times \begin{Bmatrix} l_1 & l_2 & L \\ \frac{1}{2} & \frac{1}{2} & S \\ j_1 & j_2 & J \end{Bmatrix} \begin{Bmatrix} l'_1 & l'_2 & L' \\ \frac{1}{2} & \frac{1}{2} & S \\ j'_1 & j'_2 & J \end{Bmatrix} \begin{Bmatrix} \Lambda & \lambda & L \\ S & J & j \end{Bmatrix} \begin{Bmatrix} \Lambda & \lambda' & L' \\ S & J & j \end{Bmatrix}
$$

$$
\times \left\langle\!\left\langle N\Lambda, \nu\lambda \,|\, n_1 l_1, n_2 l_2; L \right\rangle\!\right\rangle \left\langle\!\left\langle N\Lambda, \nu'\lambda' \,|\, n'_1 l'_1, n'_2 l'_2; L' \right\rangle\!\right\rangle
$$

$$
\times \hat{j}\hat{S}\hat{L}\hat{L}' \, (-1)^{L+L'} \left\{ 1 - (-1)^{\lambda+S+T} \right\}
$$

$$
\times \left\langle \nu(\lambda S)jT \right| \mathrm{o} \left| \nu'(\lambda'S)jT \right\rangle , \tag{E.1}
$$

where $\hat{j} = 2j+1$, and $\left\langle\!\left\langle ... | ... \right\rangle\!\right\rangle$ are the coefficients of the Talmi-Moshinsky transformation, also referred to as harmonic oscillator brackets [143], and (N,Λ) and $(n,\lambda),(n',\lambda')$ denote the quantum numbers of the intermediate center-of-mass and relative harmonic oscillator states.

E.2 Two-Body Matrix Element of the Density-Dependent Interaction

In analogy to the very detailed derivation of the matrix element of a zero-range interaction in [144], the jj-coupled matrix element of the density-dependent interaction

$$\mathrm{v}[\rho] = t_0 \left(1 + x_0 \mathrm{P}_\sigma \right) \rho^\alpha \left(\frac{\mathbf{r}_1 + \mathbf{r}_2}{2} \right) \delta^{(3)}(\mathbf{r}_1 - \mathbf{r}_2)\,, \tag{E.2}$$

is given by

$$\left\langle\, n_1 l_1 j_1, n_2 l_2 j_2; JT \,\middle|\, \mathrm{v}[\rho] \,\middle|\, n_1' l_1' j_1', n_2' l_2' j_2'; JT \,\right\rangle$$

$$= \frac{1}{2}(1 + (-1)^T x_0) \frac{t_0 \sqrt{\hat{j}_1 \hat{j}_2 \hat{j}_1' \hat{j}_2'}}{4\pi(2J+1)} \int dr\, r^2 \rho^\alpha(r) R_{n_1 l_1}(r) R_{n_2 l_2}(r) R_{n_1' l_1'}(r) R_{n_2' l_2'}(r)$$

$$\times \left\{ \left(1 - (-1)^{J+T+l_2'+l_4'}\right) (-1)^{j_2 - j_2' + l_2 + l_2'} \left\langle j_1 \tfrac{1}{2} j_2 - \tfrac{1}{2} \middle| J0 \right\rangle \left\langle j_1' \tfrac{1}{2} j_2' - \tfrac{1}{2} \middle| J0 \right\rangle \right.$$

$$\left. + \left(1 + (-1)^T\right) \left\langle j_1 \tfrac{1}{2} j_2 \tfrac{1}{2} \middle| J1 \right\rangle \left\langle j_1' \tfrac{1}{2} j_2' \tfrac{1}{2} \middle| J1 \right\rangle \right\}\,. \tag{E.3}$$

E.3 Argonne V18

The Argonne V18 potential is the most recent realistic NN interaction constructed by the Argonne group, and designed too be as local as possible to meet the requirements of the Green's Function Monte Carlo Method. AV18 consists of three main parts – the local coordinate space one-pion exchange (OPE) potential, a phenomenological parameterization of the intermediate- and short-range part of the NN interaction, and the electromagnetic interaction of the Nijmegen group:

$$\mathrm{v} = \mathrm{v}_\pi + \mathrm{v}_\mathrm{sr} + \mathrm{v}_\mathrm{em}\,. \tag{E.4}$$

Charge-independence breaking (CIB) is taken into account by distinguishing between the charged and neutral pion exchanges as well as nn, pp and np scattering.

The radial dependencies of the phenomenological part are parameterized by

$$v_{STM_T}^i(r) = I_{STM_T}^i Z^2(\mu r) f_Z^2(r) + \left[P_{STM_T}^i + \mu r Q_{STM_T}^i + (\mu r)^2 R_{STM_T}^i \right] W(r)\,, \tag{E.5}$$

where

$$Y(x) = \frac{e^{-x}}{x}\,, \tag{E.6}$$

$$Z(x) = \left(1 + \frac{3}{x} + \frac{3}{x^2}\right) Y(x)\,, \tag{E.7}$$

$$f_Y(r) = 1 - e^{-cr^2}\,, \tag{E.8}$$

$$f_Z(r) = \left(1 - e^{-cr^2}\right)^2\,, \tag{E.9}$$

ST(NN)	Type	$I\,[\mathrm{MeV}]$	$P\,[\mathrm{MeV}]$	$Q\,[\mathrm{MeV}]$	$R\,[\mathrm{MeV}]$
01(pp)	c	-11.27028	3346.6874	1859.5627*	0
01(np)	c	-10.66788	3126.5542	1746.4298*	0
01(nn)	c	-11.27028	3342.7664	1857.4367*	0
01	l^2	0.12472	16.7780	9.0972*	0
00	c	-2.09971	1204.4301	511.9380*	0
	l^2	-0.31452	217.4559	117.9063*	0
11(pp)	c	-7.62701	1815.4920	969.3863*	1847.8059
11(np)	c	-7.62701	1813.5315	966.2483*	1847.8059
11(nn)	c	-7.62701	1811.5710	967.2603*	1847.8059
11	l^2	0.06709	342.0669	185.4713*	-615.2339
	t	1.07985	0	-190.0949	-811.2040
	ls	-0.62697	-570.5571	-309.3605*	819.1222
	$(ls)^2$	0.74129	9.3418	5.0652*	-376.4384
10	c	-8.62770	2605.2682	1459.6345*	441.9733
	l^2	-0.13201	253.4350	137.4144*	-1.0076
	t	1.485601	0	-1126.8359	370.1324
	ls	0.10180	86.0658	46.6655*	-356.5175
	$(ls)^2$	0.07357	-217.5791	-117.9731*	18.3935

Table E.1: AV18 short-range potential parameters. The asterisk denotes that the value was computed by Eq. (E.11) and not fit. The parameters of the Woods-Saxon function are held at $r_0 = 0.5$ fm and $a_0 = 0.2$ fm, the cutoff is always $c = 2.1$ fm^{-2}.

and i runs over the different operator types $(c, t, l^2, ls, (ls)^2)$, M_T denotes the isospin projection, μ is the average of the pion masses, and

$$W(r) = \left[1 + e^{(r-r_0)/a}\right]^{-1} \tag{E.10}$$

is a *Woods-Saxon* function providing the short-range core. With the imposition of the additional regularization conditions

$$v^t_{STM_T}(r = 0) = 0 \quad \text{and} \quad \left.\frac{\partial v^{i \neq t}_{STM_T}}{\partial r}\right|_{r=0} = 0\,, \tag{E.11}$$

a total of 40 nonzero intermediate- and short-range parameters $I^i_{STM_T}, P^i_{STM_T}, Q^i_{STM_T}$, and $R^i_{STM_T}$ remain. Their values are listed in Tab. E.1.

The potential given in (STM_T)-channels can be projected onto 18 operators, thus giving AV18 its name. For this work, however, we will prefer working with the ST-projected potential. As shown in Tab. E.1, charge dependence (CD) and charge asymmetry (CA) in the phenomenological part of the potential are caused by the splitting of the central potential in the $T = 1$ channel only, while the OPE part contributes CIB effects both to the $T = 1$ central and tensor parts. The charge-dependent part of AV18
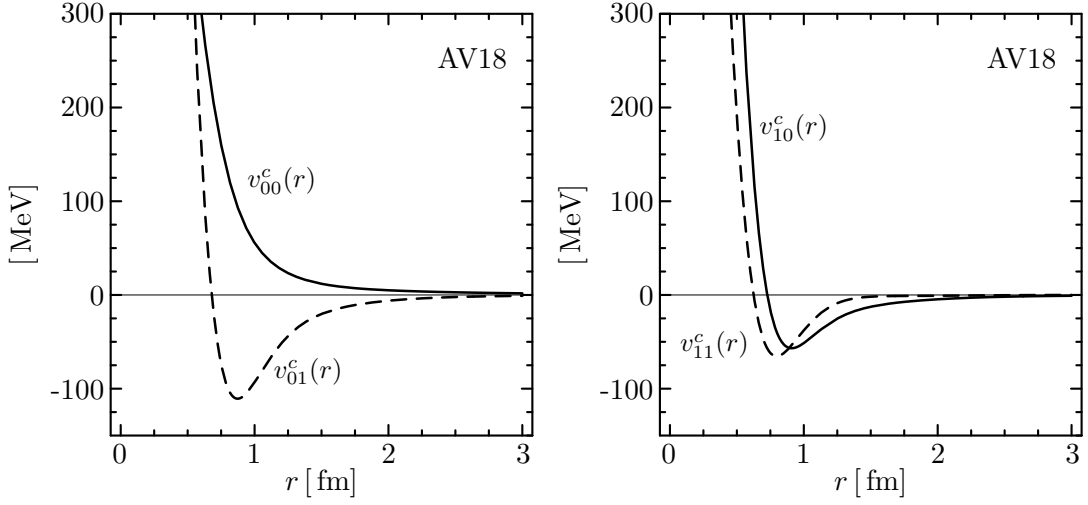
Figure E.1: Radial dependencies of the AV18 potential: central part of AV18, projected onto the four (S, T)-channels.

is then given by

$$
\begin{aligned}
\mathrm{v}_{ST}^{CD} = {}& \frac{1}{6} \left[\frac{1}{2}(v_{S1,pp}^{c}(\mathrm{r}) + v_{S1,nn}^{c}(\mathrm{r})) - v_{S1,np}^{c}(\mathrm{r}) \right] \mathrm{t}_{12} \\
& + \frac{1}{6} \left[\frac{1}{2}(v_{S1,pp}^{t}(\mathrm{r}) + v_{S1,nn}^{t}(\mathrm{r})) - v_{S1,np}^{t}(\mathrm{r}) \right] \mathrm{s}_{12}(\hat{\mathbf{r}}, \hat{\mathbf{r}})\mathrm{t}_{12} ,
\end{aligned}
\tag{E.12}
$$

where the isotensor operator

$$
\mathrm{t}_{12} \equiv 3\tau_{z,1}\tau_{z,2} - \boldsymbol{\tau}_1 \cdot \boldsymbol{\tau}_2
\tag{E.13}
$$

has been introduced, and for the charge-asymmetric part one finds

$$
\mathrm{v}_{ST}^{CA} = \frac{1}{4}(v_{S1,pp}^{c}(\mathrm{r}) - v_{S1,nn}^{c}(\mathrm{r}))(\tau_{z,1} + \tau_{z,2}) .
\tag{E.14}
$$

The charge-independent part of AV18 reads

$$
\begin{aligned}
\mathrm{v} = {}& \sum_{ST} v_{ST}^{c,CI}(\mathrm{r}) \, \Pi_{ST} + \sum_{T} v_{1T}^{t,CI}(\mathrm{r}) \, \mathrm{s}_{12}(\hat{\mathbf{r}}, \hat{\mathbf{r}})\Pi_{1T} + \sum_{ST} v_{ST}^{l^2}(\mathrm{r}) \, \mathbf{l}^2\Pi_{ST} \\
& + \sum_{T} v_{1T}^{ls}(\mathrm{r}) \, \mathbf{l} \cdot \mathbf{s} \, \Pi_{1T} + \sum_{T} v_{1T}^{(ls)^2}(\mathrm{r}) \, (\mathbf{l} \cdot \mathbf{s})^2 \, \Pi_{1T} ,
\end{aligned}
\tag{E.15}
$$

where

$$
v_{ST}^{i,CI}(r) =
\begin{cases}
\frac{1}{3} \left(v_{S1,pp}^{i}(r) + v_{S1,nn}^{i}(r) + v_{S1,np}^{i}(r) \right) & \text{for } T = 1 \\
v_{ST}^{i}(r) & \text{for } T = 0
\end{cases}
\tag{E.16}
$$

with $i = c, t$. The radial dependencies in the four ST-channels are plotted by interaction type in Figs. E.1 and E.2.
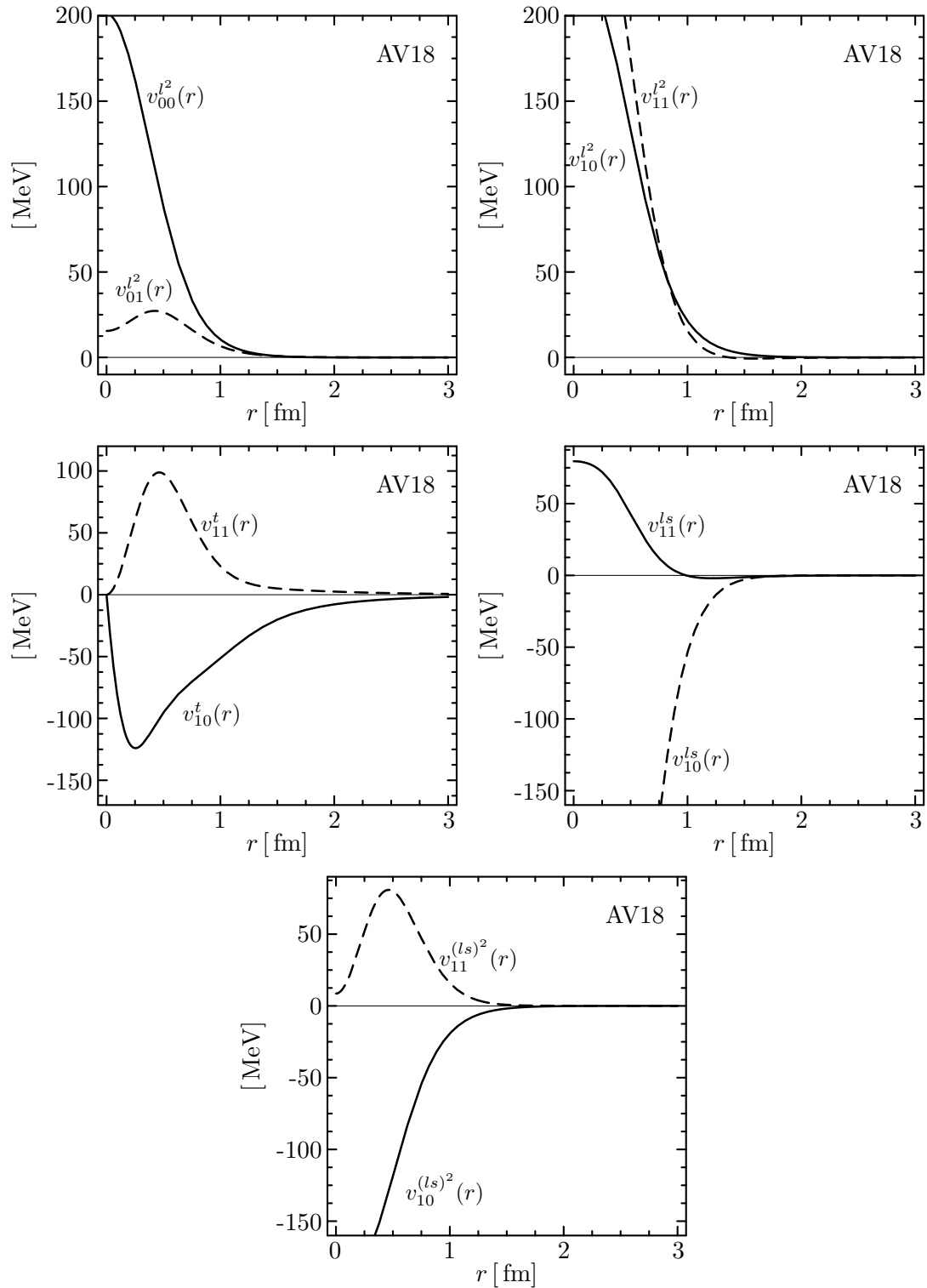
Figure E.2: Radial dependencies of the AV18 potential (cont.): tensor, angular momentum, spin-orbit, and quadratic spin-orbit parts of AV18 in the four ST-channels.

	μ [fm]	W [MeV]	B [MeV]	H [MeV]	M [MeV]	t_0 [MeV fm^4]	W_{LS} [MeV fm^5]
D1	0.7	-402.40	-100.00	-496.20	-23.56	1350.0	115.0
	1.2	-21.30	-11.77	37.27	-68.81		
D1S	0.7	-1720.30	1300.00	-1813.53	1397.60	1390.6	130.0
	1.2	103.64	-163.48	162.81	-223.93		

Table E.2: Parameters of the Gogny D1 [82] and D1S [147] interactions. For both cases, $\alpha = \frac{1}{3}$ and $x_0 = 1$.

E.4 The Gogny Interaction

E.4.1 Parameterization

The phenomenological Gogny interaction, or rather the family of Gogny interactions, was introduced by Gogny and co-workers as an alternative to existing density-dependent Skyrme forces. Their main motivation for using a finite-range force was its self-regulating behavior in the pairing channel — for zero-range pairing forces, on the other hand, a consistent regularization scheme has only become available in recent years [145, 146].

The interaction is parameterized as

$$
\begin{aligned}
\mathrm{v}_{12} = \sum_{i=1}^{2} & \exp\left(-\frac{(\mathbf{r}_1 - \mathbf{r}_2)^2}{\mu_i^2}\right) (W_i + B_i \mathrm{P}_\sigma - H_i \mathrm{P}_\tau - M_i \mathrm{P}_\sigma \mathrm{P}_\tau) \\
& + t_0 (1 + x_0 \mathrm{P}_\sigma) \rho^\alpha \left(\frac{\mathbf{r}_1 + \mathbf{r}_2}{2}\right) \delta^3 (\mathbf{r}_1 - \mathbf{r}_2) \\
& + i W_{LS} (\boldsymbol{\sigma}_1 + \boldsymbol{\sigma}_2) \cdot \left(\overleftarrow{\boldsymbol{\nabla}}_1 - \overleftarrow{\boldsymbol{\nabla}}_2\right) \times \delta^{(3)} (\mathbf{r}_1 - \mathbf{r}_2) \left(\overrightarrow{\boldsymbol{\nabla}}_1 - \overrightarrow{\boldsymbol{\nabla}}_2\right),
\end{aligned}
\quad \text{(E.17)}
$$

where the values of the D1 and D1S parameter sets are given in Tab. E.2.

E.4.2 Evaluation of the Spin-Orbit Matrix Element

The peculiar shape of the two-body spin-orbit term in (E.17) requires special attention. In the following, we will derive its matrix element in relative coordinates, which can then be used in the Talmi transformation, as explained in Sect. E.1. Using a spherical coordinate system, we first notice that the Dirac distribution reduces to

$$
\delta^3(\boldsymbol{r}_1 - \boldsymbol{r}_2) = \frac{1}{4\pi r^2} \delta(r), \quad r = |\boldsymbol{r}_1 - \boldsymbol{r}_2|.
\quad \text{(E.18)}
$$

Introducing

$$
\overrightarrow{\boldsymbol{\nabla}} \equiv \overrightarrow{\boldsymbol{\nabla}}_1 - \overrightarrow{\boldsymbol{\nabla}}_2,
\quad \text{(E.19)}
$$

and rewriting $\boldsymbol{\sigma}_1 + \boldsymbol{\sigma}_2$ in terms of the total spin operator $\mathbf{S}$, we have

$$2iW_{LS}\left\langle\, n(LS)JM\, \middle|\, \left(\overleftarrow{\boldsymbol{\nabla}} \times \frac{\delta(\mathrm{r})}{4\pi\mathrm{r}^2}\,\overrightarrow{\boldsymbol{\nabla}}\right) \cdot \mathbf{S}\, \middle|\, n'(L'S')J'M'\,\right\rangle$$

$$= 2iW_{LS}\delta_{JJ'}\delta_{MM'}\frac{1}{\sqrt{2J+1}}\left\langle\, n(LS)J\, \middle\|\, \left(\overleftarrow{\boldsymbol{\nabla}} \times \frac{\delta(\mathrm{r})}{4\pi\mathrm{r}^2}\,\overrightarrow{\boldsymbol{\nabla}}\right) \cdot \mathbf{S}\, \middle\|\, n'(L'S')J\,\right\rangle$$

$$= 2iW_{LS}\delta_{JJ'}\delta_{MM'}(-1)^{J+L'+1}\begin{Bmatrix} L & L' & 1 \\ 1 & 1 & J \end{Bmatrix}\left\langle\, nL\, \middle\|\, \overleftarrow{\boldsymbol{\nabla}} \times \frac{\delta(\mathrm{r})}{4\pi\mathrm{r}^2}\,\overrightarrow{\boldsymbol{\nabla}}\, \middle\|\, n'L'\,\right\rangle\left\langle\, S\, \middle\|\, \mathbf{S}\, \middle\|\, S'\,\right\rangle$$

$$= 2iW_{LS}\delta_{JJ'}\delta_{MM'}(-1)^{J+L'+1}\begin{Bmatrix} L & L' & 1 \\ 1 & 1 & J \end{Bmatrix}\left\langle\, nL\, \middle\|\, \overleftarrow{\boldsymbol{\nabla}} \times \frac{\delta(\mathrm{r})}{4\pi\mathrm{r}^2}\,\overrightarrow{\boldsymbol{\nabla}}\, \middle\|\, n'L'\,\right\rangle$$

$$\times \sqrt{S(S+1)(2S+1)}\delta_{SS'}$$

$$= 4\sqrt{3}W_{LS}\delta_{S1}\delta_{JJ'}\delta_{MM'}(-1)^{J+L'+1}\begin{Bmatrix} L & L' & 1 \\ 1 & 1 & J \end{Bmatrix}$$

$$\times \left\langle\, nL\, \middle\|\, \left\{\overleftarrow{\boldsymbol{\nabla}}^{(1)} \otimes \frac{\delta(\mathrm{r})}{4\pi\mathrm{r}^2}\,\overrightarrow{\boldsymbol{\nabla}}^{(1)}\right\}^{(1)}\, \middle\|\, n'L'\,\right\rangle, \quad \text{(E.20)}$$

where we have expressed the vector product as a spherical tensor by means of [138]

$$\left(\overleftarrow{\boldsymbol{\nabla}} \times \frac{1}{4\pi\mathrm{r}^2}\delta(\mathrm{r})\,\overrightarrow{\boldsymbol{\nabla}}\right)_q = -i\sqrt{2}\left\{\overleftarrow{\boldsymbol{\nabla}}^{(1)} \otimes \frac{\delta(\mathrm{r})}{4\pi\mathrm{r}^2}\,\overrightarrow{\boldsymbol{\nabla}}^{(1)}\right\}^{(1)}_q \quad \text{(E.21)}$$

$$= -i\sqrt{2}\sum_{q_1 q_2}\left\langle\, 1q_1 1q_2\, \middle|\, 1q\,\right\rangle\overleftarrow{\boldsymbol{\nabla}}^{(1)}_{q_1}\frac{\delta(\mathrm{r})}{4\pi\mathrm{r}^2}\,\overrightarrow{\boldsymbol{\nabla}}^{(1)}_{q_2}\,. \quad \text{(E.22)}$$

Unfortunately, the reduced matrix element of the coordinate-space operator cannot be extracted by making the convenient choice $M = M' = q = 0$, because the Clebsch-Gordan coefficient $\left\langle\, L010\, \middle|\, L'0\,\right\rangle$ vanishes itself. Considering the matrix element

$$\left\langle\, nL0\, \middle|\, \left\{\overleftarrow{\boldsymbol{\nabla}}^{(1)} \otimes \frac{\delta(\mathrm{r})}{4\pi\mathrm{r}^2}\,\overrightarrow{\boldsymbol{\nabla}}^{(1)}\right\}^{(1)}_1\, \middle|\, n'L'-1\,\right\rangle \quad \text{(E.23)}$$

instead, we first use Eq. (E.22) and obtain

$$\left\{\overleftarrow{\boldsymbol{\nabla}}^{(1)} \otimes \frac{\delta(\mathrm{r})}{4\pi\mathrm{r}^2}\,\overrightarrow{\boldsymbol{\nabla}}^{(1)}\right\}^{(1)}_1 = \frac{1}{\sqrt{2}}\left(\overleftarrow{\boldsymbol{\nabla}}^{(1)}_1\frac{\delta(\mathrm{r})}{4\pi\mathrm{r}^2}\,\overrightarrow{\boldsymbol{\nabla}}^{(1)}_0 - \overleftarrow{\boldsymbol{\nabla}}^{(1)}_0\frac{\delta(\mathrm{r})}{4\pi\mathrm{r}^2}\,\overrightarrow{\boldsymbol{\nabla}}^{(1)}_1\right)\,. \quad \text{(E.24)}$$

The integrand of the first term is given by

$$\mathcal{I}_{10} \equiv r^2\sin\theta\boldsymbol{\nabla}^{(1)}_1\left(R_{nL}(r)Y^*_{L0}(\Omega)\right)\frac{\delta(r)}{4\pi r^2}\boldsymbol{\nabla}^{(1)}_0\left(R_{n'L'}(r)Y_{L'-1}(\Omega)\right)\,. \quad \text{(E.25)}$$

Note that the gradient operator does not act on the integration measure by convention. Using the spherical components of the gradient operator and the properties of the

spherical harmonics [138], the separate factors are given by

$$
\boldsymbol{\nabla}_1^{(1)} \left(R_{nL}(r) Y_{L0}^*(\Omega) \right) = \sqrt{\frac{(L+1)(L+2)}{2(2L+1)(2L+3)}} A_{nL}^{(-)}(r) Y_{L+11}(\Omega)
$$

$$
- \sqrt{\frac{(L-1)L}{2(2L-1)(2L+1)}} A_{nL}^{(+)}(r) Y_{L-11}(\Omega) \,, \tag{E.26}
$$

$$
\boldsymbol{\nabla}_0^{(1)} \left(R_{n'L'}(r) Y_{L'-1}(\Omega) \right) = \sqrt{\frac{(L'+1)^2 - 1}{(2L'+1)(2L'+3)}} A_{n'L'}^{(-)}(r) Y_{L'+1-1}(\Omega)
$$

$$
+ \sqrt{\frac{L'^2 - 1}{(2L'-1)(2L'+1)}} A_{n'L'}^{(+)}(r) Y_{L'-1-1}(\Omega) \,, \tag{E.27}
$$

where

$$
A_{nL}^{(+)}(r) \equiv \frac{dR_{nL}(r)}{dr} + \frac{L+1}{r} R_{nL}(r) \,, \tag{E.28}
$$

$$
A_{nL}^{(-)}(r) \equiv \frac{dR_{nL}(r)}{dr} - \frac{L}{r} R_{nL}(r) \,. \tag{E.29}
$$

$$
\tag{E.30}
$$

Analogously, the second integrand reads

$$
\mathcal{I}_{01} \equiv r^2 \sin\theta \boldsymbol{\nabla}_0^{(1)} \left(R_{nL}(r) Y_{L0}^*(\Omega) \right) \frac{\delta(r)}{4\pi r^2} \boldsymbol{\nabla}_1^{(1)} \left(R_{n'L'}(r) Y_{L'-1}(\Omega) \right) \tag{E.31}
$$

and contributes the factors

$$
\boldsymbol{\nabla}_0^{(1)} \left(R_{nL}(r) Y_{L0}^*(\Omega) \right) = \sqrt{\frac{(L+1)^2}{(2L+1)(2L+3)}} A_{nL}^{(-)}(r) Y_{L+10}(\Omega)
$$

$$
+ \sqrt{\frac{L^2}{(2L-1)(2L+1)}} A_{nL}^{(+)}(r) Y_{L-10}(\Omega) \,, \tag{E.32}
$$

$$
\boldsymbol{\nabla}_1^{(1)} \left(R_{n'L'}(r) Y_{L'-1}(\Omega) \right) = \sqrt{\frac{L'(L'+1)}{2(2L'+1)(2L'+3)}} A_{n'L'}^{(-)}(r) Y_{L'+10}(\Omega)
$$

$$
- \sqrt{\frac{L'(L'+1)}{2(2L'-1)(2L'+1)}} A_{n'L'}^{(-)}(r) Y_{L'-10}(\Omega) \,. \tag{E.33}
$$

The angular integrals in the full expression are of the types

$$
\int d\Omega \, Y_{L\pm11}(\Omega) Y_{L'\pm1-1}(\Omega) = (-1) \int d\Omega \, Y_{L\pm1-1}^*(\Omega) Y_{L'\pm1-1}(\Omega) = -\delta_{LL'} \tag{E.34}
$$

and

$$
\int d\Omega \, Y_{L\pm11}(\Omega) Y_{L'\mp1-1}(\Omega) = (-1) \int d\Omega \, Y_{L\pm1-1}^*(\Omega) Y_{L'\mp1-1}(\Omega) = -\delta_{LL'\mp2} \,, \tag{E.35}
$$

respectively. Since we are dealing with a vector operator, it is clear that any matrix element between states with $\Delta L = \pm 2$ vanishes due to the Wigner-Eckart theorem. Thus, we only need to consider

$$
\frac{1}{\sqrt{2}} \int dr \frac{\delta(r)}{4\pi} \delta_{LL'} \Bigg\{ -\sqrt{\frac{(L+1)(L+2)((L+1)^2-1)}{2(2L+1)^2(2L+3)^2}} A_{nL}^{(-)}(r) A_{n'L}^{(-)}(r)
$$
$$
+ \sqrt{\frac{L(L-1)(L^2-1)}{2(2L-1)^2(2L+1)^2}} A_{nL}^{(+)}(r) A_{n'L}^{(+)}(r)
$$
$$
- \sqrt{\frac{L(L+1)^3}{2(2L+1)^2(2L+3)^2}} A_{nL}^{(-)}(r) A_{n'L}^{(-)}(r)
$$
$$
+ \sqrt{\frac{L^3(L+1)}{2(2L-1)^2(2L+1)^2}} A_{nL}^{(+)}(r) A_{n'L}^{(+)}(r) \Bigg\} . \tag{E.36}
$$

Plugging in spherical HO wave functions, we find that

$$
\big\langle nL0 \big| \Big\{ \overleftarrow{\boldsymbol{\nabla}}^{(1)} \otimes \frac{\delta(\mathrm{r})}{4\pi \mathrm{r}^2} \overrightarrow{\boldsymbol{\nabla}}^{(1)} \Big\}_1^{(1)} \big| n'L'-1 \big\rangle = \frac{3 N_{n1} N_{n'1}}{4\pi\sqrt{2}a^2} \mathcal{L}_n^{3/2}(0) \mathcal{L}_{n'}^{3/2}(0) \delta_{LL'} \delta_{L1} , \tag{E.37}
$$

where a is the oscillator length, N_{nL} the HO wave function normalization constant, and $\mathcal{L}_n^{L+1/2}(\frac{r^2}{a^2})$ an associated Laguerre polynomial. As expected, the coordinate-space part of the zero-range spin-orbit interaction acts only in the relative p-wave. With

$$
\big\langle L'-111 \big| L0 \big\rangle = -\frac{1}{\sqrt{2}}
$$

we can immediately read off the corresponding reduced matrix element

$$
\big\langle nL \big\| \Big\{ \overleftarrow{\boldsymbol{\nabla}}^{(1)} \otimes \frac{\delta(\mathrm{r})}{4\pi \mathrm{r}^2} \overrightarrow{\boldsymbol{\nabla}}^{(1)} \Big\}^{(1)} \big\| n'L' \big\rangle = -\frac{3\sqrt{3} N_{n1} N_{n'1}}{4\pi a^2} \mathcal{L}_n^{3/2}(0) \mathcal{L}_{n'}^{3/2}(0) \delta_{L1} \delta_{LL'} \tag{E.38}
$$

and plug it in Eq. (E.20), obtaining the final expression

$$
iW_{LS} \big\langle n(LS)JM \big| \Big(\overleftarrow{\boldsymbol{\nabla}} \times \frac{\delta(\mathrm{r})}{4\pi \mathrm{r}^2} \overrightarrow{\boldsymbol{\nabla}} \Big) \cdot (\boldsymbol{\sigma}_1 + \boldsymbol{\sigma}_2) \big| n'(L'S')J'M' \big\rangle
$$
$$
= -\frac{9}{\pi a^2} W_{LS} (-1)^J \begin{Bmatrix} 1 & 1 & 1 \\ 1 & 1 & J \end{Bmatrix} N_{n1} N_{n'1} \mathcal{L}_n^{3/2}(0) \mathcal{L}_{n'}^{3/2}(0) \delta_{L1} \delta_{LL'} \delta_{S1} \delta_{JJ'} \delta_{MM'} . \tag{E.39}
$$

For comparison, we calculate the spin-orbit field from the energy expressions given in [96] in the framework of density-functional theory. In coordinate and spin space, the density matrix and pairing tensor are then defined by

$$
\rho(\boldsymbol{r}\sigma, \boldsymbol{r}'\sigma') \equiv \big\langle \Psi \big| \Psi_\sigma^\dagger(\boldsymbol{r}) \Psi_{\sigma'}(\boldsymbol{r}') \big| \Psi \big\rangle
$$
$$
\equiv \frac{1}{2} \Big(\rho(\boldsymbol{r}, \boldsymbol{r}') \delta_{\sigma\sigma'} + \sum_i \big\langle \sigma \big| \sigma_i \big| \sigma' \big\rangle \rho_i(\boldsymbol{r}, \boldsymbol{r}') \Big) \tag{E.40}
$$
$$
\kappa(\boldsymbol{r}\sigma, \boldsymbol{r}'\sigma') \equiv \big\langle \Psi \big| \Psi_\sigma(\boldsymbol{r}) \Psi_{\sigma'}(\boldsymbol{r}') \big| \Psi \big\rangle
$$
$$
\equiv \frac{1}{2} \Big(\kappa(\boldsymbol{r}, \boldsymbol{r}') \delta_{\sigma\sigma'} + \sum_i \big\langle \sigma \big| \sigma_i \big| \sigma' \big\rangle \kappa_i(\boldsymbol{r}, \boldsymbol{r}') \Big) . \tag{E.41}
$$

For systems with time-reversal invariance, the energy contribution of the spin-orbit interaction is given by

$$E_{LS} = \frac{1}{2}W_{LS}\int d^3r \sum_{ijk}\left\{J_{ij}(\boldsymbol{r})\nabla_k\rho(\boldsymbol{r}) + \sum_q J_{q,ij}(\boldsymbol{r})\nabla_k\rho_q(\boldsymbol{r})\right\}$$
$$+ \sum_{ij,q}\left\{\tilde{J}_{q,ii}(\boldsymbol{r})\tilde{J}_{q,jj}(\boldsymbol{r}) - \tilde{J}_{q,ij}(\boldsymbol{r})\tilde{J}_{q,ji}(\boldsymbol{r})\right\} \tag{E.42}$$

where the local density is obtained as the diagonal matrix element of the spin-independent part of Eq. (E.40),

$$\rho(\boldsymbol{r}) \equiv \rho(\boldsymbol{r}, \boldsymbol{r}) \tag{E.43}$$

and the standard and pairing spin-current tensors $J_{ij}(\boldsymbol{r})$ and $\tilde{J}_{ij}(\boldsymbol{r})$ are defined by

$$J_{ij}(\boldsymbol{r}) = \frac{1}{2i}(\nabla_i - \nabla_i')\rho_j(\boldsymbol{r}, \boldsymbol{r}')|_{\boldsymbol{r}=\boldsymbol{r}'} \tag{E.44}$$

$$\tilde{J}_{ij}(\boldsymbol{r}) = \frac{1}{2i}(\nabla_i - \nabla_i')\kappa_j(\boldsymbol{r}, \boldsymbol{r}')|_{\boldsymbol{r}=\boldsymbol{r}'}, \tag{E.45}$$

with $\rho_j(\boldsymbol{r}, \boldsymbol{r}')$ and $\kappa_j(\boldsymbol{r}, \boldsymbol{r}')$ as defined above. Variation with respect to the densities gives

$$\Gamma_q(\boldsymbol{r}) = -\frac{1}{2}W_{LS}\sum_{ijk}\varepsilon_{ijk}\nabla_k\left(J_{ij}(\boldsymbol{r}) + J_{q,ij}(\boldsymbol{r})\right)$$
$$+ \frac{1}{2i}\sum_{ij}\left(\nabla_i\sigma_j B_{q,ij}(\boldsymbol{r}) + B_{q,ij}(\boldsymbol{r})\nabla_i\sigma_j\right) \tag{E.46}$$

$$\Delta_q(\boldsymbol{r}) = \frac{1}{2i}\sum_{ij}\left(\nabla_i\sigma_j\tilde{B}_{q,ij}(\boldsymbol{r}) + \tilde{B}_{q,ij}(\boldsymbol{r})\nabla_i\sigma_j\right), \tag{E.47}$$

where

$$B_{q,ij}(\boldsymbol{r}) = \frac{\partial E_{LS}}{\partial J_{q,ij}(\boldsymbol{r})} = \frac{1}{2}W_{LS}\sum_k\varepsilon_{ijk}\nabla_k\left(\rho(\boldsymbol{r}) + \rho_q(\boldsymbol{r})\right) \tag{E.48}$$

$$\tilde{B}_{q,ij}(\boldsymbol{r}) = \frac{\partial E_{LS}}{\partial \tilde{J}_{q,ij}(\boldsymbol{r})} = W_{LS}\left(\delta_{ij}\sum_k\tilde{J}_{q,kk}(\boldsymbol{r}) - \tilde{J}_{q,ji}(\boldsymbol{r})\right). \tag{E.49}$$

For spherical symmetry, the spin-current tensors are reduced to

$$J_{ij}(\boldsymbol{r}) = \frac{1}{2}J(r)\sum_k\varepsilon_{ijk}\frac{r_k}{r}, \quad \tilde{J}_{ij}(\boldsymbol{r}) = \frac{1}{2}\tilde{J}(r)\sum_k\varepsilon_{ijk}\frac{r_k}{r}, \tag{E.50}$$

where

$$J(r) = \frac{1}{4\pi r}\sum_{nn'lj}\rho_{nn'}^{(lj)}(2j+1)\left[j(j+1) - l(l+1) - \frac{3}{4}\right]R_{nl}(r)R_{n'l}(r), \tag{E.51}$$

$$\tilde{J}(r) = \frac{1}{4\pi r}\sum_{nn'lj}(-1)^l\kappa_{nn'}^{(lj)}(2j+1)\left[j(j+1) - l(l+1) - \frac{3}{4}\right]R_{nl}(r)R_{n'l}(r), \tag{E.52}$$

and analogously

$$B_{ij}(\boldsymbol{r}) = \frac{1}{2}B(r)\sum_k \varepsilon_{ijk}\frac{r_k}{r}\,, \quad \tilde{B}_{ij}(\boldsymbol{r}) = \frac{1}{2}\tilde{B}(r)\sum_k \varepsilon_{ijk}\frac{r_k}{r}\,, \tag{E.53}$$

with

$$B(r) = W_{LS}(\rho'(r) + \rho'_q(r))\,, \quad \tilde{B}(r) = W_{LS}\tilde{J}(r)\,. \tag{E.54}$$

Plugging these quantities into the fields (E.46) and (E.47), we have

$$\begin{aligned}
\Gamma_q^{(lj)}(r) =& -\frac{1}{2}W_{LS}\sum_k \nabla_k\left(J(r) + J_q(r)\frac{r_k}{r}\right)\\
&+ \frac{1}{4i}\sum_{ijk}\varepsilon_{ijk}\left(\nabla_i\sigma_j B_q(r)\frac{r_k}{r} + B_q(r)\frac{r_k}{r}\nabla_i\sigma_j\right)\\
=& -\frac{1}{2}W_{LS}\left(\frac{2}{r} + \frac{d}{dr}\right)(J(r) + J_q(r))\\
&+ \frac{1}{4i}\sum_{ijk}\varepsilon_{ijk}\sigma_j\left(\frac{dB_q(r)}{dr}\frac{r_i r_k}{r^2} + B_q(r)\left(\frac{\delta_{ik}}{r} - \frac{r_i r_k}{r^3}\right) + 2B_q(r)\frac{r_k}{r}\nabla_i\right)\\
=& -\frac{1}{2}W_{LS}\left(\frac{2}{r} + \frac{d}{dr}\right)(J(r) + J_q(r)) + \frac{1}{2i}\sum_{ijk}\varepsilon_{ijk}\sigma_j B_q(r)\frac{r_k}{r}\nabla_i\\
=& -\frac{1}{2}W_{LS}\left(\frac{2}{r} + \frac{d}{dr}\right)(J(r) + J_q(r)) + \frac{1}{2}\frac{B_q(r)}{r}\mathbf{l}\cdot\boldsymbol{\sigma}\\
=& W_{LS}\left\{\frac{1}{r}\left(\rho'(r) + \rho'_q(r)\right)\mathbf{l}\cdot\mathbf{s} - \frac{1}{2}\left(\frac{2}{r} + \frac{d}{dr}\right)(J(r) + J_q(r))\right\} \tag{E.55}
\end{aligned}$$

$$\tag{E.56}$$

and

$$\begin{aligned}
\Delta_q^{(lj)}(r) =& (-1)^l\frac{1}{4i}\sum_{ijk}\varepsilon_{ijk}\left(\nabla_i\sigma_j\tilde{B}_q(r)\frac{r_k}{r} + \tilde{B}_q(r)\frac{r_k}{r}\nabla_i\sigma_j\right)\\
=& (-1)^l\frac{1}{2i}\sum_{ijk}\varepsilon_{ijk}\sigma_j\tilde{B}_q(r)\frac{r_k}{r}\nabla_i = (-1)^l\frac{1}{2}\frac{\tilde{B}_q(r)}{r}\mathbf{l}\cdot\boldsymbol{\sigma}\\
=& W_{LS}(-1)^l\frac{\tilde{J}_q(r)}{r}\mathbf{l}\cdot\mathbf{s} \tag{E.57}
\end{aligned}$$

In Ref. [82], Dechargé and Gogny use slightly different definitions of $J(r)$ and $\tilde{J}(r)$ which we are denoting $\mathcal{J}(r)$ and $\tilde{\mathcal{J}}(r)$; their relations to $J(r)$ and $\tilde{J}(r)$, respectively, are[1]

$$\mathcal{J}(r) = rJ(r)\,, \quad \tilde{\mathcal{J}}(r) = r\tilde{J}(r)\,. \tag{E.58}$$

---

[1]The formulae in Ref. [82] contain several typos which have been corrected here.

Thus,

$$
\begin{aligned}
\Gamma_q^{(lj)}(r) =& W_{LS} \left\{ \frac{1}{r} \left(\rho'(r) + \rho_q'(r) \right) \mathbf{l} \cdot \mathbf{s} - \frac{1}{2} \left(\frac{2}{r} + \frac{d}{dr} \right) \left(\frac{\mathcal{J}(r)}{r} + \frac{\mathcal{J}_q(r)}{r} \right) \right\} \\
=& W_{LS} \left\{ \frac{1}{r} \left(\rho'(r) + \rho_q'(r) \right) \mathbf{l} \cdot \mathbf{s} - \frac{1}{2r} \left(\frac{1}{r} + \frac{d}{dr} \right) \left(\mathcal{J}(r) + \mathcal{J}_q(r) \right) \right\} ,
\end{aligned}
\tag{E.59}
$$

and

$$
\Delta_q^{(lj)}(r) = W_{LS}(-1)^l \frac{\tilde{\mathcal{J}}_q(r)}{r^2} \mathbf{l} \cdot \mathbf{s} .
\tag{E.60}
$$

Comparing both methods for the calculation of the spin-orbit Hartree-Fock and pairing-field matrix elements by using the density matrix and pairing tensor of the converged HFB solution for ^{114}Sn in an $e_{\mathrm{max}} = 8$ basis as input, we obtain an excellent agreement, with deviations of $0.4\,\mathrm{keV}$ or less.

Appendix F

Notation and Conventions

Units and Constants

The conversion factor between natural units $\hbar = c = 1$ and standard units is given by

$$\hbar c = 197.327053 \text{ MeV fm} . \tag{F.1}$$

Nucleon Properties			
$m_p \, [\text{MeV}]$	938.27231	proton mass	[137]
$m_n \, [\text{MeV}]$	939.56563	neutron mass	[137]
$m_N \, [\text{MeV}]$	938.91897	average nucleon mass	[137]
$r_p \, [\text{fm}]$	0.876	proton charge radius	[137]

Operators, Vectors, and Other Symbols

Vectors are denoted by bold-face letters, i.e. $\boldsymbol{x}$. For operators, a font of the Roman family is used: O. Vector operators are therefore written in bold-face Roman style: $\mathbf{L}$. Several common vectors and operators are listed below.

Symbol Conventions		
Vector	Operator	
$\hat{\boldsymbol{a}}$		general unit vector
$\boldsymbol{x}_i$	$\mathbf{x}_i$	single particle position
$\boldsymbol{p}_i$	$\mathbf{p}_i$	single particle momentum
$\boldsymbol{r} = \boldsymbol{x}_1 - \boldsymbol{x}_2$	$\mathbf{r}$	relative position of two particles
$\boldsymbol{q} = \frac{1}{2}(\boldsymbol{p}_1 - \boldsymbol{p}_2)$	$\mathbf{q}$	relative momentum of two particles
$\boldsymbol{R}$	$\mathbf{R}$	center-of-mass position
$\boldsymbol{P}$	$\mathbf{P}$	center-of-mass position

Operator Conventions	
Creation & Annihilation Operators	
$a_\mu^\dagger, a_\mu$	canonical particle basis
$c_k^\dagger, c_k$	general particle basis
$\alpha_\mu^\dagger, \alpha_\mu$	canonical quasiparticle basis
$\beta_k^\dagger, \beta_k$	general quasiparticle basis
Operators in A-Body & Fock Space	
o	k-body operator in k-body space
O	operator in many-body space
$O^{[k]}$	irreducible k-body part of an operator in many-body space
$o_{i_1 \ldots i_k}$	k-body operator in many-body space with respect to the subspace of particles $i_1, \ldots, i_k$
UCOM	
C	correlation operator in many-body space
$c = C_2$	correlation operator in two-body space
$\widetilde{O} = C^\dagger O C$	correlated operator in many-body space
$\widetilde{O}^{C2}$	correlated operator in two-body approximation
Other	
$t_q^{(k)}$	irreducible spherical tensor operator of rank k

Common Symbols	
$\langle j_1 m_1 j_2 m_2 \vert J M \rangle$	Clebsch-Gordan coefficient
$\begin{pmatrix} j_1 & j_2 & J \\ m_1 & m_2 & M \end{pmatrix}$	Wigner $3j$-symbol
$\begin{Bmatrix} j_1 & j_2 & j_{12} \\ j_3 & j & j_{12} \end{Bmatrix}$	$6j$-symbol
$\begin{Bmatrix} j_1 & j_2 & j_{12} \\ j_2 & j_3 & j_{23} \\ j_{12} & j_{23} & J \end{Bmatrix}$	$9j$-symbol
$\langle\langle N\Lambda, \nu'\lambda' \vert n_1'l_1', n_2'l_2'; L' \rangle\rangle$	Talmi-Moshinsky coefficient / harmonic oscillator bracket

Acronyms

EWSR	Energy-Weighted Summed Response/Sum Rule
GDR	Giant Dipole Resonance
GMR	Giant Monopole Resonance
GQR	Giant Quadrupole Resonance
GTR	Gamow-Teller Resonance
HF	Hartree-Fock
HFB	Hartree-Fock-Bogoliubov
IAR	Isobaric Analog Resonance
ISM	Isoscalar Monopole
IVD	Isovector Dipole
LN	Lipkin-Nogami (Method)
MBPT	Many-Body Perturbation Theory
NCSM	No-Core Shell Model
PNP	Particle Number Projection
PAV	Projection after Variation
PLN	Projected (after Variation) Lipkin-Nogami (Method)
QRPA	Quasiparticle Random Phase Approximation
RPA	Random Phase Approximation
SRG	Similarity Renormalization Group
UCOM	Unitary Correlation Operator Method
VAP(NP)	Variation after (Particle Number) Projection

Bibliography

[1] R. B. Wiringa, V. G. J. Stoks, and R. Schiavilla, Phys. Rev. **C51**, 38 (1995), nucl-th/9408016.

[2] R. Machleidt, Phys. Rev. **C63**, 024001 (2001), nucl-th/0006014.

[3] R. Machleidt and I. Slaus, J. Phys. **G27**, R69 (2001), nucl-th/0101056.

[4] E. Epelbaum, Prog. Part. Nucl. Phys. **57**, 654 (2006), nucl-th/0509032.

[5] P. Navratil, J. P. Vary, and B. R. Barrett, Phys. Rev. **C62**, 054311 (2000).

[6] R. Roth, H. Hergert, P. Papakonstantinou, T. Neff, and H. Feldmeier, Phys. Rev. **C72**, 034002 (2005), nucl-th/0505080.

[7] H. Feldmeier, T. Neff, R. Roth, and J. Schnack, Nucl. Phys. **A632**, 61 (1998), nucl-th/9709038.

[8] T. Neff and H. Feldmeier, Nucl. Phys. **A713**, 311 (2003), nucl-th/0207013.

[9] R. Roth, T. Neff, H. Hergert, and H. Feldmeier, Nucl. Phys. **A745**, 3 (2004), nucl-th/0406021.

[10] R. Roth, P. Papakonstantinou, N. Paar, H. Hergert, T. Neff, and H. Feldmeier, Phys. Rev. **C73**, 044312 (2006), nucl-th/0510036.

[11] N. Paar, P. Papakonstantinou, H. Hergert, and R. Roth, Phys. Rev. **C74**, 014318 (2006), nucl-th/0601026.

[12] P. Papakonstantinou, R. Roth, and N. Paar, Phys. Rev. **C75**, 014310 (2007), nucl-th/0609039.

[13] S. K. Bogner, R. J. Furnstahl, and R. J. Perry, Phys. Rev. **C75**, 061001 (2007), nucl-th/0611045.

[14] S. K. Bogner, R. J. Furnstahl, R. J. Perry, and A. Schwenk, (2007), nucl-th/0701013.

[15] H. Hergert and R. Roth, Phys. Rev. **C75**, 051001 (2007), nucl-th/0703006.

[16] M. Bender, P.-H. Heenen, and P.-G. Reinhard, Rev. Mod. PHys. **75**, 121 (2003).

[17] H. Feldmeier, personal communication.

[18] T. Neff, *Short-Ranged Central and Tensor Correlations in Nuclear Many-Body Systems*, PhD thesis, TU Darmstadt, 2002.

[19] D. J. Dean and M. Hjorth-Jensen, Rev. Mod. Phys. **75**, 607 (2003), nucl-th/0210033.

[20] J. Bardeen, L. N. Cooper, and J. R. Schrieffer, Phys. Rev. **106**, 162 (1957).

[21] P. Ring and P. Schuck, *The Nuclear Many-Body Problem*, 1st ed. (Springer, 1980).

[22] A. Zapp, *Kernstruktur mit effektiven Dreiteilchenpotentialen*, Diploma thesis, TU Darmstadt, 2000.

[23] S. Reinhardt, tba, Master's thesis, TU Darmstadt, 2008.

[24] R. Roth, *Effektive Wechselwirkungen für Quantenflüssigkeiten und Quantengase*, PhD thesis, TU Darmstadt, 2000.

[25] R. Machleidt, Adv. Nucl. Phys. **19**, 189 (1989).

[26] V. G. J. Stoks, R. A. M. Klomp, C. P. F. Terheggen, and J. J. de Swart, Phys. Rev. **C49**, 2950 (1994), nucl-th/9406039.

[27] S. K. Bogner, T. T. S. Kuo, and A. Schwenk, Phys. Rept. **386**, 1 (2003), nucl-th/0305035.

[28] S. D. Glazek and K. G. Wilson, Phys. Rev. **D48**, 5863 (1993).

[29] S. D. Glazek and K. G. Wilson, Phys. Rev. **D49**, 4214 (1994).

[30] F. Wegner, Ann. Phys. (Leipzig) **3**, 77 (1994).

[31] S. Szpigel and R. J. Perry, The Similarity Renormalization Group, in *Quantum Field Theory. A 20th Century Profile*, edited by A. N. Mitra, Hindustan Publishing Co., New Delhi, 2000, hep-ph/0009071.

[32] F. J. Wegner, Nucl. Phys. Proc. Suppl. **90**, 141 (2000).

[33] P. Navratil, G. P. Kamuntavicius, and B. R. Barrett, Phys. Rev. **C61**, 044001 (2000), nucl-th/9907054.

[34] S. K. Bogner, R. J. Furnstahl, P. Maris, R. J. Perry, A. Schwenk, and J. P. Vary, (2007), arXiv:0708.3754 [nucl-th].

[35] A. Nogga, H. Kamada, and W. Gloeckle, Phys. Rev. Lett. **85**, 944 (2000), nucl-th/0004023.

[36] L. Platter, H. W. Hammer, and U.-G. Meissner, Phys. Lett. **B607**, 254 (2005), nucl-th/0409040.

[37] R. Machleidt, F. Sammarruca, and Y. Song, Phys. Rev. **C53**, 1483 (1996), nucl-th/9510023.

[38] P. Doleschall, I. Borbely, Z. Papp, and W. Plessas, Phys. Rev. **C67**, 064005 (2003).

[39] P. Doleschall, Phys. Rev. **C69**, 054001 (2004).

[40] B. S. Pudliner, V. R. Pandharipande, J. Carlson, S. C. Pieper, and R. B. Wiringa, Phys. Rev. **C56**, 1720 (1997), nucl-th/9705009.

[41] J. L. Friar, D. Hüber, and U. van Kolck, Phys. Rev. **C59**, 53 (1999), nucl-th/9809065.

[42] D. R. Entem and R. Machleidt, Phys. Rev. **C68**, 041001 (2003), nucl-th/0304018.

[43] A. Nogga *et al.*, Phys. Rev. **C67**, 034004 (2003), nucl-th/0202037.

[44] P. Navratil, C. A. Bertulani, and E. Caurier, Phys. Rev. **C73**, 065801 (2006), nucl-th/0601019.

[45] M. E. Peskin and D. V. Schroeder, *An Introduction to Quantum Field Theory*, 5th ed. (Addison-Wesley, Reading, USA, 1997).

[46] S. Weinberg, *The Quantum Theory of Fields, Vol. I. Foundations*, 2nd ed. (Cambridge University Press, UK, 1996).

[47] R. Machleidt, (2007), arXiv:0704.0807 [nucl-th].

[48] R. B. Wiringa, S. C. Pieper, J. Carlson, and V. R. Pandharipande, Phys. Rev. **C62**, 014001 (2000), nucl-th/0002022.

[49] S. C. Pieper, K. Varga, and R. B. Wiringa, Phys. Rev. **C66**, 044310 (2002), nucl-th/0206061.

[50] S. C. Pieper, R. B. Wiringa, and J. Carlson, Phys. Rev. **C70**, 054325 (2004), nucl-th/0409012.

[51] E. Epelbaum, (2007), arXiv:0710.4250 [nucl-th].

[52] R. J. Furnstahl, personal communication.

[53] R. Roth, *Die Methode der unitären Korrelatoren und ihre Anwendung auf kurzreichweitig abstoßende Nukleon-Nukleon-Wechselwirkungen*, Diploma thesis, TU Darmstadt, 1997.

[54] I. Stetcu, B. R. Barrett, P. Navratil, and J. P. Vary, Phys. Rev. **C71**, 044325 (2005), nucl-th/0412004.

[55] I. Stetcu, B. R. Barrett, P. Navratil, and J. P. Vary, Phys. Rev. **C73**, 037307 (2006), nucl-th/0601076.

[56] Particle Data Group, S. Eidelman *et al.*, Phys. Lett. **B592**, 1 (2004).

[57] R. J. Furnstahl, Density Functional Theory for Nuclei, talk presented at *INT Workshop on New Approaches in Nuclear Many-Body Theory*, 2007, www.int.washington.edu.

[58] S. K. Bogner, R. J. Furnstahl, and R. J. Perry, (2007), arXiv:0708.1602 [nucl-th].

[59] V. I. Isakov, K. I. Erokhina, H. Mach, M. Sanchez-Vega, and B. Fogelberg, Eur. Phys. J. **A14**, 29 (2002), nucl-th/0202044.

[60] S. B. Khadkikar and V. B. Kamble, Nucl. Phys. **A225**, 352 (1974).

[61] L. Jaqua, M. A. Hasan, J. P. Vary, and B. R. Barrett, Phys. Rev. **C46**, 2333 (1992).

[62] A. Ehrlich, *Kernmaterie mit korrelierten realistischen NN-Wechselwirkungen*, Diploma thesis, TU Darmstadt, 2005.

[63] H. Hergert, *Correlated NN-Interactions and Phenomenological Corrections for Nuclear Structure Calculations*, Diploma thesis, TU Darmstadt, 2004.

[64] J. Goldstone, Proc. R. Soc. London **A239**, 267 (1957).

[65] B. D. Day, Rev. Mod. Phys. **39**, 719 (1967).

[66] M. R. Strayer, W. H. Bassichis, and A. K. Kerman, Phys. Rev. **C8**, 1269 (1973).

[67] D. J. Rowe, Phys. Rev. **175**, 1283 (1968).

[68] C. Barbieri, N. Paar, R. Roth, and P. Papakonstantinou, (2006), nucl-th/0608011.

[69] R. Roth and P. Navratil, in preparation.

[70] J. A. Sheikh and P. Ring, Nucl. Phys. **A665**, 71 (2000), nucl-th/9907065.

[71] J. A. Sheikh, E. C. Lopes, and P. Ring, Phys. Atom. Nucl. **64**, 477 (2001), nucl-th/0008009.

[72] H. Flocard and N. Onishi, Ann. Phys. **254**, 275 (1997).

[73] A. Valor, J. L. Egido, and L. M. Robledo, Nucl. Phys. **A671**, 189 (2000).

[74] T. H. R. Skyrme, Nucl. Phys. **9**, 615 (1959).

[75] D. Vautherin and D. M. Brink, Phys. Rev. **C5**, 626 (1972).

[76] M. Waroquier, K. Heyde, and H. Vincx, Phys. Rev. **C13**, 1664 (1976).

[77] A. Valor, J. L. Egido, and L. M. Robledo, Nucl. Phys. **A665**, 46 (2000), nucl-th/9911027.

[78] M. Anguiano, J. L. Egido, and L. M. Robledo, Nucl. Phys. **A696**, 467 (2001), nucl-th/0105003.

[79] J. Dobaczewski, M. V. Stoitsov, W. Nazarewicz, and P. G. Reinhard, (2007), arXiv:0708.0441 [Unknown].

[80] J.-P. Blaizot and G. Ripka, *Quantum Theory of Finite Systems* (MIT Press, 1986).

[81] J. L. Egido and P. Ring, Nucl. Phys. **A383**, 189 (1982).

[82] J. Decharge and D. Gogny, Phys. Rev. **C21**, 1568 (1980).

[83] M. Anguiano, J. L. Egido, and L. M. Robledo, Nucl. Phys. **A683**, 227 (2001), nucl-th/0008055.

[84] J. P. Vary, S. Popescu, S. Stoica, and P. Navratil, (2006), nucl-th/0607041.

[85] P. Navratil, V. G. Gueorguiev, J. P. Vary, W. E. Ormand, and A. Nogga, (2007), nucl-th/0701038.

[86] R. Roth and P. Navratil, Phys. Rev. Lett. **99**, 092501 (2007), arXiv:0705.4069 [nucl-th].

[87] J. A. Sheikh, P. Ring, E. C. Lopes, and R. Rossignoli, Phys. Rev. **C66**, 044318 (2002), nucl-th/0207080.

[88] M. V. Stoitsov, J. Dobaczewski, R. Kirchner, W. Nazarewicz, and J. Terasaki, Phys. Rev. **C76**, 014308 (2007), nucl-th/0610061.

[89] Y. Nogami, Phys. Rev. **134**, B313 (1964).

[90] H. J. Lipkin, Ann. Phys. (NY) **12**, 452 (1961).

[91] A. Kamlah, Z. Phys. **216**, 52 (1968).

[92] M. V. Stoitsov, J. Dobaczewski, W. Nazarewicz, and P. Ring, (2004), nucl-th/0406075.

[93] G. Hagen *et al.*, Phys. Rev. **C76**, 034302 (2007), arXiv:0704.2854 [nucl-th].

[94] G. Hagen, D. J. Dean, M. Hjorth-Jensen, T. Papenbrock, and A. Schwenk, Phys. Rev. **C76**, 044305 (2007), arXiv:0707.1516 [nucl-th].

[95] J. W. Negele, Rev. Mod. Phys. **54**, 913 (1982).

[96] J. Dobaczewski, H. Flocard, and J. Treiner, Nucl. Phys. **A422**, 103 (1984).

[97] B. Cochet, K. Bennaceur, J. Meyer, P. Bonche, and T. Duguet, Int. J. Mod. Phys. **E13**, 187 (2004), nucl-th/0310023.

[98] T. Duguet and P. Bonche, Phys. Rev. **C67**, 054308 (2003), nucl-th/0210057.

[99] B. Jancovici and D. H. Schiff, Nucl. Phys. **58**, 678 (1964).

[100] L. Robledo, Technical aspects of the implementation of the GCM with density-dependent forces, talk presented at *ECT* Workshop on Correlations in Nuclei: Beyond Mean-Field and Shell Model*, 2007, www.ect.it.

[101] S. Hassani, *Mathematical Physics* (Springer, 2002).

[102] B. G. Giraud, B. K. Jennings, and B. R. Barrett, (2007), arXiv:0707.3099 [nucl-th].

[103] J. Engel, Phys. Rev. **C75**, 014306 (2007), nucl-th/0610043.

[104] N. Barnea, (2007), arXiv:0711.0963 [nucl-th].

[105] J. P. Perdew and A. Zunger, Phys. Rev. **B23**, 5048 (1981).

[106] M. Bender and T. Duguet, Int. J. Mod. Phys. **E16**, 222 (2007), nucl-th/0611031.

[107] K. Dietrich, H. J. Mang, and J. H. Pradal, Phys. Rev. **135**, B22 (1964).

[108] M. V. Stoitsov, J. Dobaczewski, W. Nazarewicz, P.-G. Reinhard, and J. Terasaki, Particle-Number-Projected HFB Method with Skyrme Forces and Delta Pairing, in *Proceedings of the 8th International Spring Seminar on Nuclear Physics, Key Topics in Nuclear Structure, Paestum, Italy, 2004*, edited by A. Covello, p. 167, World Scientific, Singapore, 2005.

[109] J. Terasaki, F. Barranco, P. F. Bortignon, R. A. Broglia, and E. Vigezzi, Prog. Theor. Phys. **108**, 495 (2002), nucl-th/0109056.

[110] M. Anguiano, J. L. Egido, and L. M. Robledo, Phys. Lett. **B545**, 62 (2002), nucl-th/0205017.

[111] K. Hebeler, A. Schwenk, and B. Friman, Phys. Lett. **B648**, 176 (2007), nucl-th/0611024.

[112] H. Muther and W. H. Dickhoff, Phys. Rev. **C72**, 054313 (2005), nucl-th/0508035.

[113] J. Dobaczewski *et al.*, Phys. Rev. **C53**, 2809 (1996), nucl-th/9512008.

[114] J. Terasaki *et al.*, Phys. Rev. **C71**, 034310 (2005), nucl-th/0407111.

[115] N. Paar, P. Ring, T. Niksic, and D. Vretenar, Phys. Rev. **C67**, 034312 (2003), nucl-th/0212011.

[116] N. Paar, T. Niksic, D. Vretenar, and P. Ring, Phys. Rev. **C69**, 054303 (2004), nucl-th/0402094.

[117] D. J. Rowe, Rev. Mod. Phys. **40**, 153 (1968).

[118] D. J. Rowe, *Nuclear Collective Motion*, 1st ed. (Methuen and Co. Ltd., London, 1970).

[119] J. Suhonen, *From Nucleons to Nucleus. Concepts of Microscopic Nuclear Theory*, 1st ed. (Springer, Berlin, 2007).

[120] N. Paar, *Relativistic Mean-Field Description of Exotic Excitations in Finite Nuclei*, PhD thesis, TU München, 2003.

[121] K. L. G. Heyde, *The Nuclear Shell Model*, 2nd ed. (Springer, Berlin, Heidelberg, 1994).

[122] D. J. Thouless, Nucl. Phys. **22**, 78 (1961).

[123] F. Osterfeld, Rev. Mod. Phys. **64**, 491 (1992).

[124] J. P. Blaizot, Phys. Rept. **64**, 171 (1980).

[125] D. Vretenar, T. Niksic, and P. Ring, Phys. Rev. **C68**, 024310 (2003), nucl-th/0302070.

[126] J. Piekarewicz, Phys. Rev. **C76**, 031301 (2007), arXiv:0705.1491 [nucl-th].

[127] U. Garg, Nucl. Phys. **A788**, 36c (2007), nucl-ex/0608007.

[128] P. Papakonstantinou and R. Roth, (2007), arXiv:0709.3167 [nucl-th].

[129] O. Civitarese, A. G. Dumrauf, M. Reboiro, P. Ring, and M. M. Sharma, Phys. Rev. **C43**, 2622 (1991).

[130] A. Klimkiewicz *et al.*, Nucl. Phys. **A788**, 145c (2007).

[131] N. Paar, D. Vretenar, E. Khan, and G. Colo, Rept. Prog. Phys. **70**, 691 (2007), nucl-th/0701081.

[132] F. T. Avignone III, S. R. Elliott, and J. Engel, (2007), arXiv:0708.1033 [nucl-ex].

[133] T. Wakasa *et al.*, Phys. Rev. **C55**, 2909 (1997).

[134] T. Duguet, P. Bonche, P. H. Heenen, and J. Meyer, Phys. Rev. **C65**, 014310 (2002), nucl-th/0105049.

[135] T. Duguet, P. Bonche, P. H. Heenen, and J. Meyer, Phys. Rev. **C65**, 014311 (2002), nucl-th/0105050.

[136] M. V. Stoitsov, J. Dobaczewski, W. Nazarewicz, S. Pittel, and D. J. Dean, Phys. Rev. **C68**, 054312 (2003), nucl-th/0307049.

[137] Particle Data Group, K. Hagiwara *et al.*, Phys. Rev. **D66**, 010001 (2002).

[138] D. A. Varshalovich, A. N. Moskalev, and V. K. Khersonskii, *Quantum Theory of Angular Momentum* (World Scientific, 1988).

[139] A. R. Edmonds, *Angular Momentum in Quantum Mechanics* (Princeton University Press, 1957).

[140] J. Sakurai, *Modern Quantum Mechanics*, 1st ed. (Addison-Wesley, 1985).

[141] I. Talmi, Helv. Phys. Acta **25**, 185 (1952).

[142] M. Moshinsky, Nucl. Phys. **13**, 104 (1959).

[143] G. P. Kamuntavicius, R. K. Kalinauskas, B. R. Barrett, S. Mickevicius, and D. Germanas, Nucl. Phys. **A695**, 191 (2001), nucl-th/0105009.

[144] R. D. Lawson, *Theory of the Nuclear Shell Model* (Oxford University Press, New York, USA, 1980).

[145] A. Bulgac, Phys. Rev. **C65**, 051305(R) (2002), nucl-th/0108014.

[146] A. Bulgac and Y.-l. Yu, nucl-th/0109083.

[147] J. Berger, M. Girod, and D. Gogny, Comp. Phys. Comm. **63**, 365 (1991).

Danksagung

Lebenslauf

Zur Person

Name:	Heiko Hergert
Geburtsdatum:	09. Juni 1978
Geburtsort:	Büdingen
Staatsangehörigkeit:	deutsch
Eltern:	Johann Heinrich Hergert
	Adelheid Elisabeth Luise Hergert, geb. Brücher (†)
Familienstand:	ledig

Bildungsweg

07/1984-05/1988	Besuch der Mittelpunktschule Kefenrod (Grundschule)
07/1988-06/1997	Besuch des Wolfgang-Ernst-Gymnasiums in Büdingen
06/1997	Abitur, Gesamtnote: 1.0
08/1997-08/1998	Zivildienst in der Klinik Rabenstein, Bad Salzhausen
10/1998-02/2004	Studium der Physik an der TU Darmstadt
01/2003-01/2004	Anfertigung der Diplomarbeit *"Correlated NN-Interactions and Phenomenological Corrections for Nuclear Structure Calculations"*
02/2004	Diplom, Gesamtnote: sehr gut
03/2004-02/2008	Promotionsstudium an der TU Darmstadt und Anfertigung der Dissertation
seit 03/2004	Wissenschaftlicher Mitarbeiter am Insitut für Kernphysik